Spectrochimica Acta Part B: Atomic Spectroscopy 221 (2024) 107050

Contents lists available at ScienceDirect

Spectrochimica Acta Part B: Atomic Spectroscopy

journal homepage: www.elsevier.com/locate/sab

Resolving studies of Balmer alpha lines relevant to the LIBS analysis of hydrogen isotope retention

I. Traparic [a], D. Rankovic [b], B.D. Stankov [a], J. Savovic [c], M. Kuzmanovic [b], M. Ivkovic [a,*]

[a] Institute of Physics, University of Belgrade, 11080 Belgrade, Serbia
[b] Faculty of Physical Chemistry, University of Belgrade, 11158 Belgrade, Serbia
[c] Vinca Institute of Nuclear Sciences, University of Belgrade, 11000 Belgrade, Serbia

ARTICLE INFO

Keywords:
Hydrogen isotopes
Balmer alpha lines
LIBS, hydrogen isotope retention
Plasma-facing components

ABSTRACT

Utilizing Laser-Induced Breakdown Spectroscopy (LIBS) for detecting deuterium and tritium retention in fusion devices poses a significant challenge due to the experimental limitations in resolving hydrogen isotope Balmer alpha lines (H_α, D_α, and T_α). This study utilizes the Rayleigh criterion to distinguish T_α and D_α lines by determining the maximum line widths and corresponding plasma parameters. Experimental validation was performed through LIBS analysis of heavy water-doped graphite/silica gel targets in both argon and helium atmospheres to assess the predicted plasma parameters and line profile shapes. The optimization of laser pulse energy, gas pressure, delay, and gate times aimed at achieving fully resolved lines based on the intensity, width, and the dip between deuterium and hydrogen Balmer alpha lines. By fine-tuning these experimental parameters, the study successfully achieved a dip of less than 10 % between the H_α and D_α lines with a satisfactory signal-to-noise ratio, demonstrating the feasibility of fully resolving the T_α and D_α lines. These findings underscore the potential of LIBS in enhancing the detection of deuterium and tritium retention in fusion devices.

1. Introduction

Resolving the challenges surrounding energy production stands at the forefront of modern science and technology. Nuclear fusion is a clean and sustainable energy production that holds the promise of addressing global energy demands. A fusion reactor uses deuterium (D) and tritium (T) as fuels to produce inert gas helium, high-speed neutrons, and vast amounts of energy without producing long-lived radioactive waste. Despite its immense potential, the complexity and costliness of fusion reactors necessitate collaborative efforts on an international scale, exemplified by the joint endeavor to construct the International Thermonuclear Experimental Reactor (ITER) among participating nations such as the EU, USA, Japan, Russia, China, India, and South Korea [1].

The development and maintenance of nuclear fusion reactors are vital to sustain the promise of clean and efficient energy production. Amidst the complex operational challenges faced by fusion reactors, attention must be given to the impact on plasma-facing components (PFCs), exposed to various stresses, requiring meticulous material composition monitoring and particularly critical hydrogen isotope retention studies. In a nuclear fusion reactor, PFC faces intense plasma radiation, thermal loads, and neutron fluxes, leading to structural material damage. Thermal loads may cause re-crystallization, cracks, melting, and dust formation. Plasma exposure leads to sputtering, hydrogen isotope retention, and helium-induced morphology changes. Potential defects and transmutations may appear under neutron action. Because of this, in-situ real-time material analysis is essential to prevent an unexpected failure. Monitoring hydrogen isotope retention in PFCs is particularly important as it may affect fuel efficiency, plasma density, and the density of neutral hydrogen in the plasma boundary, essential for the safe operation of nuclear fusion installations [2]. Consequently, hydrogen isotope retention studies play a key role in PFC diagnostics [2–6].

Numerous research papers focus on various methodologies for PFC characterization [7,8]. Two currently significant techniques for the ex-situ characterization of fusion-relevant materials are accelerator-based Ion Beam Analysis (IBA) and Thermal Desorption Spectroscopy (TDS) [3,9–13]. IBA encompasses setups like Nuclear Reaction Analysis (NRA) and Elastic Recoil Detection Analysis (ERDA) crucial for quantifying light isotopes due to their sensitivity and selectivity. Additionally, TDS offers insights by analyzing demounted (from the reactor) material samples using a quadrupole mass spectrometer with an enclosed ion source to evaluate hydrogen isotope desorption behavior. However, TDS

* Corresponding author.
E-mail address: ivke@ipb.ac.rs (M. Ivkovic).

https://doi.org/10.1016/j.sab.2024.107050
Received 10 June 2024; Received in revised form 13 September 2024; Accepted 16 September 2024
Available online 21 September 2024

cannot provide information on the depth distribution of fuel concentrations. Radiofrequency Glow Discharge Spectrometry (RF-GDOES) proves effective for depth profiling of PFCs, as demonstrated in studies such as the analysis of deuterium in tungsten [2].

Laser Induced Breakdown Spectroscopy holds a prominent position among techniques applied for PFCs analysis within fusion devices. Its analytical capabilities have been extensively documented in many books and review articles [14–20]. LIBS is a minimally invasive non-contact technique suitable for multi-element analysis, including depth profiling, without requiring sample preparation. The technique is adaptable for vacuum or low-pressure gas environments and excels in remote in situ analysis. Notably, LIBS allows for on-site analysis without the need to dismantle or cut samples from the reactor, reducing costs and eliminating issues related to PFC replacement due to structural non-uniformity. Moreover, LIBS offers versatility in analyzing various reactor components beyond those that are easily disassembled. Review articles [21–23] provide an overview of the current state of LIBS development for fusion applications. Various LIBS systems were used for diverse characterization objectives, such as identifying elemental composition, depth profiling, deposited layer thickness, or spatial analysis. The efficiency of LIBS as a remote online diagnostics tool was demonstrated by analyzing multilayer structures, simulating the surface of a PFC covered with deposited impurity layers [24]. Specifically tailored LIBS configurations optimized for vacuum operation showcased promising results, including a compact system integrated onto the robotic arm of the Frascati Tokamak Upgrade (FTU) for ITER-relevant sample analysis [25], demonstrating improved spectral resolution in double-pulse (DP-LIBS) over single-pulse (SP-LIBS) configurations. Notably, the exceptional sensitivity of LIBS to lighter elements has been found application in hydrogen isotope retention investigations [26–35]. At Experimental Advanced Superconducting Tokamak (EAST) [26], a remote in situ laser-induced breakdown spectroscopic (RIS-LIBS) system has been developed for the determination of PFC composition (fuel retention, impurity deposition, and deposited layer thickness) [26]. Isotope lines D_α and H_α were identified but only partially resolved. The limit of detection of H/D was estimated to be about 200 ppm in the lithium layer on the first wall [27] applied LIBS for in-situ probing of D retention and Li deposition on a W-PFC surface after being exposed to D plasmas in a tokamak. Deuterium retention inside both pure and lithiated tungsten was investigated, and it was found that the Dα and Hα signals of lithiated W are significantly more intense than those of pure W. LIBS was also applied for in-situ diagnostics of the Li-H/D co-deposition on the first wall of EAST [28]. The results showed that the D_α and H_α signal intensities disappeared after the third laser shot, which was explained by the greater depth of the nanosecond laser ablation than the thickness of the deposited impurity layer. Additionally, femtosecond laser filamentation-induced breakdown spectroscopy combined with chemometrics methods was used to quantify deuterium content in water samples [29]. Filamentation was found to suppress spectral broadening, and well-resolved peaks of H_α and D_α were obtained. Burger et al. [30] studied the segregation of species and spectral line broadening in D_2O-H_2O plasma produced by single- and double-pulse nanosecond laser ablation in air. It was found that species segregation for laser-produced plasma formed in the air does not significantly impact the ability to distinguish D_α and H_α Balmer lines for the SP-LIBS and DP-LIBS. Fantoni et al. [31] studied the resolving of H_α and D_α lines using double pulse configuration with Nd:YAG lasers having energy of 170 mJ at 1.06 μm to irradiate, in vacuum, Mo target co-deposited with W, Al, and D using vacuum arc deposition method. With a 300 ns delay between pulses, H_α and D_α lines are almost resolved according to the Rayleigh criteria, thus enabling line intensity determination using fitting with Pseudo Voigt functions.

Kautz et al. [32,33] obained an even better resolution by using fs Ti-saphire laser (800 nm, 35 fs, 5 mJ) to irradiate H and D loaded Zircaloy-4 targets. In 10 Torr of He, using a gate of 2 μs, FWHM of hydrogen lines from 0.08 to 0.05 nm was obtained for delays from 1 to 26 μs [33]. Using an ns laser and different pressures of Ar, a slightly greater FWHM was obtained. Later [34], using the same fs laser irradiation of the Zircaloy-4 target with incorporated D or T in 26 Torr of Ar, the hydrogen Balmer alpha lines are clearly resolved from the D_α or T_α. Lowering gas pressure, the line width goes even below 0.08 nm, but the line intensity drops even faster, thus limiting the possibility for resolving D_α from T_α.

Recently [35], the analysis of the parameters influencing resolving and recordings of the fully resolved D_α and H_α lines are obtained in 30 Torr of Ar at delays of 60 μs, but without indicating other experimental conditions.

Achieving direct Laser-Induced Breakdown Spectroscopy (LIBS) analysis of hydrogen isotopes remains a formidable challenge due to the high electron density in laser-induced plasma, intensifying Stark broadening and hindering the clear distinction of closely spaced spectral lines of different H isotopes.

This research aims to enhance the resolution and sensitivity of LIBS for detecting hydrogen isotopes in fusion-relevant materials. The initial focus involved a theoretical exploration to ascertain the maximum line widths for resolving hydrogen Balmer alpha D_α and T_α lines and to determine their real intensity. Parameters such as maximum temperature, electron number density, and instrumental width in conjunction with peak intensity ratios were meticulously assessed. In addition, the influence of the applied approximations on maximum line widths was evaluated.

The experimental verification of obtained results, i.e., generation of plasma condition necessary to resolve hydrogen isotopes Balmer lines, was performed using an earlier proposed [36] CO_2 laser-based LIBS under a low-pressure helium and argon atmosphere. Different graphite targets incorporated with heavy water (D_2O) were analyzed, including the silica gel-doped wet graphite targets.

2. Theoretical considerations

In this section, the requirements for resolving Balmer alpha lines of hydrogen isotopes were analyzed and calculated. Special attention was devoted to calculating the requirements for resolving the tritium Balmer alpha line. This is necessary since tritium control and retention studies are critical for the safety operation of fusion power plants due to the possibility of tritium permeation into the coolant and the difficulties associated with its recovery [37].

However, as tritium is radioactive and its determination is experimentally challenging, laboratory studies of hydrogen retention primarily rely on analyzing deuterium content. A key parameter in applying isotopically resolved LIBS for retention studies is the relation between line broadening and the isotopic shifts. Compared to other Balmer series lines, the Balmer alpha lines, besides being the most intense visible hydrogen line, have lesser Stark broadening than isotopic shifts, so they are commonly selected for hydrogen retention studies. Namely, H_β and D_β lines cannot be resolved under typical LIBS plasma conditions ($N_e = 10^{22}$ m^{-3} and $T_e = 10.000$ K) since the isotopic shift for the Balmer beta H_β - D_β lines is 0.13 nm [38], while the Stark widths of these lines are 1 nm (according to the computer simulation (CS) calculations [39]). Contrary, under the same plasma conditions, the Stark width of the Balmer alpha lines is 0.23 nm [39], while the isotopic shift for H_α - D_α is 0.18 nm and 0.23 nm for H_α - T_α [38]. The main task of our research was to enhance the sensitivity of LIBS for the detection of hydrogen isotopes. For that purpose, optimal plasma conditions must be found under which hydrogen lines broadening is reduced, peak separation improved, and emission signal increased.

2.1. Determination of the critical FWHM for resolving hydrogen isotope lines

The first step in the analysis was to determine the limiting values of the spectral line widths necessary for resolving the H-D-T lines. From the spectroscopic point of view, lines are resolved if they fulfill the Rayleigh

criterion [29]. Therefore, the theoretical analysis of the overall line profiles (when all three isotopes are present in plasma) was performed to determine the maximum width of spectral lines that satisfy the Rayleigh criterion.

It is shown that the fitting of the hydrogen Balmer series lines with one, two, 4, 6, or seven Lorenzian excellent matches theoretical Stark profiles [40]. This and the fact that fitting the overall hydrogen profiles with one or sum of the Voigt function [40–42] also gives an excellent matching is a clear consequence of the fine structure of these lines. Since each fine structure component can be presented by the Voigt function, the resulting overall profile also has the Voigt shape [43]. Of course, such an approximation can be applied only above the fine structure limit [44]. On the contrary, it is unclear how such a fitting with several Voigt profiles can be easily applied for electron number density diagnostics.

Therefore, in many applications hydrogen profiles were fitted with a single Voigt profile. Determination of the full half width at half maximum, FWHM by such fitting procedure is adequate and is used in this work. On the contrary, deconvolution to determine Stark contribution by equalizing it with Lorentzian contribution to the overall line width may lead to significant errors [45]. More details about this approximation in determining electron density will be discussed in Section 2.3.

First, H_α, D_α, and T_α spectral lines, having the same intensity and line width, were generated using the Voigt approximation, which treats each peak as a sum of fractional contributions of the Gaussian and Lorentzian shapes:

$$w_V = 0.5346 \bullet w_L + \sqrt{0.2169 \bullet w_L^2 + w_G^2} \quad (1)$$

where w_V, w_L, and w_G are the full width at half maximum (FWHM) of the Voigt, Lorentz, and Gaussian profiles, respectively [46].

The Gaussian contribution is taken as the combination of the instrumental (w_i) and the Doppler broadening (w_D) [47]:

$$w_G = \sqrt{w_D^2 + w_i^2} \quad (2)$$

$$w_D = 7.16 \times 10^{-7} \lambda (T/M)^{1/2} \quad (3)$$

where T and M are the temperature and mass of the radiating atom in atomic mass units, and λ is the central wavelength in nm.

The estimated maximum line width (critical FWHM) for which the hydrogen isotope lines can be resolved is shown in Fig. 1. According to Rayleigh's criterion, assuming that the hydrogen isotope line intensities are the same, the critical FWHM to separate the H_α peak from the blended D_α/T_α lines is 0.18 nm (Fig. 1a), and 0.054 nm to resolve the D_α from T_α line (Fig. 1b). It should be stressed that even when D_α /H_α line pair is resolved, the information about T_α may be lost entirely. In addition, if one wants to resolve D_α /T_α line pair, the dip between the D_α and H_α lines should be 10 % or less of the smaller line peak intensity.

Resolved deuterium and hydrogen lines were obtained in LIBS spectra of samples with different deuterium concentrations, confirming that the critical FWHM for H_α/D_α line separation is attainable [29–36]. It is much harder to attain the minimum peak width necessary to separate the D_α - T_α line pair. In addition, the critical FWHM for resolving lines depends on the assumed peak intensities' ratio, R. Dependence of, determined, (critical for D_α and T_α lines resolving according to the Rayleigh criterion) FWHM dependance on a line intensity ratio in the range from 0.1 to 1 is presented in Table 1. The critical FWHM depends on the assumed ratio between D_α and T_α line intensities, R, regardless of which line is more intense, i.e., there was no difference between critical FWHM values obtained for intensity ratios of 0.5 and 2. Therefore, Table 1 presents only the values for intensity ratios between 0.1 and 1. To simplify procedure for critical FWHM determination, lines were approximated by Voigt profiles using the same line width for all lines.

As illustrated in Table 1, the determined critical FWHM of Voigt profiles for resolving D_α and T_α lines go from 0.027 to 0.054 nm, depending on the line intensity ratio. The results in Table 1 suggest that as the intensity ratio between these two lines decreases, it becomes more challenging to resolve D_α and T_α lines experimentally.

The dependence of determined critical FWHM on the assumed ratio of peak intensities of the Balmer alpha lines can be, besides in Table 1, presented by eq. (4), which enables easy calculation of the maximum FWHM necessary for resolving studied lines, for the estimated value of R:

$$FWHM_{cr} = 0.0599 - 0.0388 \times exp(-1.765 \times R) \quad (4)$$

2.2. Critical plasma parameters for resolving hydrogen isotope lines

Resolving hydrogen isotope lines requires detecting a spectral signal at reduced electron density with corresponding narrower line widths. In other words, plasma parameters (T and N_e) must be optimized to ensure the conditions necessary to decrease electron density without a

Table 1
Critical FWHM for resolving D_α and T_α for different intensity ratios.

Line intensity ratio (R)	0.1	0.3	0.5	0.67	0.8	1
Critical FWHM	0.027	0.038	0.044	0.047	0.050	0.054

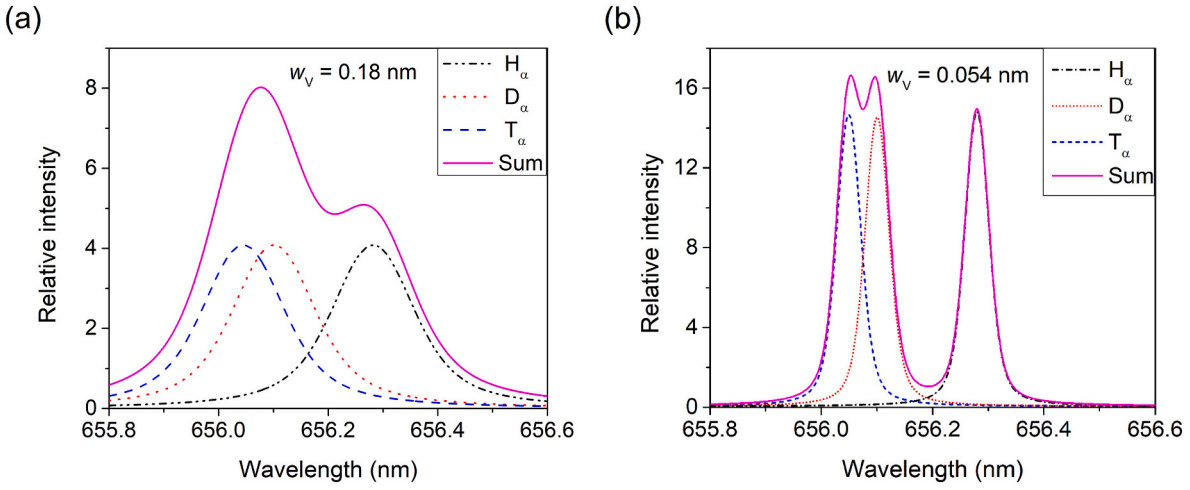

Fig. 1. Voigt approximation of hydrogen spectral lines having equal line widths and intensities and critical FWHM for resolving (a) H_α and D_α and (b) D_α and T_α peaks.

significant decrease in light emission intensity.

Electron density from the width of the H_α can be determined using different approaches since much work was devoted to studying this line. For example, it is shown [48] that using Griem theory, there is a considerable difference between electron densities determined from Balmer alpha and Balmer beta line widths. Having in mind the high accuracy of the H_β line theory, electron density can be determined using the correction factor between theories of the H_α and H_β widths.

In this work, according to the approximation that the Stark profile of the H_α line at electron densities greater than 10^{21} m^{-3} is close to Lorentzian [45], the eq. (1) was used to obtain Stark broadening contribution to overall line width, assuming $w_L = w_S$. Then, eq. (5) [39] was used to calculate N_e:

$$N_e\left[m^{-3}\right] = 10^{23} \bullet (w_S[nm]/1.098)^{1.47135} \quad (5)$$

Fig. 2 shows the maximum values of plasma parameters (T and N_e), under which critical FWHM for T_α, D_α resolving is obtained, estimated for different values of the instrumental FWHM parameter, w_i. Plasma parameters were calculated for two critical line width values corresponding to two values of R spectral line intensity ratios. Upon approaching the limit value of $N_e = 1.2 \times 10^{21}$ m^{-3} as shown in Fig. 2a, it becomes impossible to obtain the parameters (T and w_i) required to resolve both the D_α and T_α, when $R = 1$. Additionally, it is observed that for an electron density of approximately 4×10^{20} m^{-3} and temperature less than 6000 K, (corresponding to LIBS plasma at later evolution times), the instrumental FWHM should be less than 0.027 nm to resolve the T_α and D_α lines. Also, with equal peak intensities, if the temperature is higher than 10,000 K and N_e greater than 4×10^{20} m^{-3}, the instrumental width must be smaller than 0.02 nm. As shown in Fig. 2b, for an N_e lower than 1×10^{20} m^{-3} and a minimal instrumental width of less than 0.01 nm, the temperature cannot exceed 3000 K.

2.3. Validity of approximations used for simulation of line profiles

Several approximations were used to determine critical, i.e., maximal FWHM and plasma parameters necessary to resolve hydrogen isotope Balmer alpha lines. Therefore, the validity of these approximations and their influence on determined parameters will be analyzed.

2.3.1. Approximation of line profiles with Voigt function

The validity check of the Voigt approximation, in the determination of the plasma conditions required for resolving studied lines, was performed by comparing estimated parameters with those obtained using the Computer Simulation model of hydrogen spectral line profiles (CS tables) given by Gigosos et al. [39]. Previous studies [45] have confirmed the validity of approximating hydrogen Balmer alpha line shapes using the Voigt function. Conversely, determining the width by fitting hydrogen lines with the Voigt function, even by fixing the Gaussian contribution to the line width, can lead to significant errors at low electron densities. Therefore, the calculation of plasma parameters was performed using relation (5) [39,45] to improve their accuracy.

The difference in calculated values for the instrumental width $w_i = 0.01$ nm, and $w_i = 0.027$ nm respectively, (0.027 CS and 0.01 CS), was illustrated in Fig. 2 a,b, respectively. Error bars, included for these data in Fig. 2, indicate uncertainty of used formula. The slight variation between these values can be attributed to the contribution of a Doppler broadening mechanism because Voigt profiles were generated assuming identical widths of all three lines. For example, in the Voigt approximation, all three lines have a width of 0.054 nm, whereas the precise values are 0.0598 nm for H_α, 0.052 nm for D_α, and 0.049 nm for T_α.

2.3.2. Consistency in the assumption of the same stark widths and shifts

Different Stark widths of Balmer alpha lines of hydrogen and deuterium were reported [49]. The author measured the Stark-broadened line profiles of H_α and D_α in a wall-stabilized argon arc at an electron density of $N_e = 1.4 \times 10^{22}$ m^{-3} and found the half width of D_α to be about 15 % smaller than the width of H_α. It was found that only about 5 % of the measured 15 % difference between the experimental H_α and D_α profiles can be explained by differences in Doppler widths and inaccuracies in reproducing the exact electron density, while the major portion (≈ 10 %) must be attributed to ion dynamic effects. In reference [49], for the evaluation of N_e through the Stark broadening of the D_α line, the numerical factor of 0.9 was introduced in relation (5) to account for the reduced Stark broadening of the D_α compared to the H_α line.

Our study of the necessary conditions for resolving the H_α, D_α, and T_α peaks assumed the same values for FWHM of these lines. Therefore, the impact of disregarding the influence of the reduced mass on the line profile was examined using CS tables [39]. The analysis was performed for four values of a reduced mass of 0.5, 0.8, 1, and 2, corresponding (in case of equal gas and electron temperatures) to different plasma compositions: pure hydrogen, hydrogen-helium, hydrogen-argon, and a mixture of argon with deuterium or all three hydrogen isotopes, respectively. It was concluded that ion dynamics affects the line shapes, resulting in the observed difference in line widths. As a result, observed differences could impact the precision of estimated widths and plasma conditions for separating D_α and T_α peaks in the studied range of densities. Namely, according to the CS simulation results, a dip between

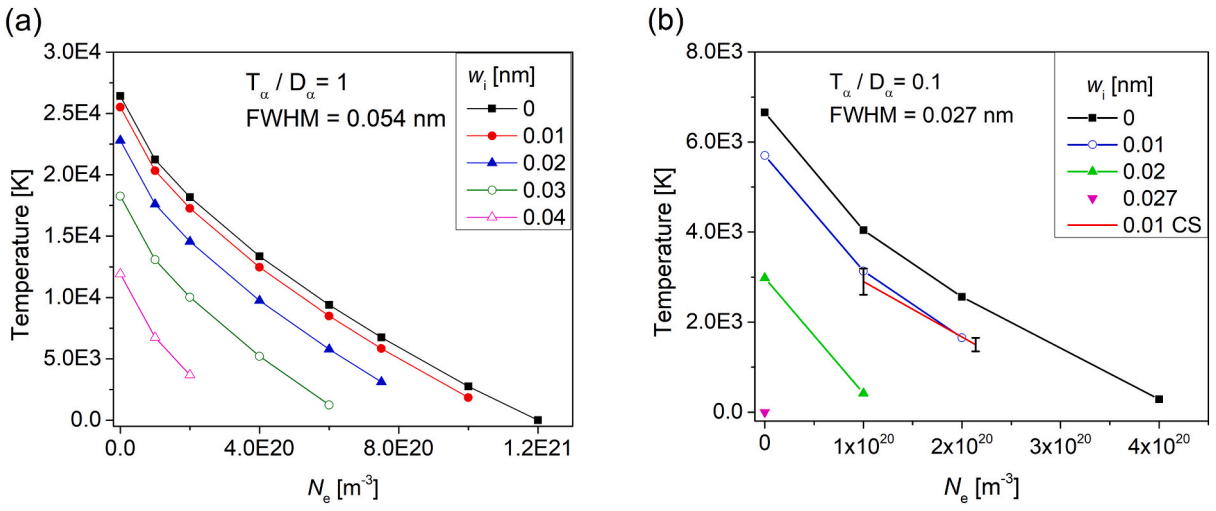

Fig. 2. Relationship of the maximal electron temperature versus the electron density corresponding to different values of the instrumental FWHM calculated for two critical line width values: a) critical FWHM = 0.054 nm, $T_\alpha/D_\alpha = 1$, and b) critical FWHM = 0.027 nm, $T_\alpha/D_\alpha = 0.1$.

lines increases with the increase of the reduced mass, which positively influences the conditions for resolving the hydrogen isotope lines. But, neglecting the influence of reduced mass on the line shapes by analyzing theoretical profiles for pure hydrogen only loosen the criteria for maximal FWHM for other μ. In addition, the hydrogen and deuterium spectral line profiles analyzed and experimentally tested in this work correspond to plasma with a simultaneous presence of hydrogen isotopes. On the contrary, in reference [49], measurements were performed for two experimental conditions (with a small percentage of the H or D added to Ar) having different reduced masses, which caused the stated difference in the hydrogen and deuterium line width.

3. Experimental methods and materials

Requirements for line resolution, analyzed in Chapter 2, were experimentally tested using the LIBS setup described in Section 3.1. Emission spectra were recorded using the spectrometer, the resolution of which is analyzed in Section 3.2. The selection of targets and their preparation procedures are described in Section 3.3. To verify the requirements for plasma parameters estimated in Chapter 2, temperature and electron number density diagnostics were performed. These results are described in Section 3.4.

3.1. Experimental setup

The breakdown on a solid target was generated using the modified carbon dioxide TEA laser (Tachisto 215G) operated at 10.6 μm, with a repetition rate of 1 Hz. The duration of the main laser pulse was 80 ns with a tail lasting 2 μs (see inset in Fig. 3). The targets were placed within the vacuum chamber mounted on the x-y table (Isel-automation 230,510). The chamber was vacuumed and filled with a continuous argon or helium gas flow at the desired pressure. The laser beam was focused perpendicular to the target surface using a ZnSe lens (L, f_1 = 100 mm), as illustrated in Fig. 3. Fast imaging was conducted through a lateral window of the vacuum chamber, capturing the plasma image and projecting it onto the entrance slit of a spectrometer. This process utilized an optical fiber settled at 15 degrees and equipped with a collimator (SolarLas PS2) for precise light transmission. For recordings of line shapes, a spectrometer (Sol Instruments MS7504i) was employed, outfitted with an iCCD camera (Andor Technology, model DH734I-18F-63 featuring 1024 × 1024 pixels, with a size of 13 × 13 μm and an 18 mm diameter intensifier). The iCCD was controlled using a pulse generator (DG-535, Stanford Research Systems), triggered optically by the occurrence of plasma on the target. A fast photodiode (PD) oriented towards the target was utilized to convert the light signal into electrical and trigger the DDG. Line shape recordings were performed with full vertical binning and different gate widths at various delay times. The acquisition gate width was varied between 15 ns and 70 μs. If not stated otherwise, the gate time was 5 μs. The shorter acquisition widths at earlier delays were favorable for tracking fast-changing plasma. Signals were recorded over ten accumulations to mitigate the influence of shot-to-shot variations.

3.2. Instrument selection and determination of instrumental profile

The initial step in experimental evaluation of the criteria for resolving hydrogen isotope Balmer alpha lines involved examining the spectrometer's resolution, i.e., determining the instrumental half-width. Namely, the instrumental half-width must be smaller than the values shown in Table 1. The shape and width of the instrumental profile of the MS 7504i spectrometer were determined by measuring radiation from the Ne pen lamp. The instrumental width (diffraction grating with 1800 groves/mm and a 15 μm wide entrance slit of spectrometer) was determined to be w_i = 0.03 nm. Thus, it was concluded that the spectrometer was suitable for resolution studies of hydrogen isotope Balmer alpha lines.

3.3. Preparation and testing of targets

The second task was selecting and preparing the targets that could serve as substitutes for the hydrogen isotope-enriched components of the plasma fusion reactor. The material selected for the present study was graphite because of its importance for fusion technology [50,51]. Two preparation procedures were used to obtain graphite targets with embedded D_2O. In the first case, a controlled amount of the D_2O was applied with a micropipette to the surface of a tablet made from spectroscopically pure graphite powder. In this way, graphite targets with a gradient concentration of hydrogen along the sample thickness were produced. These targets were suitable for depth analysis of hydrogen retention, i.e., recording LIBS spectra in which the intensity ratio of hydrogen over deuterium Balmer alpha lines changes with the number of laser shots.

In the second case, tablets were made from graphite powder doped with D_2O and mixed with silica gel (SiO_2). The silica gel was added to prevent a decrease in water content during vacuuming. Before mixing with D_2O-doped graphite, SiO_2 was ground to a fine powder and dried in an oven at 110 °C for 20 h to eliminate previously accumulated moisture. The best consistency of the tablets was achieved by mixing the graphite and silica gel powders in the proportion of 3:1. After pressing (10 tons hydraulic press for 30 min), the tablets were dried at 120 °C for

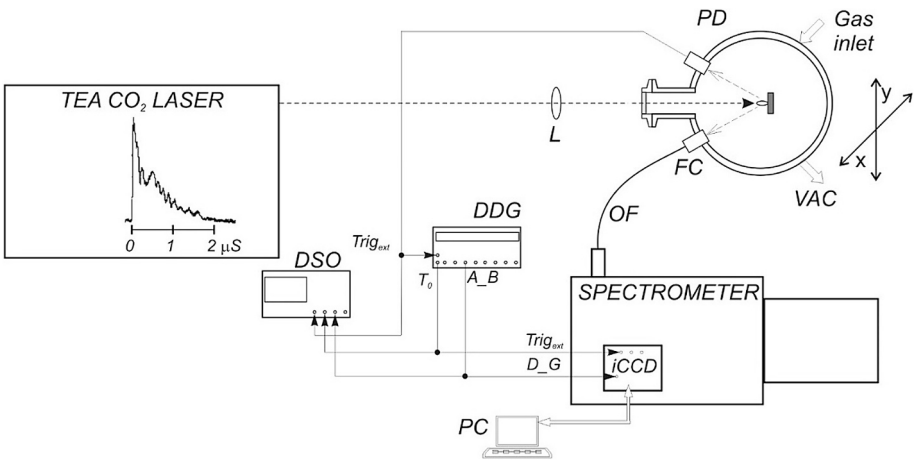

Fig. 3. Experimental setup: L-lens, PD-photodiode, OF-optical fiber, FC-focusing collimator, VAC-vacuum outlet, DSO-digital storage oscilloscope and DDG-digital delay generator.

6 h and stored in a desiccator to prevent moisture absorption. Targets prepared with this procedure had a homogeneous water distribution, as confirmed by LIBS spectra. The intensity ratio of the H_α and C II lines remained almost unchanged with increasing number of applied laser shots. The heavy water-doped graphite/silica gel targets were used in all further experiments.

3.4. Plasma diagnostics

The plasma parameter measurements were conducted to experimentally validate the conclusions drawn from the results depicted in Fig. 2. Electron number density was evaluated from the measurement of wavelength separation (s) between peaks of allowed (2p 3P°– 4d 3D) and forbidden (2p 3P°– 4d 3F°) component of the He I 447.1 nm line, using the relation (6) [52], with T_e in K, s in nm and N_e in m^{-3}:

$$log_{10}(N_e) = 21.5 + log_{10}\left[\left(\frac{s}{0.1479}\right)^{b(T_e)} - 1\right]$$

$$b(T_e) = 1.46 \times \frac{8380}{T_e^{1.2}} \quad (6)$$

From the spectra presented in Fig. 4 a, the separation between peaks was determined: $s = 0.206$ nm for shorter delay/gate times (0.5 μs / 5 μs) and 0.155 nm for longer delay/gate times (5.5 μs / 50 μs). The estimated N_e for shorter and longer delay/gate times were 2.5×10^{21} and 2.7×10^{20} m^{-3}, respectively.

In addition, N_e was determined from the parameters of the He I 492.2 nm line (2p ^{1}Po – 4d ^{1}D) with forbidden component (2p $^1P^o$ – 4f $^1F^o$ and 2p $^1P^o$ – 4p $^1P^o$ using the relation (7) [53], with Te in K, s in nm, and Ne in m^{-3}:

$$log_{10}(N_e) = 21.3065 + \left(\frac{1}{0.8766}\right) log_{10}\left[\left(\frac{s}{0.131187}\right)^{b(T_e)} - 1\right]$$

$$b(T_e) = 1.25 + \frac{994}{T_e} \quad (7)$$

Using the separation values $s = 0.203$ nm and 0.146 nm determined from Fig. 4 b, the calculated electron number density was $N_e = 1.5 \times 10^{21}$ and 2.2×10^{20} m^{-3} for shorter and longer delay/gate times, respectively. From data presented in Fig. 4, for separation between forbidden (F) and allowed (A) components ($s = 0.203$ nm and 0.146 nm) and their intensities ratios ($F/A = 0.196$ and 0.044) the following N_e values were obtained by interpolation of the data according to unified theory (BCS) [54]: 2.03×10^{21}, 3×10^{20}, 1.5×10^{21} and 3.66×10^{20} m^{-3}, which are in reasonable agreement with values obtained from the calculations based on approximative formulas [52,53].

The gas temperature was determined by comparing the synthetic and recorded spectra of the sequence $\Delta\nu = 0$ of the C_2 molecule Swann system at 515 nm. Fig. 5a shows a part of the $\Delta\nu = 0$ sequence of the C_2 molecule Swann system spectrum, obtained in an Ar atmosphere at reduced pressure (10 millibars) between the band heads (0–0) and (1–1). Spectra were obtained with different delay times (5, 10, and 15 μs), with a gate of 5 μs. As can be seen from the picture, the resolution of the spectrograph and the plasma conditions allow for obtaining spectra with a well-developed rotational structure, where the lines of the R and P branches are well-separated. Due to the decrease of plasma temperature with time, the band intensities obtained for different delay times decrease rapidly with increasing time. In general, the emission of molecular bands is characteristic of the peripheral plasma parts and/or later times of development of the laser-induced plasma: with increasing temperature, the intensity of the emission increases, but at the same time, the concentration of molecules decreases due to dissociation. The maximum emission intensity of the Swan system is usually reached at a temperature around 6700 K [55].

When the rotational structure of molecular band spectra is well resolved, it can be used to determine the temperature of heavy particles. The (0–0) band of the Swan system is very suitable for that purpose: the C_2 molecule has a sufficiently high dissociation energy (6.2 eV) and a sufficiently low excitation energy (2.4 eV) to obtain very intense spectra, and on the other hand, the structure of the energy levels is such that the components of rotational structures can also be separated using a medium-resolution spectrograph. Fig. 5 b shows a detail of the C_2 band spectrum synthesized for different temperatures, with a Gaussian profile corresponding to the instrumental profile of the spectrograph. The Pgopher program [56] was used to synthesize the spectra. The intensity ratio of R components and band head does not depend on temperature, so both synthesized and experimental spectra can be normalized to the intensity of the R component. This way of normalization is better than normalization using the (0–0) band head because of its potential self-absorption. As shown in Fig. 5 b, the intensity ratios of the R and P components of the (0–0) band strongly depend on temperature, so they can be used to estimate plasma temperature.

By comparing the normalized experimental and synthesized spectra, the temperature was estimated for different delay times: for a delay of 5 μs, a temperature value of 5000 K was determined, with an error of 10 %. With the delay time increase, a clear trend of temperature decrease was observed, from 4500 K for a delay of 10 μs to a temperature of about 3500 K for a delay of 20 μs. The intensities were significantly lower for delay times longer than 10 μs, considerably increasing the determination error.

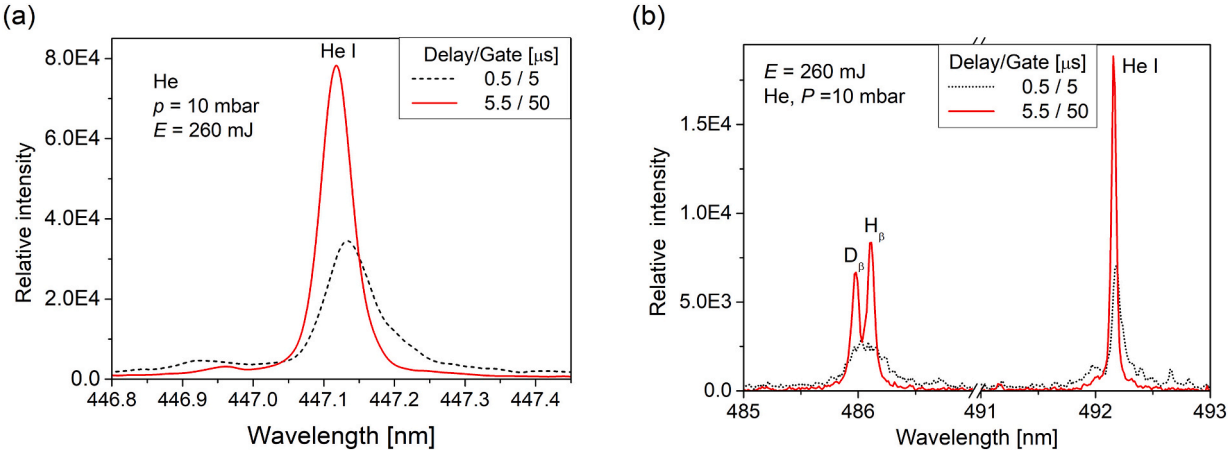

Fig. 4. Examples of the N_e diagnostics: (a) Shape of the He I line at 447.1 nm and (b) Shapes of the hydrogen isotope Balmer beta lines and He I line at 492.2 nm.

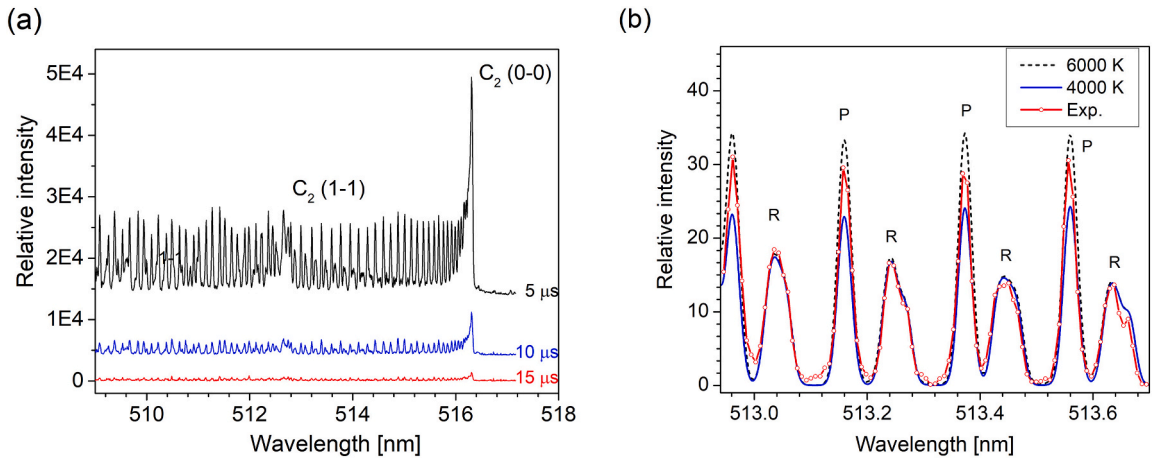

Fig. 5. (a) Experimentally obtained spectra of the Swan band ($\Delta\nu = 0$ sequence) for different delay times. (b) Synthesized normalized spectra for temperatures of 4000 and 6000 K and experimental spectrum for a delay time of 5 μs (part of the (0–0) band).

4. Results

The analysis outlined in Chapter 2 has shown that a necessary requirement for resolving hydrogen isotope lines is employing a spectroscopic instrument with minimal instrumental width and generating plasma with parameters (N_e and T) falling within the limits indicated in Fig. 2. The LIBS operation is commonly performed in air and spectral lines are recorded with some delay period to the laser pulse, to avoid the influence of continuum radiation, i.e., acquisition starts when lines of the studied elements appear in spectra and last, until their intensity becomes comparable to noise.

Typical temperature and electron number density values for laser-induced plasmas are around T = 15,000 K and $N_e = 10^{23}$ m^{-3} (or above) [14–20]. The value of N_e is almost two orders of magnitude greater than the values shown in Fig. 2. The plasma induced by Nd:YAG laser in Ar at reduced pressure is characterized by a lower N_e but still far above the values required to resolve the Balmer alpha line. For example, the H_α line measured in tungsten plasma induced in He atmosphere at 10 mbar had FWHM of around 0.5 nm [57], i.e., almost ten times greater than requested for resolving studied lines. In LIBS detection of hydrogen in molybdenum within mixtures of argon and nitrogen at atmospheric pressure it is observed that the width of the H_α line decreases (for the same delay), with shorter duration of plasma, i.e., emission intensities decrease faster than in pure argon [58]. The resolving of the H_α and D_α was obtained using double-pulsed LIBS (with ps and fs lasers) or laser-induced filamentation LIBS. However, the line widths were too wide to resolve D_α and T_α, like the line profiles shown in Fig. 1a.

Resolving D_α and T_α lines is the most critical task for LIBS analysis of hydrogen isotope retention, bearing in mind that the isotope shift between D_α and T_α is 0.0598 nm, while between H_α and $D_\alpha$is 0.1785 nm. The targets used in this study did not contain tritium. Nonetheless, the analysis presented in Section 2 (Fig. 1 b) demonstrates that when the H_α and D_α are distinctly resolved, and the dip between these lines accounts for less than 10 % of the intensity of the smaller peak, the requirements for resolving D_α and T_α are met.

In this work, we investigated the potential of LIBS based on TEA CO_2 laser for obtaining well-resolved hydrogen Balmer alpha lines. Experimental parameters were optimized by recording LIBS spectra of heavy water-doped graphite/silica gel targets under different experimental conditions. Three laser energies were used in this study, namely 260 mJ, 320 mJ and 420 mJ. Targets were irradiated in Ar and He atmosphere at different gas pressures (3–80 mbar), and spectra were recorded with variable delay (0.5–15 μs) and gate times (5–50 μs).

The characteristic dependence of the line profiles on delay time at He pressure of 30 mbar are shown in Fig. 6 a, and on He gas pressure at a delay time of 15 μs in Fig. 6 b. Each spectrum is a sum of 10 accumulated laser shots applied at the same spot on the target.

Based on Fig. 6, it can be inferred that ionized carbon lines start to emerge in the spectra during the initial phase of plasma evolution and persist for less than 5 μs. It should be stressed that the width of the C II lines (3 s ^{2}S - 3p ^{2}P^o) at 657.8 nm and 658.29 nm, recorded at the beginning of the plasma evolution, was 0.033 nm, which confirms that w_i is equal to or slightly less than the stated value. In addition, since the overall width is not greater than the instrumental width, we may conclude that the contribution of the other line-broadening mechanisms was negligible. Further, in the time window 0.5 μs – 5 μs, the N_e value was around 10^{21} m^{-3} since a Stark width of these lines, according to theory [59], is around 0.1 nm at $N_e = 10^{23}$ m^{-3}.

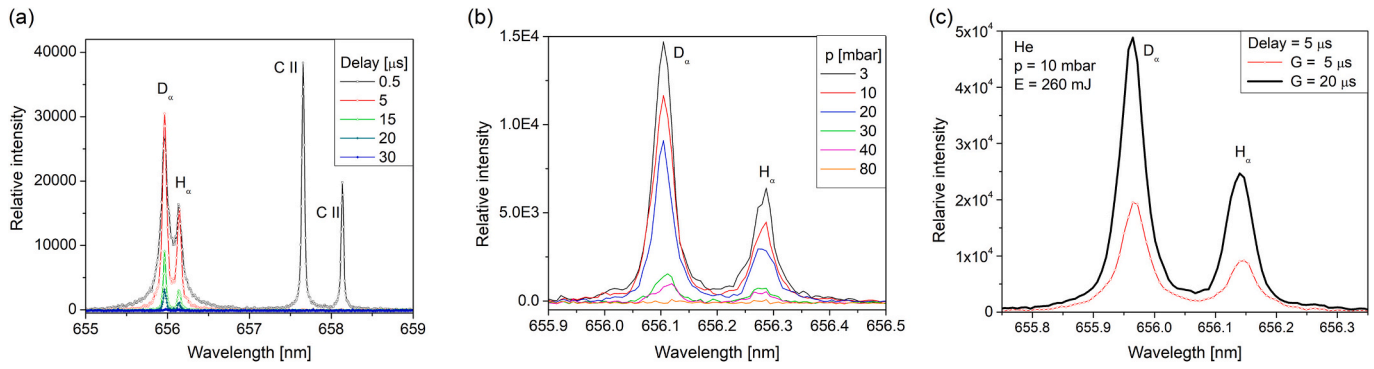

Fig. 6. Variation of line shapes: (a) with delay time at He pressure of 30 mbar and (b) on gas pressure at a delay of 15 μs. The influence of gate time on spectra (c) recorded in He at 10 mbar. All spectra were recorded using the laser energy of 260 mJ. Gate time for (a) and (b) was 5 μs. Delay for (c) was 5 μs.

After a few microseconds, the spectral lines of surrounding gas (He or Ar) and those of hydrogen become more pronounced, thus enabling adequate resolving of the Balmer alpha line from the closely spaced spectral lines of the target material. This fact is significant for studying hydrogen isotope retention in tungsten targets because the presence of the spectral line of W I at 656.32 nm or Be II line at 656.45 nm can make it difficult to separate it from the hydrogen Balmer alpha line. Furthermore, the Balmer alpha lines were not fully resolved at short delay times, see Fig. 6 a, indicating a preference for analysis at delays longer than 15 μs. Fig. 6 also shows that the dip between H_α and D_α lines decreases with increasing pressure. For pressure higher than 10 mbar, lines are fully resolved. Unfortunately, the intensities of Balmer lines diminish swiftly as the pressure and delay times increase. Hence, the primary objective of this study was to identify experimental parameters where line intensities significantly exceed the noise level and fulfill conditions required for resolution. As the plasma evolves, the line width decreases, indicating improved resolution. However, this decrease in width is accompanied by a decrease in intensity, which presents a drawback. Therefore, when the line width aligns with the instrumental resolution, the remaining signal can be captured by widening the gates for data collection. As an illustration, the spectra recorded in He at 10 mbar, using laser energy of 260 mJ and delay time of 15 μs for gate values of 20 μs and 5 μs, are shown in Fig. 6c.

In argon, under the same experimental conditions as for He gas, the intensity and shape of the hydrogen isotope Balmer alpha lines are considerably different due to the changes in electron number density, electron temperature, and different temporal and space evolution of plasma. The recorded line shapes for a laser energy of 420 mJ and a gate time of 5 μs are shown in Fig. 7a for various delay times.

Considerably greater electron number densities are obtained in LIBS with Ar compared to He. Consequently, the resolution of lines at the beginning of the plasma evolution is of poorer quality (Fig. 7a). However, plasma emission in Ar lasts longer, and for longer time delays (at 50 μs) well-resolved lines of sufficient intensity can also be obtained, see Fig. 7a. The line shapes obtained under same laser energy and gate time parameters, but under varying pressure, are depicted in Fig. 7b, for delay time of 0.5 μs.

As a figure of merit, which will clearly describe the quality of resolving of hydrogen lines, the dip between lines seems to be the most appropriate. The dip was defined as the minimum intensity between lines (presented as a percentage of the lowest peak intensity). Considering that determining the line widths requires fiting, it is clear that dip is a more adequate parameter. Namely, a dip may, without any other procedure, give a reasonable estimate of how far one is from the optimal conditions for resolving not only the H_α and D_α line, but also for resolving the deuterium and tritium Balmer alpha lines. Fig. 8 shows the dependence of the dip between hydrogen isotope lines versus studied parameters: laser energy, gas type and pressure, and delay times. For comparison, the line widths are also shown in the same figure.

In Fig. 8, it is evident that the dip value's dependency on gas pressure and laser energy is most notable during the initial stages of plasma evolution. However, as delay times progress, the line width approaches or matches the instrumental width, leading to dip changes among lines comparable to the measurement uncertainty. It is plausible to infer that employing a spectrometer of higher resolution would yield smaller dip and FWHM values, particularly at longer delays.

In argon (Ar), the dip increases with both pressure and laser energy due to the higher electron number density, resulting in an increase in the Stark width of the spectral line. Conversely, when using helium (He) as the surrounding gas, the increment in electron density is less pronounced, leading to a dip that remains nearly unaffected by changes in pressure and laser energy, under studied conditions.

Hydrogen isotope retention studies depend not only on resolving Balmer alpha lines but also on studied line peak intensities. Therefore, we presented the results for lines fitting in the form of peak intensity versus determined FWHM for all experimental parameters. In Fig. 9. gas pressure was used as a parameter, while data for various delay times are presented and labeled for each data point. On the same graph, the critical FWHM value of 0.054 nm (Chapter 2) for resolving D and T Balmer alpha lines having equal intensities is presented as a thick vertical line. The experimental points on the left side of the vertical line display plasma parameters where the line separation was deemed satisfactory. The vertical dotted line presents the value of the minimal instrumental width of the spectrometer. The red arrow indicates the data point for which optimal intensity and resolution of spectral lines were obtained.

Fig. 9 shows that resolved hydrogen isotope Balmer alpha lines can be obtained in both gases, but the line's intensity and signal-to-noise ratios is better in He than in Ar. In addition, at various line peak intensities, the dip between studied D_α and H_α lines is less than 10 % (see Fig. 8), i.e., line widths much less than 0.054 nm (see Fig. 9) can be obtained, which guarantees, according to the analysis presented in Chapter 2, resolving of D_α and T_α lines. At optimal conditions for resolving lines, the intensity is much lower than at the beginning of plasma evolution, see Fig. 10a, but still adequate for determining their intensities with high accuracy, see Fig. 10b.

5. Conclusion

This study examined the resolution of hydrogen isotope Balmer alpha lines, a crucial aspect for tritium retention investigations using LIBS. Key highlights of the study included determining the critical line

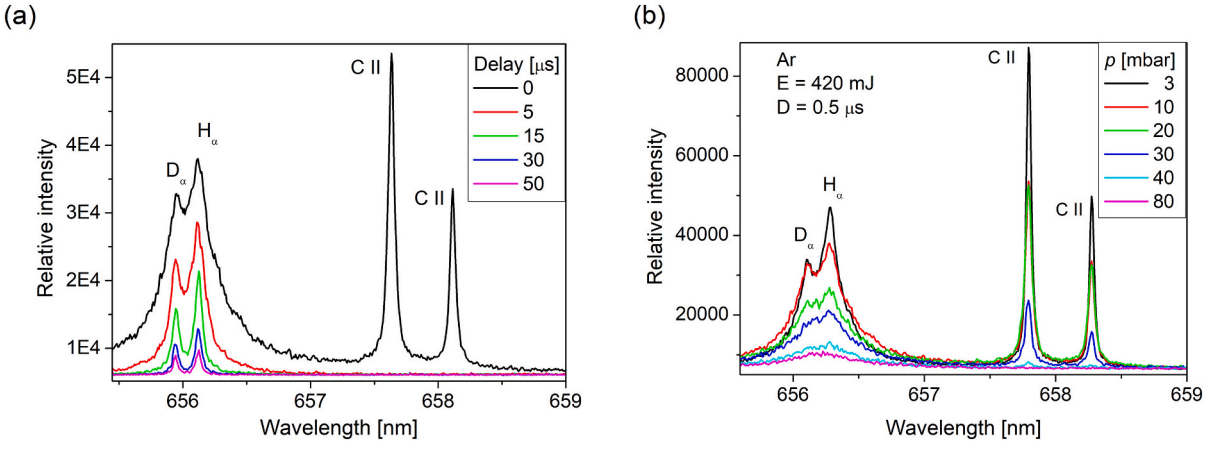

Fig. 7. Figure (a) illustrates the variation of line shapes with delay time at an argon pressure of 10 mbar, while figure (b) shows the influence of gas pressure at a delay of 0.5 μs. The laser energy and gate time used for these measurements were 420 mJ and 5 μs, respectively.

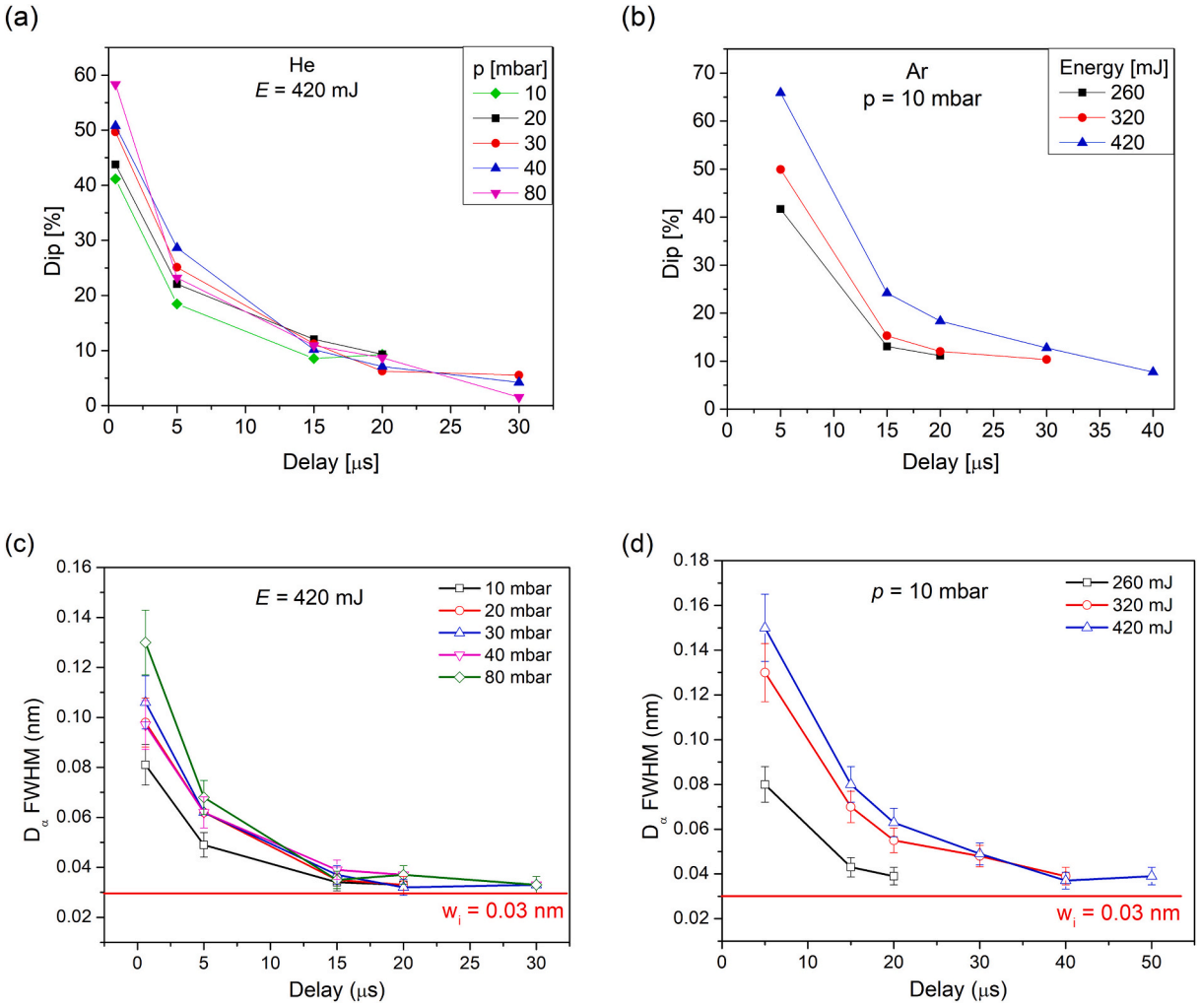

Fig. 8. Dip between H_α and D_α lines expressed in the percentage of the lower peak intensity versus delay for a different: (a) He gas pressure, (b) laser energy in Ar at 10 mbar. FWHM of the H_α and D_α lines at conditions: c) same as a) and d) same as b). All data are recorded using a gate time of 5 μs.

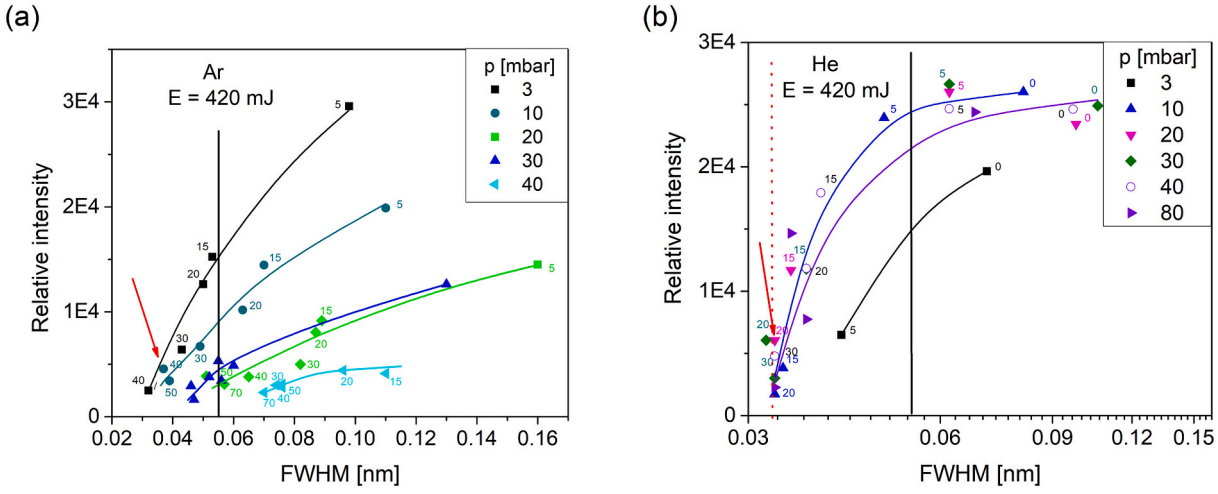

Fig. 9. Dependence of spectral line peak intensity on FWHM for different gas pressures of (a) Ar and (b) He at laser energy 420 mJ. A vertical line represents the maximum spectral line width (0.054 nm) for resolving D_α and T_α with equal peak intensity. Labels represent the values of delay time for each data point.

width ($FWHM_{cr}$) for resolving deuterium (D_α) and tritium (T_α) lines by applying Rayleigh criteria and Voigt profile approximations for hydrogen lines. The estimated $FWHM_{cr}$ ranged between 0.054 nm for equal peak intensities ($R = 1$) and 0.027 nm for $R = 0.1$. An approximate formula for calculating $FWHM_{cr}$ dependency on R was proposed. The study emphasized that fulfilling necessary conditions for resolving D_α

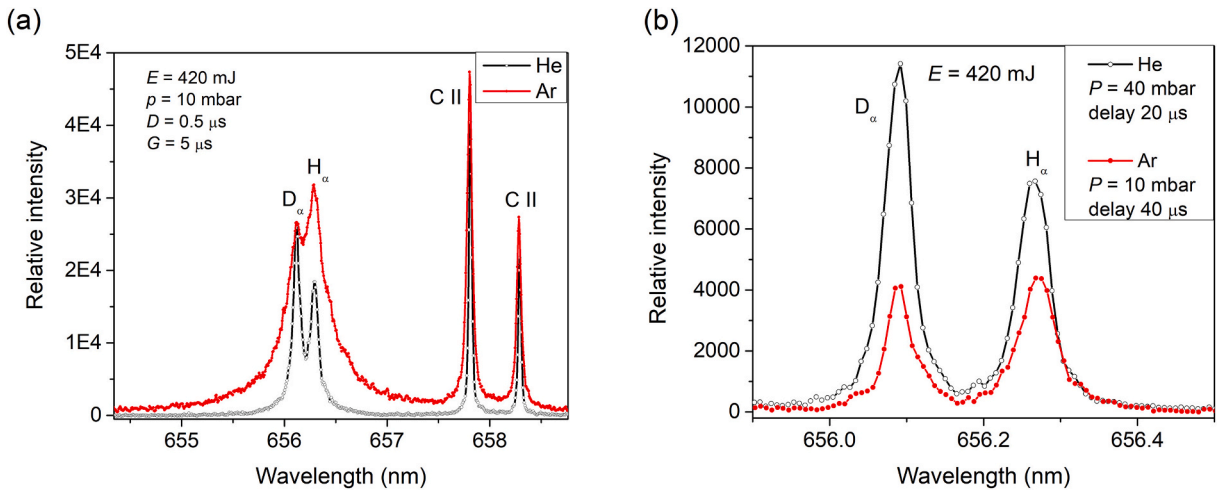

Fig. 10. Comparison of the Balmer alpha line shapes at (a) the beginning of the plasma evolution and at (b) optimal conditions: for He at 40 mbar at a delay 20 μs and for Ar at 10 mbar at a delay 40 μs.

and T_α required full resolution of H_α and D_α lines while ensuring the dip between these lines was less than 10 % of the smaller peak intensity.

Experimental validation of the determined conditions essential for resolving T_α and D_α was conducted using a LIBS setup employing a TEA CO_2 laser and recording plasma emission through an iCCD camera mounted on the spectrometer's exit slit with an instrumental width of 0.03 nm. Tests on hydrogen isotope retention in plasma-facing components were carried out using graphite samples doped with heavy water (D_2O) mixed with silica gel. Plasma parameters were assessed by determining electron number density from the separation between peaks of He I components and inferring temperature from the measured and synthetic segments of the C_2 molecule sequence $\Delta\nu = 0$. In the time frame of 0.5 μs – 5 μs, the electron number density was approximately 10^{21} m^{-3}, with plasma temperature around 5000 K and 3500 K for delays of 5 μs and 20 μs, respectively.

Spectra of hydrogen and deuterium Balmer alpha lines were obtained using different laser energies under varying experimental conditions in Ar or He atmospheres, impacting line resolution differently. Optimal conditions for plasma induced in He and Ar were identified concerning laser energy, gas pressure, and delay times, resulting in better intensities and signal-to-noise ratios. Resolving D_α and H_α lines with a dip below 10 % of the smaller peak intensity under optimal conditions showcased the potential for obtaining fully resolved T_α and D_α lines in both gas atmospheres.

Enhancement of the line intensities by using longer gate times (for recordings when at given delay time, the line width approaches instrumental width) is demonstrated.

CRediT authorship contribution statement

I. Traparic: Writing – review & editing, Investigation, Formal analysis. **D. Rankovic:** Investigation, Formal analysis. **B.D. Stankov:** Investigation, Formal analysis. **J. Savovic:** Writing – review & editing, Visualization, Formal analysis. **M. Kuzmanovic:** Writing – review & editing, Formal analysis. **M. Ivkovic:** Writing – review & editing, Writing – original draft, Supervision, Methodology, Conceptualization.

Declaration of competing interest

The authors declare that they have no known competing financial interests or personal relationships that could have appeared to influence the work reported in this paper.

Data availability

Data will be made available on request.

Acknowledgements

The research was funded by the Ministry of Science, Technological Development and Innovations of the Republic of Serbia, Contract numbers: 451-03-68/2022-14/200024 and 451-03-65/2024-03/200146, and supported by the Science Fund of the Republic Serbia, Grant no. 7753287 "NOVA2LIBS4fusion". This work was carried out under the project: "Laser induced breakdown spectroscopy for determination of LHD wall composition" (NIFS21KLPF087) within the agreement between NIFS and the University of Belgrade. The authors thank Stanko Milanovic for technical assistance in preparation´ and setting up the experiment.

References

[1] Fusion Energy and ITER. https://research-and-innovation.ec.europa.eu/research-area/energy/fusion-energy_en, 2024.
[2] L. Qiao, X. Zhang, R. He, H. Zhang, E. Fu, P. Wang, Experimental measurement of deuterium concentration and depth profiling in tungsten by radio frequency glow discharge optical emission spectroscopy, Spectrochim. Acta Part B At. Spectrosc. 173 (2020) 105975, https://doi.org/10.1016/j.sab.2020.105975.
[3] C. Cupak, E. Pitthan, M.V. Moro, M. Fellinger, D. Primetzhofer, F. Aumayr, Retention of deuterium in beryllium: a combined investigation using TDS, ERDA and EBS, Nucl. Mater. Energy. 33 (2022) 101249, https://doi.org/10.1016/j.nme.2022.101249.
[4] M. Yajima, S. Masuzaki, N. Yoshida, M. Tokitani, T. Otsuka, Y. Oya, Y. Torikai, G. Motojima, Investigation on tritium retention and surface properties on the first wall in the large helical device, Nucl. Mater. Energy. 27 (2021) 100906, https://doi.org/10.1016/j.nme.2021.100906.
[5] J. Roth, E. Tsitrone, T. Loarer, V. Philipps, S. Brezinsek, A. Loarte, G.F. Counsell, R. P. Doerner, K. Schmid, O.V. Ogorodnikova, R.A. Causey, Tritium inventory in ITER plasma-facing materials and tritium removal procedures, Plasma Phys. Control. Fusion. 50 (2008) 103001, https://doi.org/10.1088/0741-3335/50/10/103001.
[6] A.P. Zakharov, A.E. Gorodetsky, V.K. Alimov, S.L. Kanashenko, A.V. Markin, Hydrogen retention in plasma-facing materials and its consequences on tokamak operation, J. Nucl. Mater. 241–243 (1997) 52–67, https://doi.org/10.1016/S0022-3115(97)80030-X.
[7] L. Cai, Z. Wang, C. Li, X. Huang, D. Zhao, H. Ding, Development of an in situ diagnostic system for mapping the deposition distribution on plasma facing components of the HL-2M tokamak, Rev. Sci. Instrum. 90 (2019), https://doi.org/10.1063/1.5082630.
[8] W. Gonzalez, W. Biel, P. Mertens, M. Tokar, O. Marchuk, C. Linsmeier, Conceptual studies on spectroscopy and radiation diagnostic systems for plasma control on DEMO, Fusion Eng. Des. 146 (2019) 2297–2301, https://doi.org/10.1016/j.fusengdes.2019.03.176.
[9] M. Rubel, P. Petersson, E. Alves, S. Brezinsek, J.P. Coad, K. Heinola, M. Mayer, A. Widdowson, The role and application of ion beam analysis for studies of plasma-facing components in controlled fusion devices, Nucl. Instruments Methods Phys.

Res. Sect. B Beam Interact. with Mater. Atoms. 371 (2016) 4–11, https://doi.org/10.1016/j.nimb.2015.09.077.
[10] M. Mayer, S. Möller, M. Rubel, A. Widdowson, S. Charisopoulos, T. Ahlgren, E. Alves, G. Apostolopoulos, N.P. Barradas, S. Donnelly, S. Fazinić, K. Heinola, O. Kakuee, H. Khodja, A. Kimura, A. Lagoyannis, M. Li, S. Markelj, M. Mudrinic, P. Petersson, I. Portnykh, D. Primetzhofer, P. Reichart, D. Ridikas, T. Silva, S. M. Gonzalez de Vicente, Y.Q. Wang, Ion beam analysis of fusion plasma-facing materials and components: facilities and research challenges, Nucl. Fusion 60 (2020) 025001, https://doi.org/10.1088/1741-4326/ab5817.
[11] Y. Oya, H. Fujita, C. Hu, Y. Uemura, S. Sakurada, K. Yuyama, X. Li, Y. Hatano, N. Yoshida, H. Watanabe, Y. Nobuta, Y. Yamauchi, M. Tokitani, S. Masuzaki, T. Chikada, Effect of impurity deposition layer formation on D retention in LHD plasma exposed W, Nucl. Mater. Energy. 9 (2016) 84–88, https://doi.org/10.1016/j.nme.2016.07.005.
[12] V.K. Alimov, M. Yajima, S. Masuzaki, M. Tokitani, Analysis of mixed-material layers deposited on the toroidal array probes during the FY 2012 LHD plasma campaign, Fusion Eng. Des. 147 (2019) 111228, https://doi.org/10.1016/j.fusengdes.2019.06.001.
[13] Y. Oya, C. Hu, H. Fujita, K. Yuyama, S. Sakurada, Y. Uemura, S. Masuzaki, M. Tokitani, M. Yajima, Y. Hatano, T. Chikada, Development of H, D, T simultaneous TDS measurement system and H, D, T retention behavior for DT gas exposed tungsten installed in LHD plasma campaign, Fusion Sci. Technol. 71 (2017) 351–356, https://doi.org/10.1080/15361055.2017.1291039.
[14] A.W. Miziolek, V. Palleschi, I. Schechter, eds. Laser-Induced Breakdown Spectroscopy (LIBS), Cambridge University Press, Cambridge, 2006, https://doi.org/10.1017/CBO9780511541261.
[15] D.A. Cremers, L.J. Radziemski, Handbook of laser-induced breakdown spectroscopy, Wiley (2013), https://doi.org/10.1002/9781118567371.
[16] P.J. Singh, S.N. Thakur (Eds.), Laser-Induced Breakdown Spectroscopy, Elsevier, 2020, https://doi.org/10.1016/C2018-0-03938-9.
[17] R. Noll, Laser-Induced Breakdown Spectroscopy, Springer Berlin Heidelberg, Berlin, Heidelberg, 2012, https://doi.org/10.1007/978-3-642-20668-9.
[18] S. Musazzi, U. Perini, eds. Laser-Induced Breakdown Spectroscopy, Springer, Berlin Heidelberg, Berlin, Heidelberg, 2014, https://doi.org/10.1007/978-3-642-45085-3.
[19] D.W. Hahn, N. Omenetto, Laser-induced breakdown spectroscopy (LIBS), part I: review of basic diagnostics and plasma—particle interactions: still-challenging issues within the analytical plasma community, Appl. Spectrosc. 64 (2010) 335A–336A, https://doi.org/10.1366/000370210793561691.
[20] D.W. Hahn, N. Omenetto, Laser-induced breakdown spectroscopy (LIBS), part II: review of instrumental and methodological approaches to material analysis and applications to different fields, Appl. Spectrosc. 66 (2012) 347–419, https://doi.org/10.1366/11-06574.
[21] C. Li, C.-L. Feng, H.Y. Oderji, G.-N. Luo, H.-B. Ding, Review of LIBS application in nuclear fusion technology, Front. Phys. 11 (2016) 114214, https://doi.org/10.1007/s11467-016-0606-1.
[22] G.S. Maurya, A. Marín-Roldán, P. Veis, A.K. Pathak, P. Sen, A review of the LIBS analysis for the plasma-facing components diagnostics, J. Nucl. Mater. 541 (2020) 152417, https://doi.org/10.1016/j.jnucmat.2020.152417.
[23] H.J. van der Meiden, S. Almaviva, J. Butikova, V. Dwivedi, P. Gasior, W. Gromelski, A. Hakola, X. Jiang, I. Jõgi, J. Karhunen, M. Kubkowska, M. Laan, G. Maddaluno, A. Marín-Roldán, P. Paris, K. Piip, M. Pisarčík, G. Sergienko, M. Veis, P. Veis, S. Brezinsek, T. EUROfusion WP PFC team, Monitoring of tritium and impurities in the first wall of fusion devices using a LIBS based diagnostic, Nucl. Fusion. 61 (2021) 125001, https://doi.org/10.1088/1741-4326/ac31d6.
[24] S. Almaviva, L. Caneve, F. Colao, R. Fantoni, G. Maddaluno, Remote-LIBS characterization of ITER-like plasma facing materials, J. Nucl. Mater. 421 (2012) 73–79, https://doi.org/10.1016/J.JNUCMAT.2011.11.050.
[25] S. Almaviva, L. Caneve, F. Colao, V. Lazic, G. Maddaluno, P. Mosetti, A. Palucci, A. Reale, P. Gasior, W. Gromelski, M. Kubkowska, LIBS measurements inside the FTU vessel mock-up by using a robotic arm, Fusion Eng. Des. 157 (2020) 111685, https://doi.org/10.1016/j.fusengdes.2020.111685.
[26] D. Zhao, C. Li, Z. Hu, C. Feng, Q. Xiao, R. Hai, P. Liu, L. Sun, D. Wu, C. Fu, J. Liu, N. Farid, F. Ding, G.-N. Luo, L. Wang, H. Ding, Remote in situ laser-induced breakdown spectroscopic approach for diagnosis of the plasma facing components on experimental advanced superconducting tokamak, Rev. Sci. Instrum. 89 (2018), https://doi.org/10.1063/1.5024848.
[27] C. Li, X. Wu, C. Zhang, H. Ding, G. de Temmerman, H.J. van der Meiden, Study of deuterium retention on lithiated tungsten exposed to high-flux deuterium plasma using laser-induced breakdown spectroscopy, Fusion Eng. Des. 89 (2014) 949–954, https://doi.org/10.1016/J.FUSENGDES.2014.04.071.
[28] P. Liu, D.Y. Zhao, L.Y. Sun, C.L. Fu, J.M. Liu, C. Li, R. Hai, C.F. Sang, Z.H. Hu, Z. Sun, J.S. Hu, L. Wang, J.L. Chen, Y.F. Liang, G.N. Luo, H. Ding, In situ diagnosis of Li-wall conditioning and H/D co-deposition on the first wall of EAST using laser-induced breakdown spectroscopy, Plasma Phys. Control. Fusion. 60 (2018) 085019, https://doi.org/10.1088/1361-6587/aace83.
[29] G. Li, H. Hou, P. Ran, Y. Zhao, Z. Zhong, Calibration-free quantitative analysis of D/H isotopes with a fs-laser filament, J. Anal. At. Spectrom. 35 (2020) 1320–1329, https://doi.org/10.1039/D0JA00062K.
[30] M. Burger, P.J. Skrodzki, L.A. Finney, J. Hermann, J. Nees, I. Jovanovic, Isotopic analysis of deuterated water via single- and double-pulse laser-induced breakdown spectroscopy, Phys. Plasmas 25 (2018), https://doi.org/10.1063/1.5042665.
[31] R. Fantoni, S. Almaviva, L. Caneve, F. Colao, G. Maddaluno, P. Gasior, M. Kubkowska, Hydrogen isotope detection in metal matrix using double-pulse laser-induced breakdown-spectroscopy, Spectrochim. Acta B At. Spectrosc. 129 (2017) 8–13, https://doi.org/10.1016/j.sab.2016.12.008.
[32] E.J. Kautz, E.C.E. Rönnebro, A. Devaraj, D.J. Senor, S.S. Harilal, Detection of hydrogen isotopes in zircaloy-4 via femtosecond LIBS, J. Anal. At. Spectrom. 36 (2021) 1217–1227, https://doi.org/10.1039/D1JA00034A.
[33] E.J. Kautz, A. Devaraj, D.J. Senor, S.S. Harilal, Hydrogen isotopic analysis of nuclear reactor materials using ultrafast laser-induced breakdown spectroscopy, Opt. Express 29 (2021) 4936, https://doi.org/10.1364/OE.412351.
[34] S.S. Harilal, A.K. Shaik, E.J. Kautz, A. Devaraj, A.M. Casella, D.J. Senor, Detection of tritium using ultrafast laser-induced breakdown spectroscopy, J. Anal. At. Spectrom. 39 (2024) 699–703, https://doi.org/10.1039/D3JA00439B.
[35] S. Harilal, E.J. Kautz, Analysis of hydrogen and lithium isotopes using laser-induced breakdown spectroscopy, in: C.R. Phipps, V.E. Gruzdev (Eds.), High-Power Laser Ablation VIII, SPIE, 2024, p. 14, https://doi.org/10.1117/12.3015929.
[36] K.H. Kurniawan, T.J. Lie, M.M. Suliyanti, R. Hedwig, M. Pardede, D.P. Kurniawan, Y. Kusumoto, K. Kagawa, Quantitative analysis of deuterium using laser-induced plasma at low pressure of helium, Anal. Chem. 78 (2006) 5768–5773, https://doi.org/10.1021/ac060633h.
[37] C.W. Forsberg, S. Lam, D.M. Carpenter, D.G. Whyte, R. Scarlat, C. Contescu, L. Wei, J. Stempien, E. Blandford, Tritium control and capture in salt-cooled fission and fusion reactors: status, challenges, and path forward, Nucl. Technol. 197 (2017) 119–139, https://doi.org/10.13182/NT16-101.
[38] A. Kramida, Y. Ralchenko, J. Reader, N.A. Team, NIST At. Spectra Database (2024), https://doi.org/10.18434/T4W30F (ver. 5.11).
[39] M.A. Gigosos, M.Á. González, V. Cardeñoso, Computer simulated Balmer-alpha, −beta and -gamma stark line profiles for non-equilibrium plasmas diagnostics, Spectrochim. Acta B At. Spectrosc. 58 (2003) 1489–1504, https://doi.org/10.1016/S0584-8547(03)00097-1.
[40] A. Díaz-Soriano, J.M. Alcaraz-Pelegrina, A. Sarsa, M.S. Dimitrijević, C. Yubero, A simple and accurate analytical model of the stark profile and its application to plasma characterization, J. Quant. Spectrosc. Radiat. Transf. 207 (2018) 89–94, https://doi.org/10.1016/j.jqsrt.2017.12.027.
[41] A. Díaz-Soriano, M.S. Dimitrijević, J.M. Alcaraz-Pelegrina, A. Sarsa, C. Yubero, Simple and analytical function for the stark profile of the Hα line and its application to plasma characterization, J. Quant. Spectrosc. Radiat. Transf. 217 (2018) 111–115, https://doi.org/10.1016/j.jqsrt.2018.05.031.
[42] A. Ortiz-Mora, A. Díaz-Soriano, A. Sarsa, M.S. Dimitrijević, C. Yubero, A practical method for plasma diagnosis with Balmer series hydrogen lines, Spectrochim. Acta Part B At. Spectrosc. 163 (2020) 105728, https://doi.org/10.1016/j.sab.2019.105728.
[43] C.O. Laux, T.G. Spence, C.H. Kruger, R.N. Zare, Optical diagnostics of atmospheric pressure air plasmas, Plasma Sources Sci. Technol. 12 (2003) 125–138, https://doi.org/10.1088/0963-0252/12/2/301.
[44] H. Ehrich, Experimental study of Balmer-α stark broadening, Z. Für Naturforsch. A. 34 (1979) 188–191, https://doi.org/10.1515/zna-1979-0210.
[45] N. Konjević, M. Ivković, N. Sakan, Hydrogen Balmer lines for low electron number density plasma diagnostics, Spectrochim. Acta B At. Spectrosc. 76 (2012) 16–26, https://doi.org/10.1016/j.sab.2012.06.026.
[46] J.J. Olivero, R.L. Longbothum, Empirical fits to the voigt line width: a brief review, J. Quant. Spectrosc. Radiat. Transf. 17 (1977) 233–236, https://doi.org/10.1016/0022-4073(77)90161-3.
[47] H.R. Griem, Principles of plasma spectroscopy, in: fast electr. Opt. Meas., Springer Netherlands, Dordrecht, 1986: pp. 885–910. doi:https://doi.org/10.1007/978-94-017-0445-8_34.
[48] Z. Mijatović, S. Djurović, L. Gavanski, T. Gajo, A. Favre, V. Morel, A. Bultel, Plasma density determination by using hydrogen Balmer Hα spectral line with improved accuracy, Spectrochim. Acta Part B At. Spectrosc. 166 (2020) 105821, https://doi.org/10.1016/j.sab.2020.105821.
[49] S. Almaviva, L. Caneve, F. Colao, G. Maddaluno, R. Fantoni, Accessory laboratory measurements to support quantification of hydrogen isotopes by in-situ LIBS from a robotic arm inside a fusion vessel, Spectrochim. Acta Part B At. Spectrosc. 181 (2021) 106230, https://doi.org/10.1016/j.sab.2021.106230.
[50] Y. Yu, J. Hu, Y. Zhao, X. Gao, J. Li, ICRF (ion cyclotron range of frequencies) discharge cleaning with toroidal and vertical fields on east, Plasma Phys. Control. Fusion. 53 (2011) 015013, https://doi.org/10.1088/0741-3335/53/1/015013.
[51] S. Brezlnsek, C.P. Dhard, M. Jakubowski, Plasma–surface interaction in the stellarator W7-X: conclusions drawn from operation with graphite plasma-facing components, Nucl. Fusion. 62 (2022) 016006, https://doi.org/10.1088/1741-4326/ac3508.
[52] M. Ivković, M.A. Gonzalez, S. Jovićević, M.A. Gigosos, N. Konjević, A simple line shape technique for electron number density diagnostics of helium and helium-seeded plasmas, Spectrochim. Acta B At. Spectrosc. 65 (2010) 234–240, https://doi.org/10.1016/j.sab.2010.03.003.
[53] M. Ivković, M.A. Gonzalez, N. Lara, M.A. Gigosos, N. Konjević, Stark broadening of the He I 492.2 nm line with forbidden components in dense low-temperature plasma, J. Quant. Spectrosc. Radiat. Transf. 127 (2013) 82–89, https://doi.org/10.1016/j.jqsrt.2013.04.030.
[54] A.J. Barnard, J. Cooper, E.W. Smith, Stark broadening tables for He I λ4922Å, J. Quant. Spectrosc. Radiat. Transf. 15 (1975) 429–437, https://doi.org/10.1016/0022-4073(75)90062-X.
[55] A. de Giacomo, J. Hermann, Laser-induced plasma emission: from atomic to molecular spectra, J. Phys. D. Appl. Phys. 50 (2017) 183002, https://doi.org/10.1088/1361-6463/aa6585.
[56] C.M. Western, PGOPHER: a program for simulating rotational, vibrational and electronic spectra, J. Quant. Spectrosc. Radiat. Transf. 186 (2017) 221–242, https://doi.org/10.1016/j.jqsrt.2016.04.010.

[57] B. Stankov, M. Gavrilovic Bozovic, J. Savovic, M. Ivkovic, Spectroscopic characterization of laser-induced plasma on doped tungsten, in: Publ. Astron. Obs. Belgrade 102, 2022, pp. 239–242. ISBN:978–86–82296-02-7.
[58] I. Jõgi, J. Ristkok, J. Raud, J. Butikova, K. Mizohata, P. Paris, Laser induced breakdown spectroscopy for hydrogen detection in molybdenum at atmospheric pressure mixtures of argon and nitrogen, Fusion Eng. Des. 179 (2022) 113131, https://doi.org/10.1016/j.fusengdes.2022.113131.
[59] N. Larbi-Terzi, S. Sahal-Bréchot, N. Ben Nessib, M.S. Dimitrijević, Stark-broadening calculations of singly ionized carbon spectral lines, Mon. Not. R. Astron. Soc. 423 (2012) 766–773, https://doi.org/10.1111/j.1365-2966.2012.20968.x.

Spectrochimica Acta Part B: Atomic Spectroscopy 213 (2024) 106874

Contents lists available at ScienceDirect

Spectrochimica Acta Part B: Atomic Spectroscopy

journal homepage: www.elsevier.com/locate/sab

LIBS depth-profile analysis of W/Cu functionally graded material

M. Ivkovic [a,*], J. Savovic [b], B.D. Stankov [a], M. Kuzmanovic [c], I. Traparic [a]

[a] Institute of Physics, University of Belgrade, Belgrade 11080, Serbia
[b] Vinca Institute of Nuclear Sciences, University of Belgrade, Belgrade 11000, Serbia
[c] Faculty of Physical Chemistry, University of Belgrade, Belgrade 11158, Serbia

ARTICLE INFO

Keywords:
Laser-induced breakdown spectroscopy, LIBS
W/Cu composite
Functionally graded material, FGM
Quantitative analysis
Depth-profile analysis

ABSTRACT

A feature of Laser-Induced Breakdown Spectroscopy (LIBS), the ability to perform depth profiling, has been exploited to analyze a tungsten-copper functionally graded material (FGM), considered a relevant candidate for components in a nuclear fusion reactor. The proposed method relies on establishing correlations between the depth of ablation craters and the number of laser pulses, along with the accompanying LIBS spectra acquired by varying a number of laser pulses. LIBS measurements were performed using a Q-switched Nd:YAG laser at 532 nm with 100 mJ/pulse energy under reduced Ar pressure. The ablation craters were analyzed using optical profilometry. The copper concentration at each specific depth was assessed using a univariate calibration curve constructed with intensity ratios of Cu I 521.82 nm and W I 522.47 nm spectral lines. The calibration samples were pure W and homogenous W/Cu composite samples with different Cu content (10.9% - 35.3%) whose composition was determined by X-ray fluorescence. The proposed method exhibits potential applicability for quantitative analysis of multilayered materials.

1. Introduction

Functionally Graded Materials (FGM) have innovative properties and multifunctional characteristics that conventional homogeneous materials cannot achieve. In its simplest form, FGM consists of a singular material on one surface, a distinct material on the opposing surface, and an intermediary layer characterized by a gradual variation in structure, composition, and morphology spanning micron-level dimensions between the two materials. A desired function can be achieved by selecting the transition profile of FGM. Therefore, the FGM must be classified separately from conventional homogeneous composites and nanocomposite materials [1–3]. The applications of FGM are extensive and include engineering, aerospace, chemical plants, electronics, energy conversion, optics, nuclear energy, and even biomaterials [4,5]. Depending on the application, various properties, such as thermal (expansion coefficient, conductivity, stability, temperature distribution, response under transient heating), electric (conductivity, dielectric properties), elastic (deformation, strength, Young's elastic modulus), or some other can have one-, two- or three-dimensional variation in the fraction of its components.

Due to their distinctive characteristics, materials with property gradation offer significant advantages for application in nuclear fusion reactors. For example, functionally graded materials are relevant candidates for the interlayer between W plasma-facing components (PFCs) and CuCrZr heat sinks [6–15]. The challenge posed by a substantial difference in the coefficient of thermal expansion between these two materials, resulting in thermal stress on PFC, can be mitigated by introducing a transition layer consisting of a material characterized by a low thermal expansion rate, high thermal conductivity, and favorable thermomechanical properties. Promising candidates for joining layers of W to CuCrZr are W/Cu composites and W/Cu functionally graded composites [13,14]. The suitability of these materials is reflected in the ability to finely tune their macroscopic properties (microstructure and phase distribution) to attain the desired characteristics.

As an in-situ, non-contact, minimally invasive technique sensitive to light elements, with the limit of detection down to ppm (or even to ppb in some cases), laser-induced breakdown spectroscopy (LIBS) is a promising tool for analyzing plasma-facing components in fusion devices [16]. Various LIBS configurations, using either single pulse (SP-LIBS) or double pulse (DP-LIBS), have been used to explore the optimization of the technique for monitoring compositional alterations in PFCs. These changes may arise due to impurity deposition, erosion, or fuel retention [17–23]. Also, the effect of laser parameters (energy and duration of laser pulse, wavelength) and the effect of atmospheric

* Corresponding author.
E-mail address: ivke@ipb.ac.rs (M. Ivkovic).

https://doi.org/10.1016/j.sab.2024.106874
Received 26 June 2023; Received in revised form 8 December 2023; Accepted 29 January 2024
Available online 1 February 2024

conditions on the emission, mass ablation, and plasma parameters have been extensively studied [24–27]. LIBS possesses a competitive advantage over alternative techniques designed for in-depth elemental analysis due to its in-situ and remote analysis capability, which is especially important when analysis has to be performed in hostile environments like nuclear reactors.

This paper presents the research findings on the potential of LIBS for in-depth profiling of W/Cu functionally graded material using a medium-resolution spectrometer. A conventional nanosecond LIBS system was used, and the samples were analyzed under the Ar atmosphere at reduced pressure. The proposed method is based on the correlation of the depth of the ablation craters and gathered LIBS spectra for different number of accumulated laser pulses. The ablation craters were analyzed using optical profilometry. The copper content at each depth was estimated from the constructed calibration curve. For concentration calibration, homogenous W/Cu samples whose composition was determined by X-ray fluorescence were used. Subsequently, a univariate calibration curve was developed utilizing the line intensity ratios of Cu I 521.82 nm and W I 522.47 nm lines.

The proposed approach is also amenable to the analysis of elemental composition and the determination of individual layer thickness in multilayered materials.

2. Experimental

2.1. Samples

A set of tungsten-copper alloys W93Cu7, W90Cu10, W80Cu20, W70Cu30, and pure W in the form of tablets (diameter 10 mm, thickness 1 mm) were obtained from HUBEI FOTMA MACHINERY CO LTD, Wuhan, P. R. China. Since W/Cu samples' trade names represent a rough percentage of the main constituents, the precise composition of the samples was determined using X-ray fluorescence (XRF) analysis. These samples were used as calibration samples for LIBS analysis. A W/Cu functionally graded material (W/Cu FGM), i.e., tungsten with a gradient concentration of copper along the sample thickness direction, was used for LIBS depth-profile analysis. A W/Cu FGM sample was a disc with a 6 mm diameter and thickness of 1 mm.

2.2. XRF spectrometry

A portable XRF Niton XL3t970 GOLDD analyzer (Thermo Fisher Scientific) was used to analyze the composition of W/Cu standards. The instrument is equipped with an X-ray tube, working at a maximum of 50 kV, 200 μA, and a high-performance semi-conductor detector with a resolution of 185 eV. The spot diameter at the measurement point is about 3 mm. Depending on the application, the analytical range covers up to 30 elements, from sulfur to uranium. The analysis was carried out using a General Metal Mode calibration (includes elemental analysis of Ba, Sb, Sn, In, Cd, Pd, Ag, Mo, Nb, Zr, Se, Bi, Pb, Pt, Br, Au, Hg, Ta, Hf, Zn, Cu, Ni, Co, Fe, Mn, Cr, V, Ti) for a total time of 60 s (30 s Main filter and 15 s for Low and High filters).

2.3. LIBS setup

Fig. 1a shows a sketch of the focusing head for the basic single-pulse LIBS setup used in this work. A setup consists of the laser (1) mounted on the platform (2) movable vertically (0–380 mm) by the column (3) connected to the second fixed platform (4). The focusing head (5) carries a dichroic bending mirror at 45 degrees, a green diode laser (6) for indicating the position of a focal point, and a focusing mirror mount (which has the possibility for fine focal distance adjustment with accuracy of 10 μm and the range of ±10 mm). A laser source (1) was Nd:YAG Quantel Q-smart 450 laser ($\lambda = 532$ nm; energy 100 mJ; 6 ns pulses, frequency 10 Hz). The change in the laser energy density was obtained by varying the distance between the sample and lens with a 10 cm focal length.

The shape, position, and size of the laser beam spot on the target were monitored using the endoscopic camera (8) equipped with six white light-emitting diodes for illumination. The camera has a diameter of 7 mm and a 5 m long light guide connected to the computer. The resolution of the camera is 640 × 480 pixels.

Fiber optic cable (Ø = 400 μm) led the plasma emission collected by the light collector, i.e., fiber adapter Solar LS FA-2 (9), to the entrance of the imaging spectrometer Shamrock 303 Andor. The imaging spectrometer was equipped with the iCCD camera Andor iStar DH720. The camera working in full vertical binning mode (FVB) was triggered at various delays and gate times determined by a digital delay generator (SRS DG535) using the signals from the ICCD camera computer interface and Q switch trigger from the laser (controlled by the remote laser controller) by the help of the digital storage oscilloscope and computer software. Spectral sensitivity calibration of a Shamrock spectrometer system with an Andor iStar DH720 ICCD camera was performed with a calibrated tungsten lamp in the 300–800 nm wavelength range. Instrumental width (w_i) was experimentally determined by fitting a profile of the spectral line emitted from a low-pressure mercury lamp. For entrance slit width of 20 μm, w_i was 0.11 nm.

A small vacuum chamber (based on KF40 Tee, see Fig. 1b) carrying target was settled on the carrier (Thorlabs, Pitch and roll platform) (7) with the manually adjustable angle, connected to the Thorlabs XY stepper motor translation stage controlled by the computer. After the chosen number of laser pulses, n, the target position (10) was changed to

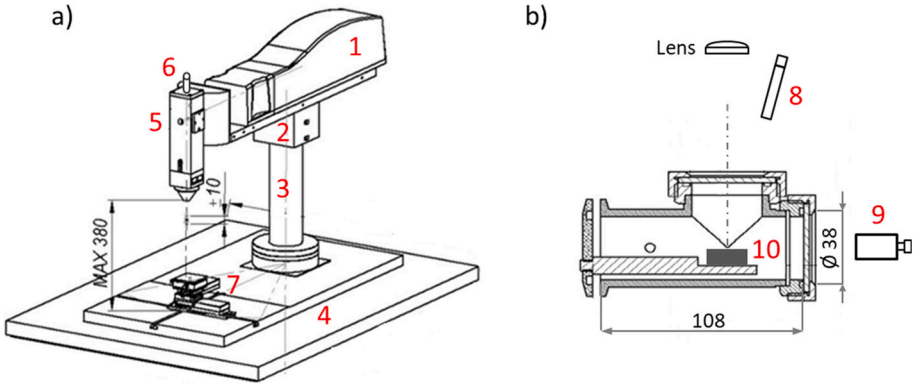

Fig. 1. a) Sketch of the focusing head for the single-pulse LIBS setup showing dimensions and range of the focal point adjustment. Legend: (1) laser, (2) platform, (3) movable column, (4) fixed platform, (5) focusing head, (6) green diode laser, (7) XY translation stage; b) Technical drawing of the vacuum chamber. Legend: (8) endoscopic camera, (9) light collector, i.e., fiber adapter, (10) target. (For interpretation of the references to colour in this figure legend, the reader is referred to the web version of this article.)

expose the "fresh" target surface. The target position was fixed when the task was to determine the ablation depth as a function of the number of applied laser shots. The appropriate gas pressure inside the chamber was adjusted using regulation and needle valves and monitored by the manometer, led to the chamber using appropriate tubing, and evacuated by the vacuum pump. All measurements reported in this work were recorded under reduced Ar pressure.

2.3.1. Profilometry analysis

The Zygo New View 7100 Scanning White Light Interferometer (optical Surface profiler) was used for fast, non-contact 3D measurement of surface morfology. The profilometer's vertical scan range is 150 μm, with the extended scan range up to 20 mm. Vertical resolution is <0.1 nm, while the lateral resolution is objective dependent and ranges from 0.36 to 9.5 μm. A data scan rate is user-selectable (camera and scan mode dependent) and goes up to 26 μm/s. RMS repeatability is <0.01 nm. The step height accuracy is ≤0.75%, while repeatability is ≤0.1%. The profilometer is equipped with the program (Zygo corporation, Metro Pro) that was used for measuring crater depths from two-dimensional (2D) profiles and their three-dimensional (3D) visualization.

3. Results and discussions

3.1. XRF spectroscopy

The composition of the W/Cu calibration standards was determined by XRF analysis. A part of the obtained XRF spectra is presented in Fig. 2. The elemental composition obtained by XRF is summarised in Table 1. Samples also contain trace levels of other elements, such as Ti, Mn, Fe, and Co. The measurement accuracy (element dependent) was typically 2% - 5% of the reported weight percent value. Concentration values obtained by XRF were used to construct the calibration curve.

3.2. LIBS analysis

A critical problem with the application of LIBS for the elemental (quantitative) analysis of W and W-alloys is the low reproducibility of the spectral line intensities caused by different grain sizes in a tungsten structure [28]. The line intensities also depend on grain distribution, causing differences in measured intensities during target irradiation at different angles [29]. In addition, explosive boiling occurs at temperatures greater than critical [30–32]. For example, threshold laser intensity for phase explosion in tungsten under interaction with Nd:YAG laser at 355 nm was estimated to be 6×10^{10} W cm^{-2} [31].

Our first step was to study the influence of different experimental parameters (e.g., gas pressure, laser energy, beam size, the number of accumulated pulses, and delay time) on the reproducibility of the measured spectral line intensities. All LIBS measurements reported in this study were done in an argon atmosphere, as it was shown that the inert background gas provides almost uniform spatial distributions of plasma temperature and densities [33,34].

Table 1
Results of the XRF analysis of W/Cu calibration samples.

	Concentration (wt%)*					
Trade name	Cu	W	Zn	Ni	Cr	Other elements
W	–	100	–	–	–	–
W93Cu7	10.9	87	1.6	0.47	–	0.03
W90Cu10	12.9	84	1.9	0.56	0.23	0.41
W80Cu20	24.3	72	2.8	0.78	–	0.12
W70Cu30	35.3	59	3.0	1.5	0.11	1.09

3.2.1. Optimization of the LIBS experimental parameters

The influence of Ar pressure on the spectral emission intensity was studied within the pressure range spanning from vacuum conditions to 1 atm. Fig. 3 shows that, in the analyzed pressure range, the highest signal-to-noise ratio (SNR) of spectral lines was obtained at 10 mbar, hence this pressure was chosen as optimal.

The influence of delay time on the intensity of Cu I 521.82 nm and W 522.47 nm lines is illustrated in Fig. 4 (a), while the SBR and signal-to-noise ratio (SNR) for a copper 521.82 nm line is illustrated in Fig. 4 (b).

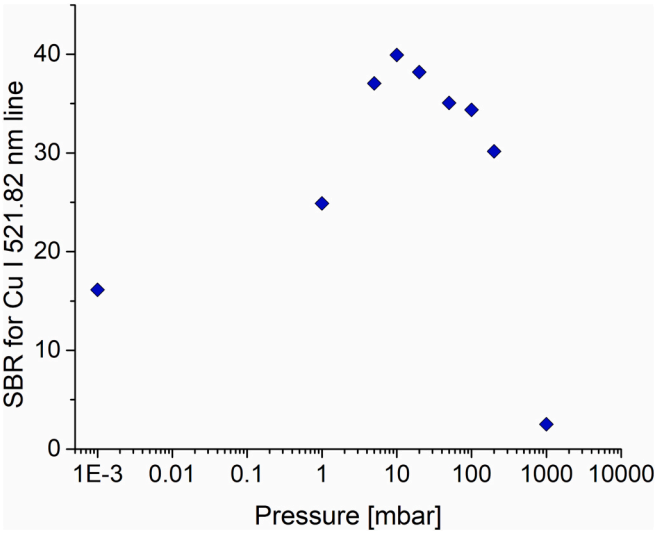

Fig. 3. The influence of Ar pressure on the signal-to-background ratio of Cu 521.82 nm line.

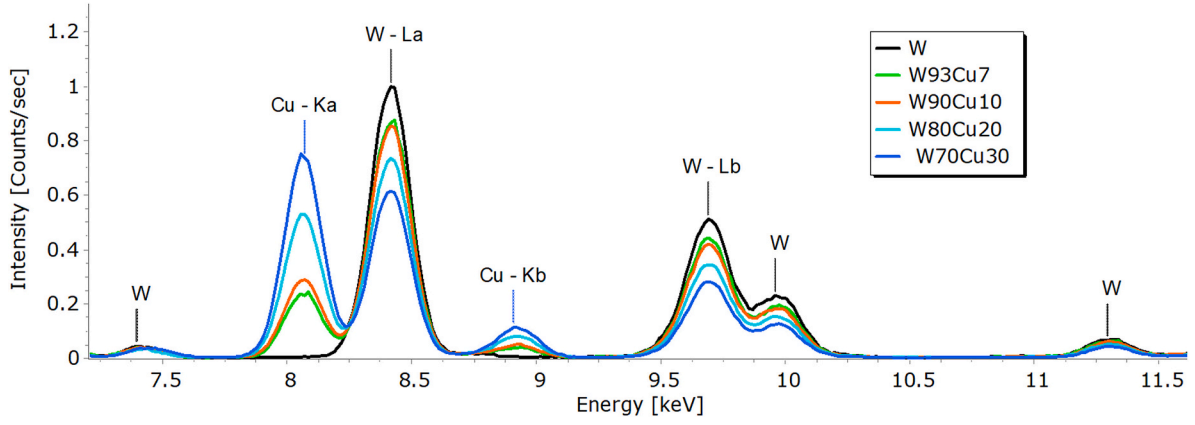

Fig. 2. Segment of the XRF spectra of W and W/Cu samples used as calibration standards for LIBS.

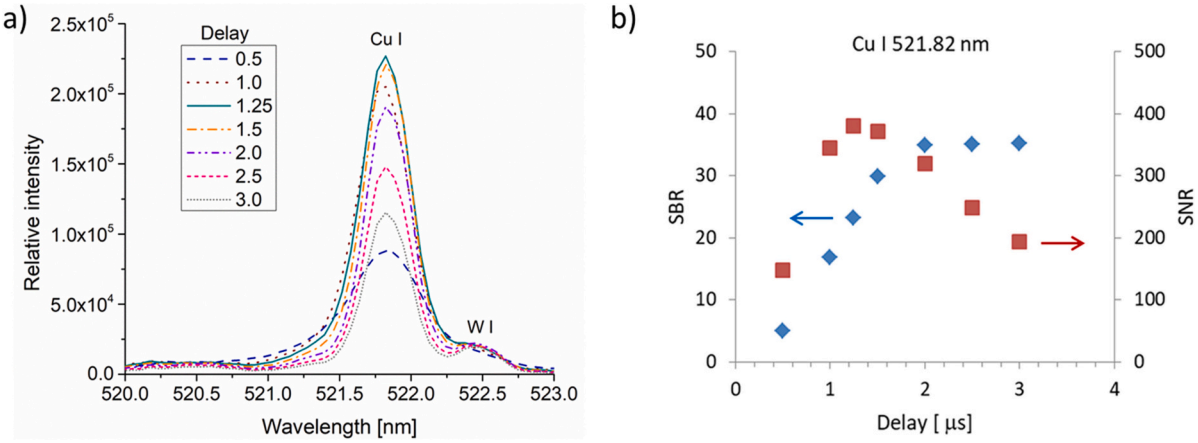

Fig. 4. (a) LIBS spectra of W93Cu7 showing Cu I 521.82 nm and W I 522.47 nm lines recorded for different gate delay times. Laser energy 100 mJ, gate 20 ns, spot diameter 1 mm. Each spectrum represents an average of ten measurements consisting of 10 accumulated consequent laser shots. (b) The SNR and the SBR of Cu 521.82 nm line, as a function of the delay time.

The highest SBR and SNR values were obtained for a delay time of around 1.5–2 µs.

The laser pulse energy threshold required for creating plasma usable for spectrochemical analysis was determined to be 30 mJ. As shown in Fig. 5, the intensity of W and Cu demonstrated a proportional increase with elevated laser energy. Nevertheless, when the beam is focused on the target and the laser energy surpasses 50 mJ, the ratio of line intensities (Cu I 521.82 nm / W I 522.47 nm) remains constant. Uniform evaporation of both components was achieved at energies exceeding 50 mJ, resulting in a constant line intensity ratio at higher laser pulse energies. A laser energy of 100 mJ was chosen for further LIBS measurements to enhance emission intensity, thereby improving the precision of intensity measurements and increasing the ablated mass compared to a pulse energy of 50 mJ (for the same spot diameter).

The spot size required optimization to ensure that the spot diameter remains significantly larger than the sample grain size. The spot size was optimized by adjusting the focus, specifically by varying the lens-to-sample distance to define the surface that would be ablated. Due to the granulation of the material, the minimal preferable spot size should be above 100 µm. A spot size of 1 mm eliminated a problem with inhomogeneous grain size distribution and reduced spectral intensity fluctuations.

The minimum number of laser shots needed to obtain reproducible spectral line intensities was determined to be 10. For the laser pulse energy of 100 mJ, the spot size of 1 mm, and 100 shots (average of ten measurements of 10 accumulated consequent laser shots), the relative standard deviation of the intensity ratio of the selected Cu and W lines was around 5%.

Because the measured line intensities may vary due to the interaction of the plasma with the crater walls, the plasma confinement, or plasma cooling by the crater walls, the influence of crater depth on the measured LIBS intensity was also investigated. Fig. 6 (a) shows spectra recorded for a sequence (1–800) of laser shots applied to the same spot on the W90Cu10 target. The effect of the crater depth on the intensity of Cu I 521.82 nm and W I 522.47 nm line and Cu/W intensity ratio is shown in Figs. 6 (b-d). The variation of the line intensities is more pronounced than the variation of the Cu/W intensity ratio. After the 100th shot at the same position, the influence on the measured Cu/W intensity ratio is significant, i.e., it decreases with a further increase of the crater depth. A possible explanation for such behavior could be a more significant effect of the changed plasma parameters (caused by crater walls) on the intensity of the line with lower excitation energy.

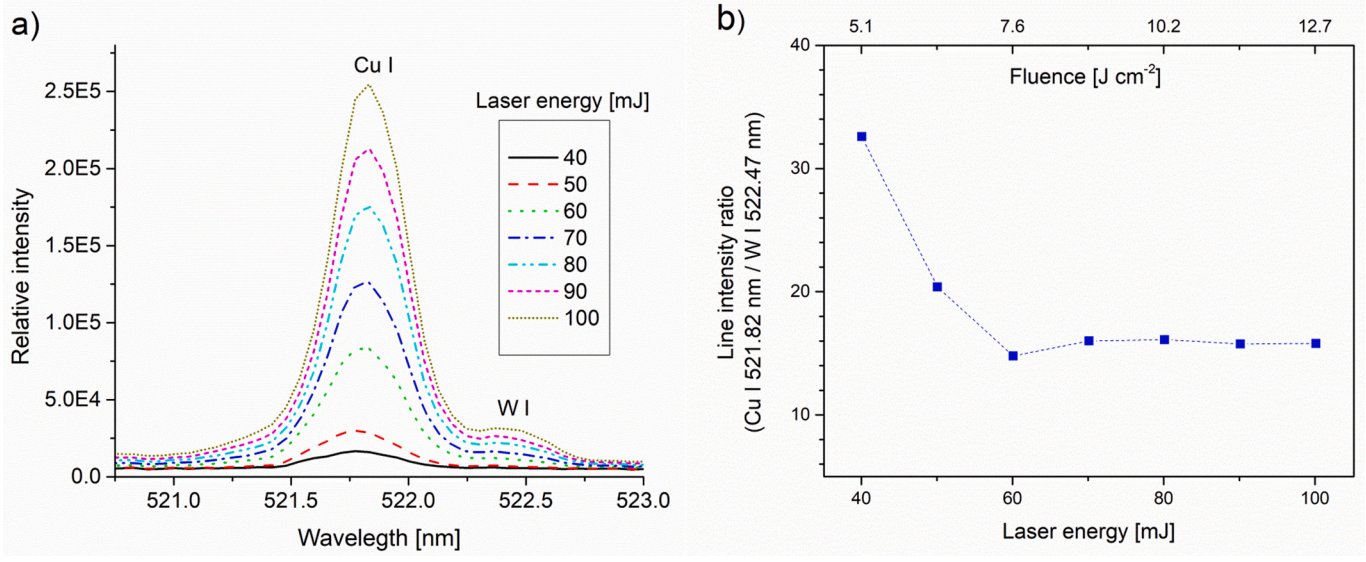

Fig. 5. (a) Effect of laser pulse energy on the LIBS emission of Cu I 521.82 nm and W 522.47 nm line. b) The influence of pulse energy and fluence on the Cu/W line intensity ratio. Target W93Cu7; delay 1.5 ms; gate 20 ns; spot diameter 1 mm.

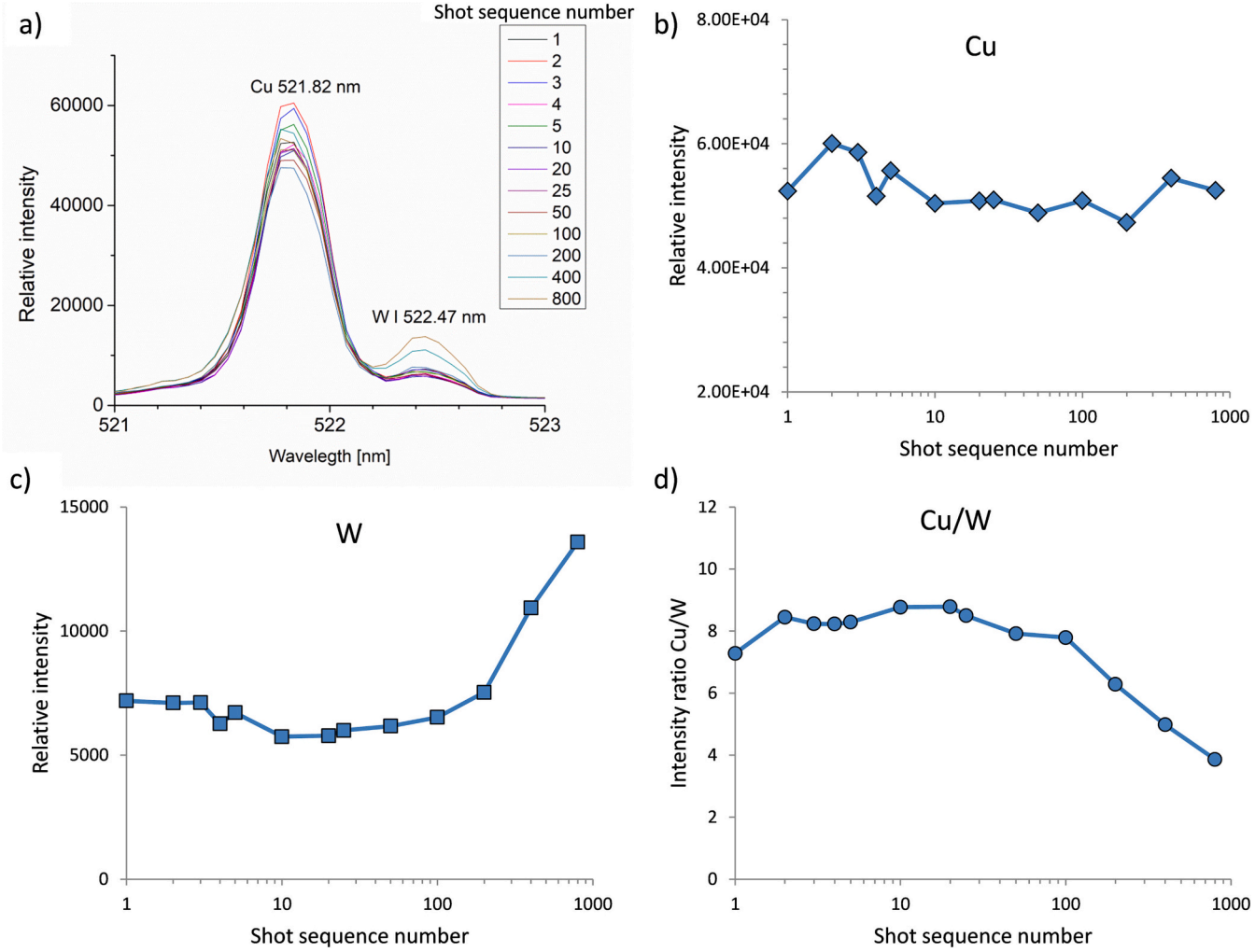

Fig. 6. (a) LIBS spectra recorded for a sequence (1–800) of laser shots applied to the same spot on the W90Cu10 target. (b-d) The effect of the crater depth on the intensity of Cu I 521.82 nm and W I 522.47 nm line and Cu/W intensity ratio.

Therefore, the influence of crater depth on the measured Cu/W intensity ratio was negligible for the number of pulses applied in this work.

3.2.2. *Plasma diagnostics*

LIBS spectrum recorded for the W70Cu30 sample was used to determine the excitation temperature from the Boltzmann plot of the selected W and Cu spectral lines. In order to cover a large spectral window (320 nm to 550 nm), several consecutive LIBS spectra were recorded, each covering a spectral portion of about 60 nm. The experimental parameters (laser energy, focusing, delay and gate time, and the number of accumulations) were held constant. Under our experimental conditions, only lines generated by neutral and single ionized W and Cu species can be detected. The list of lines and their spectral parameters (taken from the NIST Atomic Spectral Database [35]) are given in the

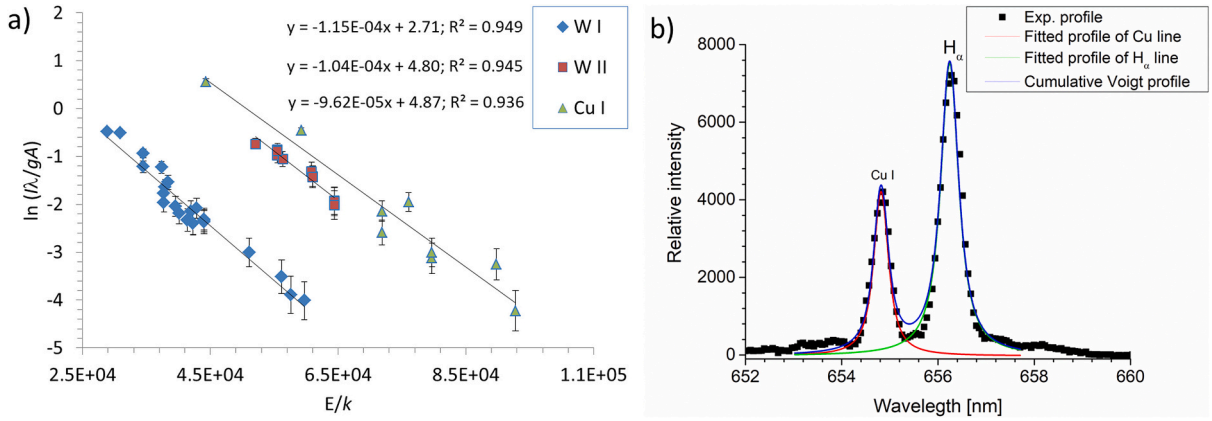

Fig. 7. a) Boltzmann plot of Cu and W spectral lines, and b) Experimental profile of the H_α line fitted to a Voigt function.

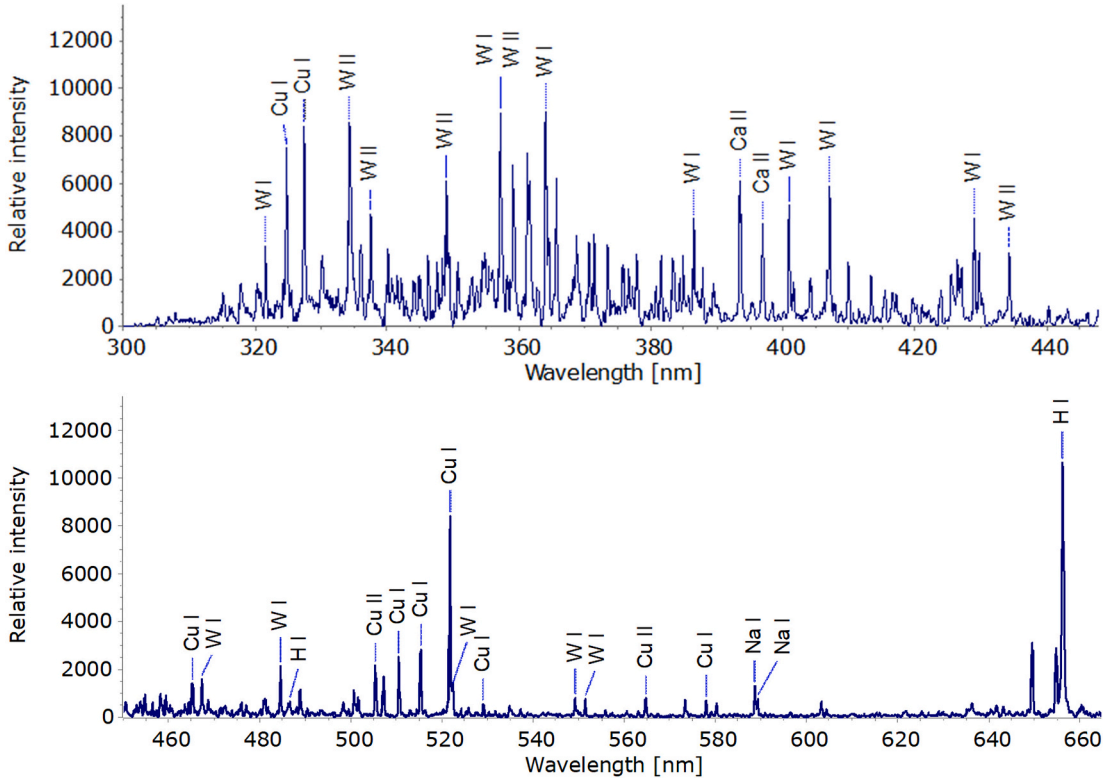

Fig. 8. LIBS spectra of the W93Cu7 alloy sample. Experimental conditions: Nd:YAG pulse energy 40 mJ; wavelength 532 nm; frequency 10 Hz; delay 0.5 μs; gate 2.5 μs; 10 mbar argon.

Appendix. The temperatures obtained from Boltzmann plots (Fig. 7a) were 8900 K, 9400 K, and 10,400 K for W I, W II, and Cu I, respectively. A Boltzmann plot using copper ionic lines was omitted because it had poor calculation accuracy of the plasma temperature due to a low number of identified Cu II spectral lines.

The electron number density was determined from the Stark width of the Balmer alpha line of the hydrogen, which is always present in the tungsten as an impurity (Fig. 7b). This line was chosen due to the low Balmer beta line intensity caused by the small amount of hydrogen. The line width was determined under the approximation that the line profile can be described with a Voigt function. The deconvolution of a Voigt function was performed using the Levenberg-Marquardt nonlinear fitting algorithm for minimum squares, with the Gaussian FWHM fixed, assuming that the Lorentzian component, w_L, is due to Stark broadening. The Gaussian fraction (w_G) is assumed to be a combination of the instrumental (w_i) and the Doppler broadening (w_D): $w_G = (w_D^2 + w_i{}^2)^{0.5} = (0.05^2 + 0.11^2)^{0.5} = 0.12$ nm. To calculate N_e, an approximate formula was used [36,37]:

$$N_e\left[m^{-3}\right] = 10^{23}\cdot\left(\frac{w_L[nm]}{1.098}\right)^{1.47135}$$

The estimated value of N_e was 2.5×10^{22} m^{-3}.

3.2.3. Univariate calibration

Characteristic spectra of the W/Cu composite sample in the 300–660 nm spectral range are shown in Fig. 8.

The possible influence of self-absorption was checked by comparing the experimental and theoretical ratios of line strengths within multiplets [38]. Based on the results shown in Table 2, it was concluded that the influence of self-absorption on the measured intensities of W and Cu lines could be neglected.

LIBS spectra of pure W and four W/Cu composite samples (Table 1) were used to construct a calibration curve. The spectra were recorded using the standard LIBS setup described in the experimental section using an optimized set of parameters: pulse energy 100 mJ; spot diameter 1 mm; delay 2 μs; gate 20 ns; 100 accumulations (average of ten measurements of 10 accumulated consequent laser shots). LIBS spectra of calibration samples are shown in Fig. 9 a.

Because the selected Cu and W lines overlap, integral intensities of these lines were determined using their approximation with Voigt functions. The line fit was performed using the Levenberg-Marquardt nonlinear fitting algorithm for minimum squares, with the Gaussian FWHM fixed (w_i = 0.11 nm). The calculated contribution of Doppler broadening was negligible for temperatures around 10,000 K, 0.005 nm for the Cu 521.82 nm line, and 0.003 for the W 522.47 nm line. The selected line pair was suitable for the Cu concentration range considered in this study. For samples with a low concentration of Cu, the intensity ratio of the strongest Cu I line at 324.75 nm with some of the nearby W lines (e.g., W I 320.72 nm) may be used.

A linear relationship was obtained between the Cu I 521.82 nm and

Table 2
Comparison of theoretical and experimental ratios of spectral line intensities.

	Configuration	λ_1 (nm)/λ_2 (nm)	$R = I_{\lambda1}/I_{\lambda2}$ (theor.)	$R = I_{\lambda1}/I_{\lambda2}$ (exp.)
W I	5d46s2 - 5d5(6S)6p	413.74 / 407.06	2.11	2.10
		436.48 / 407.06	0.32	0.29
Cu I	3d94s2 - 3d104p	510.55 / 578.21	2.42	2.27
	3d104p - 3d104d	515.32 / 521.82	0.53	0.56

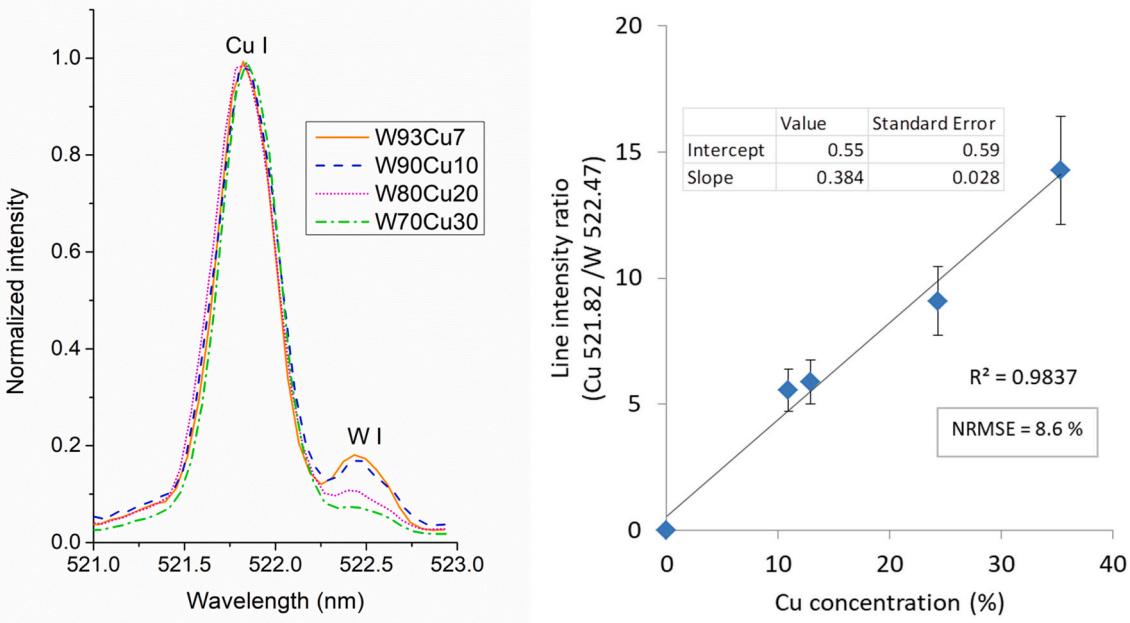

Fig. 9. (a) LIBS spectrum of W/Cu composites; (b) Calibration curve for Cu from the ratio $I_{Cu\ I}/I_{W\ I}$.

W I 522.46 nm line intensity ratio and the Cu concentration (Fig. 9 b). The calibration curve prediction error, calculated as a Root Mean Square Error (RMSE), was 0.598. The normalized value of the RMSE was 8.6%.

3.3. LIBS depth-profile analysis

A W/Cu functionally graded material (W/Cu FGM), i.e., tungsten with infiltrating copper along the sample thickness direction, was exposed to a variable number of Nd:YAG laser pulses. Time-resolved LIBS spectra were recorded to monitor the corresponding W and Cu spectral line intensity changes. The proposed depth profile analysis method was performed by combining the LIBS spectral analysis with the results of 3D-optical profilometry used to establish the depth of the ablation craters [39]. Fig. 10 shows 3D surface profiles of craters created on a W/Cu target after the increasing number of laser pulses irradiated the same spot on the target.

Corresponding 2D cross-sectional profiles used to evaluate the depth of the craters are shown in Fig. 11 a. A relationship between the number of laser pulses and crater depths is shown in Fig. 11 b.

As seen in Fig. 11 a, the paraboloid function describes the crater shape well. The volume of a paraboloid is given by $V = 1/2\,\pi\, r^2\, h$, where r is the radius of the circular "cap" of the paraboloid and h is the axial height of the paraboloid. In our case, the radius of the surface damaged area was taken as r and the crater depth as h. Using this equation, the

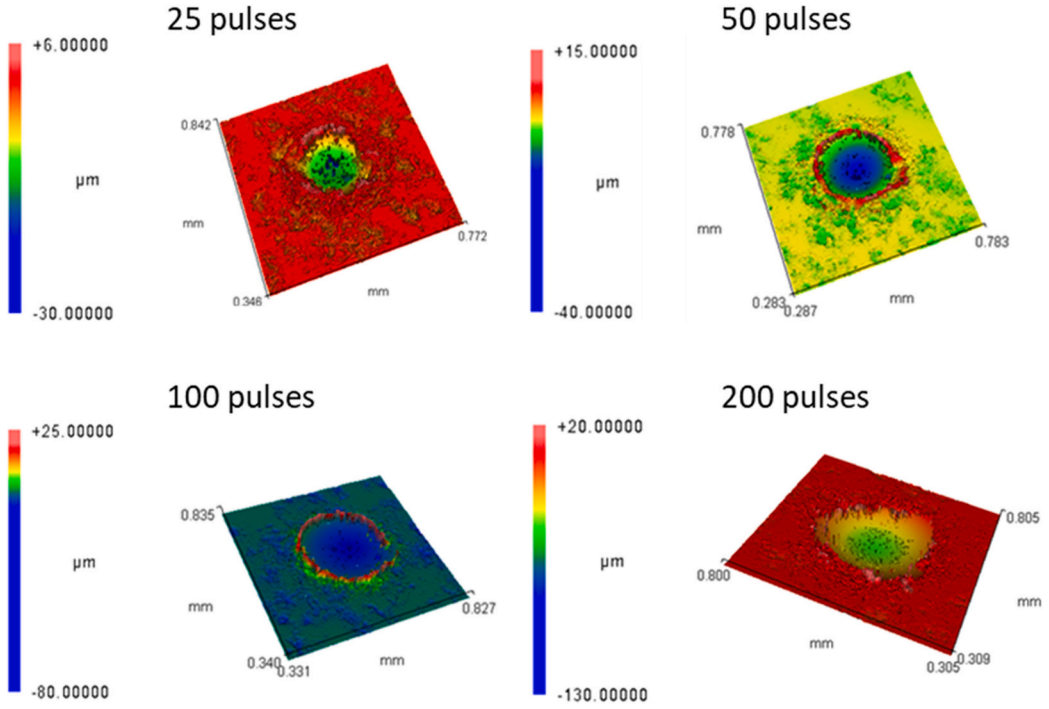

Fig. 10. Surface map of the W/Cu FGM target exposed to a different number of laser pulses.

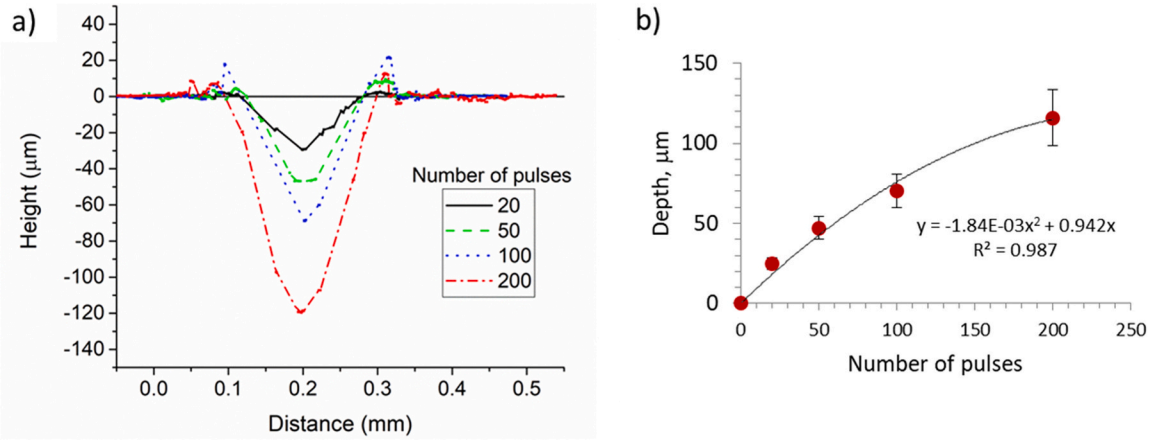

Fig. 11. (a) 2D profile of craters created on W/Cu target by a different number of laser pulses. (b) Crater depth as a function of the number of applied laser pulses.

Table 3
Characteristic parameters of craters created on W/Cu FGM target.

Number of pulses	Spot diameter (mm)	Crater depth (μm)	Spot surface area (10^{-4} cm^2)	Crater volume (10^{-7} cm^3)	Ablated mass* (μg)
25	0.16	29	2.0	3.0	5.7
50	0.16	47	2.0	4.8	9.2
100	0.16	69	2.0	6.9	13
200	0.20	120	3.1	19	36

* Calculated using tungsten density of 19.28 g/cm^3.

volume of the ablated material was calculated. Characteristic parameters of craters used to estimate the ablated volume and mass of the ablated material are given in Table 3.

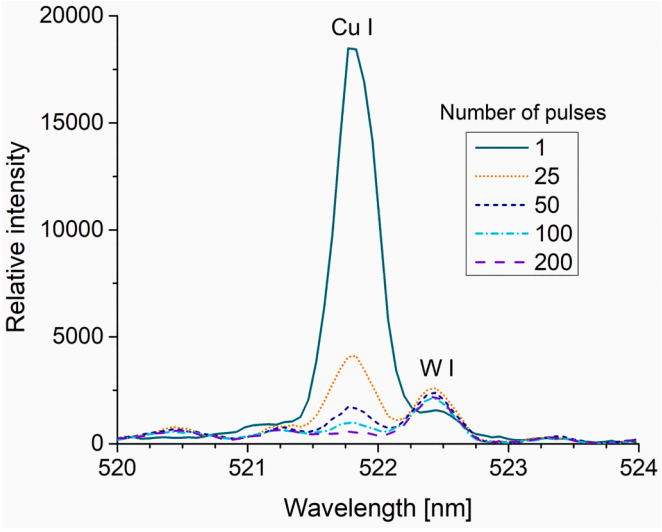

Fig. 12. LIBS spectra of a W/Cu-based gradient material. Laser energy 40 mJ; spot diameter 0.16 mm; delay 0.5 μs; gate 2.5 μs; 10 mbar argon.

LIBS spectra of a W/Cu target irradiated by an increasing number of laser pulses applied to the same target spot are shown in Fig. 12. As the figure shows, the intensity of a copper spectral line at 521.82 nm decreases with the increasing number of applied laser pulses, suggesting copper content gradually reduces from the top. The line disappeared from the spectra after 200 laser shots, indicating the complete removal of a layer containing a gradient concentration of Cu. Based on the obtained results, we estimated the depth of inbound copper into tungsten to ~120 μm. The copper concentrations at different depths were estimated from the calibration curve (Fig. 9 b) using a measured Cu I 521.82 nm and W I 522.46 nm line intensity ratios. The results are shown in Table 4.

4. Conclusion

The results have shown that a standard LIBS setup based on Nd:YAG laser using a medium spectral resolution spectrometer can be successfully applied to quantitative analysis of W/Cu functionally graded materials relevant to fusion technology.

For the W/Cu composite with Cu in the 10.9% - 35.3% concentration range, a linear relationship was found between Cu I 521.82 nm to W I 522.46 nm spectral line intensity ratio and Cu concentration. Under optimized experimental conditions (fluence, delay and gate time, number of accumulations), the selected W and Cu lines used to construct a calibration curve were optically thin.

It should be noted that the suitability of the W/Cu samples selected

Table 4
Copper content at different depths of the W/Cu FGM sample.

Number of laser shots	Depth (μm)	Intensity ratio Cu I 521.82/W I 522.46	Cu concentration (%)
1	0.9	12	30 ± 3
25	29	1.5	2.0 ± 0.2
50	47	0.7	0.39 ± 0.03
100	120	–	–

for the calibration technique should be carefully checked. Depending on the manufacturing processes, the grain size, shape of grains, distribution of additives inside the tungsten matrix, or other characteristics of W-based composites may influence the accuracy of LIBS analysis.

The copper concentration along the sample thickness direction was obtained by combining LIBS spectral analysis and optical profilometry results. The applied protocol may be suitable for depth profile analysis of tungsten-based composite in the fusion reactor, i.e., a transition layer between W tiles at the first wall of the reactor and cooling channels made of CuCrZr.

CRediT authorship contribution statement

M. Ivkovic: Conceptualization, Methodology, Supervision, Writing – original draft, Writing – review & editing. **J. Savovic:** Formal analysis, Visualization, Writing – review & editing. **B.D. Stankov:** Formal analysis, Investigation, Writing – review & editing. **M. Kuzmanovic:** Methodology, Validation, Writing – review & editing. **I. Traparic:** Formal analysis, Writing – review & editing.

Declaration of competing interest

The authors declare that they have no known competing financial interests or personal relationships that could have appeared to influence the work reported in this paper.

Data availability

Data will be made available on request.

Acknowledgements

The research was funded by the Ministry of Science, Technological Development and Innovation of the Republic of Serbia, Contract numbers: 451-03-47/2023-01/200024, 451-03-47/2023-01/200017 and 451-03-47/2023-01/200146, and supported by the Science Fund of the Republic Serbia, Grant no. 7753287.

Appendix A. Supplementary data

Supplementary data to this article can be found online at https://doi.org/10.1016/j.sab.2024.106874.

References

[1] M. Niino, T. Hirai, R. Watanabe, Functionally gradient materials. In pursuit of super heat resisting materials for spacecraft, J. Japan Soc. Compos. Mater. 13 (1987) 257–264, https://doi.org/10.6089/jscm.13.257.
[2] A. Kawasaki, R. Watanabe, Concept and P/M fabrication of functionally gradient materials, Ceram. Int. 23 (1997) 73–83, https://doi.org/10.1016/0272-8842(95)00143-3.
[3] M. Naebe, K. Shirvanimoghaddam, Functionally graded materials: a review of fabrication and properties, Appl. Mater. Today 5 (2016) 223–245, https://doi.org/10.1016/j.apmt.2016.10.001.
[4] Y. Miyamoto, W.A. Kaysser, B.H. Rabin, A. Kawasaki, R.G. Ford (Eds.), Functionally Graded Materials, Springer US, Boston, MA, 1999, https://doi.org/10.1007/978-1-4615-5301-4.
[5] K. Ichikawa (Ed.), Functionally Graded Materials in the 21st Century, Springer US, Boston, MA, 2001, https://doi.org/10.1007/978-1-4615-4373-2.
[6] S. Suzuki, M. Akiba, M. Araki, K. Yokoyama, Thermal cycling experiments of Monoblock Divertor modules for fusion experimental reactors, Fusion Technol. 21 (1992) 1858–1862, https://doi.org/10.13182/FST92-A29989.
[7] Y. Itoh, M. Takahashi, H. Takano, Design of tungsten/copper graded composite for high heat flux components, Fusion Eng. Des. 31 (1996) 279–289, https://doi.org/10.1016/0920-3796(95)00432-7.
[8] G. He, K. Xu, S. Guo, X. Qian, Z. Yang, G. Liu, J. Li, Preparation of tungsten fiber reinforced-tungsten/copper composite for plasma facing component, J. Nucl. Mater. 455 (2014) 225–228, https://doi.org/10.1016/j.jnucmat.2014.05.026.
[9] S. Wang, J. Li, Y. Wang, X. Zhang, R. Wang, Y. Wang, J. Cao, Thermal damage of tungsten-armored plasma-facing components under high heat flux loads, Sci. Rep. 10 (2020) 1359, https://doi.org/10.1038/s41598-020-57852-8.
[10] A.V. Muller, D. Ewert, A. Galatanu, M. Milwich, R. Neu, J.Y. Pastor, U. Siefken, E. Tejado, J.H. You, Melt infiltrated tungsten–copper composites as advanced heat sink materials for plasma facing components of future nuclear fusion devices, Fusion Eng. Des. 124 (2017) 455–459, https://doi.org/10.1016/j.fusengdes.2017.01.042.
[11] R. Neu, J. Riesch, A.V. Müller, M. Balden, J.W. Coenen, H. Gietl, T. Höschen, M. Li, S. Wurster, J.-H. You, Tungsten fibre-reinforced composites for advanced plasma facing components, Nucl. Mater. Energy. 12 (2017) 1308–1313, https://doi.org/10.1016/j.nme.2016.10.018.
[12] J.H. You, E. Visca, T. Barrett, B. Böswirth, F. Crescenzi, F. Domptail, M. Fursdon, F. Gallay, B.-E. Ghidersa, H. Greuner, M. Li, A.V. Müller, J. Reiser, M. Richou, S. Roccella, C. Vorpahl, European divertor target concepts for DEMO: design rationales and high heat flux performance, Nucl. Mater. Energy. 16 (2018) 1–11, https://doi.org/10.1016/j.nme.2018.05.012.
[13] Z.-J. Zhou, S.-X. Song, J. Du, Z.-H. Zhong, C.-C. Ge, Performance of W/cu FGM based plasma facing components under high heat load test, J. Nucl. Mater. 363–365 (2007) 1309–1314, https://doi.org/10.1016/j.jnucmat.2007.01.184.
[14] E. Tejado, M. Dias, J.B. Correia, T. Palacios, P.A. Carvalho, E. Alves, J.Y. Pastor, New WC-cu thermal barriers for fusion applications: high temperature mechanical behaviour, J. Nucl. Mater. 498 (2018) 355–361, https://doi.org/10.1016/j.jnucmat.2017.10.071.
[15] C. Li, D. Zhu, R. Ding, B. Wang, J. Chen, B. Gao, Y. Lei, Characterization on the melting failure of CuCrZr cooling tube of W/cu monoblocks during plasma operations in EAST, Nucl. Mater. Energy. 25 (2020) 100847, https://doi.org/10.1016/j.nme.2020.100847.
[16] D.W. Hahn, N. Omenetto, Laser-induced breakdown spectroscopy (LIBS), part II: review of instrumental and methodological approaches to material analysis and applications to different fields, Appl. Spectrosc. 66 (2012) 347–419, https://doi.org/10.1366/11-06574.
[17] S. Almaviva, L. Caneve, F. Colao, V. Lazic, G. Maddaluno, P. Mosetti, A. Palucci, A. Reale, P. Gasior, W. Gromelski, M. Kubkowska, LIBS measurements inside the FTU vessel mock-up by using a robotic arm, Fusion Eng. Des. 157 (2020) 111685, https://doi.org/10.1016/j.fusengdes.2020.111685.
[18] A. Favre, V. Morel, A. Bultel, G. Godard, S. Idlahcen, A. Benyagoub, I. Monnet, A. Sémérok, M. Dinescu, S. Markelj, P. Magaud, C. Grisolia, Double pulse laser-induced plasmas on W and Al by ps-LIBS: focus on the plasma-second pulse interaction, Fusion Eng. Des. 168 (2021) 112364, https://doi.org/10.1016/j.fusengdes.2021.112364.
[19] A. Marín Roldán, M. Pisarčík, M. Veis, M. Držík, P. Veis, Calibration-free analysis of a tungsten-based target for diagnostics of relevant fusion materials comparing picosecond and nanosecond LIBS, Spectrochim. Acta - Part B at Spectrosc. 177 (2021) 106055, https://doi.org/10.1016/j.sab.2020.106055.
[20] P. Liu, D.Y. Zhao, L.Y. Sun, C.L. Fu, J.M. Liu, C. Li, R. Hai, C.F. Sang, Z.H. Hu, Z. Sun, J.S. Hu, L. Wang, J.L. Chen, Y.F. Liang, G.N. Luo, H. Ding, In situ diagnosis of Li-wall conditioning and H/D co-deposition on the first wall of EAST using laser-induced breakdown spectroscopy, Plasma Phys. Control. Fusion. 60 (2018) 085019, https://doi.org/10.1088/1361-6587/aace83.
[21] F. Colao, S. Almaviva, L. Caneve, G. Maddaluno, T. Fornal, P. Gasior, M. Kubkowska, M. Rosinski, LIBS experiments for quantitative detection of retained fuel, Nucl. Mater. Energy. 12 (2017) 133–138, https://doi.org/10.1016/j.nme.2017.05.010.
[22] C. Li, C.-L. Feng, H.Y. Oderji, G.-N. Luo, H.-B. Ding, Review of LIBS application in nuclear fusion technology, Front. Phys. 11 (2016) 114214, https://doi.org/10.1007/s11467-016-0606-1.
[23] O.A. Waseem, H.J. Ryu, Tungsten-based composites for nuclear fusion applications, in: Nucl. Mater. Perform, InTech, 2016, https://doi.org/10.5772/62434.
[24] N. Farid, H. Wang, C. Li, X. Wu, H.Y. Oderji, H. Ding, G.-N. Luo, Effect of background gases at reduced pressures on the laser treated surface morphology, spectral emission and characteristics parameters of laser produced Mo plasmas, J. Nucl. Mater. 438 (2013) 183–189, https://doi.org/10.1016/j.jnucmat.2013.03.022.
[25] G.S. Maurya, A. Marín-Roldán, P. Veis, A.K. Pathak, P. Sen, A review of the LIBS analysis for the plasma-facing components diagnostics, J. Nucl. Mater. 541 (2020) 152417, https://doi.org/10.1016/j.jnucmat.2020.152417.
[26] P. Paris, J. Butikova, M. Laan, A. Hakola, I. Jõgi, J. Likonen, E. Grigore, C. Ruset, Comparison of LIBS results on ITER-relevant samples obtained by nanosecond and picosecond lasers, Nucl. Mater. Energy. 18 (2019) 1–5, https://doi.org/10.1016/j.nme.2018.11.018.
[27] D. Wu, L. Sun, J. Liu, Y. Lyu, H. Wu, S. Yuan, R. Hai, C. Li, C. Feng, D. Zhao, H. Ding, Parameter optimization of the spectral emission of laser-induced tungsten plasma for tokamak wall diagnosis at different pressures, J. Anal. At. Spectrom. 36 (2021) 1159–1169, https://doi.org/10.1039/D1JA00009H.
[28] M.S. Seyam, P. Koshy, M.A. Elbestawi, Laser powder bed fusion of unalloyed tungsten: a review of process, structure, and properties relationships, Metals (Basel). 12 (2022) 274, https://doi.org/10.3390/met12020274.
[29] H. Wu, C. Li, D. Wu, J. Liu, Z. He, Q. Li, S. Yuan, X. Cui, R. Hai, H. Ding, Characterization of laser-induced breakdown spectroscopy on tungsten at variable ablation angles using a coaxial system in a vacuum, J. Anal. At. Spectrom. 36 (2021) 2074–2084, https://doi.org/10.1039/D1JA00196E.
[30] S.N. Andreev, S.V. Orlov, A.A. Samokhin, Simulation of pulsed-laser-induced explosive boiling, Phys. Wave Phenom. 15 (2007) 67–80, https://doi.org/10.3103/S1541308X0702001X.
[31] K. Yahiaoui, T. Kerdja, S. Malek, Phase explosion in tungsten target under interaction with Nd:YAG laser tripled in frequency, Surf. Interface Anal. 42 (2010) 1299–1302, https://doi.org/10.1002/sia.3300.

[32] H.Y. Oderji, N. Farid, L. Sun, C. Fu, H. Ding, Evaluation of explosive sublimation as the mechanism of nanosecond laser ablation of tungsten under vacuum conditions, Spectrochim. Acta Part B At. Spectrosc. 122 (2016) 1–8, https://doi.org/10.1016/j.sab.2016.05.008.

[33] J. Hermann, C. Gerhard, E. Axente, C. Dutouquet, Comparative investigation of laser ablation plumes in air and argon by analysis of spectral line shapes: insights on calibration-free laser-induced breakdown spectroscopy, Spectrochim. Acta Part B At. Spectrosc. 100 (2014) 189–196, https://doi.org/10.1016/j.sab.2014.08.014.

[34] J. Hermann, D. Grojo, E. Axente, C. Gerhard, M. Burger, V. Craciun, Ideal radiation source for plasma spectroscopy generated by laser ablation, Phys. Rev. E 96 (2017) 053210, https://doi.org/10.1103/PhysRevE.96.053210.

[35] A. Kramida, Y. Ralchenko, J. Reader, NIST ASD Team, NIST Atomic Spectra Database (ver. 5.10), [Online], Available: https://physics.nist.gov/asd, 2022 [2023, May 30]. National Institute of Standards and Technology, Gaithersburg, MD., (n.d.). doi:doi:10.18434/T4W30F.

[36] N. Konjević, M. Ivković, N. Sakan, Hydrogen Balmer lines for low electron number density plasma diagnostics, Spectrochim. Acta - Part B At. Spectrosc. 76 (2012) 16–26, https://doi.org/10.1016/j.sab.2012.06.026.

[37] M.A. Gigosos, M.Á. González, V. Cardeñoso, Computer simulated Balmer-alpha, −beta and -gamma stark line profiles for non-equilibrium plasmas diagnostics, Spectrochim. Acta Part B At. Spectrosc. 58 (2003) 1489–1504, https://doi.org/10.1016/S0584-8547(03)00097-1.

[38] N. Konjević, M. Ivković, S. Jovićević, Spectroscopic diagnostics of laser-induced plasmas, Spectrochim. Acta Part B At. Spectrosc. 65 (2010) 593–602, https://doi.org/10.1016/j.sab.2010.03.009.

[39] V. Dwivedi, D. Prochazka, D. Janičkovič, P. Šperka, P. Švec, J. Kaiser, P. Veis, P. Pořízka, LIBS protocol for the assessment of depth profile, homogeneity, and quantification of Fe/co - based bilayer ribbon, Spectrochim. Acta Part B At. Spectrosc. 196 (2022) 106509, https://doi.org/10.1016/j.sab.2022.106509.

Fusion Engineering and Design 215 (2025) 114943

Contents lists available at ScienceDirect

Fusion Engineering and Design

journal homepage: www.elsevier.com/locate/fusengdes

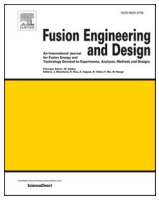

Detection of absorbed neutrons through determination of rhenium content in tungsten with laser induced fast pulse discharge

B.D. Stankov [a], I. Traparić [a], M. Gavrilović Božović [b], M. Ivković [a,*]

[a] Institute of Physics Belgrade, Pregrevica 118, 11080, Belgrade, Serbia
[b] Faculty of Engineering, Department of Electrical Engineering and Computer Science, Sestre Janjić 6, 34000, Kragujevac, Serbia

ARTICLE INFO

Keywords:
Laser-induced breakdown spectroscopy (LIBS)
Rhenium detection
Tungsten materials
Neutron absorption
Fast pulse discharge (FPD)
Fusion reactor diagnostics
Material transmutation

ABSTRACT

The diagnostics of the first wall of future fusion reactors provides a major source of information about the state of the machine and the expected lifetime of the first wall components. As the absorption of neutrons can cause induced radioactivity of the first wall tiles and produce significant structural changes to material, it is of the essence to monitor the amount of absorbed neutrons. One possibility to monitor them is via nuclear transmutation reaction where tungsten absorbs neutron and creates rhenium core. Therefore by assessing the amount of rhenium present in the material, information about neutron irradiation conditions can be deduced. Hence in this work, in order to assess the concentration of rhenium, Laser Induced Breakdown Spectroscopy (LIBS) combined with Fast Pulse Discharge (FPD) was used. The main achievement of this work is the amplification of line intensity and signal to noise ratio compared to the classical LIBS setup at reduced pressure which enables detection of *Re* in samples with less than 0.1% at of *Re*. With synergistic use of LIBS and FPD, ie. Laser Induced Fast Pulse Discharge (LIFPD), significantly enhanced Limit Of Detection (LOD) is obtained compared to the previously reported results. This result is of particular importance since only small amounts of rhenium are expected to be found in the first wall tiles, therefore making this approach suitable for this type of diagnostics.

1. Introduction

The advancement of nuclear fusion technology presents the prospect of a sustainable energy source, but it also imposes significant challenges regarding materials science and engineering. The first wall of fusion reactors, which directly absorbs neutron radiation arising from fusion reactions, plays a critical role in ensuring the reactor's structural integrity and operational efficiency. Tungsten is a leading candidate for future fusion reactors due to its high melting temperature (3422 °C), low sputter yield and high thermal conductivity (~170 W/m/K at room temperature), and low tritium retention [1,2].

Research on tungsten materials, particularly in the context of nuclear fusion, has surged, largely driven by the ITER project, leading to an increase in publications about tungsten's interactions with irradiation and plasma. Extensive studies have been conducted on neutron irradiation-induced defect formation and recovery in tungsten, offering well-characterized data crucial for understanding its properties [3].

While tungsten shows considerable potential as an armor and blanket material, it is predicted to undergo substantial transmutation under fusion neutron irradiation [4–6]. According to [7], W in the first wall substantially transmutes to Re followed by Os for the water cooled blanket. Noda et al. show a small reduction in W content is seen in the W armor as neutron fluence increases, while concentrations of Re, Ta and Os rise with fluence. In the transmutation processes induced by neutron irradiation, approximately 4% of W transmutes to Re for the W armor of all blankets, irrelevant of the blanket composition, after 10 MWy/ m^2 irradiation. At contrast, there is significant transmutation of W at the first wall position. Rhenium concentration surpasses that of tungsten at approximately 30 MWy/m^2, as illustrated in [7].

This transformation not only alters the material properties but also impacts the reactor's performance and safety. Precise measurement of Re concentrations is essential to understand the extent of transmutation, which influences the alloying behavior of tungsten and its capacity to maintain structural integrity under extreme conditions. Furthermore, the induced radioactivity associated with rhenium isotopes, particularly ^{186}Re, necessitates accurate quantification to assess potential safety concerns related to long-term radioactivity in reactor components. Consequently, comprehensive knowledge of Re concentrations in tungsten facilitates enhanced material optimization and ensures the reliability of fusion reactors in both operational and safety contexts [7].

* Corresponding author.
E-mail address: ivke@ipb.ac.rs (M. Ivković).

https://doi.org/10.1016/j.fusengdes.2025.114943
Received 25 December 2024; Received in revised form 4 March 2025; Accepted 5 March 2025
Available online 9 March 2025

In addition to rhenium being a product of tungsten transmutation after heavy neutron irradiation, the tungsten-rhenium (W-Re) alloy is very important. Adding rhenium can improve some of the drawbacks of pure tungsten, such as its low ductility at room temperature and low recrystallization temperature, leading to better overall performance as structural material in fusion reactors [8]. With idea of W-Re alloy being PFM, experiments on deuterium permeation and retention were conducted in Bo-Yu Wu et al. [9] using tungsten-rhenium samples with 3% and 25% rhenium to analyze how rhenium affects hydrogen isotope transport in tungsten. The results indicate that adding rhenium increases the D diffusion coefficient but decreases D permeability, with the diffusion coefficients for both W-3 % *Re* and W-25 % *Re* being similar, while permeability declines as Re content increases. Therefore, the detection of Re in W is important as W-Re alloy might be used as plasma facing material whose properties are largely influenced by the percentage of Re present in the material. This, on the other hand, can be closely correlated with the neutron irradiation conditions, see e.g. [10] where calculated Re contents for different neutron fluences assigned to different DPA (displacement per atom) levels are given in tabular form. Graph of predicted Re concentration under fusion DPA conditions based on the fission reactor irradiation data on pure W and W-Re alloys can be found in [11].

Detecting small percentages of rhenium in tungsten is critical for several reasons relevant to fusion reactor materials. The addition of just 5% rhenium can reduce thermal conductivity and diffusivity to half that of pure tungsten [8,12]. Furthermore, a drift in the temperature reading of a W–Re thermocouple will occur due to precipitation and compositional changes during irradiation [13]. Therefore, it is important to study the effects of compositional changes due to transmutation on the physical properties of W upon neutron irradiation, which is usually done through complex calculations and numerical simulations [14,15], while experimentally the information about the degree of transmutation could be assessed through accurate and sensitive determination of *Re* percentage in material. In [10] measurement on solid transmutations with glow discharge optical emission spectroscopy system equipped with dual interferometry system showed an excellent agreement with the results of numerical calculations. On the other hand, the authors state that the GD-OES data collection lasted at least 5 minutes, and they could not be performed in situ, or real time.

Laser Induced Breakdown Spectroscopy (LIBS) technique can provide a fast and reliable estimation of element content in the first wall of fusion reactor. It was already applied in a range of different studies related to the estimation of retained fuel in the first wall and for depth profile analysis of plasma facing components (PFCs) materials or thin film coatings relevant for PFC materials. Maddaluno and collaborators used single pulse LIBS (SP – LIBS) [16], while Colao et al [17] used double pulse LIBS (DP – LIBS) together with Calibration Free LIBS (CF – LIBS) procedure for quantitative assessment of retained fuel. Paris et al [18] studied the fuel retention in different W coatings using SP – LIBS and Nuclear Reaction Analysis (NRA). Bhat et al [19] studied depth profiles of Be coated samples with different percentages of deuterium and seeding gases using SP – LIBS in combination with CF – LIBS to evaluate the impact on fuel retention. Depth profiling using LIBS was also exploited by Feng et al [20], where they estimated lithium penetration depth in Er_2O_3 coatings and its depth concentration by CF – LIBS. The corrosion resistance of Er_2O_3 coating was determined by Li et al [21] using standard LIBS calibration curve technique. Wu et al [22] applied picosecond SP – LIBS in vacuum environment to study the depth distribution of boron in tungsten. Also, Hu et al [23] performed the quantitative analysis with CF – LIBS of deposited impurities on PFCs using a custom developed hand-held portable LIBS device. Van der Meiden et al. [24] demonstrated LIBS as a reliable method for in-situ monitoring of tritium retention and impurity deposition on tungsten plasma-facing components in fusion devices, providing quantitative depth-resolved analysis with high sensitivity. In particular, picosecond LIBS (ps-LIBS) has shown significant advantages for highly depth-resolved characterization of tungsten PFCs, achieving minimal thermal effects and an ablation rate below 40 nm per pulse, making it well-suited for diagnostic applications [25].

The lowest detection limit regarding Re detection by LIBS, that the authors are aware of, is reported by Ibano et al [26], who used a CF-LIBS to assess the concentration of Re in W-Re alloy. The authors state that relatively weak signal of Re I at 488.9 nm is observed at the right shoulder of a W-I line at 488.7 nm. In theirs experiment a line of Ar II is also present at 488.9 nm and according to the authors its influence on the line of Re cannot be ignored in cases of Re concentrations lower than 0.5 at.%. The authors confirm that the CF-LIBS results align closely with the nominal manufacturer concentration down to 0.5 at.%. However, after 12 years of full DT operation, the tungsten wall in ITER is expected to produce only about 0.18 at.% of Re [27]. Therefore, developing a more sensitive method based on the LIBS in the non-argon atmosphere is essential.

In this work, we investigate the potential enhancement of LIBS sensitivity through its integration with Fast Pulse Discharge (FPD) in a helium atmosphere, termed Laser Induced Fast Pulse Discharge (LIFPD). This approach is anticipated to significantly amplify the resultant spectral signals [28], thereby improving the limit of detection (LOD) for rhenium in predominantly tungsten targets, which is important for assessing absorbed neutron doses and consequent structural changes both in the pure and Re-alloyed tungsten.

In the following Section 2, we discuss the experimental setup of the LIFPD method. Main results of this work are presented and discussed in Section 3 which is organised as follows: Section 3.1 gives thorough description of the optimisation procedure to achieve highest analytical signal, while the achieved signal amplification with the proposed LIFPD setup is discussed in the Section 3.2. Procedure for detection limit determination of trace Re in W is presented in Section 3.3. Finally, our findings are summarized in Section 4 Conclusion. .

2. Experimental setup

The experimental setup of proposed LIFPD method is shown in the Fig. 1.

Laser beam (Nd:YAG Quantel 450, $\lambda = 532$ nm, pulse duration 6 ns, $E = 50$ mJ, 1 Hz) was focused via lens ($f = 12.5$ cm) onto the target that was placed inside the vacuum chamber. Target was rotated to expose the fresh surface on the target for each measurement. After the laser shot, laser induced plasma enters central part of the cross shaped vacuum vessel, where two electrodes were placed and connected to the capacitor battery ($C = 330$ nF). The experiment was optimized in a way that the laser produced plasma triggers the fast pulsed discharge, meaning that the HV level was careffully adjusted to be close to the breakdown voltage in order that the plasma can ignite the discharge. Targets investigated were 95 % W with 5% of Re, 90 % W with 10% of Re and 75 % W with 25% of Re. Thickness of the targets was measured to be 0.6 mm. Light emitted from LIBS plasma, as well as from the fast pulsed discharge, was collected with the collimator and guided through the fiber cable onto the entrance slit of the SOLinstruments MS7504i spectrometer equipped with Andor iStar ICCD camera (model DH734 – 18F – 63, 1024×1024 pixels, 18 mm sensor size). Camera was triggered and gated with the external digital delay generator (DDG) unit (Stanford Research SRS535), which on the other hand was triggered with signal from photodiode that monitors the LIBS plasma. HV was measured with high voltage probe that was attached to the Tektronix TDS2024C digital storage oscilloscope. Current intensity in pulsed arc was measured with Rogowski coil mounted around the current supply cable. The experiment was performed under controlled atmosphere of He gas, with the pressure adjusted in the range from 3 mbar up to 25 mbar. Each spectrum is obtained as accumulation over 10 laser pulses.

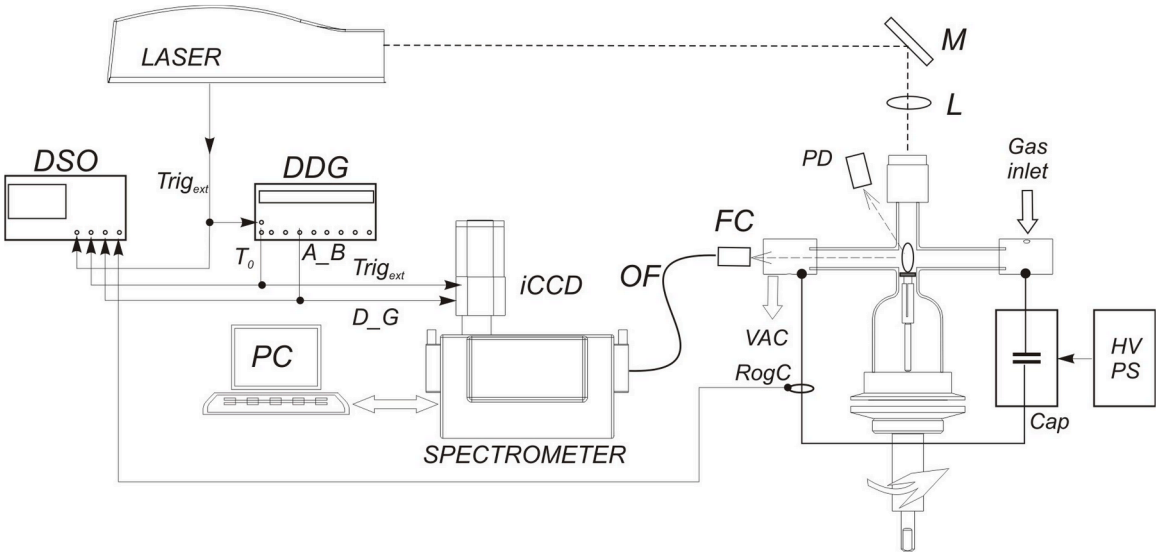

Fig. 1. Experimental setup with interaction chamber for proposed integrated LIFPD. High voltage electrodes are positioned orthogonally to the laser beam propagation direction and charged to the level that fast discharge is formed after laser pulse interaction with the sample.

3. Results and discussion

3.1. Optimization of the experiment

Experimental parameters that were optimized are working pressure inside the discharge tube, discharge voltage, the delay time and gate width of spectra recording with respect to the laser pulse. The optimisation is performed on the target sample consisting of 5 % of Re and 95 % of W.

The influence of ambient gas on the measurements was also carefully evaluated. While argon is noted for its effective performance as an infusing gas in LIBS [26,29], in the case of Rhenium detection it also imposes certain problems due to the spectral lines of Ar overlap the Re lines of interest. Our findings suggest that clear differentiation of the Re I line from tungsten can be obtained in He atmosphere under the optimized conditions within our LIFPD setup, thus avoiding any potential spectral overlaps, which led to the choice of helium as a background gas instead of argon.

For pressures of Helium gas lower than 10 mbar, the temporal reproducibility of the discharge current with respect to the laser pulse was worse than 5 μs, meaning that the appearence of LIFPD plasma was not temporaly reproducible, implying that the experiment must be done at greater pressures. For pressures above 10 mbar, temporal reproducibility was 2 μs which is acceptable for the application of interest in this paper. In other words, plasma generated by the additional discharge appears with a delay relative to the laser impulse, with a reproducibility of approximately 2 μs.

The pressure dependence of line intensities belonging to target material is shown in Fig. 2, in the pressure range of 11 mbar to 25 mbar. As can be seen, higher pressure values were preferred to ensure the increase in the intensity of the spectral lines, as well as for temporal reproducibility of the LIFPD. However, pressures exceeding 24 mbar were excluded due to instability in the discharge, which did not occur consistently following each laser pulse, possibly due to the irregular supply of target material particles which propagate at slower speed at increased pressure and experience higher number of collisions moving them out of the LIFPD interaction zone. Consequently, all subsequent measurements were conducted in an atmosphere of 24 mbar of helium, which ensures highest signal enhancement with stable and reproducible LIFPD event.

It is noteworthy that the fast pulse discharge plasma emerges after the LIBS plasma, allowing to assess separately the effects of this

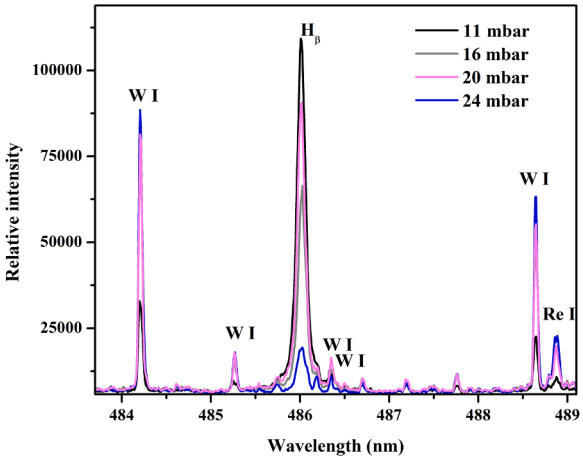

Fig. 2. Pressure optimisation for LIFPD plasma.

additional discharge. This sequence of events was assured with the proper combination of discharge voltage and gas pressure. It is concluded that the voltage of 420 V in combination with the pressure of 24 mbar leads to appearance of LIFPD plasma 7 μs after the ending of LIBS plasma. Spectra recorded from LIBS plasma for different delay time and gate width are represented in Fig. 3. From Fig. 3 it can be concluded that the LIBS plasma does not persist longer than 20 μs.

In the present study, the main task was to achieve a stable and reproducible FPD event triggered by the LIBS plasma. All working parameters, including laser energy, spot size, pressure etc were adjusted in that respect. The critical parameter to achieve this reproducibility was laser fluence achieved on the target in combination with suitable working pressure. Namely, laser fluence needed to be sufficiently high to ablate enough sample material to induce LIFPD event and create strong spectral emission of the elements of interest, but on the other hand sufficiently low to avoid explosive boiling of tungsten. Considering previous works regarding tungsten irradiation with Nd:YAG lasers [30, 31], to achieve this with the fixed laser energy of 50 mJ used here, the optimal spot size was determined to be 1 mm. The ablation rate was not studied since the target was constantly rotated, potentially creating overlapping spots which may hamper accurate profilometry measurements.

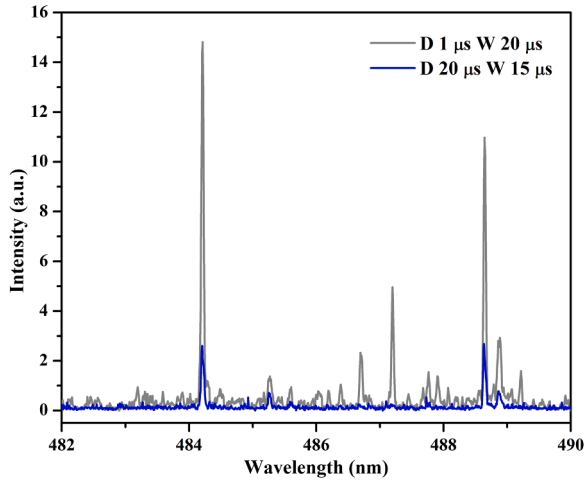

Fig. 3. Typical LIBS spectra obtained from different stages of plasma temporal evolution. Respective delays and gate widths are shown in the figure.

For the LIFPD plasma signal recordings, two options were considered: the first one was to trigger the camera at the maximum of the current signal, and the second is to trigger the camera 2 μs before the current signal. As the illustration of triggering scheme, oscilloscope signals are shown in Fig. 4.

The signal enhancement for lines of Re in the case of triggering on the current maximum is almost negligible. When the camera is triggered 2 microseconds before the current signal (Fig 4), the amplification of the signal in the resultant spectra (Fig 5) is almost 5 times for the tungsten line and almost 10 times for the Re I 488.91 nm line compared to the LIBS signal Based on these significant analytical signal enhancements, this gating scheme was adopted as optimal and used in all subsequent measurements. Two current maximums are appearing (see Fig 4) because the pulsed plasma source is not critically damped, i.e. plasma impendance and external circuit impendance are not matched.

After the selection of the pressure, voltage, and the delay time, the gate width was adjusted accordingly. The gate width for the recording of FPD was set to compensate the temporal irregularity of FPD plasma appearance by ± 2μs. The gate width was therefore chosen as the duration of LIFPD current signal plus additional 4 μs. For that reason the gate width was set to be 23 μs. Temporal evolution of LIBS and LIFPD plasma is presented in Fig. 5.

To summarize the optimization process, it was determined that the optimal gas for the experiment is helium, with a pressure of 24 mbar. Optimal voltage is 420 V. At this pressure and voltage, the ideal

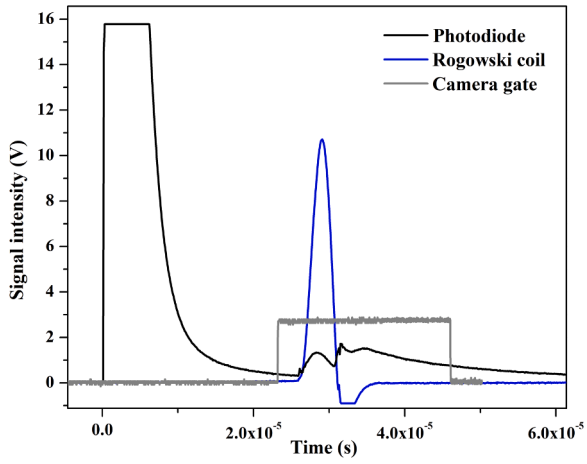

Fig. 4. Triggering and gating of the iCCD camera.

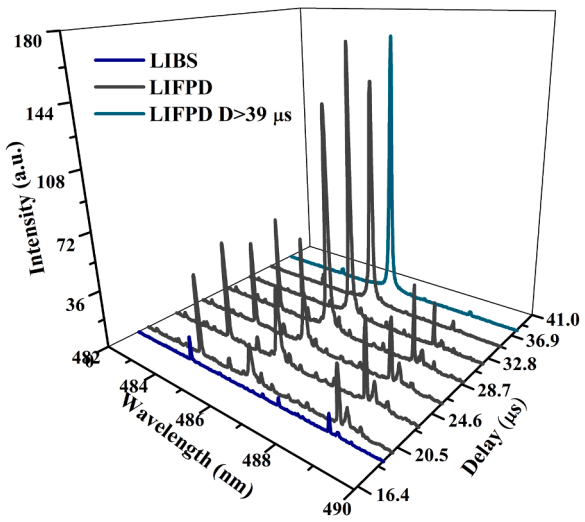

Fig. 5. Temporal evolution of LIBS and LIFPD.

triggering scheme involves initiating camera recording 2 μs prior to the current signal. The gate width is configured to match the duration of the current pulse, with an additional 4 microseconds added to accommodate the temporal irregularities associated with the discharge plasma's appearance, leading to gate width of 23 μs.

Electron temperature in LIFPD was estimated from the ratio of intensities of W I 484.381 nm and W I 488.689 nm lines, using the formula:

$$\frac{I_1}{I_2} = \frac{g_1 A_1 \lambda_2}{g_2 A_2 \lambda_1} e^{\frac{E_2 - E_1}{k_B T_e}}.$$

Measured relative intensity ratio corresponds to the excitation temperature of 12 000 K. Having this estimation in mind, we determined of electron density. For this purpose, the hydrogen H_β line was used. As a first step, the FWHM was measured to be 0.133 nm. Instrumental width was measured to be 0.025 nm and from Doppler broadening was determined from the formula:

$$\Delta\lambda = 7.16 \times 10^{-7} \cdot \lambda_0 \cdot \sqrt{\frac{T}{M}},$$

to be 0.036 nm. The deconvolution formula [32,33] was used to determine the Stark component from the total FWHM:

$$w_s = \left(w_m^{1.4} - w_{D,I}^{1.4}\right)^{1/1.4}$$

When calculated, Stark width is estimated to be 0.11 nm. Finally, using the formula [32,34]:

$$\log N_e = 22.578 + 1.478 \times \log w_s - 0.144 \times (\log w_s)^2 - 0.1265 \times \log T_e$$

The electron density was estimated to be 3.2×10^{14} cm^{-3}. Since the electron density is estimated to be 3.2×10^{14} cm^{-3}, Stark broadening of the spectral lines is negligible. Furthermore, as this work was performed at low pressures, van der Waals broadening is also negligible.

3.2. Comparison of analytical capabilities of LIBS vs LIFPD

The main objective of this work was to obtain signal amplification with application of LIFPD compared to conventional LIBS. This predicted line intensity amplification is reasonable assumption since LIFPD is much stronger spectral light source than LIBS plasma.

The achieved results regarding signal amplification are shown in the Fig. 6. Optimal camera delay to capture the LIFPD signal with the best intensity is 23 μs after LIBS plasma, where the highest SNR was achieved. This SNR is three times higher than the one obtained with the pure LIBS, while the line intensity itself is almost 5 times increased. This

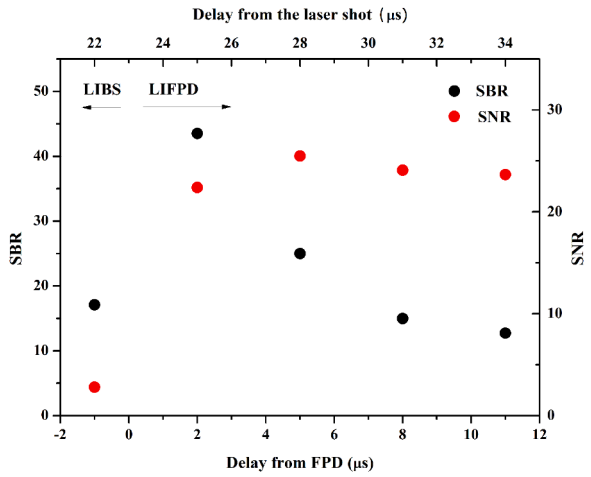

Fig. 6. SBR (Signal to Background Ratio) and SNR (Signal to Noise Ratio) for LIBS and LIFPD plasma as a function of camera delay. The trigger of the camera set 2 μs before the current pulse is regarded as 0 μs.

result bears significat importance for the analysis of the first wall of fusion reactors in terms of absorbed neutrons, since predicted concentrations of material of interest, i.e. Re, are expected to be quite low.

The possibility of target ablation via the discharge and its subsequent influence on the intensity of rhenium lines in the spectrum was also examined, as illustrated in the Fig. 7. The discharge was operated in pulsed mode, employing a sequence of 10 accumulated pulses, with the voltage set at 600 V to facilitate a pulsed discharge without the requirement for laser initiation. In the absence of the initial LIBS plasma, no spectral lines from the target material were detected in the pure FPD spectrum; the dominant feature observed was the H_β line. However, upon activation of the laser, well-resolved lines corresponding to the target material emerged, exhibiting significantly stronger intensities compared to the pure LIBS signal. This indicates that the primary source of material in the discharge is laser ablation, with contributions from sputtering and ablation due to FPD being negligible in this context. In the absence of the initial LIBS plasma, no spectral lines from the target material were detected in the pure FPD spectrum; instead, the dominant feature was the H_β line. This H_β line appears as an impurity since hydrogen is absent from both the working gas and the target material. Its presence is attributed to traces of water vapor on the walls of the discharge tube. Notably, the LIBS plasma, due to its significantly smaller size, does not induce moisture evaporation from the tube walls between the electrodes, thereby there are no hydrogen lines in the spectra.

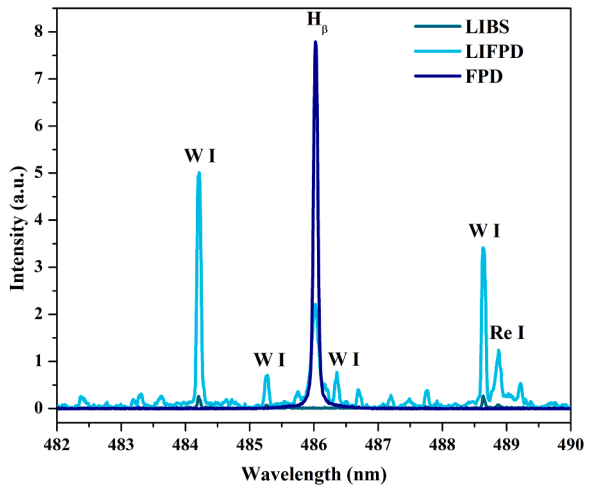

Fig. 7. LIBS, LIFPD and FPD spectra compared.

3.3. Detection threshold of trace Re in W

In this section, we present the calculation of the detection limit (LOD) as the smallest quantity of analyte that can be confidently identified in a sample, along with the quantification limit (LOQ), defined as the smallest quantity that can be reliably quantified, both with the proposed LIFPD approach and standard LIBS setup. The calculations were performed using the formulas: $LOD = 3 \times \sigma / S$ and $LOQ = 10 \times \sigma / S$, where S represents the slope of the calibration curve and σ denotes the standard deviation of the spectral recordings.

The spectra were recorded using the LIFPD setup described in the experimental section, with an optimized set of parameters: pulse energy of 50 mJ, a spot diameter of 1 mm, 10 accumulations per recording, and a gain of 100. The delay time was set to 23 μs, accompanied by a gate time width of 23 μs.

Integral intensities of the Re I lines were determined by approximating them with Lorentzian functions, which is appropriate given the negligible contribution of Doppler broadening at temperatures around 10,000. Specifically, the Doppler broadening was calculated to be 1.54 pm for Re I at 488.91 nm and 1.5 pm for W I at 488.69 nm. The Lorentzian profile effectively captures the predominant collisional and natural broadening in this temperature range. The selected line is well-suited for the range of Re concentrations considered in this study.

To evaluate the minimum measurable concentration of rhenium (Re) in relation to experimental error, we employed the Re I line at 488.9 nm recorded from three samples with known concentrations, Fig. 8.

The intensity of this spectral line was plotted against the known concentration of Re to generate a calibration curve, as depicted in Fig. 9. The standard deviation was determined as the average of eight measurements from a target mixture composed of 95% tungsten (W) and 5% rhenium (*Re*), yielding a value of 308.34.

A linear relationship was established between the intensities of the Re I line at 488.91 nm and the Re concentration, as illustrated in Fig. 9. This finding indicates that the intensity ratio can serve as a reliable indicator of Re concentration in the analyzed samples. The calibration curve's prediction error, calculated as the Root Mean Square Error (RMSE), was found to be 11,354, with a normalized RMSE value of 5.68%. These results demonstrate the robustness of the calibration curve and its potential for accurately quantifying Re concentrations in various applications.

The calculated values for LOD and LOQ were found to be 0.068% (680 ppm or 0.067% at.) and 0.23% (or 2300 ppm or 0.227% at.), respectively. These results represent a significant improvement over previous reports, which indicated a detection limit of approximately 0.5 at.% [26]. This enhancement in sensitivity is crucial for applications requiring precise quantification of trace amounts of rhenium, potentially

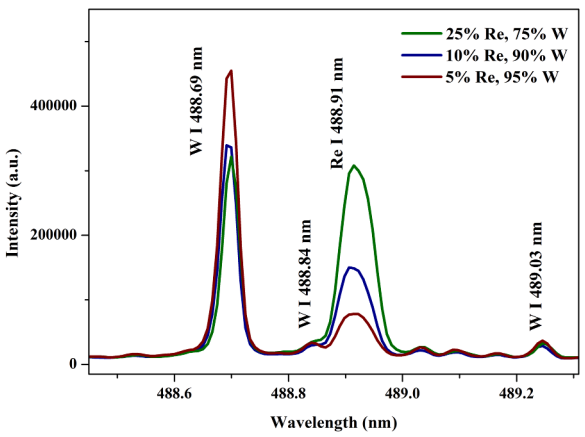

Fig. 8. W I and *Re* I lines recorded from LIFPD from three samples with known concentrations.

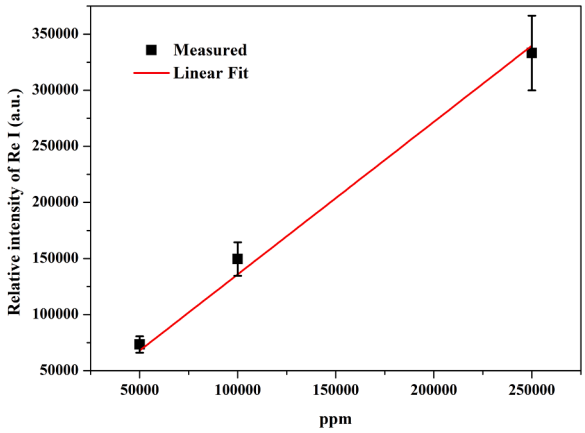

Fig. 9. Calibration curve for determination of LOD for Rhenium in LIFPD.

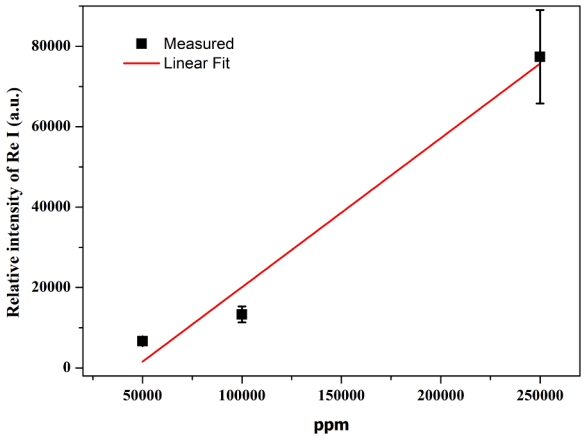

Fig. 10. Calibration curve for determination of LOD for Rhenium in LIBS.

expanding its applicability in various fields such as materials science and analytical chemistry.

The spectra were also recorded using the standard LIBS setup, with an optimized set of parameters: pulse energy of 50 mJ, a spot diameter of 1 mm, 10 accumulations per recording, and a gain of 150. The delay time was set to 1 μs, accompanied by a gate time width of 15 μs.

This is done in order to compare the two methods. For LIBS analysis the standard deviation was calculated to be 260, and the Slope of calibration curve was 0.3701, leading to the value of LOD of 2106 ppm or 0.21%, which is again fairly good result. However, it must be noted that the quality of the fiting is not nearly as god as is in the case of the results obtained with the LIFPD setup. The possible reason is that for the standard LIBS setup, spectra obtained with only 10 accumulations are usually not god enough in terms of reproducibility due to the changes in the amount of ablated material per shot, plasma target shielding for subsequent pulses, more pronounced background in the spectra etc. In addition, the calibration curve in the Fig. 10 is not passing through the coordinate origin as it should, so this additionaly speaks in the favour of better reproducibilty and higher accuracy of concentration determination wiht the LIFPD approach.

4. Conclusion

This investigation successfully demonstrates the feasibility of utilizing Laser Induced Breakdown Spectroscopy (LIBS) in conjunction with Fast Pulse Discharge (FPD) to detect low concentrations of rhenium in tungsten samples. Our findings reveal that the proposed method significantly amplifies the spectral signal, achieving a threefold increase in the signal-to-noise ratio and nearly five times greater intensity compared to the conventional LIBS techniques. This amplification is particularly crucial given the anticipated low levels of rhenium resulting from neutron transmutation reactions within the first wall of fusion reactors.

Our experimental approach involved analysis of various tungsten-rhenium alloy specimens, leading to a threshold detection limit of 0.067 at. %. This marks a substantial improvement over previous studies, which reported a detection limit of approximately 0.5 at.% [26].

Our findings indicate that the optimized conditions within our FPD-enhanced LIBS setup enable clear differentiation of the Re I line from tungsten in Helium, thus circumventing potential spectral overlaps caused by the ambient gas.

The LIFPD approach outlined in this research holds promise for enhanced diagnostics of fusion reactor components, allowing for precise monitoring of absorbed neutron levels through the quantification of rhenium. It provides a valuable tool for assessing the integrity and longevity of structural materials in fusion reactors under operational conditions. Future studies should aim to further refine this methodology and explore its application in real-time monitoring environments, thereby contributing to the development of safer and more efficient fusion energy systems. This approach is suitable for post-mortem analysis (between experimental campaigns); however, the authors are currently working on a measuring device that will enable the application of this method for real-time in situ measurements (withouth demounting the components in tokamak).

Additionally, the results of this paper have shown that a standard LIBS setup based on Nd:YAG laser can be successfully applied to quantitative analysis of W/Re composition materials relevant to fusion technology.

Further investigations will focus on optimizing the measurement conditions and exploring the applicability of this method to other analytes, thereby broadening the scope of this analytical technique.

CRediT authorship contribution statement

B.D. Stankov: Investigation, Formal analysis, Writing – original draft. **I. Traparić:** Investigation, Formal analysis, Writing – review & editing. **M. Gavrilović Božović:** Writing – original draft, Formal analysis. **M. Ivković:** Writing – review & editing, Supervision, Conceptualization, Methodology, Funding acquisition.

Declaration of competing interest

The authors declare that they have no known competing financial interests or personal relationships that could have appeared to influence the work reported in this paper.

Acknowledgements

The research was funded by the Ministry of Science, Technological Development and Innovations of the Republic of Serbia, Contract numbers: 451-03-68/2022-14/200024, 451-03-66/2024-03/200107 and supported by the Science Fund of the Republic Serbia, Grant no. 7753287 “NOVA2LIBS4fusion”. The authors thank Stanko Milanovic for technical assistance in preparation and setting up the experiment.

Data availability

Data will be made available on request.

References

[1] H. Bolt, V. Barabash, W. Krauss, J. Linke, R. Neu, S. Suzuki, N. Yoshida, ASDEX Upgrade Team, Materials for the plasma-facing components of fusion reactors, J. Nucl. Mater 329–333 (2004) 66–73, https://doi.org/10.1016/j.jnucmat.2004.04.005.

[2] V. Philipps, Tungsten as material for plasma-facing components in fusion devices, J. Nucl. Mater. 415 (Issue 1) (2011) S2–S9, https://doi.org/10.1016/j.jnucmat.2011.01.110. Supplement.
[3] M. Rieth, R. Doerner, A. Hasegawa, Y. Ueda, M. Wirtz, Behavior of tungsten under irradiation and plasma interaction, J. Nucl. Mater. 519 (2019) 334–368, https://doi.org/10.1016/j.jnucmat.2019.03.035.
[4] L.R. Greenwood, F.A. Garner, Transmutation of Mo, re, W, Hf, and V in various irradiation test facilities and STARFIRE, J. Nucl. Mater. 212-215 (1994) 635–639, https://doi.org/10.1016/0022-3115(94)90136-8.
[5] C.B.A. Forty, G.J. Butterworth, J.-Ch. Sublet, Burnup of some refractory metals in a fusion neutron spectrum, J. Nucl. Mater. 212-215 (1994) 640–643, https://doi.org/10.1016/0022-3115(94)90137-6.
[6] T. Noda, M. Fujita, Effect of neutron spectra on the transmutation of first wall materials, J. Nucl. Mater. 233-237 (1996) 1491–1495, https://doi.org/10.1016/S0022-3115(96)00108-0.
[7] T. Noda, M. Fujita, M. Okada, Transmutation and induced radioactivity of W in the armor and first wall of fusion reactors, J. Nucl. Mater. 258-263 (1998) 934–939, https://doi.org/10.1016/S0022-3115(98)00088-9. Get rights and content.
[8] M. Fujitsuka, B. Tsuchiya, I. Mutou, T. Tanabe, T. Shikama, Effect of neutron irradiation on thermal diffusivity of tungsten–rhenium alloys, J. Nucl. Mater. 283–287 (2000) 1148, https://doi.org/10.1016/S0022-3115(00)00170-7.
[9] Bo-Yu Wu, Yu-Ping Xu, Yi-Ming Lyu, Xiao-Chun Li, Xiang Geng b, Shou-An Puyang, Xin Shen, Xin-Dong Pan, Hai-Shan Zhou, Guang-Nan Luo, Effects of rhenium content on the deuterium permeation and retention behavior in tungsten, J. Nucl. Mater. 565 (2022) 153709, https://doi.org/10.1016/j.jnucmat.2022.153709.
[10] Y. Katoh, L.L. Snead, L.M. Garrison, X. Hu, T. Koyanagi, C.M. Parish, P. D. Edmondson, M. Fukuda, T. Hwang, T. Tanaka, A. Hasegawa, Response of unalloyed tungsten to mixed spectrum neutrons, J. Nucl. Mater. 520 (2019) 193–207, https://doi.org/10.1016/j.jnucmat.2019.03.045.
[11] A. Hasegawa, M. Fukuda, S. Nogami, K. Yabuuchi, Neutron irradiation effects on tungsten materials, Fusion Eng. Des. 89 (2014) 1568–1572, https://doi.org/10.1016/j.fusengdes.2014.04.035.
[12] T. Tanabe, C. Eamchotchawalit, C. Busabok, S. Taweethavorn, M. Fujitsuka, T. Shikama, Temperature dependence of thermal conductivity in W and W–Re alloys from 300 to 1000 K, Mater. Lett. 57 (2003) 2950–2953, https://doi.org/10.1016/S0167-577X(02)01403-9.
[13] R.K. Williams, F.W. Wiffen, J. Bentley, J.O. Stiegler, Irradiation induced precipitation in tungsten based, W-Re alloys, Metall. Trans. A 14A (April) (1983) 655–666, https://doi.org/10.1007/BF02643781.
[14] T. Hwang, A. Hasegawa, K. Tomura, N. Ebisawa, T. Toyama, Y. Nagai, M. Fukuda, T. Miyazawa, T. Tanaka, S. Nogami, Effect of neutron irradiation on rhenium cluster formation in tungsten and tungsten-rhenium alloys, J. Nucl. Mater. 507 (2018) 78–86, https://doi.org/10.1016/j.jnucmat.2018.04.031.
[15] A. Hasegawa, M. Fukuda, K. Yabuuchi, S. Nogami, K. Ibano, D. Nishijima, Y. Ueda, R.P. Doerner, Neutron irradiation effects on the microstructural development of tungsten and tungsten alloys, J. Nucl. Mater. 522 (2019) 324–328, https://doi.org/10.1016/j.jnucmat.2015.10.047.
[16] G. Maddaluno, S. Almaviva, L. Caneve, F. Colao, V. Lazic, L. Laguardia, P. Gasior, M. Kubkowska, FTU team, Detection by LIBS of the deuterium retained in the FTU toroidal limiter, Nucl. Mater. Energy 18 (2019) 208–211, https://doi.org/10.1016/j.nme.2018.12.029.
[17] F. Colao, et al., LIBS experiments for quantitative detection of retained fuel, Nucl. Mater. Energy 12 (2017) 133–138, https://doi.org/10.1016/j.nme.2017.05.010.
[18] P. Paris, I. Jõgi, K. Piip, M. Passoni, D. Dellasega, E. Grigore, WM. Arnoldbik, H. van der Meiden, In-situ LIBS and NRA deuterium retention study in porous W-O and compact W coatings loaded by Magnum-PSI, Fusion Eng. Des. 168 (2021) 112403, https://doi.org/10.1016/j.fusengdes.2021.112403.
[19] P.G. Bhat, et al., LIBS depth profiling of Be-containing samples with different gaseous impurity concentrations, Nucl. Mater. Energy 37 (2023) 101549, https://doi.org/10.1016/j.nme.2023.101549.
[20] S. Feng, C. Ke, Y. Chen, H. Zhang, Y. He, Y. Zhao, CF-LIBS analysis in depth profile of lithium corrosion resistance of Er_2O_3 coatings prepared by sol-gel method, Fusion Eng. Des. 170 (2021) 112506, https://doi.org/10.1016/j.fusengdes.2021.112506.
[21] Y. Li, C. Ke, X. Liu, F. Gou, X. Duan, Y. Zhao, Analysis liquid lithium corrosion resistance of Er_2O_3 coating revealed by LIBS technique, Fusion Eng. Des. 136 (2018) 1640–1646, https://doi.org/10.1016/j.fusengdes.2018.07.001.
[22] H. Wu, R. Yi, A. Houben, S. Brezinsek, M. Rasinski, C. Li, G. Sergienko, Y. Liang, T. Dittmar, H. Ding, Study of spectral features and depth distributions of boron layers on tungsten substrates by ps-LIBS in a vacuum environment, Nucl. Mater. Energy 41 (2024) 101812, https://doi.org/10.1016/j.nme.2024.101812.
[23] Z. Hu, X. Bai, H. Wu, R. Hai, F. Ding, M. Imran, C. Li, H. Ding, G.N. Luo, Quantitative analysis of impurities deposited on the Plasma-Facing components of EAST tokamak using a portable LIBS device, Nucl. Mater. Energy 41 (2024) 101785, https://doi.org/10.1016/j.nme.2024.101785.
[24] H.J. van der Meiden, S. Almaviva, J. Butikova, V. Dwivedi, P. Gasior, W. Gromelski, A. Hakola, X. Jiang, I. Jõgi, J. Karhunen, M. Kubkowska, M. Laan, G. Maddaluno, A. Marín-Roldán, P. Paris, K. Piip, M. Pisarčík, G. Sergienko, M. Veis, P. Veis, S. Brezinsek and the EUROfusion WP PFC, Monitoring of tritium and impurities in the first wall of fusion devices using a LIBS based diagnostic, 61 (2021) 125001 (14pp) doi 10.1088/1741-4326/ac31d6.
[25] Dongye Zhao, Ding Wu, Jannis Oelmann, Sebastijan Brezinsek, Qingmei Xiao, Rongxing Yi, Laizhong Cai, Hongbin Ding, Highly depth-resolved characterization of fusion-related tungsten material based on picosecond laser-induced breakdown spectroscopy, J. Anal. At. Spectrom. 35 (12) (2020) 2867–2879, https://doi.org/10.1039/D0JA00340A.
[26] K. Ibano, D. Nishijima, Y. Ueda, R.P. Doerner, LIBS measurement of trace tantalum and rhenium in tungsten for in-situ diagnostic of nuclear transmutation, J. Nucl. Mater. 522 (2019) 324–328, https://doi.org/10.1016/j.jnucmat.2019.05.030.
[27] M.R. Gilbert, J.-C. Sublet, Neutron-induced transmutation effects in W and W-alloys in a fusion environment, Nucl. Fusion 51 (2011) 043005, https://doi.org/10.1088/0029-5515/51/4/043005.
[28] M. Vinić, M. Ivković, Laser ablation initiated fast discharge for spectrochemical applications, Hem. Ind. 68 (3) (2014) 381–388, https://doi.org/10.2298/HEMIND130314065V.
[29] D. Nishijima, Y. Ueda, R.P. Doerner, M.J. Baldwin, K. Ibano, Laser-induced breakdown spectroscopy measurement of a small fraction of rhenium in bulk tungsten, Spectrochim. Acta Part B At. Spectrosc. 141 (2018) 94–98, https://doi.org/10.1016/j.sab.2018.01.013.
[30] J. Liu, D. Wu, X. Hu, S. Liu, H. Wu, R. Hai, C. Li, H. Ding, Study of spectral intensity of the laser ablated tungsten plasma and ablation mass at various laser spot sizes and laser fluence in vacuum environment, Spectrochim. Acta Part B At. Spectrosc. 199 (2023) 106569, https://doi.org/10.1016/j.sab.2022.106569.
[31] M. Ivkovic, J. Savovic, B.D. Stankov, M. Kuzmanovic, I. Traparic, LIBS depth-profile analysis of W/Cu functionally graded material, Spectrochim. Acta Part B At. Spectrosc. 213 (2024) 106874, https://doi.org/10.1016/j.sab.2024.106874.
[32] N. Konjević, M. Ivković, N. Sakan, Hydrogen balmer lines for low electron number density plasma diagnostics, Spectrochim. Acta Part B At. Spectrosc. 76 (2012) 16–26, https://doi.org/10.1016/j.sab.2012.06.026.
[33] D.E. Kelleher, Stark broadening of visible neutral helium lines in a plasma, J. Quant. Spectrosc. Radiat. Transf. 25 (1981) 191–220.
[34] A. Czernichowski, J. Chapelle, Use of the 447 nm He I line to determine electron concentrations, J. Quant. Spectrosc. Radiat. Transf. 33 (1985) 427–436.

scientific reports

Check for updates

OPEN

Hydrogen isotopes retention studies using laser and microwave induced plasma coupling

N. Vujadinovic[1], I. Traparic[1], B. D. Stankov[1], D. Rankovic[2,3], M. Kuzmanovic[2] & M. Ivkovic[1]✉

The detection of deuterium and tritium retention in fusion devices via optical emission spectroscopy (OES) faces significant challenges due to experimental limitations, particularly in resolving hydrogen isotope Balmer alpha lines (H_α, D_α, and T_α). In this study, we propose and evaluate the coupling of laser ablation and laser-induced desorption with microwave-induced plasma (MIP) as an approach to resolve this problem. This approach effectively meets the resolution requirements for Balmer alpha lines, overcoming limitations of standard laser-induced breakdown spectroscopy (LIBS) setups. Optimization of Nd:YAG laser ablation was performed using pure copper and tungsten targets, while desorption, including femtosecond (fs) laser-induced desorption, was studied on graphite powder mixed with heavy water and water. The results demonstrate a significant improvement in spectral resolution and analytical performances, highlighting the potential of this technique for tritium retention studies in plasma-facing components.

Keywords Hydrogen isotopes retention, Laser ablation, Laser induced desorption, Microwave induced plasma, Plasma-facing components, LIBS

Diagnostics of the fusion plasma reactors are critical for ensuring their safe and proper stable operation. Among these diagnostics, the hydrogen isotope retention, particularly tritium, in plasma facing components (PFC) are probably the most important ones[1]. Techniques such as ion beam analysis (IBA) and thermal desorption spectroscopy studies (TDS) are highly reliable and commonly used PFC diagnostics methods[2–5]. However, these methods are constrained to laboratory settings and require complex equipment. Consequently, sections of the PFC or test targets positioned on various places within the vacuum vessel must be demounted from the reactor wall[6] to be analyzed.

To enable in-situ analysis of PFC, laser induced breakdown spectroscopy (LIBS) is used as an effective solution to overcome limitations of traditional methods. LIBS is a minimally invasive, non-contact technique suitable for multi-element analysis, including depth profiling, without requiring sample preparation. The technique is adaptable for vacuum or low-pressure gas environments and has been applied across diverse fields, such as nitrogen detection in soil[7], explosives detection[8], olive oil classification[9], cadmium detection in drinking water[10], and even the identification of malaria biomarkers[11], bacteria[12] or SARS[13]. LIBS is also commonly used for analyzing metal purity, alloys, jewelry[14], archaeological and other samples. Reviews[15–18] and recent studies[19–21] provide comprehensive insights into the advancements of LIBS for fusion applications, particularly its potential for in-situ diagnostics.

The most important application of LIBS for plasma fusion reactor wall diagnostics is the study of hydrogen isotope retention, which relies on measurement of their Balmer alpha spectral lines. A significant challenge in this application is resolving the closely spaced lines caused by the small isotope shift. Even high-resolution spectrometers struggle to resolve these lines, due to significant Stark broadening under standard LIBS plasma conditions[22]. Partial resolving of a hydrogen and deuterium Balmer alpha lines (with isotope shift of 0.18 nm) has been achieved in studies using double-pulsed LIBS, where line fitting with a Voigt function was employed[17,23,24]. More recently, approaches based on femtosecond (fs) laser ablation[25] and fs LIBS[26] have been applied to hydrogen isotope retention diagnostics, demonstrating further advancements in this field[27–32].

The use of the TEA CO_2 lasers or Nd:YAG in He[33–35] or filament fs laser LIBS[27,30] demonstrates the possibility of LIBS to resolve H_α and D_α lines. However, resolving T_α lines presents a greater challenge due to the stricter requirements for low electron density[22]. In this study, we propose overcoming these challenges by coupling laser and microwave-induced plasma (MIP) to achieve the necessary plasma conditions. Two sample introduction

[1]Institute of Physics, University of Belgrade, 11080 Belgrade, Serbia. [2]Faculty of Physical Chemistry, University of Belgrade, 11158 Belgrade, Serbia. [3]Present address: Vinca Institute of Nuclear Science, University of Belgrade, 11000 Belgrade, Serbia. ✉email: ivke@ipb.ac.rs

methods are employed: laser ablation using an Nd:YAG laser and fs laser-induced desorption, both integrated with microwave-induced low-pressure plasma.

Experiment

Microwave induced plasma is the primary method used in this research for excitation and resolution of hydrogen isotope lines. The combination of MIP and laser induced plasma was used earlier for the enhancement of the LIBS[36,37], where the addition of microwaves increased electron density, temperature, and plasma duration and dimensions. However, this enhancement also increased Stark broadening, making the method unsuitable for tritium retention studies. In contrast, MIP source operating at atmospheric pressure has plasma parameters[38,39] suitable for resolving D_α and T_α spectral lines, as analyzed in[22]. At low gas pressures, MIP achieves even smaller electron densities[40], minimizing Stark and Van der Waals broadening, making them negligible in comparison with other broadening mechanisms (Doppler and instrumental). For this study, a Beenakker resonator cavity with an 8 mm diameter and 14 cm long capillary tube was used, with an optical window and evacuation port mounted at the end. MIP was generated using an AHF Analysen Technik GMW 24–301 DR 2.45 GHz microwave generator with a maximum power of 100 W. A double gauge gas regulator and needle valve regulated gas flow withing the tube. Gas pressure was measured with a manometer, and a mechanical vacuum pump was used for evacuation and maintaining stable argon gas flow.

The first method used for sample introduction was laser ablation, a widely used technique in analytical spectroscopy for introducing samples into excitation sources such as inductively coupled plasma (ICP), MIP, LIBS or mass spectrometry[41–43]. For this purpose, we used a laboratory made laser ablation cell, see Fig. 1. This cell was constructed as an elongation of the capillary tube thus enabling the most efficient transport of the ablated material into the MIP. The target was placed in a custom built holder with vacuum feedthrough, allowing rotation to expose fresh target surface area to the laser beam. Ablation was performed using Quantel 450 Nd:YAG (1064 nm, 6 ns pulse duration, 10 Hz maximum repetition rate, 450 mJ maximum energy). Laser beam was focused with a f= 12.5 cm lens through the window and onto the target. Special cell design enables irradiation of the target at approximately 45 degrees. Small variation of incident angle enables irradiation at a variable distance from the center of the target. That way, laser induced plasma radiation, which always propagates normal to the target surface, does not reach detection system and enables recording of the radiation coming from the MIP only.

The emitted light from the MIP was collected through an optical window at the end of the capillary using a collimator (COLL) and guided via fiber optic cable (OF) either to medium resolution spectrometer Andor Shamrock 303i (with grating 1200 g/mm) or high-resolution spectrometer SOL instruments MS7504i spectrometer (with grating 1800 g/mm). The Andor spectrometer was equipped with Andor iStar DH720 - 18 F-63 ICCD camera (256 × 1024 pixels, 26 μm pixel size), while SOL instruments spectrometer was equipped with Andor iStar DH734 - 18 F- 63 ICCD camera (1024 × 1024 pixels, 13 μm pixel size), that were used as detectors. Delay and gating of cameras were controlled with external digital delay generator (DDG, Stanford Research SRS 535), which was triggered with the signal for opening of a Nd:YAG laser Q switch. It should be noted that the

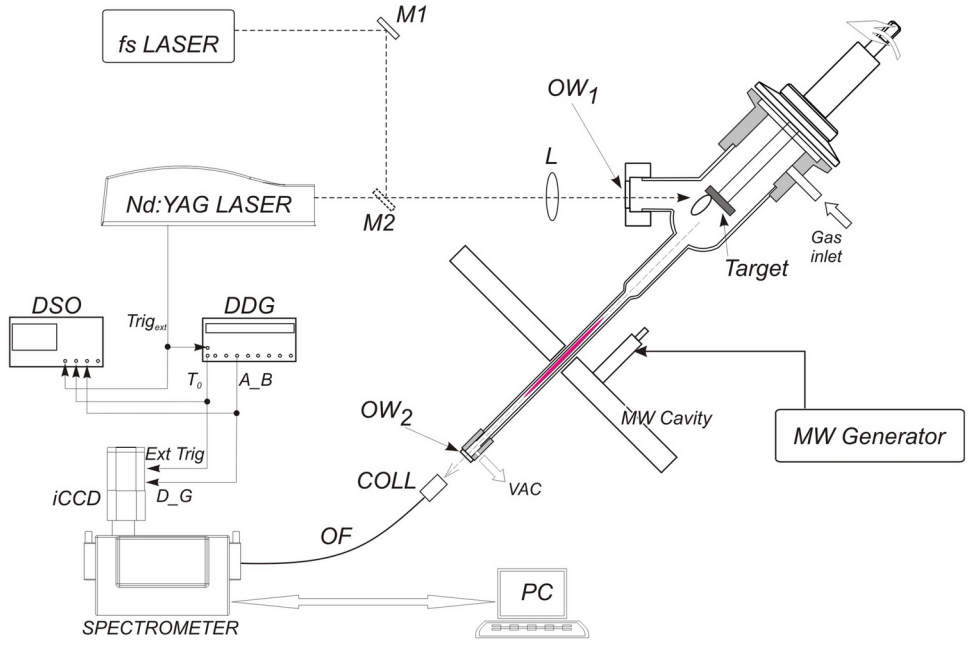

Fig. 1. Experimental setup for laser ablation (using Nd:YAG) and laser induced desorption (using fs Yb:YAG laser) as methods for sample introduction in microwave induced plasma (MIP). DSO—digital storage oscilloscope, DDG—digital delay generator, COLL—collimator of the emitted radiation into the fiber, OF—optical fiber, M—folding mirrors, VAC—vacuuming port, L—focusing lens, OW—optical windows.

separation of the optical emission signals created by LIBS and by MIP can also be achieved by changing the delay and gate time of the camera exposure.

The Nd:YAG laser, commonly used for plasma creation, is known to ablate a thick layer of material, making it unsuitable for analyzing thin films or surface-bound elements. For detecting hydrogen isotopes within thin surface layers, laser-induced desorption (LID)[44–46], often paired with quadrupole mass spectrometry (LID-QMS)[47], is a more suitable approach. To test the feasibility of using MIP as an alternative to the more complex QMS, a femtosecond Yb:YAG laser (Solar FX200, 1030 nm, 150 fs pulse duration, 105 nJ peak energy, 71 MHz repetition rate, 7 W average power) was employed for laser-induced desorption of hydrogen isotopes. In this setup, the detection system was triggered by the camera's internal trigger with a variable exposure time. While this study utilized the femtosecond laser, laser-induced desorption can also be achieved with other lasers capable of heating the target without causing significant ablation.

The selected targets for these studies included a copper target for the experiment optimization in terms of gas pressure, delay time, microwave power and laser energy. A tungsten target was then introduced to verify the optimized conditions for resolving Balmer alpha spectral lines. Finally, a pill composed of graphite powder mixed with water and heavy water (D_2O), was prepared using a hydraulic press, as previously described in[22]. This pill was tested for both laser-induced desorption and vacuum-induced desorption.

Results

In the investigation of MIP for hydrogen isotope detection, the initial task involved optimizing the transport and excitation of sample components. Due to the challenges associated with tritium's radioactivity, most previous research has focused on deuterated samples as a safer alternative. In this study, tungsten (W) samples containing incorporated deuterium were analyzed using laser ablation as the method for introducing samples into the MIP.

Laser ablation

The investigation of Nd:YAG laser ablation as a method for introducing tungsten samples with incorporated deuterium into the MIP proved nearly impossible with our experimental setup. This was due to several factors: The high reflectivity of the polished samples, the shallow retention of the deuterium and high laser ablation rate. As a result, the application of MIP for hydrogen isotopes detection using laser ablation was limited to optimizing parameters for resolving hydrogen isotope Balmer alpha lines. According to[22], D_α and T_α spectral lines can be resolved only if full width at half maximum (FWHM) of lines is less than 0.056 or even 0.027 nm, depending on their intensity ratio (1:1 or 1:10, respectively). Furthermore, FWHMs of the neighbor spectral lines must also be smaller than the wavelength separation between them and hydrogen isotope lines.

To obtain the best resolving results, using laser ablation, the signal to noise ratio (i.e., line intensities) has to be maximized by optimizing several experimental parameters, while keeping FWHM as minimal as possible. For MIP operation, microwave power and gas pressure are the most important parameters. The line intensities increase with microwave power, but the reflected power also increases. If the reflected power exceeds 15 W, there is a risk of damaging the microwave generator or overheating the discharge tube. Optimal gas pressure, which corresponds to the flow rate, must also be determined, as it dictates the time the sample remains within the MIP resonator cavity for excitation.

Additionally, the dependence of spectral line intensities on laser energy was analyzed, as laser energy influences the ablation process, specifically the ablated mass and particle dimensions. Although higher energy increases the ablated mass, it is important to assess whether larger particle dimensions might affect MIP performance by altering microwave coupling to the plasma or causing particle deposition on the tube walls.

Optimization of gas pressure

The optimal gas pressure range for stable MIP operation was determined by analyzing the maximal intensity of the Ar I line at 516.22 nm ($3s^23p^5(^2P^0{}_3/_2)4p \rightarrow 3s^23p^5(^2P^0{}_3/_2)6d$), as shown in Fig. 2a. The Ar I line was used to establish the optimal gas pressure range since its intensity is independent of the camera recording delay. In contrast, the intensities of the target lines, such as Cu I, depend on the gas flow rate, which determines when the ablated material reaches the plasma.

From Fig. 2b, the optimal gas pressure range for stable MIP operation was between 15 and 20 mbar.

The optimal gas pressure can be determined using the most intense spectral line, the Cu I line at 521.82 nm ($3d^{10}4p \rightarrow 3d^{10}4d$). Since this line is susceptible to self-absorption, its optical thickness was evaluated. The Cu I lines at 515.32 nm (λ_1) and 521.82 nm (λ_2) belong to the same multiplet (transition $3d^{10}4p \rightarrow 3d^{10}4d$) as shown in Fig. 2a. To assess self-absorption of the 521.82 nm line, the intensity ratio $R = I_{\lambda 1}/I_{\lambda 2}$ was compared at various pressures to the theoretical value of $R = 0.53$ (Table 1)[48]. Results indicated no significant self-absorption for all pressures except at 10 mbar, where the lines exhibited low intensity.

Since the Cu I line has a significantly higher intensity at 20 mbar, see Fig. 2b, this line was used in optimization of several experimental parameters in all further investigations.

Optimization of material transport to the MIP

Gas pressure and flow regulate the duration for which the ablated material remains in the discharge, thereby influencing the recording parameters (delay and gate times). The delay corresponds to the time required for the material to travel from the target to the resonator cavity, while the gate time determines the duration the material spends in the discharge zone. An analysis of the optimal delay time is presented in Fig. 3. It should be noted that for this and all further analyses the gate was fixed to 10 ms.

Based on Fig. 3 it was concluded that the delay time should be 20 ms and that the 10 ms gate time is appropriate. During these measurements, microwave power was set to 75 W and laser energy was 250 mJ. The final spectrum was the accumulated spectrum of 20 laser shots.

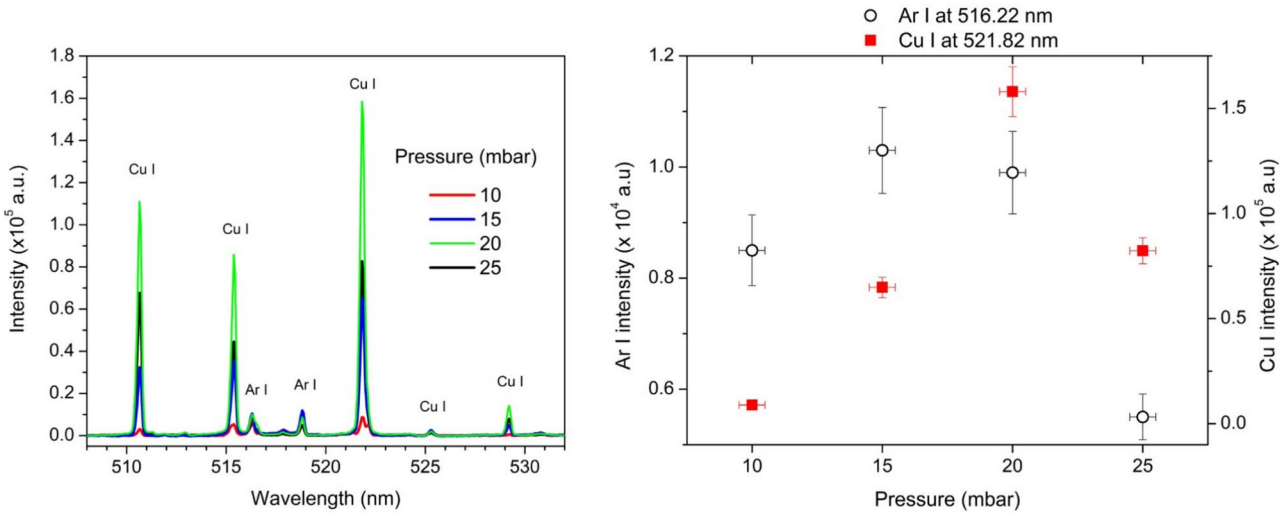

Fig. 2. (**a**) MIP spectra of a laser-ablated Cu target in Ar at various pressures. Experimental parameters: MIP power: 75 W, delay: 8 ms, gate: 10 ms, number of accumulations: 20. (**b**) Selected Ar and Cu line intensities as a function of pressure.

Pressure (mbar)	$R = I_{\lambda 1}/I_{\lambda 2}$ (exp.)
10	0.66
15	0.54
20	0.53
25	0.54

Table 1. Experimental ratios of the intensities of Cu I spectral lines at various pressures.

Optimization of ablated material quantity

The amount of ablated material is directly influenced by the laser energy used. To optimize this parameter, the laser energy was adjusted by varying the delay between the triggering of the flash lamps and the opening of the laser Q switch (FLQS). Three energy values were tested: 130, 250 and 430 mJ. The resulting graph is shown in Fig. 4.

With the increase of the laser energy, the intensity of the Cu I line also increases. This is primarily due to the ablation rate, as when the energy of the laser is higher, the ablation rate is also higher, and more material is entering the discharge region. Here, the energy of 250 mJ was chosen, as for the higher energy, the mass of the incoming material was too large, which caused the MIP discharge to shut down.

Selection of microwave generator power

Dependence of the line intensity on the microwave power supplied to the cavity (for optimal pressure, delay, gate and laser energy) was analyzed. Here, four powers were considered (50, 60, 75 and 90 W). Besides supplied power, the reflected power was also measured. The obtained dependance on the supplied power is shown in Fig. 5.

The results indicate that increasing the supplied power leads to a corresponding increase in line intensity. However, the reflected power also rises with higher input power. In Fig. 5, a dashed vertical line marks the input power at which the reflected power reaches 15 W. Since exceeding this threshold could overheat the source, it is not advisable to operate beyond this limit. Consequently, 75 W was selected as the optimal power setting to ensure safe and reliable generator operation.

Spectral resolution requirements for hydrogen isotopes retention studies

After optimizing experimental parameters for laser ablation and MIP operation the potential of this setup for hydrogen isotopes retention studies was analyzed. For such analysis, the FWHM of Balmer alpha lines should be less than 0.027 nm if one wants to detect small amounts of tritium in the first wall of future fusion reactors. The first step in this direction was to assess the instrument broadening on the spectral lines' widths. Given the negligible Stark broadening at low MIP gas pressures ($Ne \sim 10^{12}$ cm^{-3}), and the electron temperature between 2000 and 3000 K, we can safely assume that the major influence in the line broadening comes from the Doppler and instrument broadening. To determine the instrumental FWHM of device, the recorded Cu I line at 521.82 nm from Fig. 2 was fitted with a Gaussian function. The resulting FWHM was 0.27 nm, which greatly exceeds the goal of having lines as narrow as 0.027 nm. This result is reasonable, considering that medium resolution

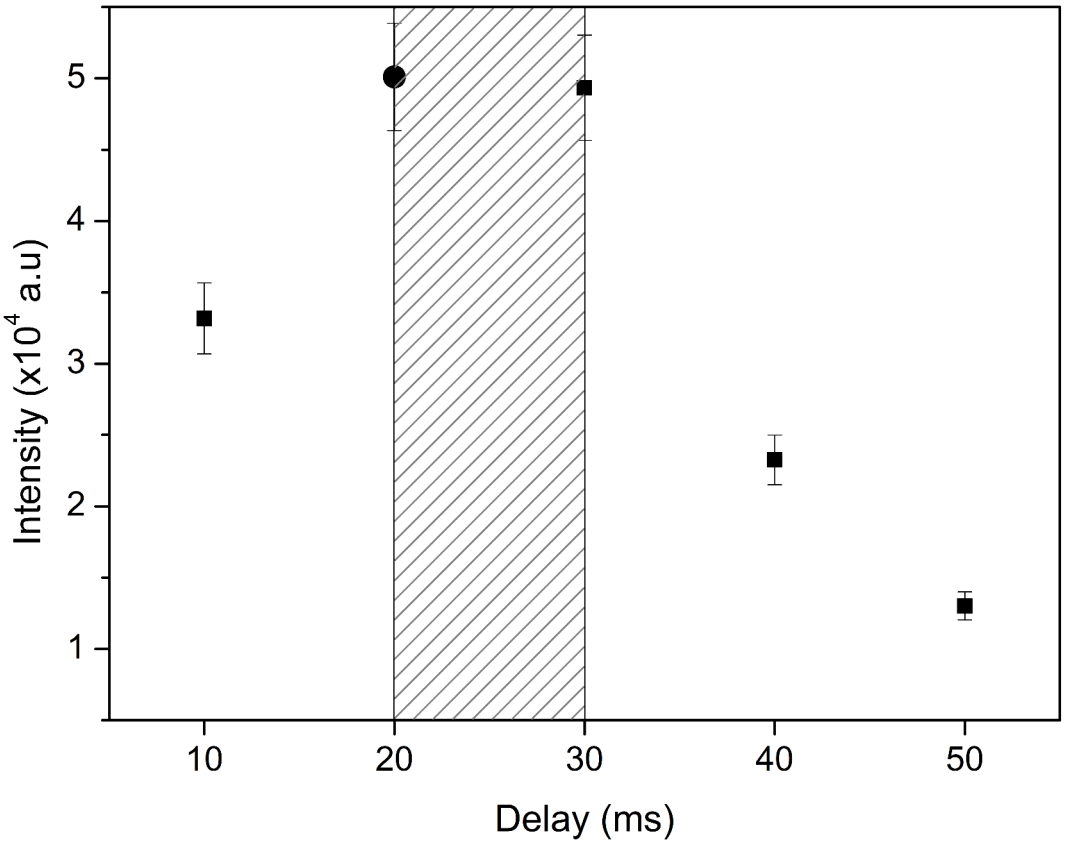

Fig. 3. Optimization of the delay time between the laser pulse and camera triggering by maximizing intensity of the 521.82 nm Cu I line. Shaded area represents the gate time.

Shamrock 303 imaging spectrograph with the entrance slit width of 50 µm equipped with Andor iStar DH720 ICCD camera was used for these measurements.

To reduce the instrumental broadening of the lines, the high resolution MS7504i spectrometer with the entrance slit width of 30 µm equipped with Andor iStar DH734 - 18 F- 63 ICCD camera was used for recording spectral lines of tungsten. As part of the optimization of the optical system (selection of the spectrometer and slit width), W target was used to verify whether the W line FWHM is less than 0.04 nm, which corresponds to the wavelength separation between hydrogen Balmer alpha line at 656.28 nm and W I line at 656.32 nm.

Gaussian fitting of the W I lines (Fig. 6) showed the FWHM of 0.024 nm at 429.46 nm and 0.025 nm at 430.21 nm, meeting the required resolution. This demonstrates that the setup is capable of enabling precise determination of the H_α line intensity.

Desorption as a method for sample introduction in MIP

To obtain the H_α and D_α FWHM values and to test whether resolving the D_α and T_α lines is possible in this configuration, and for previously determined optimal experimental parameters of 20 ms delay and 10 ms gate time, 75 W MIP input power and a 30 µm entrance slit width of the high resolution spectrometer, a mixture of graphite powder, heavy water and water, pressed into a pill, was used as the target. In section"Desorption due to vacuuming", the results of the MIP spectrum for desorption induced by the vacuuming alone are presented, while in section"Laser induced desorption", the results of desorption induced by fs laser heating in combination with the vacuum pump are presented.

Desorption due to vacuuming

Due to the composition of the target pill, water and heavy water were not fully bonded to the graphite, resulting in their evaporation from the target during vacuum pump outgassing. The corresponding MIP spectra with deuterium and hydrogen Balmer alpha lines is shown in Fig. 7. As can be seen, the lines are narrow and fully resolved.

Laser induced desorption

As a final step, we examined whether a 1030 nm fs laser with very low energy (100 nJ) could induce desorption of hydrogen isotopes from the target and introduce them into MIP. Two cycles of heating were performed and recorded. During target heating, an increase in the D_α and H_α line intensities was observed, without a corresponding increase in their FWHMs. MIP spectra, after turning off the laser following the second heating cycle, is shown in Fig. 8. The effect of laser induced desorption is evident: During the cooling of the target, the

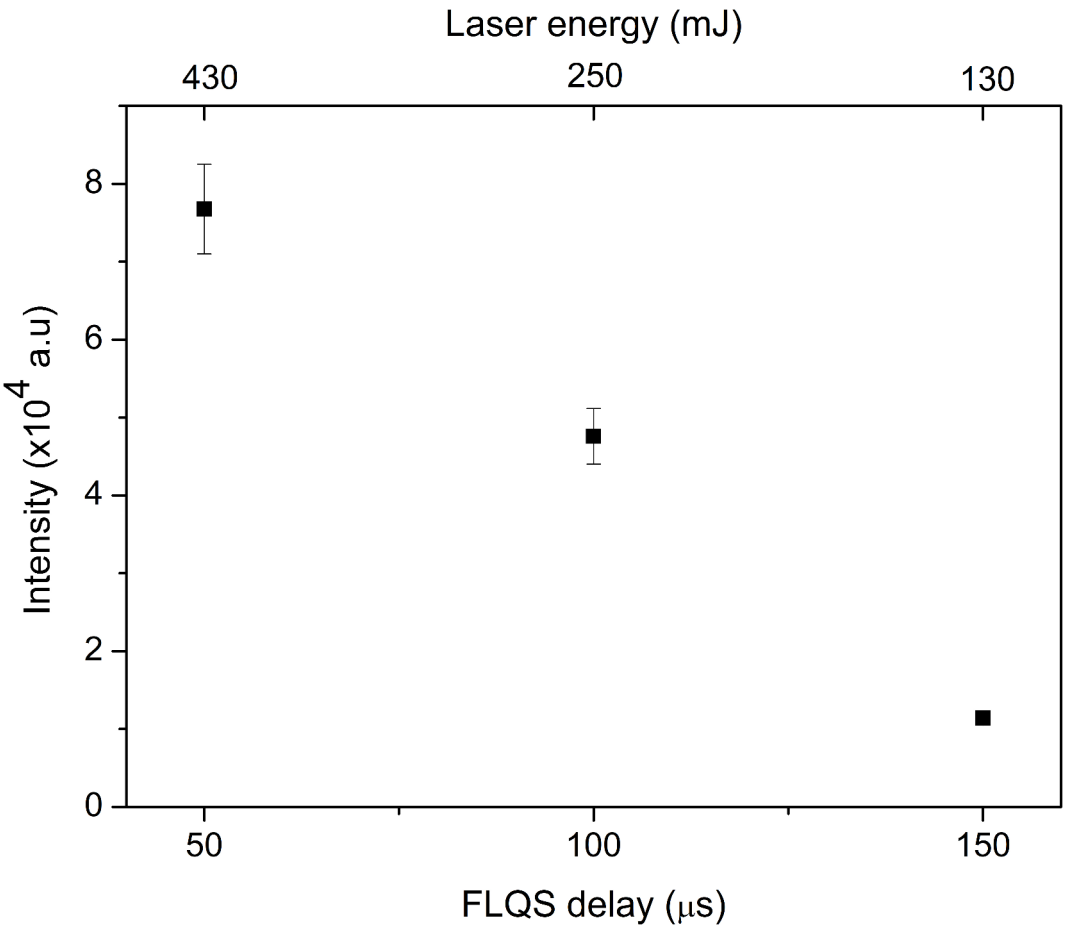

Fig. 4. Dependence of the 521.82 nm Cu I line intensity on the laser energy controlled with FLQS delay, for the optimal pressure, delay and gate time.

line intensities gradually decrease to the levels seen in Fig. 7, where desorption was induced by the vacuum pump alone.

As can be noted from Figs. 7 and 8 (6 min after), the ratio of D_α and H_α peaks remained the same after laser irradiation, but for other measurements that ratio varies. The target was made with equal shares of D_2O (> 99% purity) and H_2O, but there is additional contribution to the H_α peak that comes from the desorption of water vapor from the walls of the discharge tube. The time dependency of the D_α line intensity during both cycles is shown in Fig. 9. The effects of laser heating and laser induced desorption are clear. The intensity increased while the laser was active, peaking at the moments when the laser was turned off. After that, intensity decreased gradually. This confirms that the deuterium comes from laser induced desorption, rather than solely from outgassing due to the vacuum pump. It should be noted that the intensity from the first measurement is higher than it should be, because not enough time has passed for the target to cool from the previous test measurements. The starting value should be close to the one shown in Fig. 7, as that was recorded before the laser heating.

Before proceeding to the estimation of hydrogen isotope line widths, plasma parameters were estimated. The excitation temperature was estimated from the Boltzmann plot of Ar I lines to be 2600 K. Boltzmann plot is given in Fig. 10. Complete data for the lines used to obtain the Boltzmann plot can be found in the Supplementary Table S1.

Given the expected low electron density and negligible Stark broadening for both hydrogen and argon lines, an attempt was made to estimate the upper limit for electron density. The merging of spectral lines of hydrogen is a suitable method for this estimation. If the final detectable spectral line of Balmer series is found, then the use of Inglis – Teller relation[49] can give the upper limit on the electron density. The final observed member of the Balmer series in this study was H-η (9 → 2, 383.5 nm), shown in Fig. 11. Assuming $N_e = N_i$, and that for hydrogen atoms the effective nuclear charge (z) is 1, the upper limit of electron density $Ne \sim 6.3 \cdot 10^{15}$ cm^{-3} was obtained. This value is a huge overestimation, since the upper members of the series couldn't be detected due to the presence of different molecular bands. For precise resolution of superimposed signals, whether due to electric noise or molecular bands, more detailed measurements with even higher spectral resolution would need to be conducted. Regarding Balmer alpha lines, molecular bands close to them have negligible intensities, if they are present at all, and they have no influence on $H_\alpha/D_\alpha/T_\alpha$ intensity ratio.

$$\log(N_e + N_i) = 23.26 - 7.5\log n_{max} + 4.5\log z \quad (1)$$

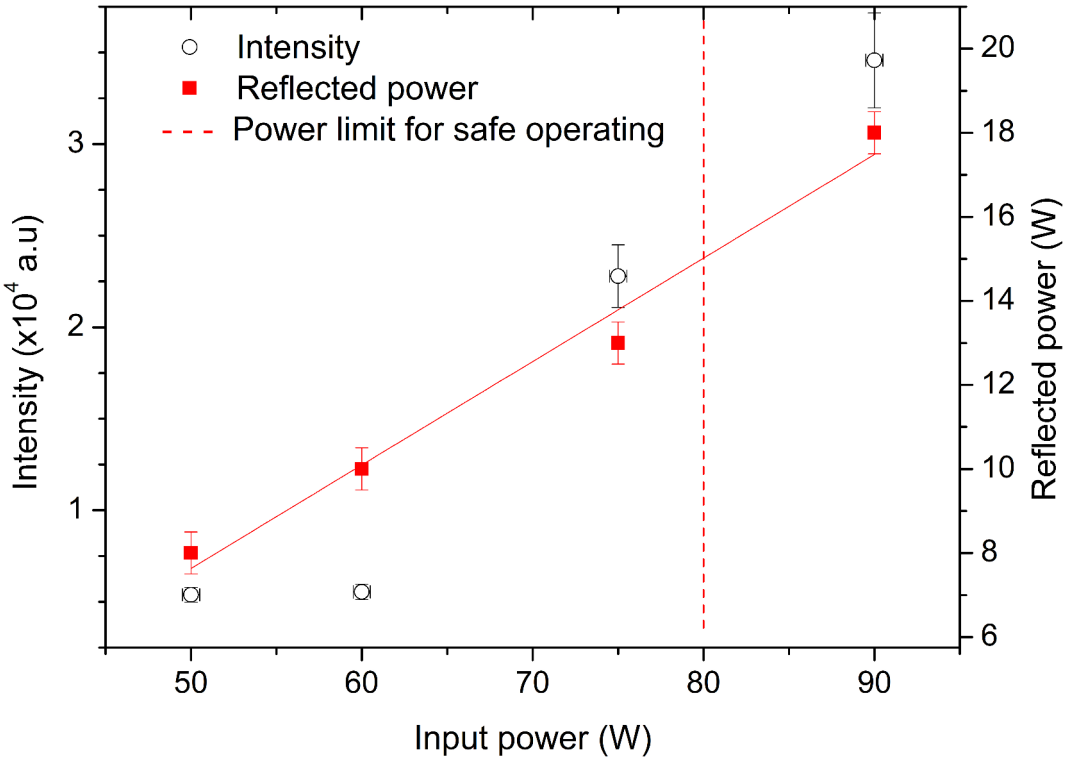

Fig. 5. Intensity of the 521.82 nm Cu I line and microwave generator reflected power as a function of microwave generator input power.

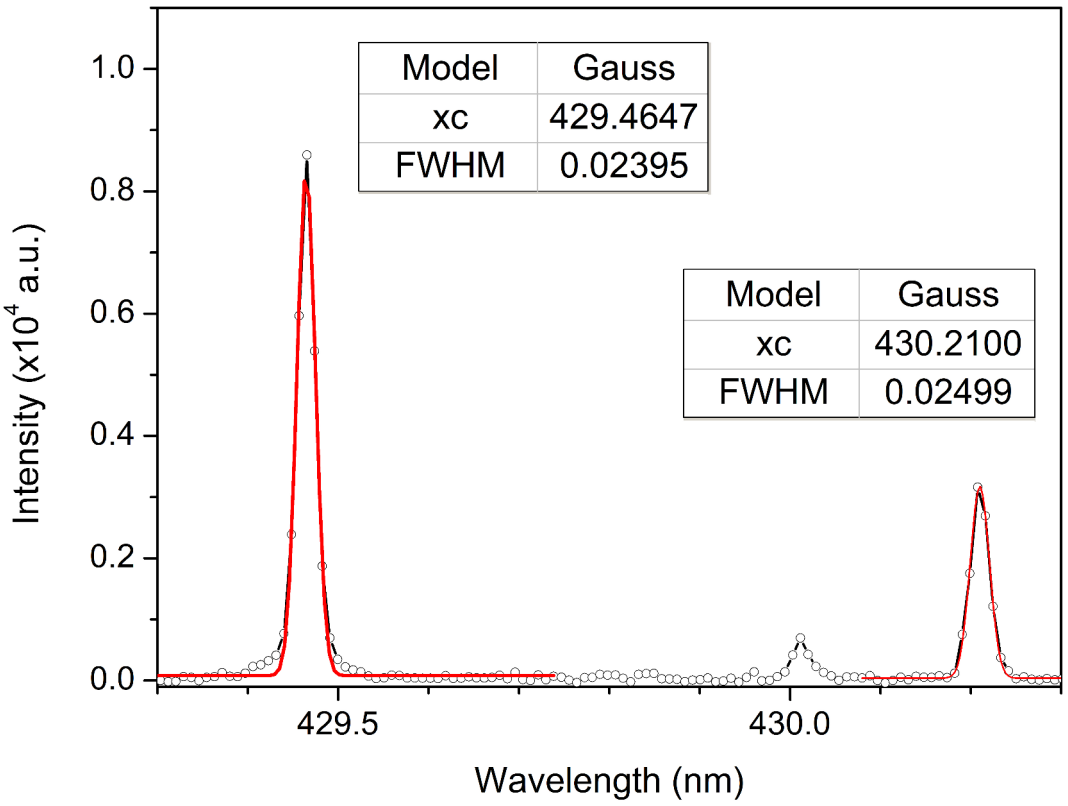

Fig. 6. Gaussian fit of W I lines recorded with high resolution spectrometer with a 30 μm entrance slit width.

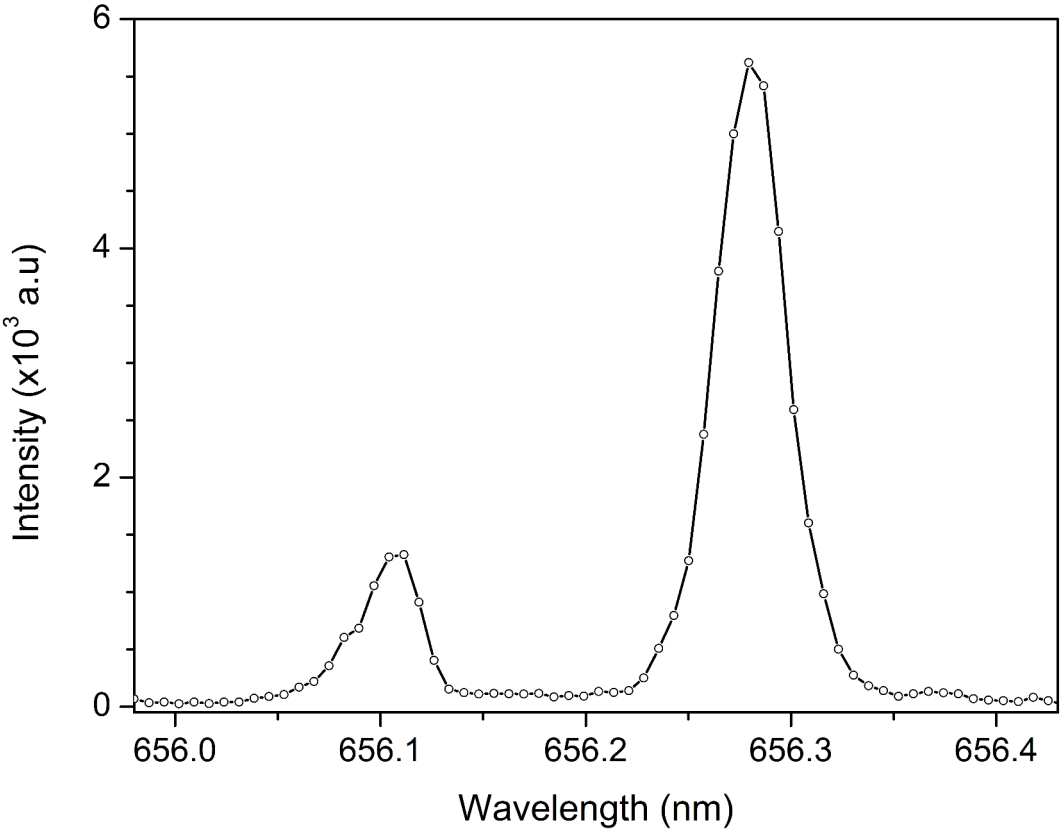

Fig. 7. D_α and H_α lines from MIP when the vacuum pump is the sole contributor to the sample's desorption.

Another approach for determining the electron density is through the Stark broadening of the upper members of the Balmer series. Since the highest detected member of the Balmer series has the width close to the instrumental width, and considering the errors during the fitting procedure, it can be estimated that the Stark width of the Balmer alpha lines doesn't exceed 0.01 nm. If this value is inserted into the formula for the estimation of line widths from the higher members of the Balmer series[50]

$$N_e = 8 \cdot 10^{18} \cdot \left(\frac{w_S\,(nm)}{\alpha^n_{1/2}} \right)^{1.5} \tag{2}$$

the resulting value, with $\alpha^n{}_{1/2} = 0.345$ (for $n = 9$), would be $N_e = 1.25 \cdot 10^{12}$ cm^{-3}, which is a more realistic estimation than the one obtained by the Inglis – Teller equation.

Finally, to confirm the necessary resolution for the hydrogen retention studies, both lines were fitted with a Voigt profile (Fig. 12). Gaussian fitting was also attempted, but Voigt profile showed better performance in terms of wing fitting.

Approximative equation for Voigt profile FWHM[51]

$$W_V \approx 0.5346 W_L + \sqrt{0.2166 W_L^2 + W_G^2} \tag{3}$$

was used with coefficients obtained from Fig. 12. The resulting line widths are 0.033 nm for D_α line and 0.038 nm H_α line. Although Voigt line widths are correct, the Gaussian and Lorentzian parts are off. Gaussian parts can be calculated using the equation

$$W_G = \sqrt{(W_D^2 + W_I^2)}, \tag{4}$$

where W_D represents the Doppler line width and W_I is the instrumental line width. Doppler broadening FWHM can be calculated using the equation

$$W_D = 7.16 * 10^{-7} \lambda \sqrt{\frac{T}{M}}, \tag{5}$$

where M is the mass of the emitter, given in atomic mass units, and T is the temperature estimated using a Boltzmann plot of the Ar I lines (Fig. 10). Since the instrumental FWHM was estimated at 0.024 nm, based on

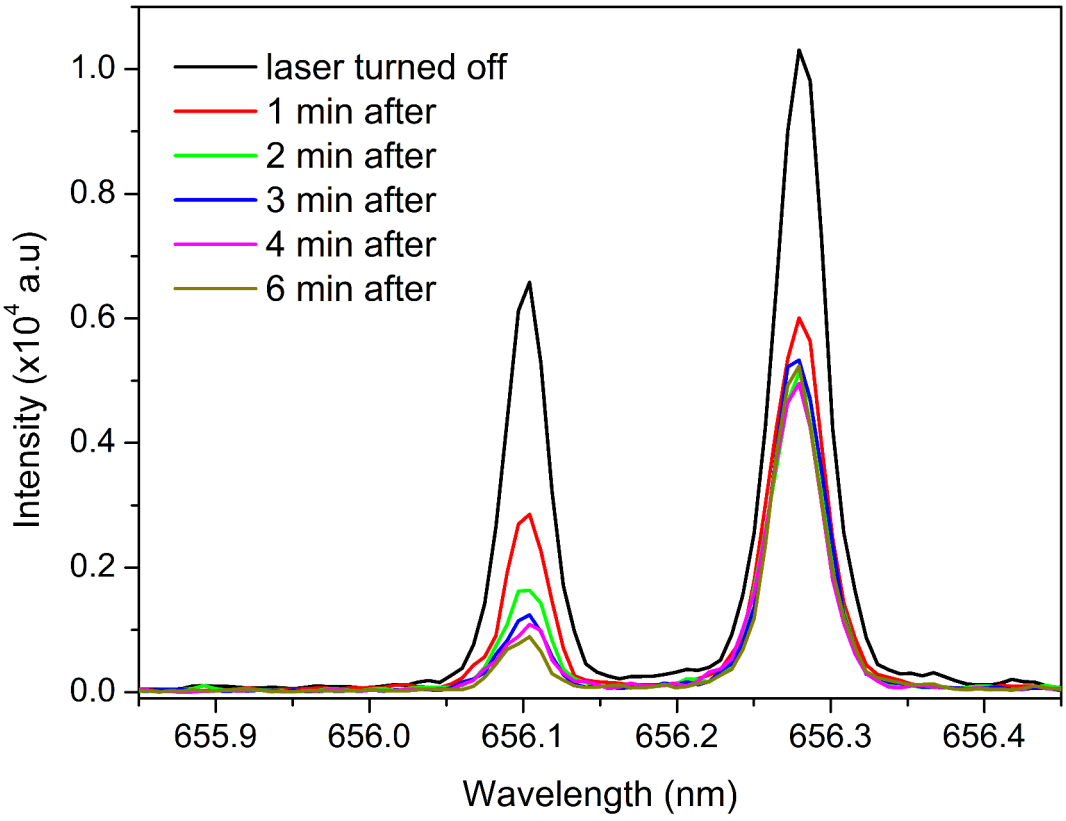

Fig. 8. D_α and H_α line intensities after heating the target with the fs laser in the second cycle.

FWHM of W I 429.46 nm line from Fig. 6, Gaussian parts of the Voigt profiles are 0.029 nm and 0.034 nm for D_α and H_α, respectively. Lorentzian parts are then calculated using the Eq. (3), and they are 0.007 nm for both D_α and H_α.

Finally, using the formula suggested in[22], the intensity ratio of T_α and D_α for which both lines could be resolved was obtained. The critical FWHM at which mentioned lines can be resolved relates to the intensity ratio $R = T_\alpha/D_\alpha$ through the following formula[22]:

$$FWHM_{cr} = 0.0599 - 0.0388 \times e^{-1.765 \times R} \tag{6}$$

Now, for the determined FWHM of D_α 0.033 nm, the theoretical ratio of lines is $R = 0.2$. Therefore, our proposed method could resolve D_α and T_α lines up to the point where D_α is five times more intense than T_α, or vice versa.

Conclusion

In this work, we explored the coupling of laser-induced desorption and laser ablation with microwave-induced plasma as an effective method for studying hydrogen isotope retention in plasma-facing components of fusion devices. The experimental setup was optimized to achieve high spectral resolution, demonstrating great separation of hydrogen and deuterium Balmer alpha lines, which would theoretically enable the separation of deuterium and tritium Balmer alpha lines up to the point where D_α is five times more intense than T_α, or vice versa. The application of femtosecond laser for desorption facilitated sample introduction into the MIP, as evidenced by the clear enhancement of the D_α line. Under low-pressure MIP conditions, line broadening effects were minimized, enabling precise isotopic analysis. It should be stressed that stoichiometry problem[52], i.e., whether the H/D ratio in the plasma corresponds to the H/D ratio in the target is under study.

This study presents a significant advancement in the diagnostics of tritium retention, offering a minimally invasive, high-resolution approach that addresses the limitations of traditional methods such as ion beam analysis and thermal desorption spectroscopy. The findings underscore the potential of this technique for in-situ applications in fusion research, contributing to the development of safer and more efficient plasma diagnostics systems. Future work will focus on scaling this approach for broader fusion reactor applications and extending it to analyze mixed material deposits.

Currently, this approach is suitable for post-mortem analysis (between experimental campaigns). The authors are working on a measuring device that will enable the application of this method for real-time in situ measurements (without demounting the components in tokamak).

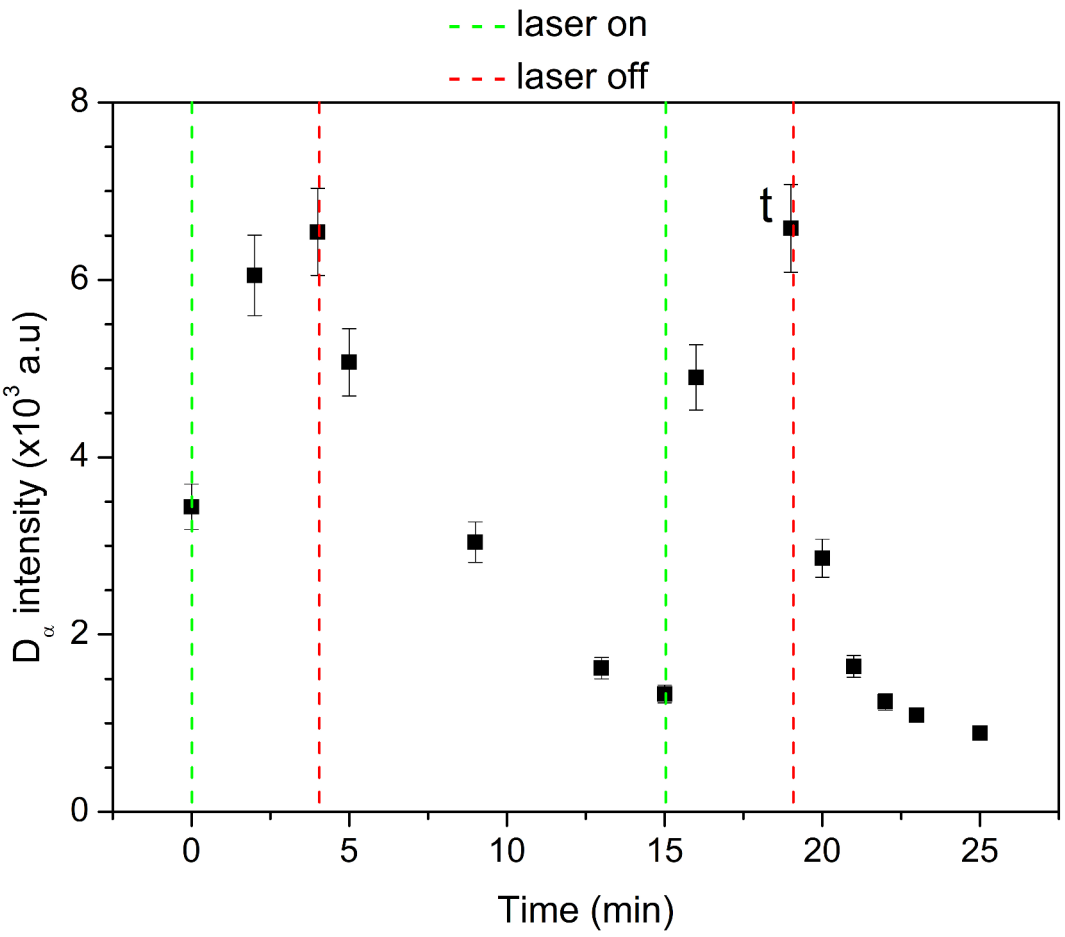

Fig. 9. Time evolution of the D_α line intensity during two cycles of heating and cooling of the target.

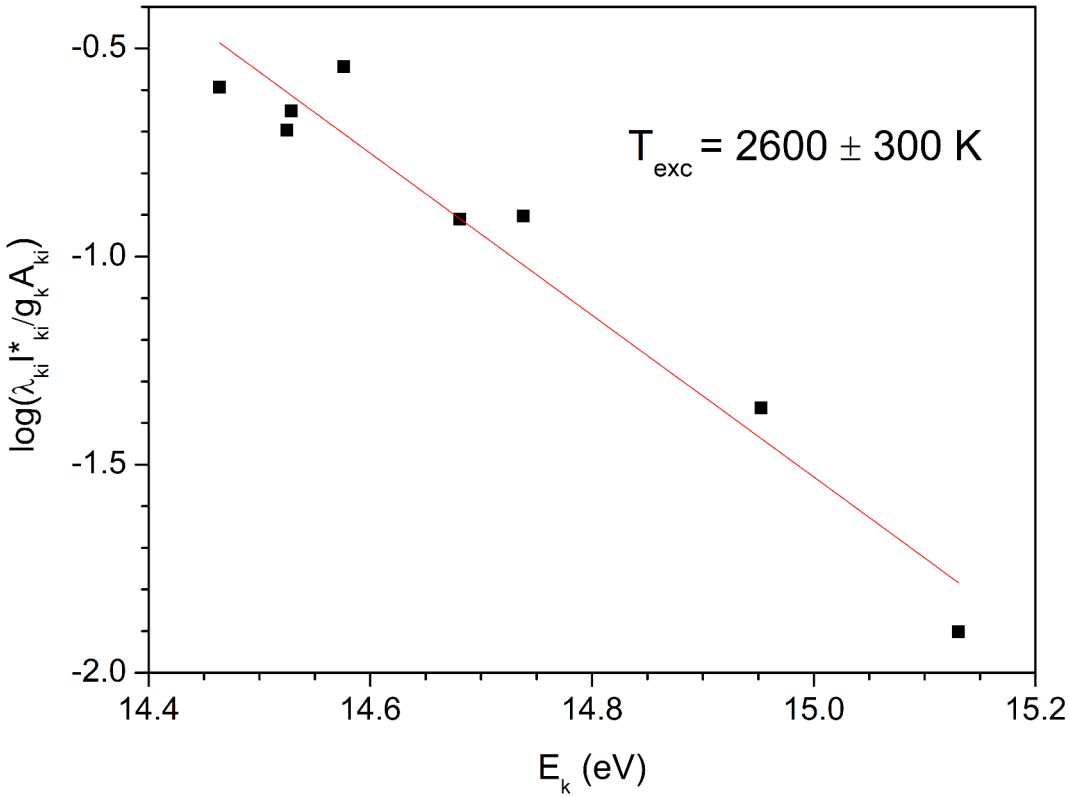

Fig. 10. Boltzmann plot of the Ar I lines for excitation temperature estimation.

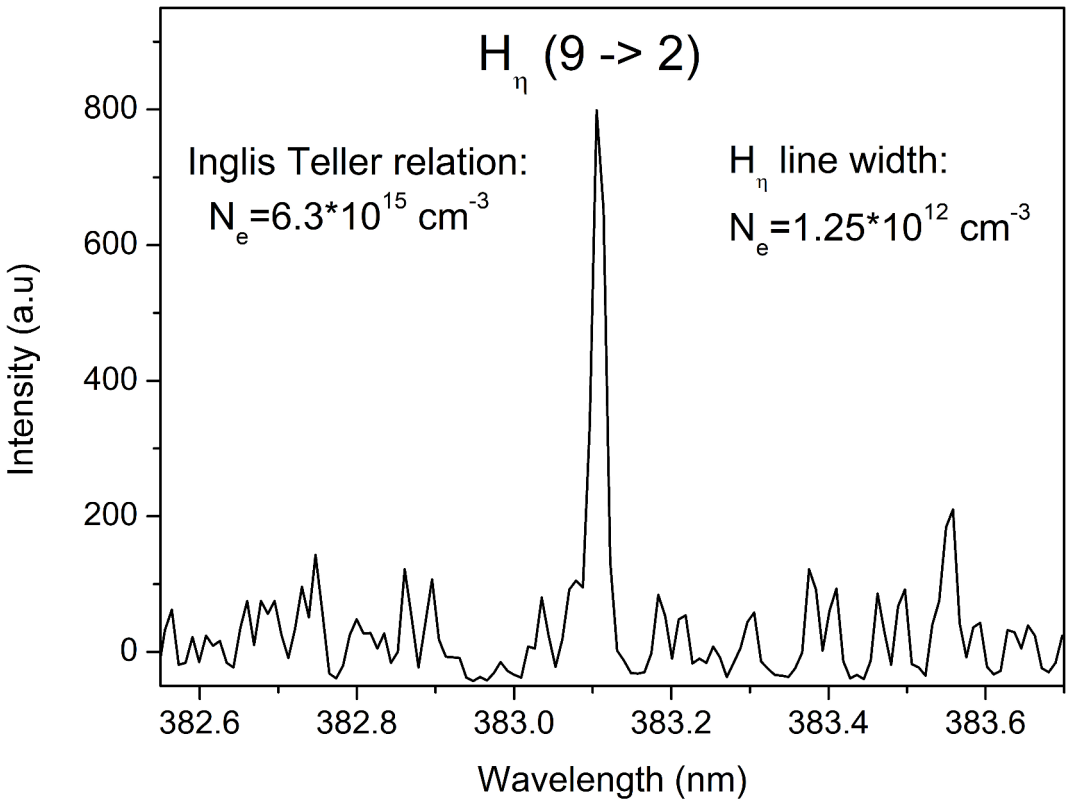

Fig. 11. Balmer Hη line at 383.5 nm recorded for estimation of electron density.

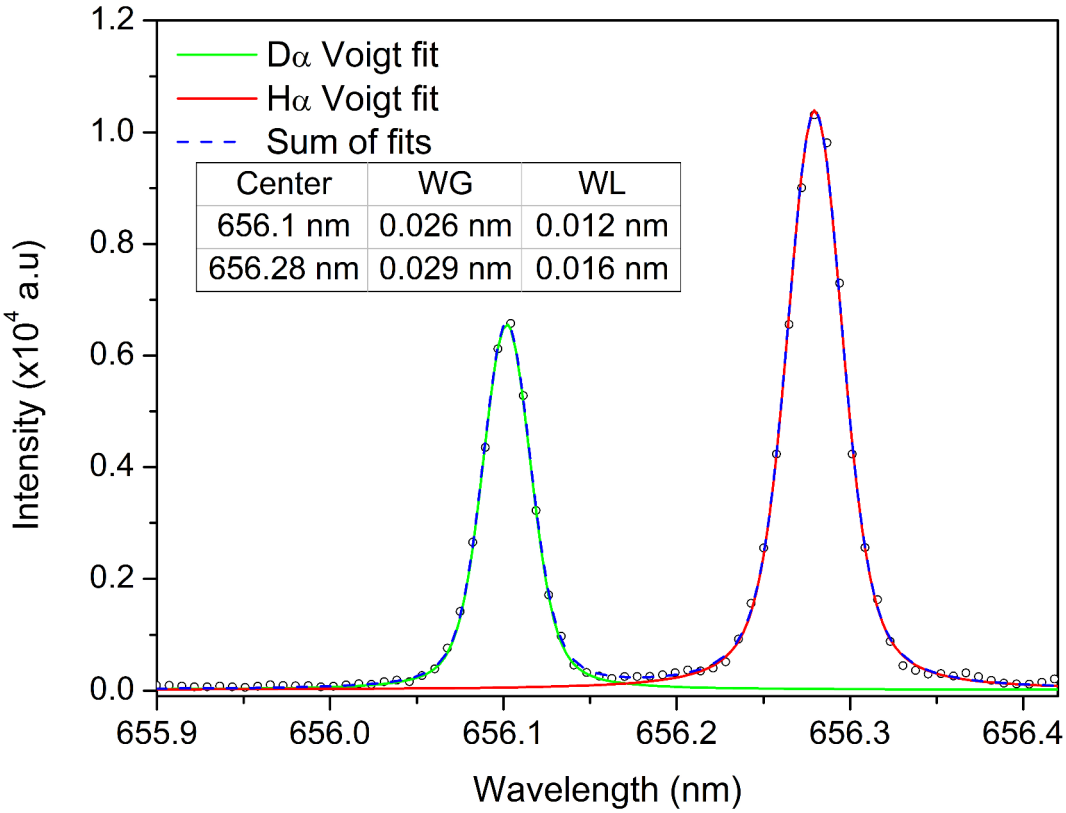

Fig. 12. Voigt profile fitting of the D_α and H_α lines for the measurement at time t, marked in Fig. 9.

Data availability

The data that supports the findings of this study is available from the corresponding author upon reasonable request.

Received: 27 January 2025; Accepted: 28 March 2025
Published online: 12 April 2025

References

1. Brezinsek, S. et al. Fuel Retention Studies with the ITER-like Wall in JET. *Nucl. Fusion* **53**, 083023 (2013).
2. Rubel, M. et al. The role and application of ion beam analysis for studies of plasma-facing components in controlled fusion devices. *Nucl. Instrum. Method. Phys. Res. Sect. B.* **371**(4), 11 (2016).
3. Mayer, M. et al. Ion beam analysis of fusion plasma-facing materials and components: Facilities and research challenges. *Nucl. Fusion* **60**, 025001 (2020).
4. Oya, Y. et al. Development of H, D, T simultaneous TDS measurement system and H, D, T retention behavior for DT Gas exposed tungsten installed in LHD plasma campaign. *Fusion Sci. Technol.* **71**, 351–356 (2017).
5. Oya, Y. et al. Effect of impurity deposition layer formation on D retention in LHD plasma exposed W. *Nucl. Mater. Energy* **9**, 84–88 (2016).
6. Alimov, VKh., Yajima, M., Masuzaki, S., Tokitani, M., LHD Experiment Group. Analysis of mixed-material layers deposited on the toroidal array probes during the FY 2012 LHD plasma campaign. *Fusion Eng. Des.* **147**, 111228 (2019).
7. Hossen, M. A., Diwakar, P. K. & Ragi, S. Total nitrogen estimation in agricultural soils via aerial multispectral imaging and LIBS. *Sci. Rep.* **11**, 12693 (2021).
8. Myakalwar, A. K. et al. Less is more: Avoiding the LIBS dimensionality curse through judicious feature selection for explosive detection. *Sci. Rep.* **5**, 13169 (2015).
9. Gyftokostas, N., Stefas, D., Kokkinos, V., Bouras, C. & Couris, S. Laser-induced breakdown spectroscopy coupled with machine learning as a tool for olive oil authenticity and geographic discrimination. *Sci. Rep.* **11**, 5360 (2021).
10. Tian, H., Jiao, L. & Dong, D. Rapid determination of trace cadmium in drinking water using laser-induced breakdown spectroscopy coupled with chelating resin enrichment. *Sci. Rep.* **9**, 10443 (2019).
11. Musyoka, W. D., Kalambuka, A. H., Alix, D.-M. & Amiga, K. K. Rapid diagnosis of malaria by chemometric peak-free LIBS of trace biometals in blood. *Sci. Rep.* **12**, 20196 (2022).
12. Killiny, N. et al. Laser-induced breakdown spectroscopy (LIBS) as a novel technique for detecting bacterial infection in insects. *Sci. Rep.* **9**, 2449 (2019).
13. Berlo, K. et al. Laser induced breakdown spectroscopy for the rapid detection of SARS-CoV-2 immune response in plasma. *Sci. Rep.* **12**, 1614 (2022).
14. Khalilian, P. et al. Jewelry rock discrimination as interpretable data using laser-induced breakdown spectroscopy and a convolutional LSTM deep learning algorithm. *Sci. Rep.* **14**, 5169 (2024).
15. Li, C., Feng, C.-L., Oderji, H. Y., Luo, G.-N. & Ding, H.-B. Review of LIBS application in nuclear fusion technology. *Front. Phys.* **11**, 114214 (2016).

16. Maurya, G. S., Marín-Roldán, A., Veis, P., Pathak, A. K. & Sen, P. A review of the LIBS analysis for the plasma-facing components diagnostics. *J. Nucl. Mater.* **541**, 152417 (2020).
17. Van der Meiden, H. J. et al. Monitoring of tritium and impurities in the first wall of fusion devices using a LIBS based diagnostic. *Nucl. Fusion.* **61**, 125001 (2021).
18. Harilal, S. S., Brumfield, B. E., LaHaye, N. L., Hartig, K. C. & Phillips, M. C. Optical spectroscopy of laser-produced plasmas for standoff isotopic analysis. *Appl. Phys. Rev.* **5**, 021301 (2018).
19. Cai, L. et al. Development of an in situ diagnostic system for mapping the deposition distribution on PFC of the HL-2M tokamak. *Rev. Sci. Instrum.* **90**, 053503 (2019).
20. Gonzalez, W. et al. Conceptual studies on spectroscopy and radiation diagnostic systems for plasma control on DEMO. *Fusion Eng. Des.* **146**, 2297 (2019).
21. Almaviva, S. et al. LIBS measurements inside the FTU vessel mock-up by using a robotic arm. *Fusion Eng. Des.* **157**, 111685 (2020).
22. Traparic, I. et al. Resolving studies of Balmer alpha lines relevant to the LIBS analysis of hydrogen isotope retention. *Spectrochim. Acta. Part B* **221**, 107050 (2024).
23. Fantoni, R. et al. Hydrogen isotope detection in metal matrix using double-pulse laser-induced breakdown-spectroscopy. *Spectrochim. Acta. Part B* **129**, 8–13 (2017).
24. Burger, M. et al. Isotopic analysis of deuterated water via single- and double-pulse laser-induced breakdown spectroscopy. *Phys. Plasmas.* **25**, 083115 (2018).
25. LaHaye, N. L., Kurian, J., Diwakar, P. K., Alff, L. & Harilal, S. S. Femtosecond laser ablation-based mass spectrometry: An ideal tool for stoichiometric analysis of thin films. *Sci. Rep.* **5**, 13121 (2015).
26. Sheta, S., Hou, Z., Wang, Y. & Wang, Z. Evaluation of femtosecond laser-induced breakdown spectroscopy system as an offline coal analyzer. *Sci. Rep.* **11**, 15968 (2021).
27. Li, G., Hou, H., Ran, P., Zhao, Y. & Zhong, Z. Calibration-free quantitative analysis of D/H isotopes with a fs-laser filament. *J. Anal. At. Spectrom.* **35**, 1320–1329 (2020).
28. Kautz, E. J., Ronnebro, E. C. E., Devaraj, A., Senor, D. J. & Harilal, S. S. Detection of hydrogen isotopes in zircaloy-4 via femtosecond LIBS. *J. Anal. At. Spectrom.* **36**, 1217–1227 (2021).
29. Kautz, E. J., Devaraj, A., Senor, D. J. & Harilal, S. S. Hydrogen isotopic analysis of nuclear reactor materials using ultrafast laser-induced breakdown spectroscopy. *Opt. Expr.* **29**, 4936 (2021).
30. Mittelmann, S. et al. Hydrogen isotope analysis in W-tiles using fs-LIBS. *Sci. Rep.* **13**, 2285 (2023).
31. Harilal, S. S. et al. Detection of tritium using ultrafast laser-induced breakdown spectroscopy. *J. Anal. At. Spectrom.* **39**, 699–703 (2024).
32. Harilal, S.S. & Kautz, E.J. Analysis of hydrogen and lithium isotopes using Laser-Induced Breakdown Spectroscopy. In *Proc. SPIE* 12939, *High-Power Laser Ablation VIII*, 1293908 (2024).
33. Kurniawan, K. H. et al. Quantitative analysis of deuterium using laser-induced plasma at low pressure of helium. *Anal. Chem.* **78**, 5768–5773 (2006).
34. Kurniawan, K. H., Tjia, M. O. & Kagawa, K. Review of laser-induced plasma, its mechanism, and application to quantitative analysis of hydrogen and deuterium. *Appl. Spectrosc. Rev.* **49**, 323–434 (2014).
35. Pardede, M. et al. High sensitivity hydrogen analysis in zircaloy-4 using helium-assisted excitation laser-induced breakdown spectroscopy. *Sci. Rep.* **11**, 21999 (2021).
36. Ikeda, Y., Soriano, J. K., Ohba, H. & Wakaida, I. Laser ablation plasma expansion using microwaves. *Sci. Rep.* **13**, 13901 (2023).
37. Ikeda, Y., Soriano, J. K., Ohba, H. & Wakaida, I. Analysis of gadolinium oxide using microwave-enhanced fiber-coupled micro-laser-induced breakdown spectroscopy. *Sci. Rep.* **13**, 4828 (2023).
38. Jovicevic, S., Ivkovic, M., Pavlovic, Z. & Konjevic, N. Parametric study of an atmospheric pressure microwave-induced plasma of the mini MIP torch – I. Two-dimensional spatially resolved electron-number density measurements. *Spectrochim. Acta. Part. B.* **55**, 1879–1893 (2000).
39. Jovicevic, S., Ivkovic, M. & Konjevic, N. Parametric study of an atmospheric pressure microwave-induced plasma of the mini MIP torch - II Two-dimensional spatially resolved excitation temperature measurements. *Spectrochim. Acta, Part. B.* **56**(2419), 2428 (2001).
40. Jovicevic, S., Ivkovic, M., Konjevic, N., Popovic, S. & Vuskovic, L. Excessive Balmer line broadening in microwave-induced discharges. *J. Appl. Phys.* **95**(24), 29 (2004).
41. Ciocan, A., Uebbing, J. & Niemax, K. Analytical application of the microwave induced plasma used with laser ablation of solid samples. *Spectrochim. Acta.* **47B**, 611–617 (1992).
42. Matusiewicz, H. Design concept and characterization of a laser ablation - inductively coupled plasma/microwave induced plasma optical emission spectrometric system. *Ecol. Chem. and Eng. S* **16**(S1), 9–17 (2009).
43. Brunnbauer, L. et al. Combined LA-ICP-MS/LIBS: powerful analytical tools for the investigation of polymer alteration after treatment under corrosive conditions. *Sci. Rep.* **10**, 12513 (2020).
44. Yehia-Alexe, S.-A. et al. Considerations on hydrogen isotopes release from thin films by laser induced ablation and laser induced desorption techniques. *Spectrochim. Acta. Part B* **208**, 106774 (2023).
45. Zlobinski, M. et al. Laser-induced desorption of co-deposited deuterium in Beryllium layers on Tungsten. *Nucl. Mater. Energy* **19**(503), 509 (2019).
46. Zlobinski, M. et al. Efficiency of laser-induced desorption of D from Be/D layers and surface modifications due to LID. *Phys. Scr.* **2020**, 014075 (2020).
47. Zlobinski, M. et al. First results of laser-induced desorption - quadrupole mass spectrometry (LID-QMS) at JET. *Nucl. Fusion* **64**, 086031 (2024).
48. NIST Atomic Spectra Database: https://www.nist.gov/pml/atomic-spectra-database (last update to data content: November 2024).
49. Inglis, D. & Teller, E. Ionic depression of series limits. *Astrophys. J.* **90**, 439–448 (1939).
50. Jovicevic, S., Ivkovic, M. & Konjevic, N. Review: Low electron density diagnostics: development of optical emission spectroscopic techniques and some applications to microwave induced plasmas. *Spectrochim. Acta, Part B* **59**, 591–605 (2004).
51. Olivero, J. J. & Longbothum, R. L. Empirical fits to the Voigt line width: A brief review. *J. Quant. Spectrosc. Radiat. Transf.* **17**, 233–236 (1977).
52. Mercadier, L., Hermann, J., Grisolia, C. & Semerok, A. Plume segregation observed in hydrogen and deuterium containing plasmas produced by laser ablation of carbon fiber tiles from a fusion reactor. *Spectrochim. Acta, Part B* **65**, 715–720 (2010).

Acknowledgements

This work was supported by the Ministry of Education, Science and Technological Development of the Republic of Serbia (contract numbers: 451 - 03 - 47/2023 - 01/200024 and 451 - 03 - 47/2023 - 01/200146), the Science Fund of the Republic of Serbia through the NOVA2LIBS4fusion project (grant number: 7753287), within the IDEAS call and under the project: NIFS21 KLPF087. We also acknowledge Stanko Milanović, our technical associate, who drew the schematic figure of the experimental setup.

Author contributions

N. V. – Investigation, Formal Analysis, Visualization, Writing—Review & Editing I. T. – Investigation, Formal Analysis, Writing—Review & Editing B. D. S. – Investigation, Formal Analysis, Writing—Review & Editing D. R. – Investigation, Resources M. K. – Writing—Review & Editing M. I. – Conceptualization, Funding Acquisition, Methodology, Supervision, Writing—Original Draft, Project Administration.

Funding

Ministarstvo Prosvete, Nauke i Tehnološkog Razvoja, 451-03-47/2023-01/200024, 451-03-47/2023-01/200146, Science Fund of the Republic of Serbia, 7753287.

Declarations

Competing interests

The authors declare no competing interests.

Additional information

Supplementary Information The online version contains supplementary material available at https://doi.org/10.1038/s41598-025-96546-x.

Correspondence and requests for materials should be addressed to M.I.

Reprints and permissions information is available at www.nature.com/reprints.

Publisher's note Springer Nature remains neutral with regard to jurisdictional claims in published maps and institutional affiliations.

micromachines

IMPACT FACTOR 3.0

Indexed in: PubMed

CITESCORE 6.0

Article

Microstructure Formations Resulting from Nanosecond and Picosecond Laser Irradiation of a Ti-Based Alloy under Controlled Atmospheric Conditions and Optimization of the Irradiation Process

Dubravka Milovanović, Boris Rajčić, Dragan Ranković, Biljana Stankov, Miha Čekada, Jovan Ciganović, Dragica Đurđević-Milošević, Zoran Stević, Miroslav Kuzmanović, Tatjana Šibalija et al.

Special Issue

Research Progress of Ultra-Precision Micro-Nano Machining

Edited by

Dr. Huaizhong Li and Dr. Xiubing Jing

MDPI

https://doi.org/10.3390/mi15010005

micromachines

Article

Microstructure Formations Resulting from Nanosecond and Picosecond Laser Irradiation of a Ti-Based Alloy under Controlled Atmospheric Conditions and Optimization of the Irradiation Process

Dubravka Milovanović [1,*], Boris Rajčić [1], Dragan Ranković [2], Biljana Stankov [3], Miha Čekada [4], Jovan Ciganović [5], Dragica Đurđević-Milošević [1], Zoran Stević [6], Miroslav Kuzmanović [2], Tatjana Šibalija [7] and Sanja Petronić [1]

[1] Institute of General and Physical Chemistry, Studentski Trg 12/V, 11158 Belgrade, Serbia
[2] Faculty of Physical Chemistry, University of Belgrade, Studentski Trg 12-16, 11158 Belgrade, Serbia
[3] Institute of Physics, University of Belgrade, Pregrevica 118, 11080 Belgrade, Serbia
[4] Jožef Stefan Institute, Jamova cesta 39, 1000 Ljubljana, Slovenia
[5] Vinca Institute of Nuclear Sciences-National Institute of the Republic of Serbia, University of Belgrade, Mike Petrovića Alasa 12-14, 11351 Belgrade, Serbia
[6] School of Electrical Engineering, Technical Faculty in Bor, University of Belgrade, 11000 Belgrade, Serbia
[7] Faculty of Information Technology, Belgrade Metropolitan University, 11158 Belgrade, Serbia
* Correspondence: dmilovanovic@iofh.bg.ac.rs

Abstract: This paper presents a study and comparison of surface effects induced by picosecond and nanosecond laser modification of a Ti6Al4V alloy surface under different ambient conditions: air and argon- and nitrogen-rich atmospheres. Detailed surface characterization was performed for all experimental conditions. Damage threshold fluences for picosecond and nanosecond laser irradiation in all three ambient conditions were determined. The observed surface features were a resolidified pool of molten material, craters, hydrodynamic effects and parallel periodic surface structures. Laser-induced periodic surface structures are formed by multi-mode-beam nanosecond laser action and picosecond laser action. Crown-like structures at crater rims are specific features for picosecond Nd:YAG laser action in argon-rich ambient conditions. Elemental analysis of the surfaces indicated nitride compound formation only in the nitrogen-rich ambient conditions. The constituents of the formed plasma were also investigated. Exploring the impact of process control parameters on output responses has been undertaken within the context of laser modification under different environmental conditions. Parametric optimization of the nanosecond laser modification was carried out by implementing an advanced method based on Taguchi's parametric design and multivariate statistical techniques, and optimal settings are proposed for each atmosphere.

Keywords: Ti6Al4V; picosecond laser; nanosecond laser; surface modification; argon-rich atmosphere; nitrogen-rich atmosphere; laser-induced periodic surface structures; laser-induced breakdown spectroscopy; Taguchi's robust parameter design

Citation: Milovanović, D.; Rajčić, B.; Ranković, D.; Stankov, B.; Čekada, M.; Ciganović, J.; Đurđević-Milošević, D.; Stević, Z.; Kuzmanović, M.; Šibalija, T.; et al. Microstructure Formations Resulting from Nanosecond and Picosecond Laser Irradiation of a Ti-Based Alloy under Controlled Atmospheric Conditions and Optimization of the Irradiation Process. *Micromachines* **2024**, *15*, 5. https://doi.org/10.3390/mi15010005

Academic Editors: Huaizhong Li and Xiubing Jing

Received: 16 November 2023
Revised: 7 December 2023
Accepted: 12 December 2023
Published: 19 December 2023

1. Introduction

Tremendous metal and metallic material consumption in contemporary everyday life and various branches of industry has resulted in metals like titanium and copper being considered critical raw materials. Titanium and its alloys are extensively used in aerospace, nuclear, marine and biomedical applications due to their superior physico-chemical properties, such as excellent corrosion resistance and biocompatibility, high specific strength, good ductility, and deformability [1,2]. This is the reason for continuous research interest focused on enabling prolonged usage of Ti-based materials by improving their wear resistance and biocompatibility, e.g., by protecting their surfaces [3].

Various techniques of surface modification for Ti-based alloys for improving their tribological properties, functionality and durability are being continuously investigated. Significant research interest is oriented towards selective surface hardening, spark plasma sintering methods, plasma nitriding and surface coating, as well as laser-based techniques, such as laser shock peening, laser deposition of coatings and thin films, pulsed laser remelting, laser hardening, laser surface texturing and laser patterning [4–12]. One of the challenges is achieving specific and selective modification, and this is the main advantage of laser-based techniques, due to laser beams' high monochromaticity, coherence, directionality and intensity [13]. Using pulsed laser irradiation, from nanosecond to femtosecond pulse durations, enables accurate and effective enhancement of materials' properties and functionality. Despite the complexity of the interaction of laser light with materials' surfaces, this process is established as a highly controllable and precise way of producing surface modifications for various applications. The resulting effects, which vary from periodic surface structures like ripples, columns and craters in the macro-, micro- and nanometer ranges for the improvement of biocompatibility to structural coloration by modifying absorption properties or patterning to obtain antiadhesive surfaces and improve materials' physical properties, such as the microhardness of surfaces predisposed to additional stress, strongly depend on laser irradiation parameters (wavelength, pulse duration, pulse count, energy, frequency, beam mode, etc.) and materials' properties (melting temperature, absorption coefficient, surface roughness, etc.) [12,14–17].

Besides the properties of the sample material and the laser irradiation properties, the resulting effects also depend on the environmental conditions. In recent years, materials' modification with various assisted gases in controlled environments is gaining significant research attention [15,18–21] due to the possibility of protective-coating synthesis and/or suppressing the hydrodynamic effects that can affect modification precision. The environmental conditions in which the laser–material interaction takes place play an important role because many metallic alloys are prone to the formation of oxide layers on their surfaces that can affect their optical properties as well as increase the absorption of laser irradiation, but which can also lead to the formation of favorable compounds, such as nitrides, on the alloy surface, which can lead to improved chemical and mechanical properties in the material [15,18–22]. Specific qualities of laser irradiation have enabled its use as a rapid analytical tool for complex materials in the laser-induced breakdown spectroscopy (LIBS) technique [23]. Since a sample is ablated during LIBS, forming a plasma, it is significant to investigate the influence of the environmental conditions on LIBS qualitative analysis of Ti6Al4V [24].

Over the past few decades, extensive research efforts have been dedicated to studying the interaction between lasers and various materials across diverse optimization operations. The aim of optimizing irradiation conditions is to ensure the fulfilment of the desired, i.e., set, quality characteristics (i.e., process reactions). Various approaches have been implemented for laser material processing, including soft computing approaches [25–27] and statistical approaches [28,29]. The first approaches are based on neural models [27,30] that require a large amount of data that is not always possible to obtain experimentally. Another issue concerns the implementation of metaheuristic algorithms, such as particle swarm optimization (PSO) [25–27]. If the parameters of the algorithm are not properly selected, the algorithm converges to a local optimum [31], since its efficiency largely depends on the setting of its internal parameters. Statistical approaches are mainly based on the response surface method (RSM) [28], the desirability function approach [29] and the Taguchi method. Although the RSM is one of the most widely used methods for dealing with multiple responses, it does not directly incorporate response variation. The optimization method used in this study is based on Taguchi's method and adequately solves the shortcomings of the aforementioned statistical methods.

In this study, picosecond and nanosecond laser modification of the titanium-based Ti6Al4V alloy surface under controlled environmental conditions is presented. The surface effects achieved by laser interaction in standard atmospheric conditions and argon- and

nitrogen-rich atmospheres as well as a comparison of the resulting surface effects and nitriding possibilities are investigated and discussed. The influence of the different environmental conditions on spectral intensities in the LIBS analysis is also considered. The optimization of the laser parameters is carried out in standard atmospheric conditions and argon- and nitrogen-rich atmospheres in the nanosecond pulse regime.

2. Materials and Methods

The experiment involved the use of Ti6Al4V samples, each with dimensions of 60 × 60 × 2 mm. These samples were prepared by undergoing mechanical polishing and thorough cleaning prior to the laser irradiation process. The irradiation was conducted using nanosecond TEA CO_2, nanosecond Nd:YAG, and picosecond Nd:YAG lasers under standard atmospheric conditions, which included an air atmosphere with a pressure of 1013 mbar and standard relative humidity. In addition to standard atmospheric conditions, the experiment also involved the use of nitrogen- and argon-rich atmospheres. These gases were supplied to the experimental setup through a nozzle connected to gas cylinders and equipped with a flow meter. The flow rate of these gases was maintained at approximately 1 L min^{-1}. This setup enabled precise control of the environmental conditions during the laser irradiation of the Ti6Al4V samples. The parameters of the lasers and the conditions of laser irradiation are given in Table 1.

Table 1. The conditions and parameters of TEA CO_2 nanosecond, Nd:YAG nanosecond and Nd:YAG picosecond laser irradiation in the interaction with Ti6Al4V alloy.

Laser	Nanosecond TEA CO_2	Nanosecond Nd:YAG	Picosecond Nd:YAG
Wavelength	10.6 µm	1064 nm	1064 nm
Focal length (mm) *	135	100	170
Pulse duration	~100 ns	~5 ns	~150 ps
Number of accumulated pulses, (N_p)	50, 100, 400, 800, 2000	1, 5, 10, 100, 800, 2000	10, 50, 100, 150, 200, 400
Pulse energy, E_p (mJ)	155 ± 5 175 ± 5	50 ± 3 170 ± 5 250 ± 10	6.0 ± 0.5 15 ± 2 30 ± 4
Environmental conditions		Standard atmospheric conditions (SA) Nitrogen-rich atmosphere (NA) Argon-rich atmosphere (AA)	
Fluence, F (J cm^{-2})	SA: 3.9; 5.3 NA: 5.5; 6.2 AA: 4.7; 6.0	SA: 19.1; 64.9; 95.5 NA: 16.3; 55.5, 81.7 AA: 17.0; 57.7; 84.9	SA: 6.1; 15.2; 30.5 NA: 5.4; 13.6; 27.2 AA: 9.4; 23.5; 47.1

* The stand-off distance, i.e., the distance between the sample and lens, is the same as the focal length with all lasers, to achieve the most effective ablation.

The effects of nanosecond TEA CO_2, nanosecond Nd:YAG and picosecond Nd:YAG laser interactions with Ti6Al4V alloy under various environmental conditions were examined through a comprehensive analysis. An optical microscope Carl Zeiss EPITZP 2 (Jena, Germany) and scanning electron microscope JEOL JSM-6610LV SEM (Tokyo, Japan) coupled with an energy-dispersive spectrometer X-Max Large Area Analytical Silicon Drift EDS (Oxford, UK) were used to analyse changes on the alloy surface caused by lasers. For the surface topography characterization, the non-contact optical profilometer Zygo NewView 7100 (Middlefield, CT, USA) was used. Several surface parameters were examined via profilometry analysis: *Ra* is average surface roughness [32]; *rms* is the root-mean-square average of profile height deviations from the mean line [32]; *PV* is peak to valley [32]; and the ablation depth measurements were 2D profiles and 3D surface topography maps. The international standard ISO 25178 Surface Texture (Areal Roughness Measurement) was consulted for the filtering and evaluation processes [33]. The results obtained from profilometry analysis were processed in the Origin program (version 9.0). For the analysis of plasma generated in front of the sample target in different environmental conditions, the LIBS (laser-induced breakdown spectroscopy) technique was used. In general, plasma formed over the solid target emits spectral lines of elements found in the tested sample, and the intensities of these lines depend on the concentration of the emitting elements in the sample. In addition to the lines of elements from the target, lines of atoms that make up the atmosphere in which the

plasma is induced by the laser will also be emitted in the plasma [34,35]. The spectrographs used in this work were the StellarNet LSR-UV2-14 and LSR-VIS4-14 (Tampa, FL, USA) with wavelength ranges of 200–400 nm and 400–600 nm, respectively.

Supplementary experiments for Nd:YAG nanosecond laser irradiation were conducted to further investigate the impact of various process control parameters on multiple output responses. These parameters included the number of accumulated laser pulses (N_p) and the pulse energy (E_p). The study focused on assessing the effects of these parameters on the following output responses: (1) R_a; (2) *rms*; (3) *PV*; (4) *Kr*—presence of craters or crater formation (bulk material removal); (5) *DA*—depth of ablation; (6) *VA*—velocity of ablation (ablation rate, drilling depth per laser pulse); and (7) *C*—circularity (the ratio between the maximum and minimum diameters of the laser spot). These experiments were designed to identify the specific conditions that would result in the most precise modification and efficient ablation of the material, based on the surface characterization results obtained.

3. Results and Discussion

After laser irradiation of a material, several processes can be observed. Due to the high temperature of a laser beam, thermal melting occurs, as well as some plastic deformations of the material and, finally, cooling and resolidification. Also, depending on the pulse energy, crater formation and ablation may occur. Laser radiation primarily interacts with valence and conduction electrons, and the energy transfer time is determined by the laser pulse duration. In the case of very short pulses, the resulting distribution of energy to the electrons at the end of the pulse is not thermal [36–39]. Furthermore, the transferred (deposited) energy is redistributed to different energy states of the system; that is, the electrons transfer energy to the crystal lattice. The essential difference in the interaction of radiation of different lengths of impulse is presented more clearly when considering the timescale of the processes that are characteristic for those interactions [39]. Impulses with duration much longer than any process are considered to cause long energy relaxation in the system. This is the case for pulses in the nanosecond domain, as well as longer ones. Since all relaxation processes take place much faster than the duration of the impulse, the entire system is in an equilibrium state during the interaction [39]. When the laser pulses last longer than the lattice heating time, thermalization between the electronic subsystem and the lattice takes place during the pulse. In the nanosecond regime, the absorbed energy first heats the target surface to the melting point and then to the vaporization temperature. In the case of ablation with longer laser pulses, there is enough time for propagation of the heat wave in the target and a relatively large layer of molten material is formed. Evaporation occurs from the liquid metal, which significantly reduces the accuracy of laser metal processing. If micrometer-sized structures are preferred, sufficient precision can be achieved with nanosecond laser radiation. However, if it is necessary to form a structure of nanometer dimensions, it is preferable to use lasers with picosecond or femtosecond pulses. In the picosecond regime, the lattice temperature during the pulse remains much lower than the electron temperature. Balance is achieved only after the cessation of impulse. During the interaction of picosecond laser pulses with metals, energy transfer occurs for a few picoseconds, i.e., during the interaction. In this case, the material is confined in the area of the impact; it heats up at the end of the pulse, so theoretically there is no photon interaction with the melted or vaporized material, which results in more precise ablation.

Ti6Al4V is a titanium α + β alloy. In addition to the basic elements that make up the alloy, and depending on the application, oxygen may be present in the alloy, ranging from 0.08–0.4 wt%, where a high percentage of oxygen (0.4 wt%) plays the role of an enhancer of the alloy's properties while a lower percentage of oxygen (with a lower percentage of nitrogen and aluminum) can improve characteristics such as ductility, corrosion resistance and resistance to crack growth [40]. The thermal conductivity of the alloy is 7.2 W m^{-1} K^{-1}, the melting point is 1877–1941 K, and the thermal diffusivity is 0.022 cm^2 s^{-1} [41]. Unmodified surface morphology and a two-dimensional profile are presented in Figure 1.

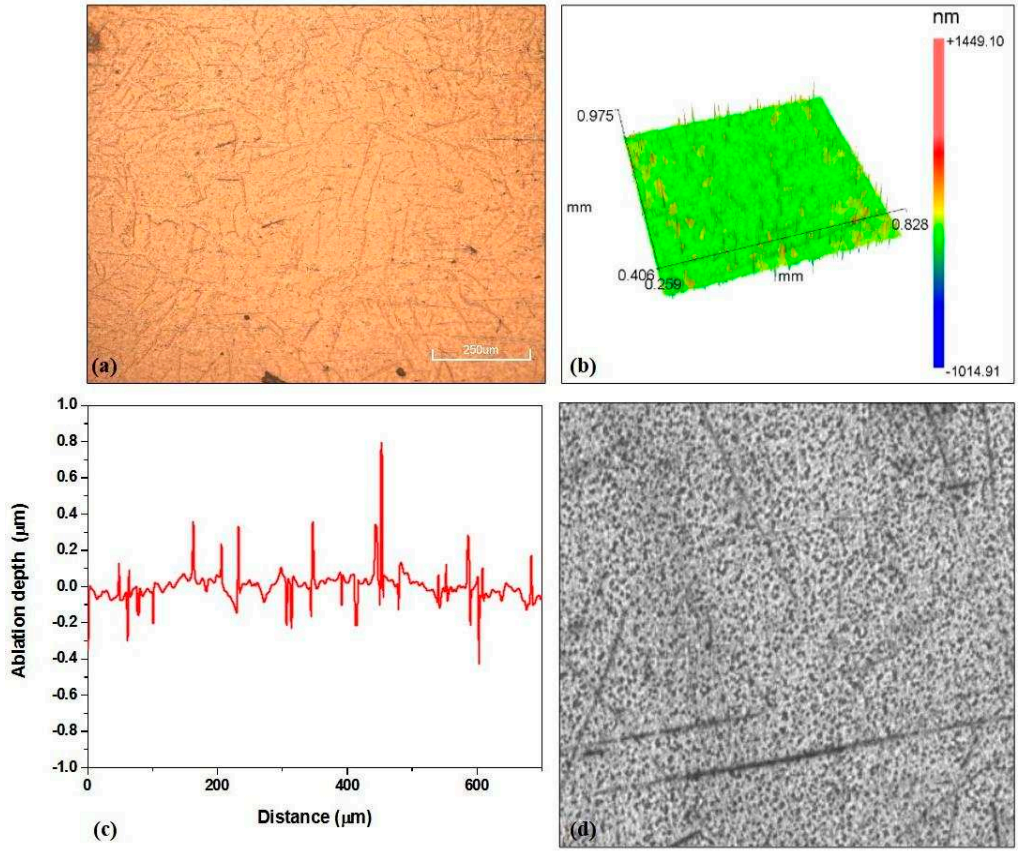

Figure 1. Unmodified surface of the Ti6Al4V alloy: (**a**) SEM microphotograph; (**b**) 3D map; (**c**) 2D profile; (**d**) intensity map.

3.1. Determining Damage Threshold Fluence and Heat Affected Zone (HAZ)

Damage thresholds, F_{th}, which represent the minimum laser energy density value that causes visible changes on the target surface, were determined for Ti6Al4V alloy irradiated by picosecond and nanosecond laser radiation in the atmosphere, argon and nitrogen by the method proposed for Gaussian-shaped beams [42]. The threshold energy density values were determined by plotting the dependence of the diameter of the laser radiation trace in relation to the logarithmic value of the pulse energy [42]. From the linear fit slope and intercept, the value of the laser beam diameter, ω_0, is obtained, and on the basis of this value the threshold fluence is calculated [42] (Figure 2). The obtained values ω_0 are 250.4 µm in air, 264.9 µm in a nitrogen-rich atmosphere and 201.4 µm in an argon-rich atmosphere, for a 150 ps laser pulse. The values of estimated ω_0 for a 5 ns laser pulse are 408.3 µm in air, 441.6 µm in a nitrogen-rich atmosphere and 433.2 µm in an argon-rich atmosphere.

However, this method is not suitable in the case of a multimode beam structure, as is the output beam of the TEA CO_2 laser, so the threshold energy density values were estimated by direct observation of the target after each accumulated pulse with increasing pulse energy values until the first visible damage to the alloy surface was detected. The determined values of F_{th} for Ti6Al4V in the present experimental conditions are given in Table 2. As expected, the inert nature of argon and nitrogen represses the laser/material interaction, and for 5 ns and 100 ns (long) laser pulse irradiation of the alloy surface, the F_{th} value is lowest in air. However, for 150 ps (short) laser pulse irradiation, F_{th} in air is higher by an average of 55 percent than in argon and nitrogen ambient conditions. This effect of argon and nitrogen environmental conditions is the opposite in the case of 5 ns and 100 ns (long) laser pulse interactions with the alloy surface, where the F_{th} value is lowest in air, probably due to the 10 Hz laser repetition rate [43] and overall more intensive interaction, which caused more intensive plasma generation in front of the target and, subsequently, a plasma shielding effect in the air.

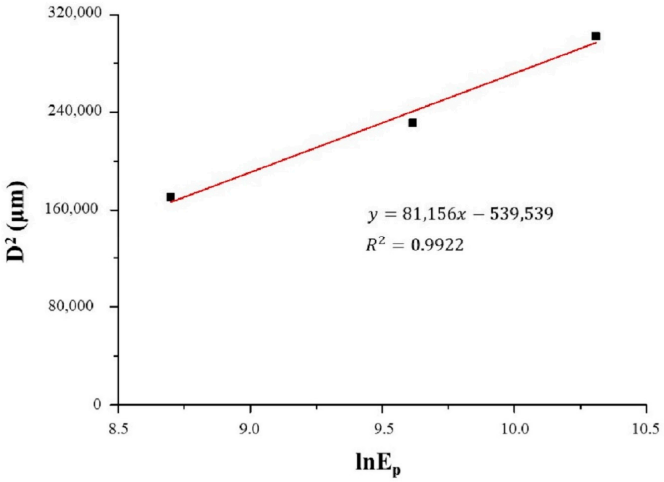

Figure 2. Example of the linear fit of $D^2 = f\ (ln\ E_p)$ for 10 p, for Ti6Al4V irradiated by a laser beam of 150 ps pulse duration.

Table 2. Damage threshold fluences, F_{th} (J cm^{-2}), for Ti6Al4V.

Environmental Conditions	F_{th} (J cm^{-2})		
	Nd:YAG (150 ps)	Nd:YAG (5 ns)	TEA CO_2 (100 ns)
Standard atmosphere (SA)	2.13	3.09	3.92
Nitrogen-rich atmosphere (NA)	1.13	9.31	5.54
Argon-rich atmosphere (AA)	1.21	14.46	4.65
HAZ (nm)	~18	~105	~469

The effect that laser irradiation causes on the Ti6Al4V surface is determined by the amount of incident laser radiation absorbed by the material. For picosecond and nanosecond lasers, energy transfer from the laser beam to material is described by the heat effect zone, *HAZ*, which depends on the pulse duration and the thermal diffusivity of the material [44]:

$$l_{th} = \sqrt{D \times \tau} \quad (1)$$

where l_{th} (µm) is the length of thermal diffusion, i.e., *HAZ*, D (cm^2 s^{-1}) is thermal diffusivity, and τ (s) is pulse duration. Under the given experimental conditions, *HAZ* values are presented in Table 2.

The different morphological structures that form on the surface of the sample during the interaction with laser radiation also depend on the temperature reached on the surface of the material. For nanosecond laser radiation, estimation of the surface temperature value during laser/material interaction is done using the one-dimensional thermal conductivity equation [45]:

$$\Delta T \approx \frac{(1-R)I_o\tau}{\rho C\sqrt{2D\tau}} \quad (2)$$

where R (%) is reflectivity (0.57% for TiAl4V for the wavelength of 1064 nm [46]), I_o (W cm^{-2}) is laser intensity, C (J kg^{-1} K^{-1}) is thermal capacity (560 J kg^{-1} K^{-1} for Ti6Al4V [41]), ρ (g cm^{-3}) is alloy density, D (cm^2 s^{-1}) is thermal diffusivity, and τ (s) is pulse duration.

For the interaction of nanosecond laser irradiation, under the present experimental conditions, the calculated temperatures were in the range of ~7000 K for 5 ns and ~15,000 K for 100 ns laser interaction. These temperatures, compared to the melting temperature of the Ti6Al4V alloy (1877–1941 K [41]), are more than sufficient for melting its surface and activating the gas above the surface, thus causing a reaction between the alloy sample and the surrounding gas. For picosecond laser interaction with the materials, the temperature model is more complex, and the two-dimensional equation has to be solved [45].

3.2. Surface Characterization

3.2.1. Nanosecond Laser Irradiation—100 ns Pulse Duration, 10.6 μm Wavelength

Analysis of the morphological changes on the surface of the Ti6Al4V alloy after the effects of TEA CO_2 nanosecond laser radiation at 155 and 175 mJ pulse energies and 6.0 J cm^{-2} and 6.2 J cm^{-2} fluences was subsequently performed using SEM. A multi-pulse mode of irradiation of the alloy sample was carried out, applying 50 to 2000 laser pulses. Although the values of the fluences are close, when analyzing the SEM microphotographs, the changes induced by 155 mJ pulses are not prominent, so the investigation focus is on the topography effects induced by laser action with 175 mJ pulse energy and 6.2 J cm^{-2} fluence (Figures 3 and 4).

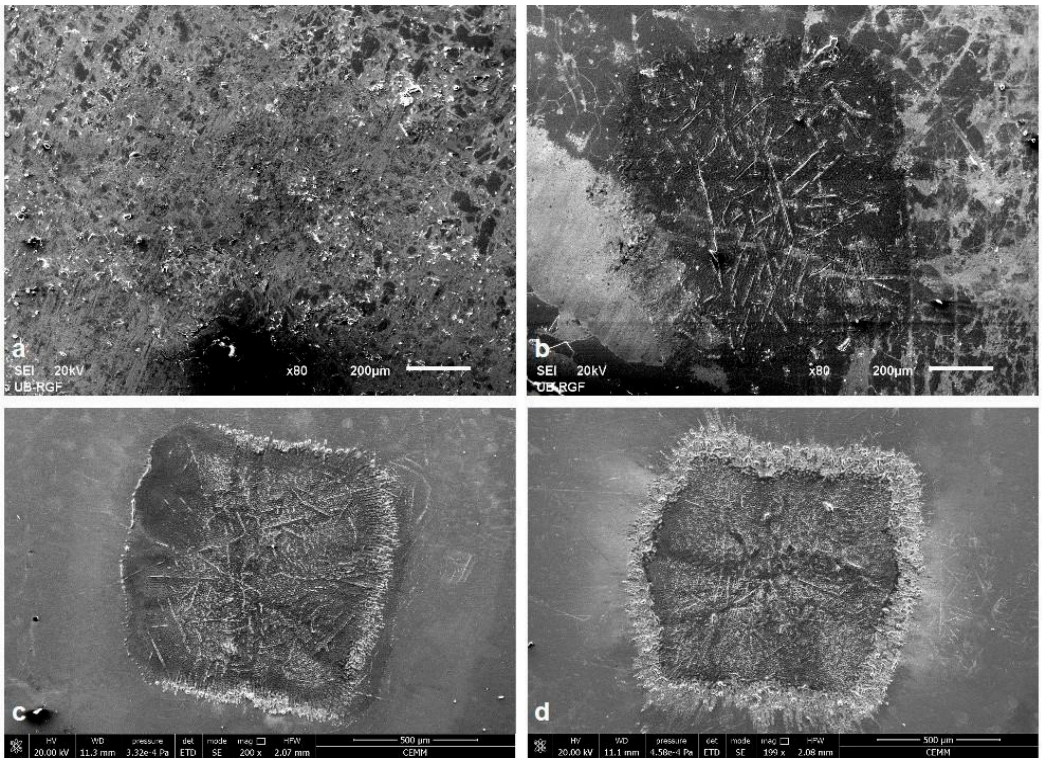

Figure 3. Ti6Al4V surface damaged areas after TEA CO_2 laser action with (**a**) 50, (**b**) 400, (**c**) 800 and (**d**) 2000 pulses of 10.6 μm wavelength, 6.2 J cm^{-2} fluence and 100 ns pulse duration, in a nitrogen-rich atmosphere.

The TEA CO_2 laser beam was in multi-mode; hence, the modification of the surface at the damaged areas is relatively homogeneously distributed and the spots are square-shaped (Figure 1). Irradiation of the surface with nanosecond laser radiation in all three ambient conditions leads to more prominent morphological changes on the surface of the alloy sample after 400 accumulated pulses (Figure 4(a1,b1,c1)) where material corrugation and cracking of the surface of the alloy followed by the appearance of microcracks, as well as the partial formation of granular structures probably matching the phase boundaries of the material, can be distinguished at the damaged areas.

With an increase in the number of applied pulses, the central and periphery can be distinguished, as can be seen after 800 and 2000 accumulated laser pulses (Figure 3c,d). There is melting of the alloy surface material as well as its cooling and hardening in the form of a "spike" near the periphery of the target, which is a consequence of the propagation of the molten material from the center to the periphery of the damaged area, as well as the occurrence of explosive ejection of the molten material or solidification of the front of the molten material from the center to the periphery. The center of the modified areas in air is characterized by resolidified molten areas and pronounced grain boundaries

(Figure 4(a1–a3)) which is in accordance with expected thermal melting and subsequent cooling, without ablation and removal of material [15,21]. Also, the grains with pronounced boundaries and microcracks, due to rapid cooling, are noted at the center of the modified area after 800 and 2000 accumulated pulses in a nitrogen-rich atmosphere (Figure 4(c2,c3)) and, at the periphery of the modified area, there is a formation of periodic structures, but, due to excessive cracking of the alloy surface, they are of low intensity and period values could not be determined. However, modification in an argon-rich atmosphere leads to the formation of parallel laser-induced periodic surface structures (LIPSS) relatively uniformly over the modified area (Figure 4(b2,b3)) proportional to the laser wavelength of 10.6 μm, which are usually reported as the result of short (picosecond) and ultra-short (femtosecond) laser interactions with materials [47–51]. The periods of the LIPSS structures in the argon-rich atmosphere, close to the alloy irradiation wavelength (10.6 μm), are ~9.3 and ~11.0 μm for 800 and 2000 accumulated pulses, respectively. It can be concluded that low-frequency (LF) LIPSS structures are formed. There is not much reported research on LIPSS on Ti6Al4V in the nanosecond laser regime, because it is generally difficult to obtain such structures with long nanosecond pulses. LIPSS induced by TEA CO_2 laser pulses have previously been reported on silicon [50]. On titanium, modified at a higher fluence value of 28 J cm^{-2}, in an air and nitrogen-rich atmosphere, no LIPSS were reported [21]. Reported experiments with fiber laser multi-line scanning presented the formation of LIPSS only on a Ti6Al4V surface modified in nitrogen [15]. From our experiment, it can be concluded that the 10.6 μm pulse duration TEA CO_2 multimode laser output at relatively low fluence values, approximately 6.0 J cm^{-2}, could be used for patterning of the Ti6Al4V surface in argon- and nitrogen-rich ambient conditions. LIPSS formation is probably possible due to the low value of fluences and suppressed hydrodynamic effects under the influence of the inert nature of argon and nitrogen. It is important to note that, analyzing the SEM micrographs, no ablation, e.g., crater formation, was observed with the TEA CO_2 nanosecond laser with multi-mode intensity distribution.

In the realm of structure formation in the molten phase and their subsequent transition into the solid phase through solidification, a noteworthy mechanism emerges when metals are subjected to laser irradiation at fluences near the threshold with a relatively low pulse count. Under these conditions, intriguing surface patterns manifest in the form of parallel waves that recur at intervals matching the wavelength of the incident laser. These distinctive patterns are commonly referred to as "laser-induced periodic surface structures" (LIPSS) [52,53]. The characteristics and properties of LIPSS are profoundly influenced not only by the number of laser pulses, often synonymous with the exposure time, but also by a range of other pivotal laser processing parameters. In accordance with the widely accepted plasmon combination theory, the formula used to determine LIPSS periods is expressed as:

$$\Lambda_{LIPSS} = \frac{\lambda}{\eta \pm \sin\theta} \tag{3}$$

where λ is the laser wavelength, $\eta = R\,[\varepsilon_m\varepsilon_d/(\varepsilon_d + \varepsilon_m)]^{1/2}$ is the real part of the effective refractive index for metal/air (~1), R is surface reflectivity, ε_d is the dielectric constant, ε_m is the complex dielectric constant of a metal, and θ is the incident angle [54]. It is evident from Equation (3) that the LIPSS period is proportional to the laser irradiation wavelength and, therefore, LIPSS formed as a result of TEA CO_2 laser action should have values of ~10.6 μm, which corresponds to the obtained experimental values of LIPSS periods of 9.3 and 11.0 μm. In addition to the pulse number, LIPSS are influenced by various factors, including the laser wavelength, the angle at which the laser beam is incident, and the intrinsic properties of the material. Notably, LIPSS have demonstrated significant effects on altering the optical characteristics of metal surfaces, enhancing the active surface area, and improving biocompatibility [55].

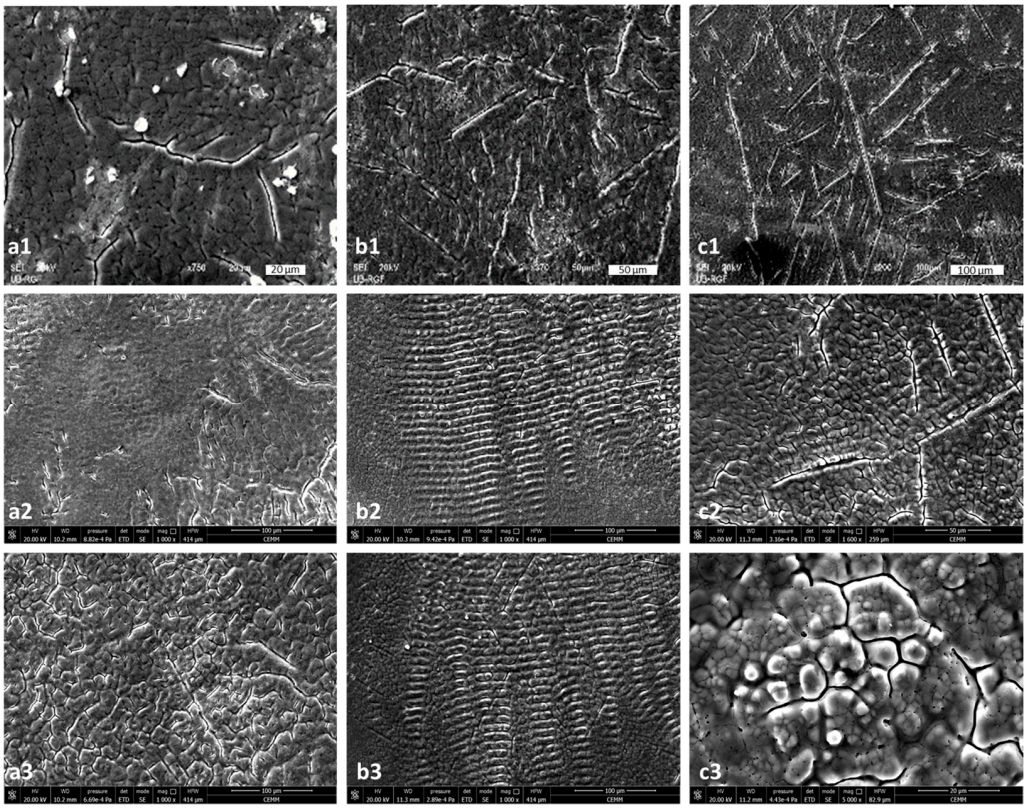

Figure 4. SEM microphotographs of the Ti6Al4V surface after TEA CO_2 laser irradiation with a 100 ns pulse duration and 175 mJ pulse energy: (**a1**–**a3**)—air, fluence 5.3 J cm^{-2}, (**b1**–**b3**)—argon-rich atmosphere, fluence 6.0 J cm^{-2}, (**c1**–**c3**)—nitrogen-rich atmosphere, fluence 6.2 J cm^{-2}; 1–400 pulses, 2–800 pulses and 3–2000 pulses.

3.2.2. Nanosecond Laser Irradiation—5 ns Pulse Duration, 1064 nm Wavelength

The irradiation of the Ti6Al4V alloy with nanosecond laser radiation (Figure 5) is characterized by pronounced thermal effects on the surface, which is expected because the nanosecond pulses have a longer duration than the time required for relaxation processes on the target [37] and the Gaussian beam intensity distribution in the Nd:YAG laser system means that the intensity of the pulse is focused at the center and it decreases towards the periphery. Therefore, the obtained fluences for the same value of pulse energy are higher than with the multi-mode beam intensity distribution. Induced effects also include crater formation, which implies that material removal, e.g., ablation occurred and LIPSS were not observed under the present experimental conditions.

After irradiating the alloy with a single pulse with a pulse energy of 50 mJ and relatively low values of fluence (Table 1) the traces of the laser radiation spot are clearly distinguishable from material corrugation due to melting in all three ambient conditions. After 10 accumulated pulses, in addition to the more intense corrugation of the surface material in the center of the damaged area, the melting of the material caused the propulsion of the material and its movement towards the periphery of the target, Figure 5(a1,b1,c1). After 100 and more applied pulses, in an argon-rich atmosphere, at the higher energy density values of 57.7 and 84.9 J cm^{-2}, the initial formation of a crater in the center of the modified target can be observed (Figure 5(a2,b2,c2)) as confirmed by the profilometry analysis, presented in Section 3.3. Profilometry analysis of the modified areas presented in Section 3.3 shows this trend continues after 800 accumulated pulses, now ocurring in air and nitrogen-rich atmospheres, but more dominant crater formation is again found in an argon-rich atmosphere, especially with a further increase in the applied pulses of 170 mJ energy and 57.7 J cm^{-2} fluence. With a further increase in the number of accumulated pulses, more pronounced hydrodynamic effects occur in the form of the formation of clearly

defined crater edges in the form of solidified and pre-melted material, most pronounced in an argon-rich atmosphere (Figure 5(b2,b3)). The formation of granular structures on the periphery of the irradiated target is noticeable in atmospheres of argon, with a diameter of about 6.4 μm (Figure 5(b2,b3)) and nitrogen, with a diameter of about 4.3 μm, at lower pulse energy values (Figure 5(c2,c3)). The appearance of microcracks was observed with 100 accumulated pulses in a nitrogen-rich atmosphere and at an energy density value of 16.3 J cm^{-2}. Crater formation is evident after applying a large number of pulses in all three ambient conditions, but as the crater inner walls in air and argon are relatively smooth, the craters formed in a nitrogen-rich atmosphere have a cone-like structure, distributed on the inner walls (Figure 5(c2,c3)). This is probably due to nitride formation, enabled by the optical breakdown of plasma in nitrogen, enabling chemical reactions of the surface material with the surrounding gas, as proposed in previous investigations [21].

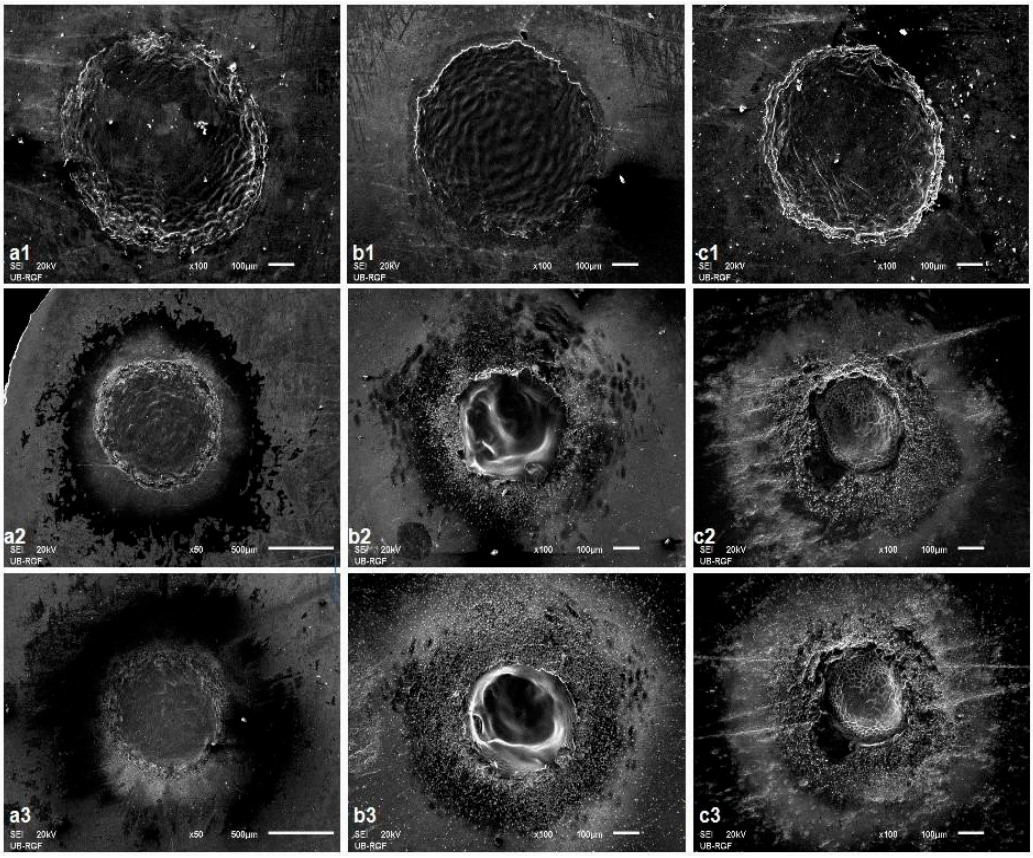

Figure 5. SEM microphotographs of the Ti6Al4V surface after 1064 nm Nd:YAG laser irradiation with a 5 ns pulse duration and 50 mJ pulse energy: (**a1**–**a3**)—air, fluence 19.1 J cm^{-2}, (**b1**–**b3**)—argon-rich atmosphere, fluence 17.0 J cm^{-2}, (**c1**–**c3**)—nitrogen-rich atmosphere, fluence 16.3 J cm^{-2}; 1–10 pulses, 2–800 pulses and 3–2000 pulses.

3.2.3. Picosecond Laser Irradiation—150 ps Pulse Duration, 1064 nm Wavelength

The effects of 150 ps laser irradiation on the Ti6Al4V alloy surface are prominent with an increasing pulse count from 10 to 400 and output energy ranging from 6 to 30 mJ in air and in argon- and nitrogen-rich atmospheres (Figures 6 and 7). The main features are craters, increased roughness, microcracks and LIPSS. However, the morphological changes that arise significantly differ at different ambient conditions, with an increase in accumulated pulses (Figure 6). At a low pulse count of 10 pulses, there are small, uniformly distributed changes in topography, material corrugation and therefore surface roughness (Figure 6(a1,b1,c1)). An increase in the pulse count at constant pulse energy leads to prominent crater formation in the air and argon-rich atmospheres (Figure 6(a2,a3,b2,b3)). In nitrogen-rich atmosphere, a pool of resolidified molten material and corrugation occur,

as well as shallow craters (Figure 6(c2,c3)). The reason for the absence of deeper craters may lie in the fact that the energy of the laser radiation is not sufficient to eject the molten material or its vaporization has already had dominant thermal effects, so the molten material is partially accumulated at the bottom of the crater. An interesting feature is noted after 100 accumulated pulses in an argon-rich atmosphere (Figure 6(b2)). The rim of the formed crater exhibits an organized, crown-like pattern, which is probably the result of hydrodynamic effects due to the propagation of the molten material.

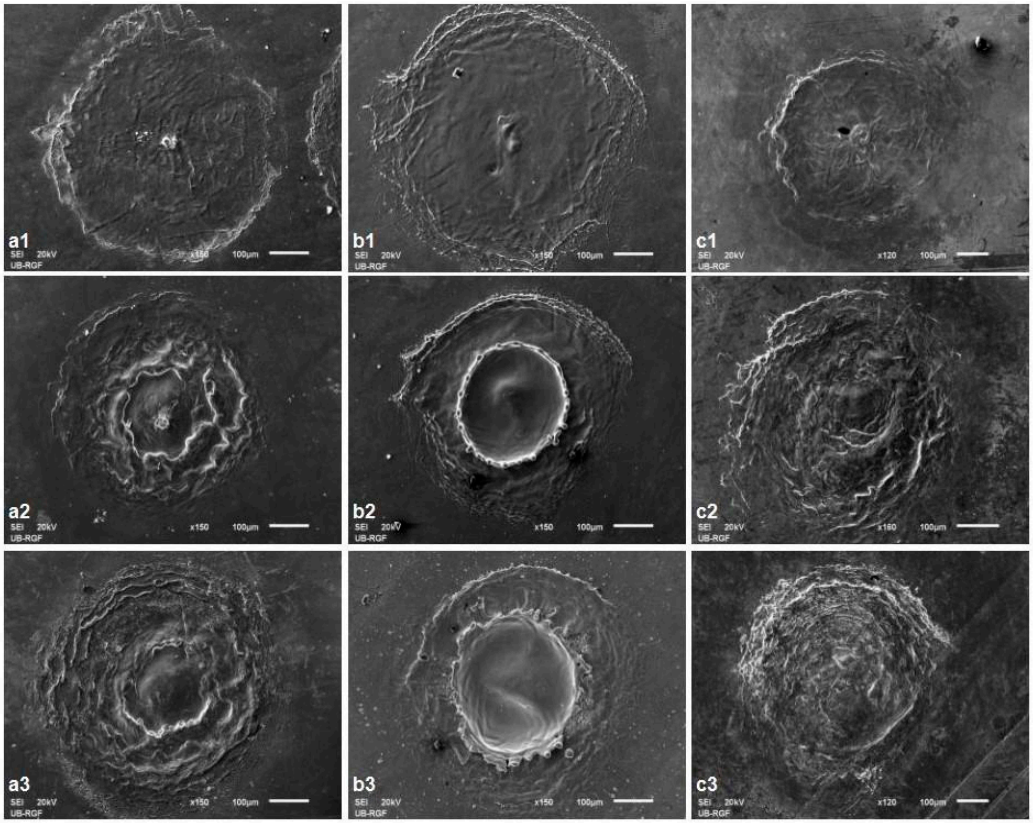

Figure 6. SEM microphotographs of the 1064 nm Ti6Al4V surface after Nd:YAG laser irradiation with a 150 ps pulse duration and 30 mJ pulse energy: (**a1**–**a3**)–air, fluence 30.5 J cm^{-2}, (**b1**–**b3**)—argon-rich atmosphere, fluence 47.1 J cm^{-2}, (**c1**–**c3**)—nitrogen-rich atmosphere, fluence 27.2 J cm^{-2}; 1–10 pulses, 2–100 pulses and, 3–400 pulses.

At the higher values of pulse energies, there is mostly the absence of a smooth central part in the modified target. At an output energy of 15 mJ, after 50 accumulated pulses in air, microcracks are observed at the irradiated areas caused by the rapid cooling of the target surface after the end of the irradiation. These microcracks appeared at both the peripheral and central parts of the modified area. With an increase in the number of accumulated pulses, there is also the appearance of granular structures in the air at 30.5 J cm^{-2} fluence, which are more pronounced in the nitrogen-rich atmosphere at 13.6 J cm^{-2} after 200 applied laser pulses. The average diameters of these granular structures are 1.8 µm.

Picosecond laser irradiation of the Ti6Al4V alloy produced LIPSS structures at pulse energy values of 6 and 15 mJ, located on the periphery of the modified target. At a higher energy value of 30 mJ, no LIPSS structures were observed, probably due to the excessive energy of the pulse, which led only to intensive melting of the material both in the center and on the periphery of the modified target. Selected SEM microphotographs of LIPSS structures are shown in Figure 7a–e. The most pronounced LIPSS structures were formed in a nitrogen-rich atmosphere at 5.4 J cm^{-2} fluence with 200 accumulated pulses (Figure 7b). With a period value of approximately 900 nm, these can be classified as LF-LIPSS structures. After interaction with 100 accumulated pulses at 13.6 J cm^{-2} fluence in a nitrogen-rich

atmosphere, LIPSS are observed relatively close to the center of the damaged area with a period value of ~570 nm, which is significantly below the value of the laser wavelength (Figure 7e). It can be observed that, with fluence increase, there is a decrease in the value of the period of LIPSS. In the air, structures are visible at the periphery of the modified target with period values of ~629 and 645 nm (HF-LIPSS structures) at pulse energy density values of 6.1 and 15.2 J cm^{-2}, respectively, and for 100 and 200 accumulated pulses (Figure 7a–e). Regarding irradiation in the argon-rich atmosphere, LIPSS structures are only formed after 400 accumulated pulses and with an energy density value of 23.5 J cm^{-2}. The period values of these structures are below the wavelength of laser radiation and are approximately 685 nm.

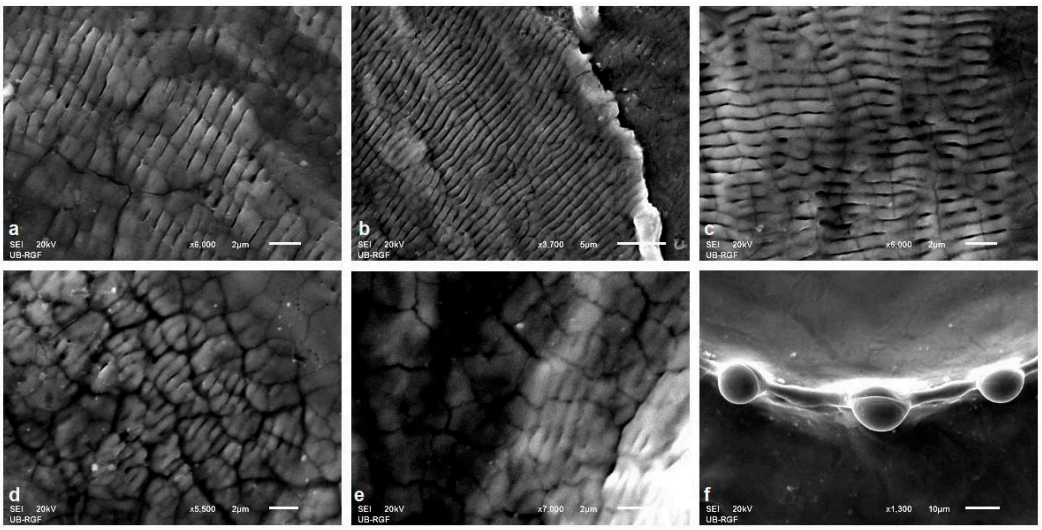

Figure 7. Periodic surface structures on a picosecond laser modified Ti6Al4V surface after (**a**) 400 pulses at 6.10 J cm^{-2} in air; (**b**) 200 pulses at 5.40 J cm^{-2} in a nitrogen-rich atmosphere; (**c**) 400 pulses at 23.5 J cm^{-2} in an argon-rich atmosphere, (**d**) 100 pulses at 15.2 J cm^{-2} in air, (**e**) 100 pulses at 3.6 J cm^{-2} in a nitrogen-rich atmosphere, (**f**) 100 pulses at 47.1 J cm^{-2} in an argon-rich atmosphere.

Besides the laser parameters (laser fluence, number of applied laser pulses, laser wavelength, polarization, incidence angle) and material properties (surface roughness, index of refraction, absorption coefficient, reflectivity, conductivity), LIPSS formation is influenced by environmental conditions, ambient pressure and molten material reorganization, if thermal effects occur during laser/material interaction. Generally, LIPSS period values show a decrease with an increasing number of accumulated pulses and/or increased laser fluence value, probably due to the fact that every subsequent pulse of the incident laser beam is deposited to the surface with altered properties, like increased roughness and specific surface [48,56,57]. The most interesting structures obtained in this experimental setting are the structures formed in an argon-rich atmosphere with an energy density value of 47.1 J cm^{-2} after 100 and 200 accumulated pulses (Figures 6(b2) and 7f). Solidified drops of molten material are located at nearly equivalent distances of ~39 µm, forming a regular crown-shaped rim around the crater. The diameter of the resolidified droplet is ~10 µm. The proposed explanation is that the thermocavitation instability of the molten material on the surface can occur in the form of a micrometer-sized crown on the surface, and, as a result of the action of a larger number of laser pulses, energy density values are close to the ablation threshold density value [58]. It is likely that these structures form due to thermodynamic instability. The formation of structures of this type has been reported on thin metal films deposited on silicon and on the surface of silicon after the action of femtosecond laser radiation, with nanometer dimensions, under standard experimental conditions [58,59]. The formation of such structures after the action of picosecond laser radiation has not been reported in the studied literature.

3.3. Surface Roughness Investigation

After TEA CO_2 laser irradiation, at a 10.6 μm wavelength and 100 ns pulse duration, pronounced corrugation and no crater formation is evident in all ambient conditions. Examination of the two-dimensional profiles and three-dimensional maps of the Ti6Al4V surface confirmed the accumulation and redistribution of the molten and cooled material and no crater formation (Figure 8). Nd:YAG laser action at a 1064 nm wavelength, 5 ns pulse duration and output energy of 50 mJ caused ablation and crater formation on the alloy surface (Figures 9d,e and 10d–f). A Ti6Al4V area modified by Nd:YAG picosecond laser irradiation of 10 pulse at a 6 mJ output energy is characterized by shallow craters and increased surface roughness (Figures 11 and 12).

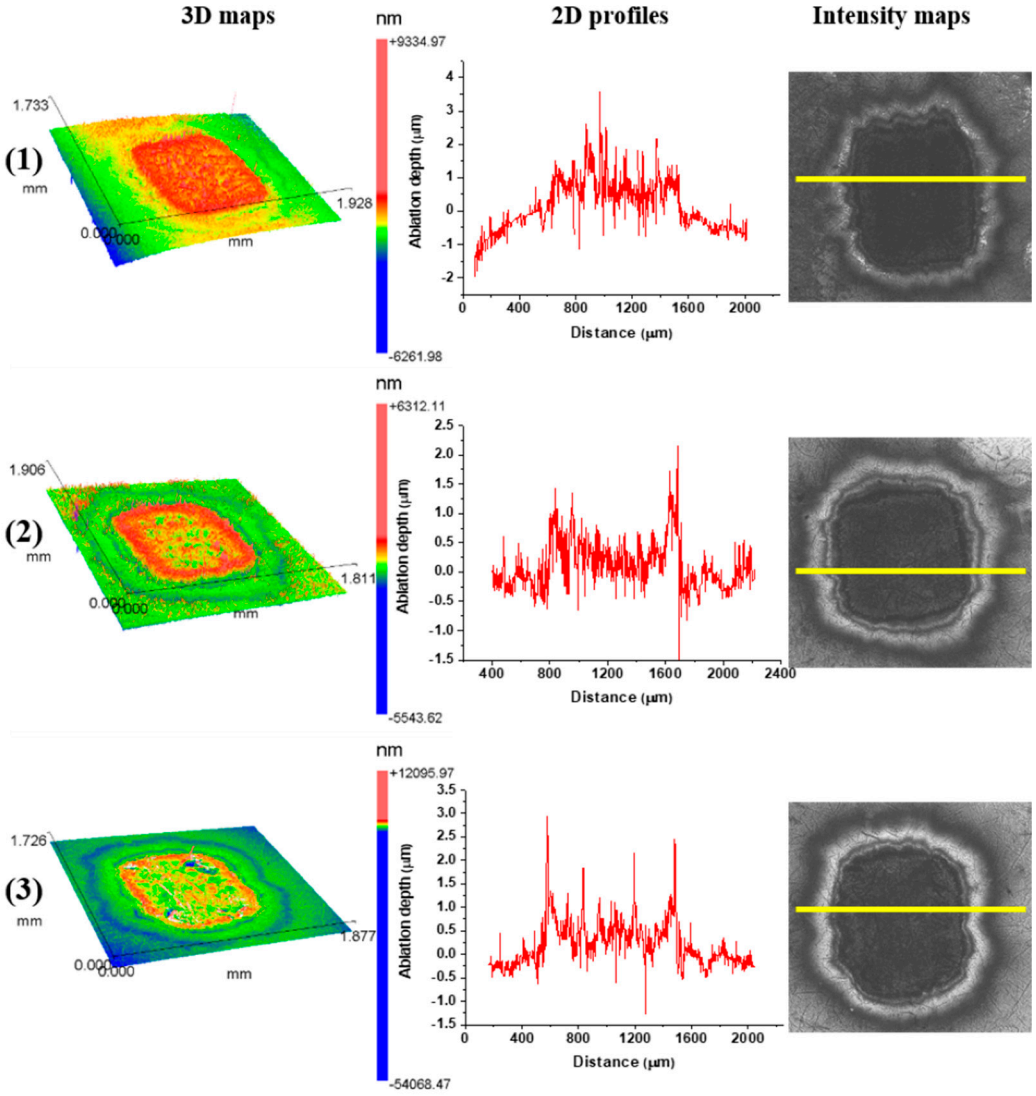

Figure 8. Cross-sectional profiles, three-dimensional representations and intensity maps of the Ti6Al4V surface after laser irradiation at 10.6 μm, pulse duration 100 ns, pulse energy 175 mJ and pulse count 400 in (**1**) air and (**2**) argon-rich and (**3**) nitrogen-rich ambient conditions. Yellow lines in the intensity maps indicate cross-section lines of the 2d profiles.

The dependence of the average surface roughness, R_a, on accumulated pulse number, pulse count N_p, is given in Figure 9a. The value of R_a ranges from ~0.2–0.3 μm for 200 pulses to ~1.3 μm for 2000 pulses for 155 mJ pulse energy. At a pulse energy value of 175 mJ, up to 200 accumulated pulses, R_a is about 0.25 μm, while, after 400 pulses, an increase in the roughness value is again noticeable (Figure 9a). In air, R_a increases up to ~0.75 μm for

N_p = 2000 in an argon-rich atmosphere, up to ~1.4 µm for N_p = 2000, and, in a nitrogen-rich atmosphere, the highest value of the R_a parameter is ~3.25 µm for N_p = 800. The biggest increase in roughness is in the presence of nitrogen, probably due to the formation of cone-like structures, i.e., nitrides, which were detected by SEM. Under the given experimental conditions, it can be concluded that the ablation efficiency is low, but, considering the clear formation of LIPSS structures (Figure 3) as well as the good values of the surface roughness parameter, this alloy irradiation is suitable for patterning the alloy surface.

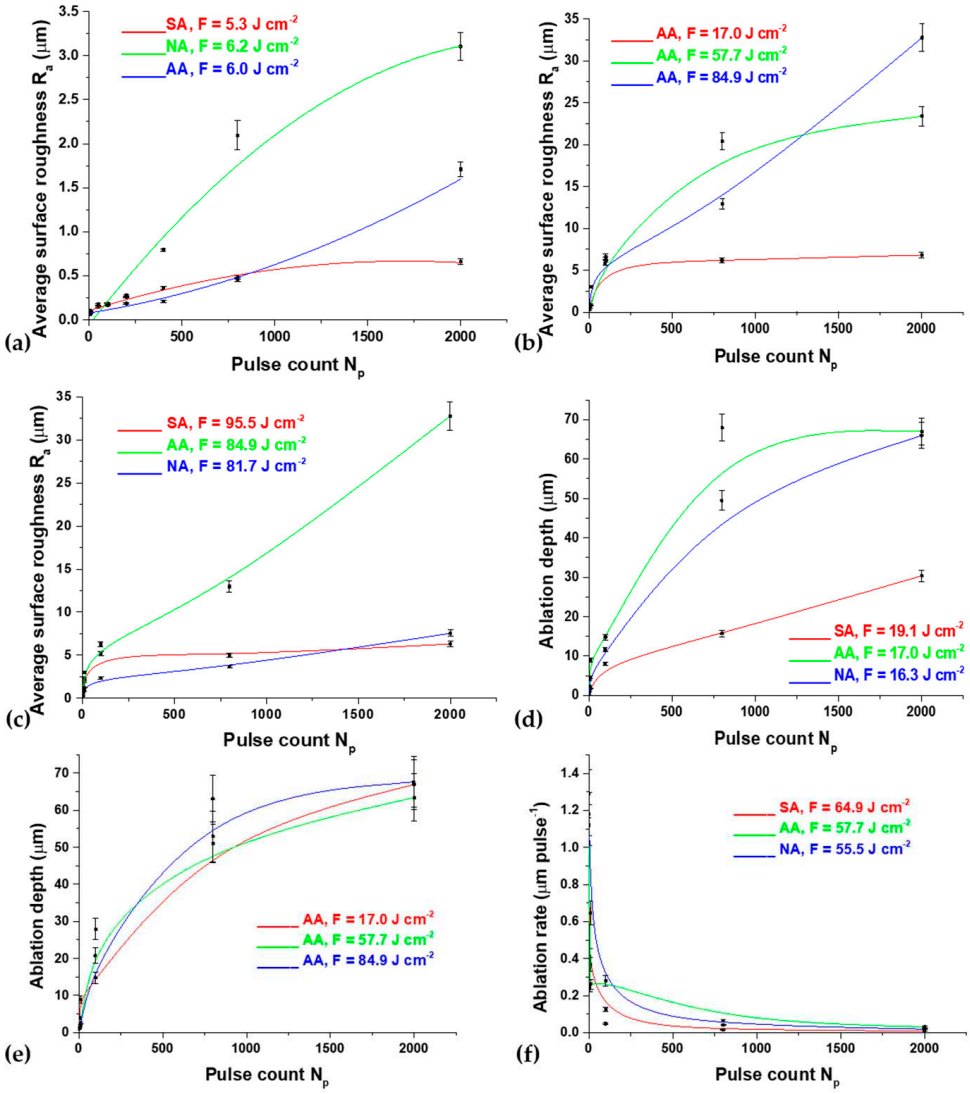

Figure 9. Nanosecond irradiation of Ti6Al4V—diagrams of surface parameters' dependence on pulse count, N_p: (**a**) average surface roughness, R_a, at 175 mJ energy, 10.6 µm wavelength and 100 ns pulse duration; (**b**) average surface roughness, R_a, at 250 mJ energy, 1064 nm wavelength and 5 ns pulse duration; (**c**) average surface roughness, R_a, at 1064 nm wavelength and 5 ns pulse duration with different pulse energies in an argon-rich atmosphere; (**d**) ablation depth at 50 mJ energy, 1064 nm wavelength and 5 ns pulse duration; (**e**) ablation depth at 1064 nm wavelength and 5 ns pulse duration with different fluences in an argon-rich atmosphere and (**f**) ablation rate at 170 mJ pulse energy, 1064 nm wavelength and 5 ns pulse duration.

Considering the variety of morphological changes at the surface of the Ti6Al4V alloy induced by nanosecond laser radiation of a 1064 nm wavelength and 5 ns pulse duration, profilometric analysis provided more detailed information regarding surface profile, topography, ablation depth, ablation rate and surface roughness (Figure 9b–f).

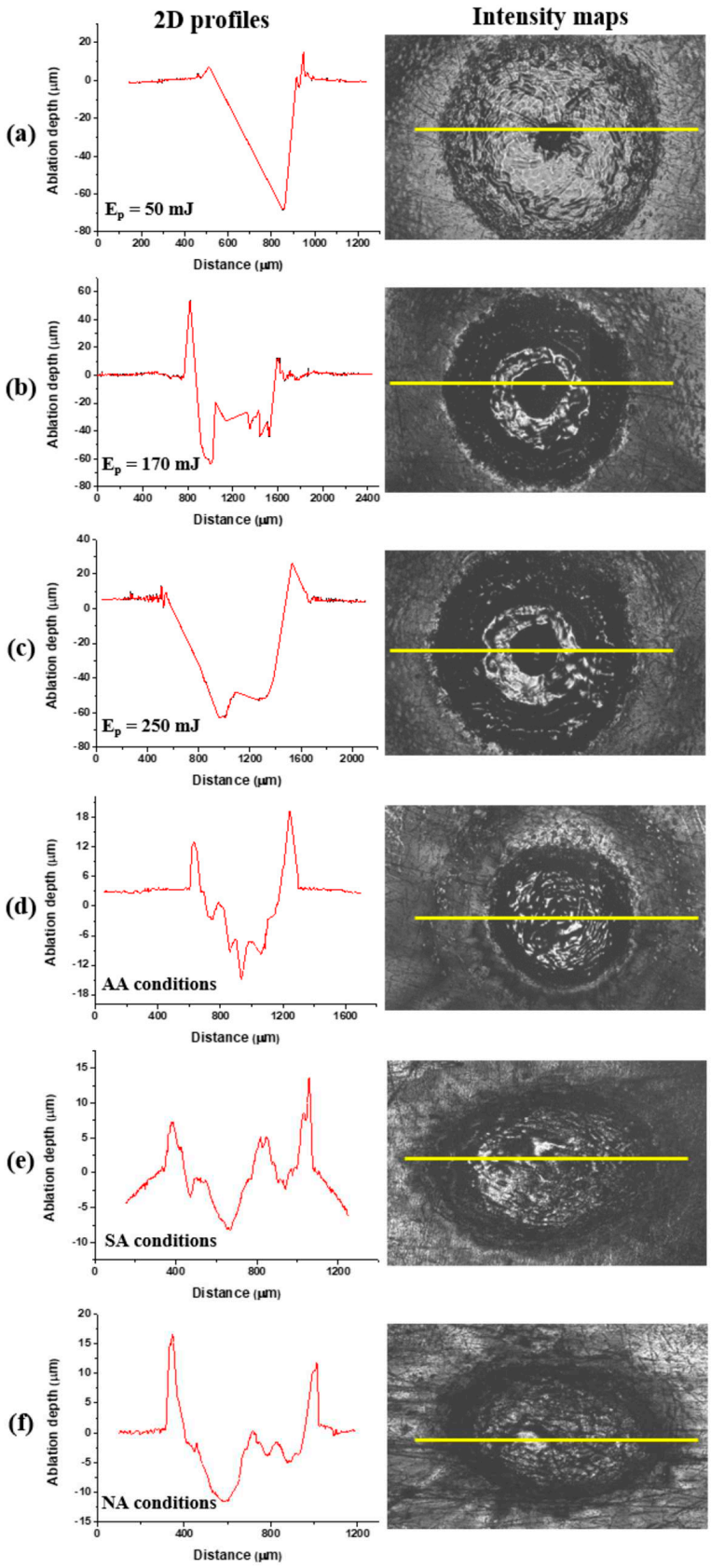

Figure 10. Cross-sectional profiles and intensity maps of the Ti6Al4V surface after laser irradiation at 1064 nm wavelength, pulse duration 5 ns and (**a**–**c**) N_p = 800, argon-rich atmosphere; (**d**–**f**) N_p = 100, E_p = 50 mJ. Yellow lines in the intensity maps indicate the cross-section lines of the 2d profiles.

By plotting the dependence of R_a in relation to the number of accumulated pulses, it can be concluded that at $N_p \leq 10$, R_a does not exceed the value of ~3 μm. By increasing the pulse count up to 2000 accumulated pulses at the lowest fluences, the R_a values in air at 19.1 J cm^{-2} fluence and a nitrogen-rich atmosphere at 16.3 J cm^{-2} fluence are similar and amount to ~13 μm, while, in an argon-rich atmosphere at 17.0 J cm^{-2} fluence, R_a amounts to ~6.8 μm. Roughness is more pronounced at higher fluences, where the R_a value of ~32.8 μm is the highest in the argon-rich atmosphere at 84.9 J cm^{-2} fluence. In general, in the presented experimental conditions, the surface roughness is similar in air and a nitrogen-rich atmosphere as opposed to an argon-rich atmosphere. Again, it is concluded that the argon-rich atmosphere, at 17.0 J cm^{-2} fluence, is the most suitable for the controlled production of a clearly defined crater on the surface of the Ti6Al4V alloy, considering that, at this fluence, the average surface roughness of the alloy in the argon-rich atmosphere has the lowest value. This can be confirmed by the diagram in Figure 9c, where the value of the R_a parameter does not increase but reaches saturation after 10 accumulated pulses.

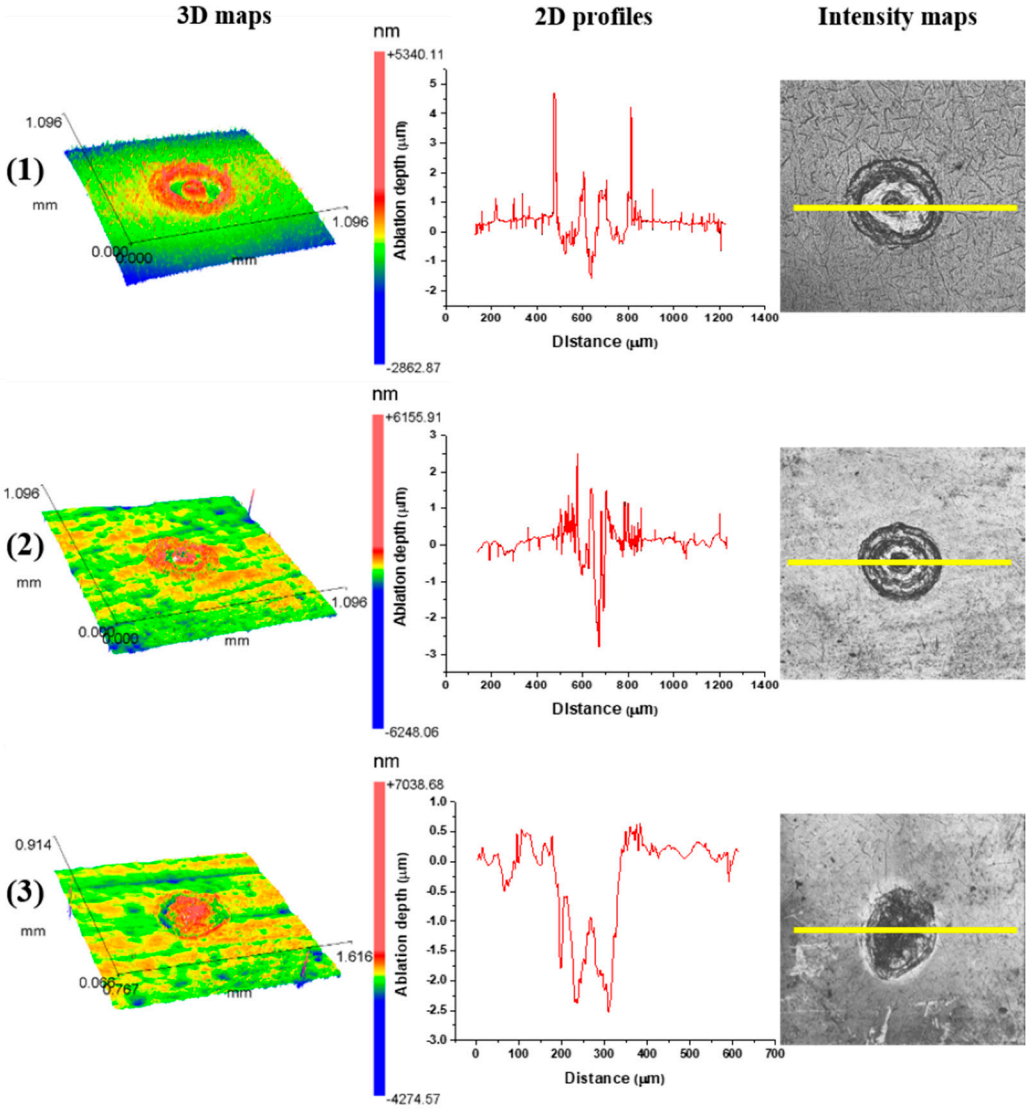

Figure 11. Cross-sectional profiles, three-dimensional representations and intensity maps of the Ti6Al4V surface after laser irradiation at 1064 nm, pulse duration 150 ps, pulse energy 6 mJ and pulse count 10 in (**1**) air and (**2**) argon-rich and (**3**) nitrogen-rich ambient conditions. Yellow lines in the intensity maps indicate the cross-section lines of the 2d profiles.

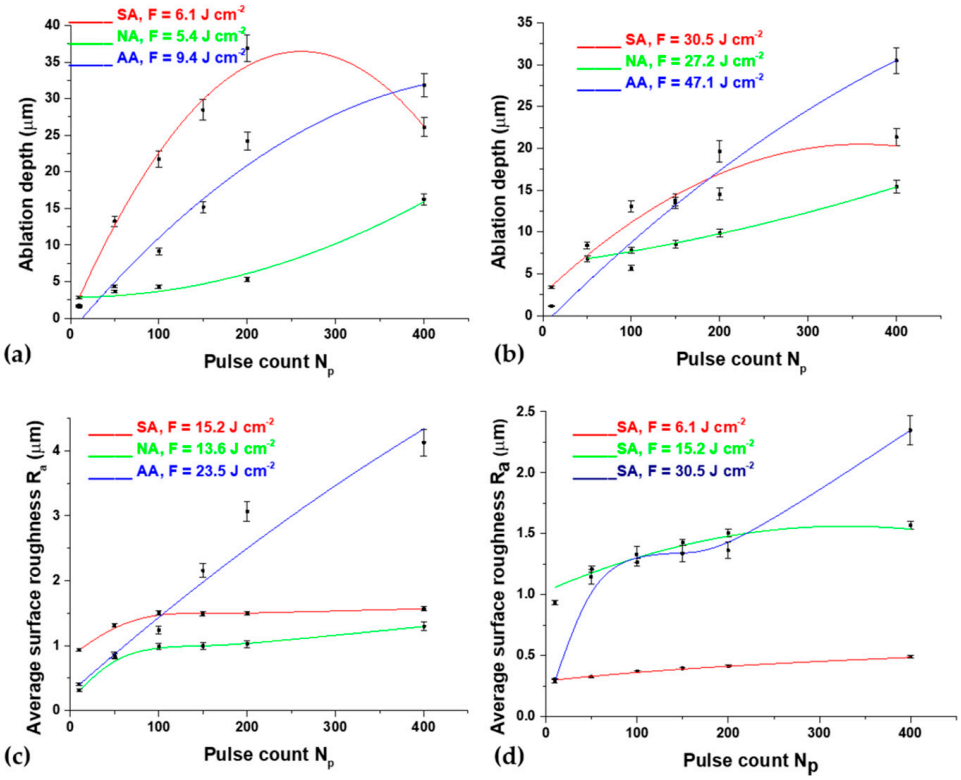

Figure 12. Picosecond irradiation of Ti6Al4V at a 1064 nm wavelength and 150 ps pulse duration—diagrams of surface parameters' dependence on pulse count, N_p, in different experimental conditions: (**a**) ablation depth at 6 mJ pulse energy, (**b**) ablation depth at 30 mJ pulse energy, (**c**) average surface roughness, R_a, at 15 mJ pulse energy and (**d**) average surface roughness, R_a, at different fluences, in standard atmospheric conditions.

The dependence of the ablation depth in relation to the number of accumulated pulses in different ambient conditions under the action of a laser beam of energy 50 mJ is presented in Figure 9d. At a pulse count below 10, the ablation depth is relatively low with an average value of ~2–4 μm in air and nitrogen-rich atmospheres. In an argon-rich atmosphere at 17.0 J cm^{-2} fluence with 10 accumulated pulses, there is an increase in the value of the ablation depth up to ~9 μm (Figure 9d). After 10 accumulated pulses, at 84.9 J cm^{-2} fluence, the value of the ablation depth significantly increases and reaches values up to ~67.6 μm with 2000 accumulated pulses (Figure 9e) in an argon-rich atmosphere, which is also verified by the cross-section profile in Figure 10c. In air, the lowest values of ablation depth are at the lowest values of pulse energy density, 19.1 J cm^{-2} and 64.9 J cm^{-2}, while, at the highest value of energy density of 95.5 J cm^{-2}, the ablation depth is similar to that in a nitrogen-rich atmosphere and is ~30 μm. After 2000 accumulated pulses, the ablation depth values generally reach saturation (Figure 9d). It can be noted that effective ablation of the Ti6Al4V alloy surface is achieved after nanosecond laser irradiation with a wavelength of 1064 nm and a pulse duration of 5 ns at all investigated fluences in an argon-rich atmosphere (Figure 9e).

The dependence of ablation speed on an increase in the applied pulses with 170 mJ energy under different ambient conditions is shown in Figure 9f. With an increase in the number of accumulated pulses, the values of the ablation rates drop sharply to N_p = 100. In an argon-rich atmosphere, at lower values of pulse energy density and at a small number of accumulated pulses, the ablation rate has the highest value with a 2.37 μm pulse^{-1}. That value decreases by a factor of three after 10 accumulated pulses. In air and a nitrogen-rich atmosphere, the values of ablation rates at a low number of accumulated pulses are, on average, 0.25–0.40 μm pulse^{-1} and decrease with an increase in the number of applied pulses by a factor of 2–3. At higher values of pulse energy density, in air and an argon-rich

atmosphere, ablation rate values are similar and, on average, 1.10–1.29 μm pulse^{-1} (Figure 9f). With N_p > 100, the values of the ablation rates reach saturation below ~0.03 μm pulse^{-1}. These results are in agreement with the results for the value of the ablation depth and with the SEM analysis, so it can be concluded that, under the presented experimental conditions, the ablation effect for Ti6Al4V alloy is the most dominant in an argon-rich atmosphere.

The dependence of the ablation depth achieved on the surface of the Ti6Al4V alloy by 150 ps laser pulses at a 1064 nm wavelength is presented in Figures 11 and 12a,b. It is notable that the highest ablation depth value, about 36 μm, is obtained in the air at 6.1 J cm^{-2} fluence and 200 accumulated pulses (Figure 12a). In general, the average lowest values of ablation depth are obtained in the nitrogen-rich atmosphere (Figure 12a,b). The highest achieved depth value in the nitrogen-rich atmosphere is about 15 μm at an energy density value of 5.4 J cm^{-2} with 400 accumulated pulses (Figure 12a). With a pulse count up to 50, the average value of the ablation depth is ~5 μm, and the value of the ablation depth increases with a further increase in pulse count. From 50 to 200 accumulated pulses, the tendency of the ablation depth value to increase is prominent, especially in air and argon-rich atmospheres. After 400 accumulated pulses, the values of ablation depth either decrease or saturate, probably due to excessive melting of the material inside the target and its redistribution, e.g., the inability to expel the molten material from the surface of the modified areas (Figure 12a). In air, the maximum value of ablation depth at a 200 pulse count decreases to ~25 μm at a 400 pulse count. However, from a comparison of the SEM and the ablation depth values, it can be concluded that the most ideal crater formation is achieved in an argon-rich atmosphere.

After picosecond laser action in an argon-rich atmosphere, the highest value of average surface roughness R_a, 4.13 μm, is achieved with 400 accumulated pulses at 23.5 J cm^{-2} fluence (Figure 12c). This is in agreement with SEM, where it is noted that the most pronounced surface effects are obtained in an argon-rich atmosphere. Up to 100 accumulated pulses, R_a values are relatively low and amount to ~1.5 μm (Figure 12c). After increasing pulse counts up to 400, at 13.6 J cm^{-2} fluence, the lowest R_a value, 1.98 μm, is obtained in a nitrogen-rich atmosphere, and the highest value is achieved in an argon-rich atmosphere. The dependence of R_a on the pulse count at different fluences in air is presented in Figure 12d. Modification in air up to 100 accumulated laser pulses at lower fluences is characterized by a slight increase in the R_a value and a prominent increase in R_a at 30.5 J cm^{-2} fluence. With a further increase in the pulse count at 6.1 and 15.2 J cm^{-2} fluence values, R_a subsequently reaches a plateau at 0.5 and 1.5 μm due to the flattening of the molten pool of material, but, after 200 pulses at 30.5 J cm^{-2} fluence, average surface roughness increases up to 2.4 μm.

3.4. Chemical Analysis

Estimation of changes in elemental composition influenced by TEA CO_2 nanosecond and Nd:YAG picosecond laser interaction with the Ti6Al4V surface under three different ambient conditions was performed with EDS and LIBS techniques.

The EDS spectrum of the alloy before modification, selected spectra after nanosecond laser irradiation of the surface and corresponding measurement locations are presented in Figure 13. EDS analysis was performed at several locations on each irradiated target, including the center and periphery of the target, and the results are presented as weight percentages of the elements (Table 3).

In air, at 3.9 J cm^{-2} fluence, there is an expected detection of Ti, Al and V, which represent constituents of the Ti6Al4 alloy, but also the detection of oxygen, which indicates the formation of oxides on the surface of the alloy. However, in a nitrogen-rich atmosphere, at 6.2 J cm^{-2} fluence, a much larger number of applied pulses is needed to form nitride compounds, so, at 400 accumulated pulses, no nitrogen is detected, while, at 2000 pulses, nitrogen appears both in the center and on the periphery of the modified target, at 12.63 and 9.89 weight percent, respectively (Table 3). In an argon-rich atmosphere,

at 6.2 J cm^{-2} fluence, oxygen was detected in the amounts of 35.04 and 38.14 percent by weight in the center of the target and on the periphery, respectively (Table 3).

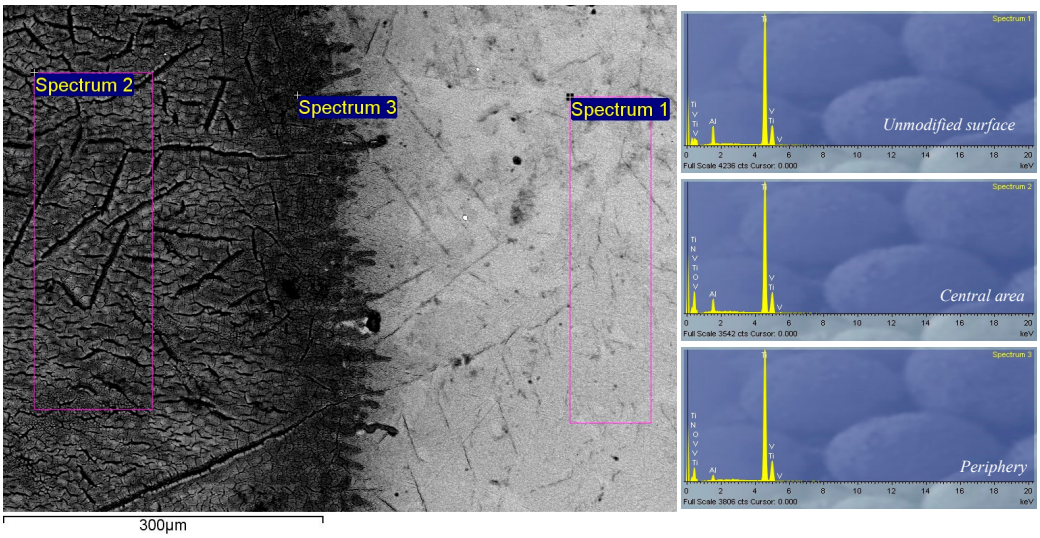

Figure 13. Locations and EDS spectra of unmodified and nanosecond-laser-modified Ti6Al4V surface in a nitrogen-rich atmosphere; E_p = 175 mJ, N_p = 2000. Locations of EDS-recorded spectra: spectrum 1—unmodified surface; spectrum 2—central area; spectrum 3—periphery.

Table 3. EDS analysis of the Ti6Al4V surface before and after nanosecond laser irradiation in different experimental conditions.

Environmental Conditions	Irradiation Conditions	Location	N	O	wt% Al	Ti	V
	Unmodified				5.6 ± 0.26	90.9 ± 0.78	3.5 ± 0.22
SA	F = 6.2 J cm^{-2} N_p = 100	center		10.4 ± 0.81	4.8 ± 0.13	82.2 ± 0.74	2.6 ± 0.21
NA	F = 6.2 J cm^{-2}	center		34.2 ± 0.94	3.6 ± 0.13	59.5 ± 0.88	2.7 ± 0.19
	N_p = 400	periphery		38.9 ± 0.91	3.8 ± 0.12	55.3 ± 0.85	2.0 ± 0.19
	F = 6.2 J cm^{-2}	center	12.6 ± 0.45	10.0 ± 0.64	3.7 ± 0.15	71.0 ± 0.76	2.7 ± 0.29
	N_p = 2000	periphery	9.9 ± 0.38	11.1 ± 0.68	3.1 ± 0.15	72.7 ± 0.76	3.2 ± 0.33
AA	F = 6.2 J cm^{-2}	center		35.0 ± 0.91	3.6 ± 0.18	58.6 ± 0.69	2.8 ± 0.36
	N_p = 400	periphery		38.1 ± 0.98	3.4 ± 0.14	56.2 ± 0.65	2.3 ± 0.22

The EDS spectrum of the alloy before modification, selected spectra after picosecond laser irradiation of the surface and corresponding measurement locations are presented in Figure 14. EDS analysis was performed at several locations on each irradiated target, including the center and periphery of the target, and the results are presented as weight percentages of the elements (Table 4). At a pulse energy of 15 mJ, in air, irradiation of the alloy leads to oxidation of its surface, in the center as well as on the periphery of the modified area (Table 4).

As the amount of oxygen increased on the surface, the amounts of titanium, aluminum, and vanadium decreased. Given the higher reactivity of titanium compared to aluminum and vanadium, titanium oxides were probably the first to be formed. These oxides have a significant impact on applications in biomedicine in terms of the longevity of an implant because it is known that titanium oxides increase resistance to corrosion [60]. Also, they influence the bioactivity of titanium implants as well as the role of the central layer in combination with hydroxyapatite, exhibiting osteoinductive properties [60].

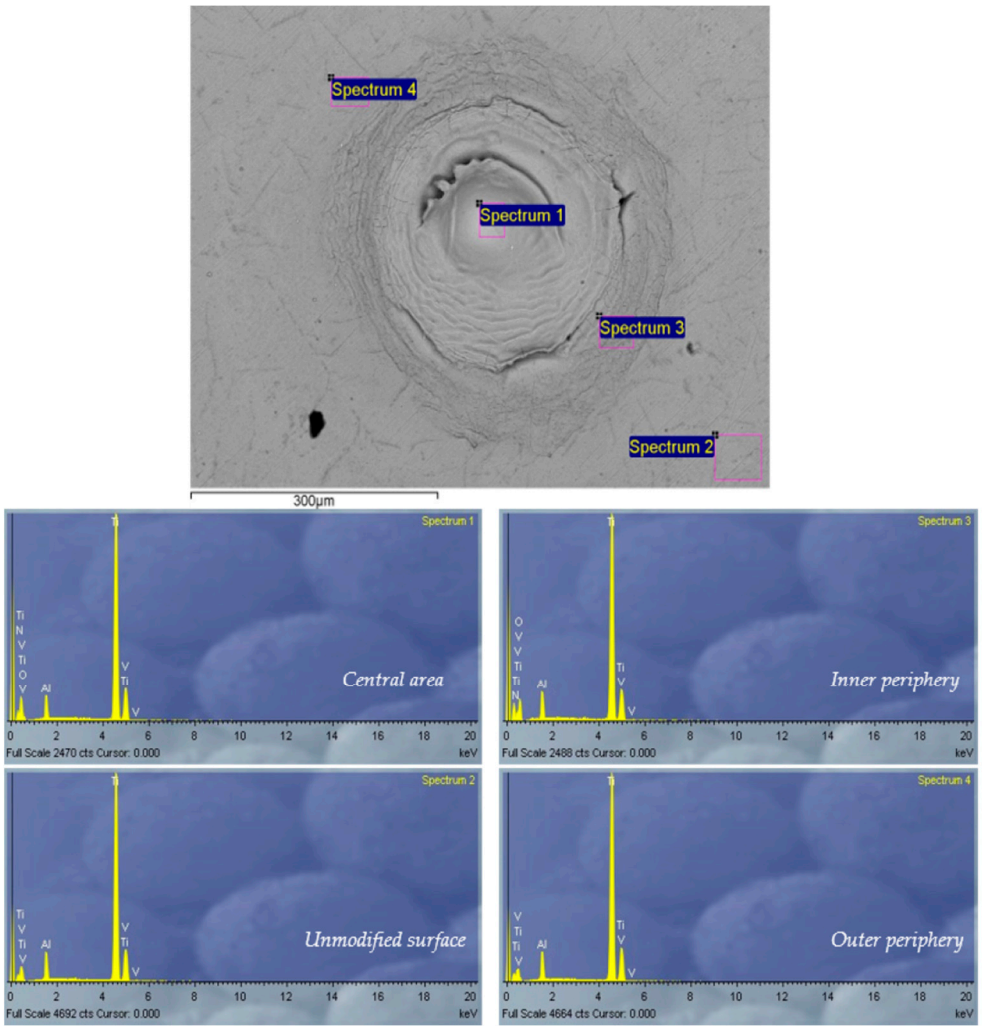

Figure 14. Locations and EDS spectra of unmodified and picosecond-laser-modified Ti6Al4V surface in a nitrogen-rich atmosphere; E_p = 15 mJ, N_p = 100. Locations of EDS-recorded spectra: spectrum 1—central area; spectrum 2—unmodified surface; spectrum 3—inner periphery; spectrum 4—outer periphery.

Table 4. EDS analysis of the Ti6Al4V surface before and after picosecond laser irradiation in different experimental conditions.

Environmental Conditions	Irradiation Conditions	Location	N	O	wt% Al	Ti	V
	Unmodified				5.6 ± 0.25	90.9 ± 0.85	3.5 ± 0.38
SA	F = 15.2 J cm^{-2}	center		18.3 ± 0.64	4.0 ± 0.41	74.7 ± 0.82	3.0 ± 0.33
	N_p = 200	periphery		29.8 ± 0.85	4.0 ± 0.42	63.5 ± 0.74	2.7 ± 0.0.28
NA	F = 13.6 J cm^{-2}	center	13.7 ± 0.44	10.0 ± 0.74	3.7 ± 0.39	69.9 ± 0.75	2.7 ± 0.28
	N_p = 100	periphery	10.6 ± 0.40	18.4 ± 0.66	3.9 ± 0.44	64.4 ± 0.69	2.7 ± 0.29
AA	F = 9.4 J cm^{-2}	center		16.3 ± 0.58	4.1 ± 0.48	76.5 ± 0.72	3.1 ± 0.31
	N_p = 400	periphery		15.7 ± 0.57	4.7 ± 0.51	76.4 ± 0.72	3.2 ± 0.35

Regarding the irradiation of the Ti6Al4V alloy in a nitrogen-rich atmosphere, it is evident that the formation of nitride compounds occurs. After irradiation at every pulse energy value, EDS surface analysis detected nitrogen in the range of an average of 10 wt% at the center and the periphery of the spot area (Table 4), even though its presence could be

expected as the result of laser interaction with the alloy surface in air and in an argon-rich atmosphere. Oxygen is detected on the surface of each irradiated target, but in a smaller percentage due to the increase in nitrogen content. Regarding the irradiation of the Ti6Al4V alloy in an argon-rich atmosphere, no significant changes occur in terms of the formation of compounds other than oxides. The share of oxygen ranges up to ~20 wt% at each pulse energy value (Table 4).

Analysis of the plasma formed during the interaction of the picosecond laser beam with the Ti6Al4V surface was performed using LIBS. The spectra for the Ti6Al4V alloy obtained after irradiation with a picosecond Nd:YAG laser with air, argon and nitrogen as the surrounding gases are presented in Figure 15. It can be concluded that the induced plasma is hot and dense due to the dominance of the ion lines of the constituent elements of the alloy. As for the emission of elements of the surrounding atmosphere, in all the presented results, the spectral lines of the elements are practically absent, which could indicate that the experimental conditions, primarily the position of the laser focus in relation to the target, favored the emission of metal elements from the sample target.

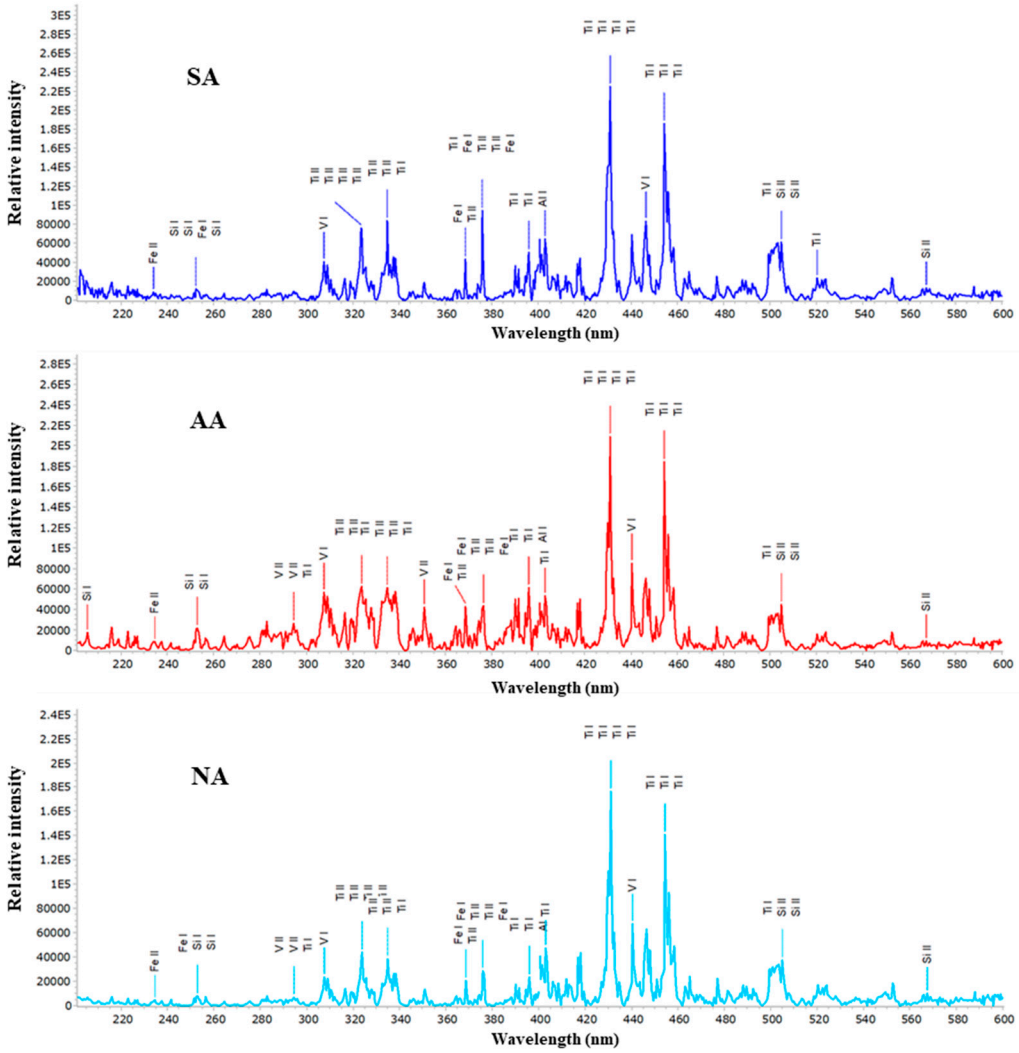

Figure 15. LIBS spectra of the Ti6Al4V alloy obtained by irradiation with a picosecond Nd:YAG laser in different atmospheres at atmospheric pressure.

The preferred surface feature resulting from laser/material interaction depends on the intended application of the material. For example, the modification can be (i) crater formation, favorable for lubricating the surface to reduce friction; (ii) nitride/oxide formation as

a protective layer; or (iii) formation of periodic surface structures and increased roughness, which can increase the biocompatibility of an implant material's surface.

3.5. Process Optimization for Nanosecond Laser Modification

Exploring the impact of process control parameters on output responses has been undertaken within the context of laser modification (1064 nm wavelength, 5 ns pulse duration) under different environmental conditions, which have been determined to yield the most precise modification and efficient ablation. This determination is based on the analysis provided in this paper (Sections 3.2 and 3.3). Tables 5–7 display the experimental outcomes obtained under different atmospheres. Each response was subjected to three measurements (resulting in a sample size of three), and the tables present the average values derived from these measurements.

Table 5. Experimental results for standard atmospheric conditions.

Exp. Trial No.	Process Variables		Responses						
	E_p (mJ)	N_p	R_a (µm)	*rms* (µm)	*PV* (µm)	*Kr*	*DA* (µm)	*VA* (µm pulse^{-1})	*C*
1	50	1	1.23	6.52	0.22	0	0.71	0.710	0.89
2	50	5	1.66	13.71	0.95	0	1.02	0.204	0.89
3	50	10	1.15	59.60	1.65	0	1.68	0.168	0.90
4	50	100	3.11	27.09	4.17	1	8.12	0.081	0.91
5	50	800	6.51	67.59	8.05	1	15.69	0.020	0.93
6	50	2000	13.08	65.58	12.73	1	30.35	0.015	0.92
7	170	1	0.93	35.89	1.15	0	1.29	1.290	0.84
8	170	5	1.01	19.56	1.35	0	2.06	0.412	0.84
9	170	10	1.48	23.41	2.02	0	3.69	0.369	0.90
10	170	100	2.27	23.62	2.89	0	4.91	0.049	0.94
11	170	800	4.42	40.22	5.14	0	13.46	0.017	0.91
12	170	2000	7.84	154.95	9.11	0	20.44	0.010	0.90
13	250	1	1.64	8.21	0.21	0	0.66	0.660	0.86
14	250	5	1.87	54.04	0.21	0	1.07	0.214	0.86
15	250	10	2.29	25.34	0.19	0	3.23	0.323	0.85
16	250	100	5.15	65.24	0.33	1	17.23	0.172	0.80
17	250	800	5.00	116.92	4.72	1	21.19	0.026	0.80
18	250	2000	6.30	113.94	8.03	1	32.27	0.016	0.80

Table 6. Experimental results for an argon-rich atmosphere.

Exp. Trial No.	Process Variables		Responses						
	E_p (mJ)	N_p	R_a (µm)	*rms* (µm)	*PV* (µm)	*Kr*	*DA* (µm)	*VA* (µm pulse^{-1})	*C*
1	50	1	0.35	4.42	0.20	0	2.37	2.370	0.93
2	50	5	0.59	5.81	0.17	0	3.98	0.796	0.93
3	50	10	0.99	7.56	0.20	0	8.97	0.897	0.96
4	50	100	5.83	43.89	0.64	0	14.84	0.148	0.96
5	50	800	6.18	136.43	5.95	1	67.96	0.085	0.86
6	50	2000	6.81	92.42	13.97	1	67.01	0.034	0.90
7	170	1	0.27	3.85	1.15	0	1.12	1.120	0.93
8	170	5	0.47	20.40	0.78	0	1.22	0.244	0.93
9	170	10	0.81	23.11	1.31	0	2.62	0.262	0.97
10	170	100	6.64	68.05	9.14	0	27.93	0.279	0.94
11	170	800	20.40	145.76	21.02	1	51.01	0.064	0.95
12	170	2000	23.40	158.31	36.98	1	63.42	0.032	0.88
13	250	1	0.52	37.85	4.11	0	1.06	1.060	0.88
14	250	5	0.89	25.37	0.89	0	1.27	0.254	0.88

Table 6. *Cont.*

Exp. Trial No.	Process Variables		Responses						
	E_p (mJ)	N_p	R_a (µm)	*rms* (µm)	*PV* (µm)	*Kr*	*DA* (µm)	*VA* (µm pulse^{-1})	*C*
15	250	10	3.03	28.71	1.51	0	2.02	0.202	0.93
16	250	100	6.27	63.22	8.92	1	20.74	0.207	0.93
17	250	800	12.90	107.92	17.02	1	63.01	0.079	0.93
18	250	2000	32.80	219.95	35.81	1	67.61	0.034	0.91

Table 7. Experimental results for a nitrogen-rich atmosphere.

Exp. Trial No.	Process Variables		Responses						
	E_p (mJ)	N_p	*Ra* (µm)	*rms* (µm)	*PV* (µm)	*Kr*	*DA* (µm)	*VA* (µm pulse^{-1})	*C*
1	50	1	0.57	14.48	0.20	0	0.21	0.210	0.83
2	50	5	0.67	9.65	0.21	0	2.30	0.460	0.83
3	50	10	1.25	30.22	0.20	0	4.64	0.464	0.91
4	50	100	2.97	44.51	0.22	0	11.62	0.116	0.90
5	50	800	8.48	83.97	8.32	1	49.47	0.062	0.79
6	50	2000	13.40	92.39	17.63	1	65.98	0.033	0.82
7	170	1	1.44	8.43	0.23	0	0.54	0.540	0.86
8	170	5	2.25	21.43	0.25	0	1.81	0.362	0.86
9	170	10	2.88	11.44	0.19	0	6.45	0.645	0.91
10	170	100	2.71	20.04	0.21	0	12.56	0.126	0.94
11	170	800	4.27	144.18	7.08	1	33.92	0.042	0.88
12	170	2000	7.05	136.94	10.01	1	38.73	0.019	0.90
13	250	1	0.27	9.03	0.15	0	1.04	1.040	0.87
14	250	5	0.79	19.53	0.16	0	2.09	0.418	0.87
15	250	10	1.24	28.38	0.18	0	3.57	0.357	0.86
16	250	100	2.33	21.81	0.23	1	11.78	0.118	0.81
17	250	800	3.67	122.02	4.58	1	16.69	0.021	0.92
18	250	2000	7.55	136.01	8.41	1	29.39	0.015	0.92

The optimization procedure is motivated by the quality loss (QL) function, proposed by G. Taguchi, which stipulates the user's dissatisfaction when utilizing a product whose feature (response) diverges from the target value. This consideration becomes more complex when a product is defined by multiple responses, so the relative significance of each response for the users can be expressed by its QL value, without imposing any subjective weights. QL estimation implies the signal-to-noise ratio, simultaneously including both the response mean and the variation. Three types of responses are suggested by G. Taguchi [61]: nominally the best (NTB), whose goal is to reach a nominal (target) value; the smaller the better (STB), aiming to minimize the response value; and the larger the better (LTB), focused on maximizing the response value.

For the considered process, the response *Kr* belongs to the NTB type, and the remaining ones belong to the LTB type. Depending on the application, for instance, the micro-lubrication of tools, the goal value for response crater occurrence (*Kr*) is a nominal value of 1 and a circularity (*C*) value near 1, which means that a circular-shaped crater is formed. In the case of micro-patterning for increased biocompatibility or a more developed surface, responses related to surface roughness, such as R_a, *rms*, and *PV* should be as high as possible. The computed QL values for the seven responses are normalized (NQL $\in$ [0, 1]) (Tables 8–10). Aiming to scrutinize the interdependencies among the response NQLs, principal component analysis (PCA) is applied to identify a set of uncorrelated components (j—the principal component number, k—the experimental trial number, i—the response number, V_{ij}—the eigenvector's elements) [62]:

$$Y_k = \sum_{i=1}^{p} NQL_i(k)V_{ij} \quad (4)$$

Table 8. Results of experimental data processing for standard atmospheric conditions.

Exp. Trial No.	Normalized Quality Losses (NQLs)							Principal Component Scores							Process Index
	NQL *Ra*	NQL *rms*	NQL *PV*	NQL *Kr*	NQL *DA*	NQL *VA*	NQL *C*	Y1	Y2	Y3	Y4	Y5	Y6	Y7	
1	0.570	1.000	0.754	1.000	0.864	0.000	0.302	1.803	−0.094	0.159	−0.616	−0.061	−0.141	0.202	0.5697
2	0.310	0.225	0.040	1.000	0.418	0.001	0.302	0.816	−0.307	−0.258	−0.586	0.062	−0.490	−0.010	0.5898
3	0.652	0.010	0.013	1.000	0.154	0.002	0.254	0.679	−0.432	−0.608	−0.648	0.141	−0.234	0.045	0.5420
4	0.085	0.056	0.002	0.000	0.006	0.008	0.175	0.057	0.107	−0.074	−0.111	−0.079	−0.004	0.047	0.9190
5	0.015	0.008	0.000	0.000	0.001	0.141	0.055	−0.032	−0.010	0.045	−0.126	−0.057	0.030	0.004	0.9785
6	0.000	0.008	0.000	0.000	0.000	0.254	0.114	−0.066	−0.004	0.093	−0.232	−0.096	0.036	0.007	0.9273
7	1.000	0.031	0.027	1.000	0.261	0.000	0.665	0.869	−0.197	−0.902	−0.935	−0.048	−0.166	0.017	0.5403
8	0.848	0.110	0.019	1.000	0.102	0.000	0.665	0.767	−0.176	−0.814	−0.900	−0.002	−0.237	0.184	0.5628
9	0.392	0.076	0.009	1.000	0.032	0.000	0.237	0.556	−0.400	−0.441	−0.585	0.215	−0.365	0.175	0.5706
10	0.164	0.075	0.004	1.000	0.018	0.023	0.000	0.463	−0.534	−0.228	−0.427	0.309	−0.421	0.162	0.6084
11	0.039	0.025	0.001	1.000	0.002	0.196	0.175	0.339	−0.447	−0.128	−0.629	0.289	−0.488	0.149	0.6567
12	0.009	0.000	0.000	1.000	0.001	1.000	0.237	0.097	−0.665	0.243	−1.197	0.065	−0.305	0.113	0.6990
13	0.318	0.630	0.829	1.000	1.000	0.000	0.513	1.638	0.126	0.210	−0.761	0.146	−0.296	−0.119	0.5393
14	0.244	0.013	0.829	1.000	0.380	0.001	0.513	0.986	0.096	−0.078	−0.853	0.633	−0.182	−0.057	0.6084
15	0.161	0.065	1.000	1.000	0.041	0.000	0.585	0.873	0.201	−0.044	−0.904	0.822	−0.116	0.244	0.5976
16	0.028	0.008	0.330	0.000	0.001	0.002	1.000	0.140	0.807	−0.147	−0.628	0.026	−0.107	0.107	0.7245
17	0.030	0.001	0.001	0.000	0.001	0.113	1.000	−0.025	0.666	−0.209	−0.651	−0.202	−0.233	0.080	0.7419
18	0.017	0.002	0.000	0.000	0.000	0.245	1.000	−0.066	0.624	−0.139	−0.736	−0.238	−0.206	0.076	0.7359

Table 9. Results of experimental data processing for an argon-rich atmosphere.

Exp. Trial No.	Normalized Quality Losses (NQLs)							Principal Component Scores							Process Index
	NQL *Ra*	NQL *rms*	NQL *PV*	NQL *Kr*	NQL *DA*	NQL *VA*	NQL *C*	Y1	Y2	Y3	Y4	Y5	Y6	Y7	
1	0.613	0.759	0.717	1.000	0.206	0.000	0.303	1.294	−0.068	−0.457	−0.566	0.444	0.440	0.040	0.5164
2	0.220	0.439	1.000	1.000	0.071	0.001	0.303	1.001	0.247	−0.282	−0.898	0.545	0.305	0.025	0.5080
3	0.075	0.259	0.717	1.000	0.014	0.001	0.037	0.805	0.340	−0.008	−0.611	0.590	0.323	0.008	0.5998
4	0.002	0.007	0.069	1.000	0.005	0.044	0.087	0.443	0.025	0.325	−0.293	0.574	0.541	0.054	0.6903
5	0.002	0.000	0.001	0.000	0.000	0.134	1.000	−0.246	−0.600	−0.266	−0.649	−0.098	0.306	0.055	0.6573
6	0.001	0.001	0.000	0.000	0.000	1.000	0.557	−0.489	−0.443	−0.635	−0.214	0.625	0.189	0.019	0.5685
7	1.000	1.000	0.021	1.000	0.894	0.001	0.283	1.615	−0.893	−0.332	0.020	0.441	0.392	−0.102	0.4383
8	0.324	0.035	0.046	1.000	0.753	0.016	0.283	0.818	−0.625	0.347	−0.324	0.659	0.178	0.060	0.4977
9	0.110	0.027	0.016	1.000	0.171	0.014	0.000	0.571	−0.073	0.364	−0.175	0.589	0.445	0.061	0.6484
10	0.002	0.003	0.000	1.000	0.001	0.012	0.259	0.398	−0.102	0.332	−0.372	0.508	0.623	0.060	0.6693
11	0.000	0.000	0.000	0.000	0.000	0.239	0.129	−0.116	−0.103	−0.151	−0.048	0.150	0.044	0.004	0.8766
12	0.000	0.000	0.000	0.000	0.000	0.956	0.759	−0.513	−0.555	−0.650	−0.356	0.554	0.249	0.031	0.5368
13	0.267	0.010	0.002	1.000	1.000	0.001	0.795	0.754	−1.076	0.354	−0.663	0.611	0.197	−0.010	0.4622
14	0.091	0.023	0.035	1.000	0.696	0.015	0.795	0.581	−0.835	0.324	−0.728	0.566	0.365	−0.054	0.5064
15	0.008	0.018	0.012	1.000	0.280	0.023	0.313	0.488	−0.297	0.362	−0.411	0.571	0.473	−0.020	0.5936
16	0.002	0.003	0.000	0.000	0.002	0.022	0.312	−0.066	−0.187	−0.075	−0.205	−0.045	0.095	0.016	0.8910
17	0.000	0.001	0.000	0.000	0.000	0.154	0.343	−0.125	−0.218	−0.149	−0.205	0.046	0.107	0.017	0.8289
18	0.000	0.000	0.000	0.000	0.000	0.856	0.464	−0.417	−0.371	−0.540	−0.175	0.538	0.158	0.016	0.6105

Table 10. Results of experimental data processing for a nitrogen-rich atmosphere.

Exp. Trial No.	Normalized Quality Losses (NQLs)							Principal Component Scores							Process Index
	NQL *Ra*	NQL *rms*	NQL *PV*	NQL *Kr*	NQL *DA*	NQL *VA*	NQL *C*	Y1	Y2	Y3	Y4	Y5	Y6	Y7	
1	0.222	0.336	0.568	1.000	1.000	0.004	0.653	1.212	0.602	0.178	−0.713	0.022	−0.650	0.340	0.4691
2	0.161	0.762	0.501	1.000	0.008	0.001	0.653	1.154	0.190	−0.028	0.162	0.451	−0.733	0.386	0.5817
3	0.046	0.075	0.568	1.000	0.002	0.001	0.196	0.827	−0.187	−0.294	−0.164	−0.061	−0.629	0.371	0.5857
4	0.008	0.033	0.480	1.000	0.000	0.014	0.205	0.745	−0.166	−0.316	−0.183	−0.045	−0.613	0.424	0.5993
5	0.001	0.007	0.000	0.000	0.000	0.051	1.000	0.037	0.800	−0.022	0.329	−0.010	−0.475	0.165	0.7956
6	0.000	0.005	0.000	0.000	0.000	0.186	0.747	−0.031	0.561	0.067	0.227	0.006	−0.451	0.137	0.8085
7	0.034	1.000	0.412	1.000	0.159	0.000	0.464	1.181	0.121	0.030	−0.015	0.730	−0.609	0.311	0.6228
8	0.014	0.152	0.348	1.000	0.013	0.001	0.464	0.753	0.077	−0.281	−0.079	0.087	−0.649	0.521	0.6395
9	0.008	0.541	0.605	1.000	0.001	0.000	0.169	1.028	−0.218	−0.178	−0.087	0.318	−0.618	0.244	0.5665
10	0.009	0.174	0.501	1.000	0.000	0.012	0.000	0.806	−0.337	−0.264	−0.221	0.064	−0.523	0.351	0.5601
11	0.004	0.000	0.000	0.000	0.000	0.112	0.322	−0.025	0.234	0.048	0.095	0.002	−0.214	0.063	0.8949
12	0.001	0.000	0.000	0.000	0.000	0.540	0.202	−0.206	0.029	0.297	0.000	0.045	−0.438	0.080	0.8236
13	1.000	0.872	1.000	1.000	0.040	0.000	0.403	1.751	−0.128	0.510	0.347	−0.020	−0.625	0.267	0.4816
14	0.116	0.183	0.875	1.000	0.010	0.001	0.403	1.067	−0.075	−0.255	−0.054	−0.118	−0.837	0.218	0.6059
15	0.047	0.085	0.687	1.000	0.003	0.001	0.493	0.909	0.033	−0.317	−0.062	−0.101	−0.815	0.345	0.6305
16	0.013	0.146	0.417	0.000	0.000	0.014	0.795	0.318	0.565	−0.022	0.301	−0.049	−0.541	−0.146	0.6964
17	0.005	0.001	0.001	0.000	0.000	0.447	0.134	−0.170	−0.004	0.251	−0.010	0.036	−0.348	0.062	0.8565
18	0.001	0.000	0.000	0.000	0.000	1.000	0.140	−0.395	−0.136	0.562	−0.078	0.088	−0.709	0.111	0.6754

The principal components (Tables 8–10) present input for grey relational analysis (GRA) that transforms them into the grey relational coefficient ε_j (k), and, finally, develops a single process performance index—the gray relational grade (γ_k) [62]:

$$\gamma_k = \sum_{j=1}^{p} \omega_j \varepsilon_j(k) \quad (5)$$

The ultimate process indexes ($\gamma_k \in [0, 1]$) for different atmospheric conditions are listed in Tables 8–10. The γ_k values are enumerated using the response weights from PCA (w_j): (i) for the standard atmospheric conditions: 0.425, 0.189, 0.165, 0.106, 0.081, 0.020, 0.014; (ii) for the argon-rich atmosphere: 0.462, 0.216, 0.160, 0.093, 0.049, 0.018, 0.002; and (iii) for the nitrogen-rich atmosphere: 0.459, 0.185, 0.133, 0.121, 0.065, 0.026, 0.011. Therefore, all principal components are entailed in an entirely objective manner to encapsulate the total response variance. The details of the suggested process optimization procedure are given in [62], and its implementation in [26].

The optimal process variables (parameter values) are the ones that boost the process performance index. As presented in Table 8, for standard atmospheric conditions, the optimal process variables are E_p = 50 and N_p = 800, resulting in an excellent process index (0.9785). The settings E_p = 50 and N_p = 800 (process index = 0.9273) and E_p = 50 and N_p = 100 (process index = 0.9190) are also favorable since they produce high process performance. From Table 9, for the argon-rich atmosphere, the optimal process setting is E_p = 250 and N_p = 100, delivering a good process index (0.8910). The setting E_p = 170 and N_p = 800 is also favorable for reaching satisfactory process performance (process index = 0.8766). For the nitrogen-rich atmosphere (Table 10) the optimal process setting is E_p = 170 and N_p = 800, producing good process performance (process index = 0.8949). In addition, the setting E_p = 250 and N_p = 800 is also acceptable in terms of generating relatively good process performance (process index = 0.8565). Overall, it is evident that the optimal setting for the standard atmosphere (air) is the most beneficial since it achieves a very high process performance, while the optimal parameters for the argon- and nitrogen-rich atmospheres provide similar, satisfactorily high levels of process performance.

4. Conclusions

A titanium-based Ti6Al4V alloy surface was modified by laser action in the infrared spectral region in various conditions: 10.6 μm and 1064 nm wavelengths, nanosecond (100 ns and 5 ns) and picosecond (150 ps) pulse durations, increasing numbers of accumulated pulses at different values of pulse energy and different ambient conditions: standard air and argon-rich and nitrogen-rich atmospheres. Irradiation of the Ti6Al4V alloy by a TEA CO_2 laser beam at a 100 ns pulse duration, in all three ambient conditions, led to pronounced morphological changes on the surface: increased surface roughness, microcracks, partial formation of granular structures and formation of LIPSS, which is a novelty regarding nanosecond modification with multi-mode laser beams. Surface features on Ti6Al4V after interaction with a nanosecond Gaussian laser beam, a Nd:YAG laser with a 5 ns pulse duration, imply the ablation process is more pronounced, as crater formation is evident after applying a larger number of pulses in all three ambient conditions. In general, the lowest average ablation depth values are obtained in a nitrogen-rich atmosphere. Picosecond laser irradiation of the Ti6Al4V alloy was characterized by crater formation and LIPSS located at the periphery of the modified target at pulse energy values of 6 and 15 mJ in all three ambient conditions. The most pronounced LIPSS structures are formed in a nitrogen-rich atmosphere after 200 accumulated pulses at 5.4 J cm^{-2} fluence. It was noted that the highest ablation depth value achieved, about 36 μm, is obtained after 200 accumulated pulses at 6.1 J cm^{-2} fluence in standard laboratory conditions. The results of the chemical composition investigation imply that titanium nitride is probably formed after laser irradiation in a nitrogen-rich atmosphere under specific experimental conditions. Optimization of the laser parameters was performed for the Nd:YAG laser with

a 5 ns interaction with the alloy surface. The optimum setting for a standard atmosphere (air) is the most useful as it achieves very high process performance, while the optimum parameters for an argon-rich atmosphere and for a nitrogen-rich atmosphere give a similar, satisfactory high, level of process performance. The most accurate and precise modification is achieved when laser/material interaction is performed in an argon-rich atmosphere.

Author Contributions: Conceptualization, D.M. and B.R.; methodology, D.M., S.P. and M.K.; investigation, B.R., D.M., B.S., D.R., T.Š., J.C., Z.S., D.Đ.-M. and M.Č.; formal analysis, B.R., D.M., T.Š. and M.K.; writing—original draft preparation, D.M., B.R. and T.Š.; writing—review and editing, S.P. and M.K.; supervision, D.M. All authors contributed to the interpretation of the results. All authors have read and agreed to the published version of the manuscript.

Funding: This research was funded by the Ministry of Science, Technological Development and Innovation of the Republic of Serbia, grant numbers: 451-03-47/2023-01/200051.

Data Availability Statement: The data presented in this study are available on request from the corresponding author. The data are not publicly available due to institutional policies.

Acknowledgments: This work was supported by the Ministry of Science, Technological Development and Innovation of the Republic of Serbia, grant numbers 451-03-47/2023-01/200024, 451-03-47/2023-01/200146, RS-200017, the Science Fund of the Republic of Serbia, Program PRISMA, Project No. 6706 ASPIRE and the Slovenian Research Agency, Project No. P2-0082.

Conflicts of Interest: The authors declare no conflict of interest.

References

1. Zhu, Y.; Liu, D.; Tian, X.; Tang, H.; Wang, H. Characterization of microstructure and mechanical properties of laser melting deposited Ti-6.5Al-3.5Mo-1.5Zr-0.3Si titanium alloy. *Mater. Des.* **2014**, *56*, 445–453. [CrossRef]
2. Parthasarathy, J.; Starly, B.; Raman, S.; Christensen, A. Mechanical evaluation of porous titanium (Ti6Al4V) structures with electron beam melting (EBM). *J. Mech. Behav. Biomed. Mater.* **2010**, *3*, 249–259. [CrossRef] [PubMed]
3. Zhang, L.C.; Chen, L.Y. A Review on Biomedical Titanium Alloys: Recent Progress and Prospect. *Adv. Eng. Mater.* **2019**, *21*, 1801215. [CrossRef]
4. Wei, Q.; Zhang, Z. A Novel Treatment to Selectively Harden Ti6Al4V Surfaces. *ACS Omega* **2023**, *8*, 24552–24560. [CrossRef] [PubMed]
5. Huang, H.; Zhang, P.; Tang, M.; Shen, L.; Yu, Z.; Shi, H.; Tian, Y. Biocompatibility of micro/nano structures on the surface of Ti6Al4V and Ti-based bulk metallic glasses induced by femtosecond laser. *Biomater. Adv.* **2022**, *139*, 212998. [CrossRef] [PubMed]
6. Shaikh, S.; Kedia, S.; Majumdar, A.G.; Subramanian, M.; Sinha, S. 45S5 bioactive glass coating on Ti6Al4V alloy using pulsed laser deposition technique. *Mater. Res. Express* **2019**, *6*, 125428. [CrossRef]
7. Abe, J.O.; Popoola, A.P.I.; Popoola, O.M. Consolidation of Ti6Al4V alloy and refractory nitride nanoparticles by spark plasma sintering method: Microstructure, mechanical, corrosion and oxidation characteristics. *Mater. Sci. Eng. A* **2020**, *774*, 138920. [CrossRef]
8. Grabowski, A.; Florian, T.; Wieczorek, J.; Adamiak, M. Structuring of the Ti6Al4V alloy surface by pulsed laser remelting. *Appl. Surf. Sci.* **2021**, *535*, 147618. [CrossRef]
9. Grabowski, A.; Sozanska, M.; Adamiak, M.; Kepinska, M.; Florian, T. Laser surface texturing of Ti6Al4V alloy, stainless steel and aluminium silicon alloy. *Appl. Surf. Sci.* **2018**, *461*, 117–123. [CrossRef]
10. Petronić, S.; Čolić, K.; Đorđević, B.; Milovanović, D.; Burzić, M.; Vučetić, F. Effect of laser shock peening with and without protective coating on the microstructure and mechanical properties of Ti-alloy. *Opt. Lasers Eng.* **2020**, *129*, 106052. [CrossRef]
11. Balasubramanian, K.; Bragadeesvaran, S.R.; Ajay Adarsh, S.; Baranitharan, M.; Gokulakrishnan, K. Surface properties of Ti-6Al-4V alloy treated by plasma ion nitriding process. *Mater. Today Proc.* **2021**, *45*, 957–961. [CrossRef]
12. Rajab, F.H.; Liauw, C.M.; Benson, P.S.; Li, L.; Whitehead, K.A. Production of hybrid macro/micro/nano surface structures on Ti6Al4V surfaces by picosecond laser surface texturing and their antifouling characteristics. *Colloids Surf. B* **2017**, *160*, 688–696. [CrossRef] [PubMed]
13. Jelinkova, H.; Šulc, J. Laser characteristics. In *Woodhead Publishing Series in Electronics and Optical Materials, Lasers for Medical Applications*; Jelinkova, H., Ed.; Woodhead Publishing: Cambridge, UK, 2013; pp. 17–46. [CrossRef]
14. Rajčić, B.; Petronić, S.; Čolić, K.; Stević, Z.; Petrović, A.; Mišković, Ž.; Milovanović, D. Laser Processing of Ni-Based Superalloy Surfaces Susceptible to Stress Concentration. *Metals* **2021**, *11*, 750. [CrossRef]
15. Wang, C.; Huang, H.; Qian, Y.; Zhang, Z.; Huang, W.; Yan, J. Nitrogen assisted formation of large-area ripples on Ti6Al4V surface by nanosecond pulse laser irradiation. *Precis. Eng.* **2022**, *73*, 244–256. [CrossRef]
16. Melo-Fonseca, F.; Guimaraes, B.; Gasik, M.; Silva, F.S.; Miranda, G. Experimental analysis and predictive modelling of Ti6Al4V laser surface texturing for biomedical applications. *Surf. Interfaces* **2022**, *35*, 102466. [CrossRef]

17. Liu, Y.; Ding, J.; Qu, W.; Su, Y.; Yu, Z. Microstructure Evolution of TiC Particles In Situ, Synthesized by Laser Cladding. *Materials* **2017**, *10*, 281. [CrossRef]
18. Rajčić, B.; Šibalija, T.; Nikolić, V.; Čekada, M.; Savović, J.; Petronić, S.; Milovanović, D. Structural and Functional Picosecond Laser Modification of the Nimonic 263 Superalloy in Different Environmental Conditions and Optimization of the Irradiation Process. *Materials* **2023**, *16*, 1021. [CrossRef]
19. Wang, C.; Hong, J.; Cui, M.; Huang, H.; Zhang, L.; Yan, Y. The effects of simultaneous laser nitriding and texturing on surface hardness and tribological properties of Ti6Al4V. *Surf. Coat. Technol.* **2022**, *437*, 128358. [CrossRef]
20. Ahmed Obeidi, M.; McCarthy, E.; Brabazon, D. Laser surface processing with controlled nitrogen-argon concentration levels for regulated surface life time. *Opt. Lasers Eng.* **2018**, *102*, 154–160. [CrossRef]
21. Ciganovic, J.; Stasic, J.; Gakovic, B.; Momcilovic, M.; Milovanovic, D.; Bokorov, M.; Trtica, M. Surface modification of the titanium implant using TEA CO_2 laser pulses in controllable gas atmospheres—Comparative study. *Appl. Surf. Sci.* **2012**, *258*, 2741–2748. [CrossRef]
22. Liu, L.H.; Yang, C.; Wang, F.; Qu, S.G.; Li, X.Q.; Zhang, W.W.; Li, Y.Y.; Zhang, L.C. Ultrafine grained Ti-based composites with ultrahigh strength and ductility achieved by equiaxing microstructure. *Mater. Des.* **2015**, *79*, 1–5. [CrossRef]
23. Hahn, D.W.; Omenetto, N. Laser-Induced Breakdown Spectroscopy (LIBS), Part II: Review of Instrumental and Methodological Approaches to Material Analysis and Applications to Different Fields. *Appl. Spectrosc.* **2012**, *66*, 347–419. [CrossRef] [PubMed]
24. Hamad, T.K.; Salloom, H.T. Determination of Species Concentrations of Ti-6Al-4V Titanium Alloys using Calibration Free Laser Induced Breakdown Spectroscopy. *Eur. J. Eng. Technol. Res.* **2018**, *3*, 50–55. [CrossRef]
25. Shrivastava, P.K.; Pandey, A.K. Geometrical quality evaluation in laser cutting of Inconel-718 sheet by using Taguchi based regression analysis and particle swarm optimization. *Infrared Phys. Technol.* **2018**, *89*, 369–380. [CrossRef]
26. Šibalija, T.; Petronić, S.; Milovanović, D. Experimental Optimization of Nimonic 263 Laser Cutting Using a Particle Swarm Approach. *Metals* **2019**, *9*, 1147. [CrossRef]
27. Chaki, S.; Bose, D.; Bathe, R.N. Multi-Objective Optimization of Pulsed Nd:YAG Laser Cutting Process Using Entropy-Based ANN-PSO Model. *Lasers Manuf. Mater.* **2020**, *7*, 88–110. [CrossRef]
28. Read, N.; Wang, W.; Essa, K.; Attallah, M.M. Selective laser melting of AlSi10Mg alloy: Process optimisation and mechanical properties development. *Mater. Des.* **2015**, *65*, 417–424. [CrossRef]
29. Venkatesan, K.; Ramanujam, R. Statistical approach for optimization of influencing parameters in laser assisted machining (LAM) of Inconel alloy. *Measurement* **2016**, *89*, 97–108. [CrossRef]
30. McDonnell, M.D.T.; Arnaldo, D.; Pelletier, E.; Grant-Jacob, J.A.; Praeger, M.; Karnakis, D.; Eason, R.W.; Mills, B. Machine learning for multi-dimensional optimisation and predictive visualisation of laser machining. *J. Intell. Manuf.* **2021**, *32*, 1471–1483. [CrossRef]
31. Šibalija, T.V. Particle swarm optimisation in designing parameters of manufacturing processes: A review (2008–2018). *Appl. Soft. Comput.* **2019**, *84*, 105743. [CrossRef]
32. *ASME B46.1:2019*; International Standard—ASME Surface Texture: Surface Roughness, Waviness, and Lay. American Society of Mechanical Engineers: New York, NY, USA, 2020.
33. *ISO 25178-6:2010*; Geometrical Product Specifications (GPS), Surface Texture: Areal, Part 6: Classification of Methods for Measuring Surface Texture. ISO: London, UK, 2010.
34. Chaudhary, K.; Haider, Z.; Ali, J. Laser-Induced Plasma and its Applications. In *Plasma Science and Technology*, 1st ed.; Mieno, T., Ed.; IntechOpen: London, UK, 2016. [CrossRef]
35. Rai, V.N.; Thakur, S.N. Physics and dynamics of plasma in laser-induced breakdown spectroscopy. In *Laser-Induced Breakdown Spectroscopy*, 2nd ed.; Singh, J.P., Thakur, S.N., Eds.; Elsevier: Amsterdam, The Netherlands, 2020; pp. 71–106. [CrossRef]
36. Poprawe, R. *Tailored Light 2: Laser Application Technology*; Springer: Berlin/Heidelberg, Germany, 2011. [CrossRef]
37. Nolte, S.; Momma, C.; Jacobs, H.; Tunnermann, A.; Chichkov, B.N.; Wellegehausen, B.; Welling, H. Ablation of metals by ultrashort laser pulses. *J. Opt. Soc. Am. B* **1997**, *14*, 2716–2722. [CrossRef]
38. Momma, C.; Nolte, S.; Chickov, B.N.; Alvensleben, F.V.; Tunnermann, A. Precise laser ablation with ultrashort pulses. *Appl. Surf. Sci.* **1997**, *109–110*, 15–19. [CrossRef]
39. Cerami, L.; Mazur, E.; Nolte, S.; Schaffer, C.B. Femtosecond Laser Micromachining. In *Ultrafast Nonlinear Optics*, 1st ed.; Thomson, R., Leburn, C., Reid, D., Eds.; Springer: Berlin/Heidelberg, Germany, 2013; pp. 287–321. [CrossRef]
40. Freese, H.L.; Volas, M.G.; Wood, J.R.; Textor, M. Titanium and its Alloys in Biomedical Engineering. In *Encyclopedia of Materials: Science and Technology*, 2nd ed.; Jurgen Buschow, K.H., Cahn, R.W., Flemings, M.C., Ilschner, B., Kramer, E.J., Mahajan, S., Veyssiere, P., Eds.; Elsevier: Amsterdam, The Netherlands, 2001; pp. 9374–9380. [CrossRef]
41. Boyer, R.; Welsch, G.; Collings, E.W. *Materials Properties Handbook: Titanium Alloys*; ASM International: Novelty, OH, USA, 1994; ISBN 978-0-87170-481-8.
42. Mannion, P.T.; Magee, J.; Coyne, E.; O'Connor, G.M.; Glynn, T.J. The effect of damage accumulation behaviour on ablation thresholds and damage morphology in ultrafast laser micro-machining of common metals in air. *Appl. Surf. Sci.* **2004**, *233*, 275–287. [CrossRef]
43. Brygo, F.; Dutouquet, C.; Le Guern, F.; Oltra, R.; Semerok, A.; Weulersse, J.M. Laser fluence, repetition rate and pulse duration effects on paint ablation. *Appl. Surf. Sci.* **2006**, *252*, 2131–2138. [CrossRef]
44. Prokhorov, A.M. *Laser Heating of Metals*, 1st ed.; CRC Press: Boca Raton, FL, USA, 1990; pp. 1203–1204. [CrossRef]

45. Cheng, J.; Perrie, W.; Sharp, M.; Edwardson, S.P.; Semaltianos, N.G.; Dearden, G.; Watkins, K.G. Single-pulse drilling study of Au, Al and Ti alloy by using a picosecond laser. *Appl. Phys. A* **2009**, *95*, 739–746. [CrossRef]
46. Milovanović, D. Interaction of Picosecond and Nanosecond Pulsed Laser Radiation on Ti6Al4V Alloy Surface. Ph.D. Thesis, University of Belgrade, Belgrade, Serbia, 14 October 2013.
47. Milovanović, D.; Rajčić, B.; Petronić, S.; Radulović, A.; Radak, B.; Gaković, B.; Zamfirescu, M.; Albu, C.; Savović, J. Comprehensive ablation study of near-IR femtosecond laser action on the titanium-based alloy Ti6Al4V: Morphological effects and surface structures at low and high fluences. *Eur. Phys. J. D* **2022**, *76*, 2. [CrossRef]
48. Milovanović, D.S.; Radak, B.B.; Gaković, B.M.; Batani, D.; Momčilović, M.D.; Trtica, M.S. Surface morphology modifications of titanium based implant induced by 40 picosecond laser pulses at 266 nm. *J. Alloys Compd.* **2010**, *501*, 89–92. [CrossRef]
49. Trtica, M.S.; Radak, B.B.; Gaković, B.M.; Milovanović, D.S.; Batani, D.; Desai, T. Surface modifications of Ti6Al4V by a picosecond Nd:YAG laser. *Laser Part. Beams* **2009**, *27*, 85–90. [CrossRef]
50. Milovanović, D.S.; Gaković, B.; Radu, C.; Zamfirescu, M.; Radak, B.; Petrović, S.; Rogić Miladinović, Z.; Mihailescu, I.N. Femtosecond laser surface patterning of steel and titanium alloy. *Phys. Scr.* **2014**, *T162*, 014017. [CrossRef]
51. Trtica, M.S.; Gaković, B.M. Pulsed TEA CO_2 laser surface modifications of silicon. *Appl. Surf. Sci.* **2003**, *205*, 336–342. [CrossRef]
52. Samad, R.E.; Machado, L.M.; Viera, N.D., Jr.; de Rosi, W. Ultrashort Laser Pulses Machining. In *Laser Pulse—Theory, Technology, and Applications*, 1st ed.; Peshko, I., Ed.; BoD GmbH: Hamburg, Germany, 2012; pp. 143–174. [CrossRef]
53. Bonse, J.; Hohm, S.; Kirner, S.V.; Rosenfeld, A.; Kruger, J. Laser-Induced Periodic Surface Structures—A Scientific Evergreen. *IEEE J. Sel. Top. Quantum Electron.* **2017**, *23*, 9000615. [CrossRef]
54. Garrelie, F.; Colombier, J.P.; Pigeon, F.; Tonchev, S.; Faure, N.; Reynauld, S.; Parriaux, O. Evidence of surface plasmon resonance in ultrafast laser-induced ripples. *Opt. Express* **2011**, *19*, 9035–9043. [CrossRef] [PubMed]
55. Ursu, I.; Mihailescu, I.N.; Prokhorov, A.M.; Tokarev, V.N.; Konov, V.I. High-intensity laser irradiation of metallic surfaces covered by periodic structures. *J. Appl. Phys.* **1987**, *61*, 2445–2457. [CrossRef]
56. Bonse, J.; Kruger, J.; Hohm, S.; Rosenfeld, A. Femtosecond laser-induced periodic surface structures. *J. Laser Appl.* **2012**, *24*, 042006. [CrossRef]
57. Dominic, P.; Bourquard, F.; Reynaud, S.; Weck, A.; Colombier, J.-P.; Garrelie, F. On the Insignificant Role of the Oxidation Process on Ultrafast High-Spatial-Frequency LIPSS Formation on Tungsten. *Nanomaterials* **2021**, *11*, 1069. [CrossRef]
58. Peyre, P.; Fabbro, R. Laser Shock Peening: A review of the physics and applications. *Quantum Electron.* **1995**, *27*, 1213–1229. [CrossRef]
59. Peyre, P.; Scherpereel, X.; Berthe, L.; Carboni, C.; Fabbro, R.; Beranger, G.; Lemaitre, C. Surface modifications induced in 316L steel by laser peening and shot-peening. Influence on pitting corrosion resistance. *Mater. Sci. Eng. A* **2000**, *280*, 294–302. [CrossRef]
60. Kumar, A.; Biswas, K.; Basu, B. Hydroxyapatite-titanium bulk composites for bone tissue engineering applications. *J. Biomed. Mater. Res. Part A* **2015**, *103*, 791–806. [CrossRef]
61. Taguchi, G.; Chowdhury, S.; Wu, Y. *Taguchi's Quality Engineering Handbook*; John Wiley & Sons, Inc.: Hoboken, NJ, USA, 2005; pp. 225–228. [CrossRef]
62. Šibalija, T.V.; Majstorović, V.D. Implementation of the Intelligent Method for Multiresponse Process Optimisation. In *Advanced Multiresponse Process Optimisation*, 1st ed.; Šibalija, T.V., Majstorović, V.D., Eds.; Springer: London, UK, 2016; pp. 165–260. [CrossRef]

ПУБЛИКАЦИЈЕ АСТРОНОМСКЕ ОПСЕРВАТОРИЈЕ У БЕОГРАДУ
PUBLICATIONS OF THE ASTRONOMICAL OBSERVATORY OF BELGRADE
Св. 102 No. 102

31st Summer School and International Symposium on the Physics of Ionized Gases

Belgrade, Serbia,
September 5 - 9, 2022

CONTRIBUTED PAPERS

&

ABSTRACTS of INVITED LECTURES, TOPICAL INVITED LECTURES and PROGRESS REPORTS

Editors:
Dragana Ilić, Vladimir Srećković,
Bratislav Obradović and Jovan Cvetić

БЕОГРАД
2022

PUBL. ASTRON. OBS. BELGRADE No. 102, 1 - 302 BELGRADE, AUGUST 2022

31st Summer School and International Symposium on the Physics of Ionized Gases

September 5 – 9, 2022, Belgrade, Serbia

S P I G 2022

CONTRIBUTED PAPERS

&

ABSTRACTS OF INVITED LECTURES,
TOPICAL INVITED LECTURES AND
PROGRESS REPORTS

Editors

Dragana Ilić, Vladimir Srećković,
Bratislav Obradović and Jovan Cvetić

University of Belgrade –
School of Electrical
Engineering

University of Belgrade –
Faculty of Physics

Serbian Academy of
Sciences and Arts

Belgrade, 2022

PUBLICATIONS OF THE ASTRONOMICAL OBSERVATORY OF BELGRADE

FOUNDED IN 1947

All papers in this Publication are peer reviewed.

Director of the Astronomical Observatory: Dr. Gojko Djurašević

Typesetting: Tatjana Milovanov

Internet address http://www.aob.rs

ISSN 0373-3742
ISBN 978-86-82296-02-7

Number of copies / tiraž : 200
Production: Skripta Internacional, Mike Alasa 54, Beograd

CIP - Каталогизација у публикацији - Народна библиотека Србије, Београд

537.56(082)
539.186.2(082)
539.121.7(082)
533.9(082)

SUMMER School and International Symposium on the Physics of Ionized Gases (31 ; 2022 ; Belgrade)

Contributed papers & abstracts of invited lectures, topical invited lectures and progress reports / 31st Summer School and International Symposium on the Physics of Ionized Gases - SPIG 2022, September 5-9, 2022, Belgrade, Serbia ; editors Dragana Ilić ... [et al.]. - Belgrade : Astronomical Observatory, 2022 (Beograd : Skripta Internacional). - 302 str. : ilustr. ; 24 cm. - (Publications of the Astronomical Observatory of Belgrade, ISSN 0373-3742)

Na nasl. str.: University of Belgrade, School of Electrical Engineering; University of Belgrade, Faculty of Physics; Serbian Academy of Sciences and Arts. - Tiraž 200. - Str. 17-18: Preface / editors Dragana Ilić ... [et al.]. - Bibliografija uz svaki rad. - Registar.

ISBN 978-86-82296-02-7

1. Ilić, Dragana, 1978- [уредник] [аутор додатног текста]

а) Јонизовани гасови – Зборници б) Атоми – Интеракција – Зборници в) Плазма – Зборници

COBISS.SR-ID 72751881

SPIG 2022

SCIENTIFIC COMMITTEE

D. Ilić (Co-chair), Serbia
V. Srećković (Co-chair), Serbia

A. Antoniou, Greece
D. Borka, Serbia
J. Burgdörfer, Austria
J. Cvetić, Serbia
V. Guerra, Portugal
M. Ivković, Serbia
K. Kutasi, Hungary
I. Mančev, Serbia
D. Marić, Serbia
N. J. Mason, UK
A. Milosavljević, France
V. Milosavljević, Serbia
K. Mima, Japan
Z. Mišković, Canada
L. Nahon, France
B. Obradović, Serbia
G. Poparić, Serbia
P. Roncin, France
I. Savić, Serbia
Y. Serruys, France
N. Simonović, Serbia
M. Škorić, Japan
M. Trtica, Serbia
S. Tošić, Serbia
R. White, Australia

ADVISORY COMMITTEE

D. Belić
N. Bibić
M. S. Dimitrijević
S. Đurović
N. Konjević
M. M. Kuraica
J. Labat
G. Malović
B. P. Marinković
Z. Mijatović
M. Milosavljević
Z. Lj. Petrović
L. Č. Popović
J. Purić
B. Stanić

ORGANIZING COMMITTEE

J. Cvetić (Co-chair)
B. Obradović (Co-chair)

M. Ignjatović (Co-secretary)
L. Gavanski (Co-secretary)

N. Konjević
N. Cvetanović
T. Gajo
I. Krstić
N. Sakan

Publ. Astron. Obs. Belgrade No. 102 (2022), 239 - 242 *Contributed Paper*

SPECTROSCOPIC CHARACTERIZATION OF LASER-INDUCED PLASMA ON DOPED TUNGSTEN

BILJANA STANKOV[1], MARIJANA R. GAVRILOVIĆ BOŽOVIĆ[2], JELENA SAVOVIĆ[3] and MILIVOJE IVKOVIĆ[1]

[1]*Institute of Physics, University of Belgrade, Pregrevica 118, 11080 Belgrade, Serbia*

[2]*Faculty of Engineering Sciences, University of Kragujevac, Sestre Janjić 6, 34000 Kragujevac, Serbia*

[3]*Vinca Institute of Nuclear Sciences, University of Belgrade, Mike Petrovića Alasa 12-16, 11000 Belgrade, Serbia.*

E-mail ivke@ipb.ac.rs

Abstract. In this paper, the dependence of plasma characteristics, excitation temperature, and electron number density on the presence of fusion relevant doping elements (La and Th) in tungsten is evaluated and compared with a pure tungsten sample. It was found that different doping elements have little to no influence on plasma temperature, while electron number density seems to be more sensitive to the doping element type.

1. INTRODUCTION

The properties of tungsten, i.e., high melting point, high thermal conductivity, and low tritium retention, make it a promising material for fusion-related applications. On the other hand, its high Z number limits allowed concentration in plasma, which, with poor machinability, explosion dust potential, and irradiation-induced transmutations, pose a significant challenge for stable and safe operation. Although a large variety of tungsten grades and alloys already exist, numerous attempts to further optimize these materials are ongoing, Waseem et al., 2016. Investigations are needed to address many different issues related to the plasma-facing material (PFM) performance when exposed to thermal loads, neutron irradiation, and the plasma, Pintsuk et al. 2019. Erosion of tungsten under high localized thermal loads occurring during plasma disruption, vertical displacement events (VDEs), and the edge-localized mode (ELM) have an analogy with W erosion during laser ablation, Oderji et al. 2016. Following this analogy, the present research was undertaken to study plasma properties produced by laser ablation of pure and doped tungsten

(with La and Th) using optical emission spectroscopy methods. Both doping elements are relevant for fusion technology, Gietl et al., 2022, and Raj et al., 2022. The idea is to get insight into the dependence of plasma characteristics on different doping elements present in tungsten targets, which is essential for clarifying the impact of these elements in fusion-related applications.

2. EXPERIMENTAL SETUP

Different tungsten targets (pure W; 98,5%W+1.5%La_2O_3, 98%W+2%ThO_2) were placed on the PC controllable x-y table. A Q-switched Nd:YAG pulsed laser (Quantel, λ = 532 nm, energy 40 mJ, pulse duration 0.6 ns) was used to induce plasma on the target. The laser beam was focused on a target using a lens of 10 cm focal length. Light emitted from a plasma was collected with a fiber optic cable (Ø = 400 μm) and detected using an imaging spectrometer Shamrock 303 Andor equipped with the Andor iStar DH734 camera. The iCCD camera was operated in the full-vertical binning mode and controlled using a pulse generator (DDG 535, Stanford Research Systems). Delay was set to 0.5 μs, and the gate used was 2.5 μs. All measurements were performed in an argon atmosphere at 10 mbar pressure.

3. RESULTS

Typical spectra obtained with the employed setup are shown in Fig 1.

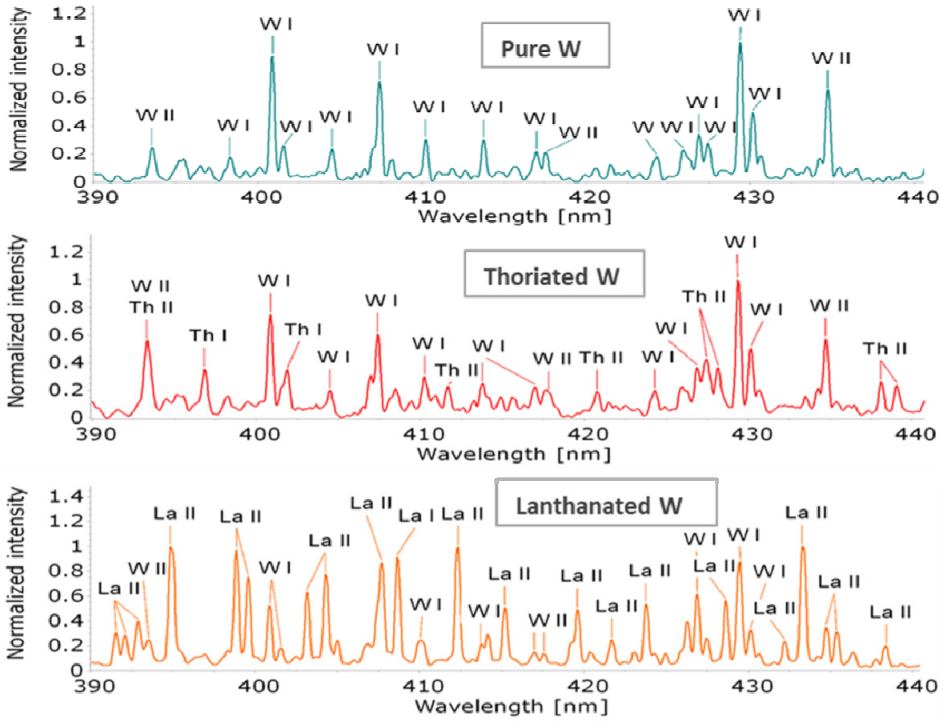

Figure 1: Characteristic LIBS spectra of pure and doped tungsten samples.

The most dominant lines belong to neutral and singly ionized tungsten for all target materials. These rich spectra of tungsten were suitable for excitation temperature determination by a Boltzmann plot method. An example of a Boltzmann plot for a pure tungsten target is given in Fig 2. The excitation temperature, T_{exc} calculated from the lines of singly ionized W was 13500K±1000K, slightly higher than the calculated temperature using neutral W lines (12300K±900K). The observed difference in temperature values obtained from a neutral atom and ion emissions is expected for spatially integrated measurements. As explained by J.A. Aguilera et al., 2004, in that case, the Boltzmann plots of neutral atoms and ions provide two different apparent excitation temperatures that correspond to the respective population averages of the local electronic temperature in the plasma. For all target materials, the obtained temperature values were similar (within the measurement uncertainty), implying an insignificant influence of doping elements on the plasma temperature.

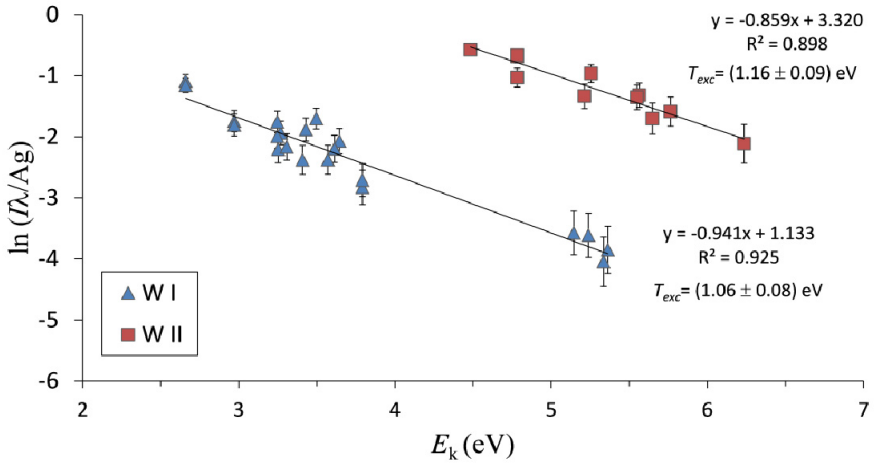

Figure 2: Boltzmann plot used to determine excitation temperature in LIBS plasma induced on a pure tungsten target.

For electron number density, N_e, estimation, a Stark broadening of the H_α line was used, Fig. 3. Based on the FWHM of the H_α spectral line and using the approximative formula (1), N_e was calculated. The results are shown in Table 1.

$$N_e[m^{-3}] = 10^{23} * (w_{SA}[nm]/1.098)^{1.47135} \quad (1)$$

Table 1: Electron number density determined using Stark broadening of H_α line.

Target	H_α	N_e (10^{22} m^{-3})
Pure W	0.503	2.84
Thoriated W	0.557	3.37
Lanthanated W	0.510	2.91

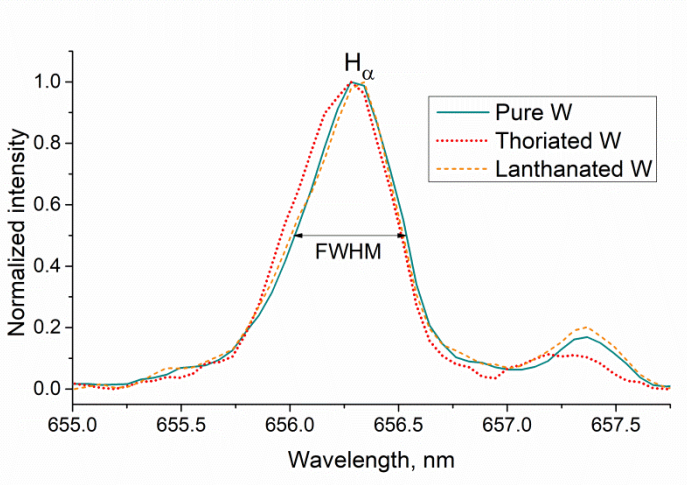

Figure 3: Stark broadened H_α line profiles used to evaluate N_e.

4. CONCLUSION

Different doping elements seem to have a negligible impact on laser-induced plasma excitation temperature. Electron number density shows slightly higher values in the case of thoriated W compared both to pure and lanthanated tungsten. A possible reason for this is the lower energy needed for significant erosion of thorium doped tungsten, already observed in experiments with tungsten-based cathodes, Casado et al., 2002. For a deeper understanding of the influence of doping elements on plasma properties, temporally and spatially resolved measurements are needed and are currently underway.

Acknowledgements

The research was funded by the Ministry of Education, Science and Technological Development of the Republic of Serbia, Contract numbers: 451-03-68/2022-14/200024 and 451-03-68/2022-14/200017, and supported by the Science Fund of the Republic of Serbia, Grant no. 3108/2021.

References

Oderji H.Y., Farid N., et al.: 2016, *Spectrochimica Acta Part B*, **122**, 1.
Pintsuk G., Hasegawa A.: 2019, *Comprehensive Nuclear Materials 2nd edition*, Elsevier.
Waseem O., Ryu H.J.: 2016, *Nuclear Material Performance*, Chapter 7, InTech.
Aguilera J.A., Aragón C.: 2004, *Spectrochimica Acta Part B*, **59**, 1861.
Gietl H., et al. 2022 *Journal of Alloys and Compounds*, **901**, 163419.
Raj D., Kannan U.: 2022, *Annals of Nuclear Energy*, **174**, 109162.
Casado E., Colomer V., et al.: 2002, *J. Phys. D: Appl. Phys*., **35**, 992.

Publ. Astron. Obs. Belgrade No. 103 (2024), 152 *Poster*
https://doi.org/10.69646/aob103p152

DETECTION OF RHENIUM IN TUNGSTEN USING LIBS WITH ADDITIONAL FAST PULSE DISCHARGE

IVAN TRAPARIĆ, BILJANA STANKOV and MILIVOJE IVKOVIĆ

Institute of Physics Belgrade, Pregrevica 118, 11080, Belgrade
E-mail traparic@ipb.ac.rs
E-mail biljanas@ipb.ac.rs
Email ivke@ipb.ac.rs

Abstract. The diagnostics of the first wall of future fusion reactors represents a major source of information about the state of the machine and the expected lifetime of the first wall components. As the absorption of neutrons can cause induced radioactivity of the first wall tiles, it is of the essence to monitor the amount of absorbed neutrons. One possibility to monitor them is via nuclear transmutation reaction where tungsten absorbs neutron and create rhenium core [1]. Therefore by assessing the amount of rhenium present in the material, the number of absorbed neutrons can be deduced. In this work Laser Induced Breakdown Spectroscopy (LIBS) combined with fast pulse discharge was used to assess the concentration of rhenium. The main result is the amplification of line intensity and signal to noise ratio compared to the classical LIBS setup at reduced pressure. This results is of particular importance since only small amounts of rhenium are expected to be found, therefore making this approach suitable for this type of diagnostics. Additionally, univariate calibration method based on intensity ratio of W I 488.7 nm and Re I 488.9 nm spectral lines was proposed for determination of rhenium concentrations.

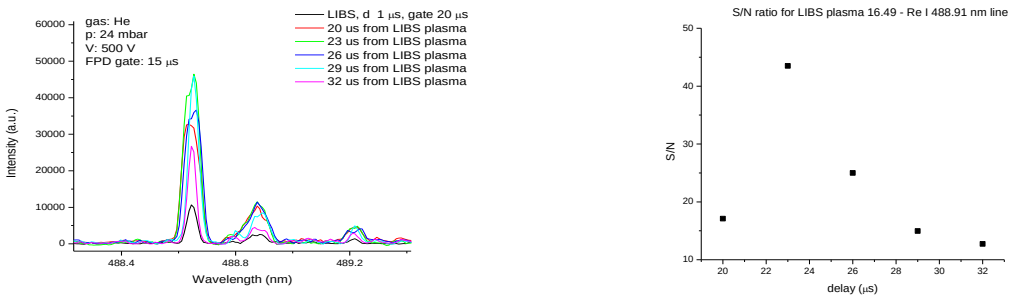

Figure 1: Amplification of Re I 488.9 nm line intensity with FPD (left) and resulting signal to noise ratio (right).

References

Ibano et al, *Journal of Nuclear Materials* **522** (2019) 324-328

Publ. Astron. Obs. Belgrade No. 103 (2024), 147 *Poster*
https://doi.org/10.69646/aob103p147

FAST PHOTOGRAPHY IN THE SERVICE OF SPATIALLY AND TEMPORALLY RESOLVED LIBS DIAGNOSTICS OF DOPED TUNGSTEN

BILJANA STANKOV[1], MARIJANA R. GAVRILOVIĆ BOŽOVIĆ[2], DRAGAN RANKOVIĆ[3], JELENA SAVOVIĆ[4] and MILIVOJE IVKOVIĆ[1]

[1]*Institute of Physics, University of Belgrade, Pregrevica 118, 11080 Belgrade, Serbia*
[2]*Faculty of Engineering, University of Kragujevac, Sestre Janjić 6, 34000 Kragujevac, Serbia*
[3]*Faculty of Physical Chemistry, University of Belgrade, 11158 Belgrade, Serbia*
[4]*Vinca Institute of Nuclear Sciences, University of Belgrade, Mike Petrovića Alasa 12-16, 11000 Belgrade, Serbia.*
E-mail biljanas@ipb.ac.rs

Abstract. The spectroscopic diagnostic of laser induced plasma is challenged by its spatial inhomogeneity and dynamic evolution, which simultaneously alters plasma parameters and emission of ablated material in plasma plume (Lazic at al. 2006, A. Singh at al. 2010). Those difficulties become more pronounced when conducting spatially and temporally resolved measurements. Choosing appropriate conditions for LIBS, such as delay time, gate width, and observed plasma section is paramount. At atmospheric pressure, plasma tends to stay more localized in the vicinity of the target, with specific flattened shape. In contrast, plasma expanding into low pressure exhibits rapid and pronounced dispersion, potentially causing plasma to move out of the field of view, and/or not being captured completely. This can make determing the time of the maximum plasma emission intensity challenging. In this study influence of different additives in tungsten samples on plasma plume dynamics and expansion is investigated and possible impact on the spectroscopic diagnostics is assesed.

Acknowledgements. The research was funded by the Ministry of Science, Technological Development and Innovations of the Republic of Serbia, Contract numbers: 451-03-68/2022-14/200024 and 451-03-65/2024-03/200146, and supported by the Science Fund of the Republic Serbia, Grant no. 7753287 "NOVA2LIBS4fusion".

References

V. Lazic and S. Jovicevic: 2006, *Spectrochimica Acta Part B: Atomic Spectroscopy*, vol. **61**, no. 7, 856

A. Singh and P. K. Rai, "Challenges in Diagnostics of Laser-Induced Plasma," *Journal of Physics D: Applied Physics*, **vol. 43**, no. 43, p. 434013, 2010.

Publ. Astron. Obs. Belgrade No. 103 (2024), 153 *Poster*
https://doi.org/10.69646/aob103p153

INFLUENCE OF THE ABLATION ANGLE CHANGE ON SPECTRAL LINE INTENSITIES IN LIBS EXPERIMENTS

IVAN TRAPARIĆ*, BILJANA STANKOV, NIKOLA VUJADINOVIĆ, MILICA VINIĆ and MILIVOJE IVKOVIĆ

Institute of Physics Belgrade, Pregrevica 118, 11080, Belgrade
**Corresponding author: traparic@ipb.ac.rs*

Abstract. Laser Induced Breakdown Spectroscopy - LIBS is the most promising technique for the in-situ analysis of the plasma fusion reactor walls, see (Cong Li at al, 2016). The setup which is most frequently used in fusion reactors is so-called remote in-situ RIS LIBS, see (Cai et al, 2019). This configuration uses a scanning system which controls the Mo mirror to direct the laser beam to a different position inside the fusion reactor. In this study, it was investigated how changes in the ablation angles affect the intensity of the emitted spectral lines, considering that the incident beam is not always perpendicular to the PFCs. To this end, the classical LIBS setup at atmospheric pressure was employed. The angle of collection fiber with respect to the laser beam was fixed to 17 degrees. Chosen targets were tungsten-based alloys relevant to fusion research. The spectrum of the plasma was recorded with a Solar MS7504i spectrometer and a fast camera. Results show that there is a non-trivial dependance of the line intensity on the ablation angles, which was attributed to the change of laser focus and ablation surface as the angles were varied both in poloidal and toroidal directions. Additionally, the line intensity correction factor was calculated as the ratio of the intensity for the beam incident at an angle to that of the beam at normal incidence, and it exhibited a complex dependence on both angles.

Acknowledgements
The research was funded by the Ministry of Education, Science and Technological Development of the Republic of Serbia, Contract number: 451-03-68/2022-14/200024, and supported by the Science Fund of the Republic Serbia, Grant no. 7753287.

References

Cong Li at al.: 2016, Front. Phys. **11**, 114214.
Laizhong Cai et al.: 2019, Rev. Sci. Instrum. **90**, 053503.

Publ. Astron. Obs. Belgrade No. 103 (2024), 85 *Poster*
https://doi.org/10.69646/aob103p085

TARGET SELECTION FOR LIBS STUDIES OF HYDROGEN ISOTOPE RETENTION

DRAGAN RANKOVIĆ[1], BILJANA STANKOV[2], IVAN TRAPARIĆ[2], MIROSLAV KUZMANOVIĆ[1] and MILIVOJE IVKOVIĆ[2*]

[1]*Faculty of Physical Chemistry, University of Belgrade, 11158 Belgrade, Serbia*
[2]*Institute of Physics, University of Belgrade, Pregrevica 118, 11080 Belgrade, Serbia*
[*]*E-mail ivke@ipb.ac.rs,*

Abstract. The study of the hydrogen's isotope retention in the first wall of the fusion reactors is the main task in diagnostics of plasma facing components (PFC). Laser Induced Breakdown Spectroscopy (LIBS) enables in-situ PFC diagnostics without any sample preparation making it a most promising technique for this purpose, see H.J. van der Meiden et al, 2021. The basis of this diagnostics is the measurement of the emission of hydrogen isotopes Balmer alpha lines. The most challenging task is the resolving of these lines. Therefore, the first task was the selection and preparation of the targets from which, due to the laser irradiation and consequent plasma formation, hydrogen and deuterium spectral lines will be emitted. Such targets should be substitutes of the hydrogen isotopes enriched components of PFC of future fusion reactors. The main idea was to use the heavy water D_2O embedded in various substrates that are good absorbers of water. For this purpose, following substrates were tested: NaCl - salt, copper sulfate pentahydrate $CuSO_4 \cdot 5H_2O$ - known as blue vitriol or blue stone, active coal - charcoal, microporous aluminosilicates - zeolites, calcium carbonate $CaCO_3$ - quicklime, $CaSO_4 \cdot 2H_2O$ – gypsum. Several forms of graphite were also considered: factory made graphite discs, electrodes with controlled amount of the D_2O on it and spectroscopically pure (or mixed with silica gel) graphite powder, which was doped with water before or after pressing it by hydraulic press. Testing was performed using a 6 ns Q – switched Nd:YAG and TEA CO_2 laser (having 80 ns pulse with 2 μs long tail) in low pressure argon or helium atmosphere. The best results are obtained using gypsum and graphite doped with silica gel, see Traparic at al 2024.

Acknowledgements. The research was funded by the Ministry of Science, Technological Development and Innovations of the Republic of Serbia, Contract numbers: 451-03-68/2022-14/200024 and 451-03-65/2024-03/200146, and supported by the Science Fund of the Republic Serbia, Grant no. 7753287 "NOVA2LIBS4fusion".

References

Van der Meiden, H.J. et al. : 2021, *Nucl. Fusion.* **61** 125001
Traparic, I et al.: 2024, submitted to *Spectrochimica Acta B*

Serbian Ceramic Society Conference
ADVANCED CERAMICS AND APPLICATION XII
New Frontiers in Multifunctional Material Science and Processing

Serbian Ceramic Society
Institute of Technical Sciences of SASA
Institute for Testing of Materials
Institute of Chemistry Technology and Metallurgy
Institute for Technology of Nuclear and Other Raw Mineral Materials
Institute of General and Physical Chemistry

PROGRAM AND THE BOOK OF ABSTRACTS

Serbian Academy of Sciences and Arts, Kneza Mihaila 35
Serbia, Belgrade, 18-20. September 2024.

Serbian Ceramic Society Conference
ADVANCED CERAMICS AND APPLICATION XII
New Frontiers in Multifunctional Material Science and Processing

Serbian Ceramic Society
Institute of Technical Sciences of SASA
Institute for Testing of Materials
Institute of Chemistry Technology and Metallurgy
Institute for Technology of Nuclear and Other Raw Mineral Materials
Institute for General and Physical Chemistry

PROGRAM AND THE BOOK OF ABSTRACTS

Serbian Academy of Sciences and Arts, Kneza Mihaila 35
Serbia, Belgrade, 18-20th September 2024.

Book title: Serbian Ceramic Society Conference - ADVANCED CERAMICS AND APPLICATION XII Program and the Book of Abstracts

Publisher:
Serbian Ceramic Society

Editors:
Dr. Nina Obradović
Dr. Lidija Mančić

Technical Editors:
Dr. Adriana Peleš Tadić
Dr. Jelena Živojinović
Dr. Marina Vuković

Printing:
Serbian Ceramic Society, Belgrade, 2024.

Edition:
120 copies

CIP - Каталогизација у публикацији Народна библиотека Србије, Београд

666.3/.7(048)
66.017/.018(048)

SRPSKO keramičko društvo. Conference Advanced Ceramics and Application : New Frontiers in Multifunctional Material Science and Processing (12 ; 2024 ; Beograd)
Program ; and the Book of abstracts / Serbian Ceramic Society Conference Advanced Ceramics and Application XII New Frontiers in Multifunctional Material Science and Processing, Serbia, Belgrade, 18-20. September 2024 ; [editors Nina Obradović, Lidija Mančić]. - Belgrade : Serbian Ceramic Society, 2024 (Belgrade : Serbian Ceramic Society). - 82 str. ; 28 cm

Tiraž 120.

ISBN 978-86-905714-1-3

a) Керамика -- Апстракти b) Наука о материјалима -- Апстракти

COBISS.SR-ID 151937545

activated electrode surface and its interaction with HER intermediates, is expected to help understanding the electrode process from the fundamentals to the application level.

INV17

Spectroscopic Analysis of Beryllium Ceramics

Biljana D. Stankov

Institute of Physics, University of Belgrade, Pregrevica 118, 11080 Belgrade, Serbia
biljanas@ipb.ac.rs

Beryllium and beryllium ceramics are highly valued for their exceptional properties crucial in aerospace, telecommunications, and nuclear reactors. They boast superior thermal conductivity, electrical insulation, and mechanical strength, essential for electronic substrates, heat sinks, and as neutron reflectors in reactors such as ITER. Their resilience in challenging environments, including fusion reactors, underscores their versatility. This study utilizes beryllium ceramics to compare two experimental designs for spectroscopic observation of beryllium lines. The first design involves the erosion of beryllium ceramics, leading to the production of beryllium dust critical for plasma diagnostics and erosion monitoring. This novel plasma source was developed to safely record beryllium lines, optimizing conditions for spectral line appearance and measuring electron density and temperature. In the second design, efforts are focused on preventing dust production to ensure a dust-free environment for precise measurements. This comparison highlights the differences in experimental design and their implications for studying beryllium spectral lines. It investigates the impact of dust on line parameters, offering insights into the utilization of beryllium ceramics in advanced scientific and industrial applications.

INV18

HEMP COMPOSITES: A Sustainable Alternative for Advanced Material Applications

Stevan N. Blagojević

Institute of General and Physical Chemistry, Studentski trg 12/V, Belgrade, Serbia

Hemp composites have emerged as a promising material in the field of sustainable engineering due to their unique combination of mechanical properties, environmental benefits, and cost-effectiveness. This study explores the potential of hemp-based composites as an alternative to conventional synthetic materials, focusing on their mechanical properties, biodegradability, and potential applications in various industries.
The research investigates the preparation, characterization, and performance evaluation of hemp fiber-reinforced composites. The results highlight the significant impact of fiber treatment processes and composite manufacturing techniques on the overall properties of the final material. By comparing hemp composites with traditional materials such as glass and carbon fibers, the study emphasizes the advantages of hemp in terms of weight reduction, energy efficiency, and lower environmental footprint.

European Winter Conference on Plasma Spectrochemistry

Ljubljana, Slovenia,
January 29th – February 3rd , 2023

Book of Abstracts

Book of abstracts of the 19th European Winter Conference on Plasma Spectrochemistry

Publisher:
National Institute of Chemistry
Hajdrihova 19
1000 Ljubljana
Slovenia

Editors:
Vid Simon Šelih and Martin Šala, National Institute of Chemistry, Slovenia

Graphical design:
Repster

Ljubljana, January 2023
Publication is not for sale

Kataložni zapis o publikaciji (CIP) pripravili v Narodni in univerzitetni knjižnici v Ljubljani
COBISS.SI-ID 139103747
ISBN 978-961-6104-85-2 (PDF)

Study of the beryllium spectral line shape using Laser Induced Breakdown Spectroscopy

Marijana Gavrilović Božović[1], Biljana Stankov[2], Miroslav Kuzmanović[3], MilivojeIvković[2]

[1]Faculty Of Engineering Sciences University of Kragujevac, Kragujevac, Serbia, [2]Institute of Physics University of Belgrade, Belgrade, Serbia, [3]Faculty of Physical Chemistry, University of Belgrade, Belgrade, Serbia

Beryllium is a naturally occurring element in metal-poor stars and has been chosen as the element to cover the first wall of ITER (International Thermonuclear Experimental Reactor).Erosion of beryllium under transient plasma loads will determine the lifetime of the ITER first wall, so the presence of Be dust particles in plasma should be monitored. In addition, the Be deposits on other fusion reactor components should be studied by, for example, a calibration-free LIBS method. This method requires determination of the plasma parameters, which can be derived from the parameters and shape of the Be spectral lines. The study of the Be lines shapes was performed using spectra recording of the plasma emission due to interaction of the fourth harmonic Nd:YAG laser radiation at 266 nm, pulse energy 70 mJ at 10 Hz repetition rate with the BeO target. The target made from BeO ceramics was rotated by the motor in the low-pressure chamber. The 1:1 image of the plasma plume was projected by optical mirrors on the entrance slit (20 μm wide) of a 0.5 m Ebert-type spectrometer with an iCCD camera operated in the image mode and controlled using a pulse generator (DDG 535, Stanford ResearchSystems) triggered optically by the plasma. The plasma emission was accumulated over 160 ablation events to exclude the influence of shot-to-shot fluctuations in the signal. The acquisition gate width was 100 ns. Since previous studies have shown some discrepancies between obtained line shape parameters and theory2, the main task was to enable spatially and temporally resolved measurements of Be lines of interest, which was readily achievable with the used experimental setup. Careful inspection of the ablation and plasma creation process provided insurance that the dust-free environment is indeed obtained in the experimental setup. This is a quite important aspect since dust can have a significant influence on the line shape parameters. Knowledge about its impact on the line shapes will be highly beneficial in the future, where large amount of ITER-related dust is expected to be formed and interfere with the plasma and its emission. Further improvement of this study is the possibility of testing the less obvious influence of self-absorption on the line shapes and intensities. This was achieved using the setup with the lens and flat mirror3.

beryllium, LIB S, spectral line shapes, plasma diagnostics, plasma fusion reactor

Stankov et.al., Rev. Sci., 2018, 89,053108.

Stankov et.al., EPL, 2018, 123, 63001.

Konjević, Physics reports, 1999, 316 (6), 339-401.